Parity Violation and Cold Neutron Capture: A study of the detailed interaction between hadrons

by

Mark McCrea

A thesis submitted to
The Faculty of Graduate Studies of
The University of Manitoba
in partial fulfillment of the requirements
of the degree of

Doctor of Philosophy

Department of Physics and Astronomy
The University of Manitoba
Winnipeg, Manitoba, Canada
September 2016

Thesis advisor

Michael Gericke

Author

Mark McCrea

Parity Violation and Cold Neutron Capture: A study of the detailed interaction between hadrons

Abstract

Despite decades of theoretical and experimental investigation, the fundamental interactions between nucleons remains poorly understood. While the strong interaction is responsible for binding quarks into nucleons, and nucleons into nuclei, there is no consistent description of these processes. At the low energies where nucleon binding occurs, the interactions are in principle calculable from quantum chromodynamics, but the required non-perturbative calculations are not possible. Instead different models have been created to describe different phenomena.

These models require experimental input to constrain them. As the expected weak interaction effects are not seen in the strangeness-conserving systems as have been seen in other systems, it is believed that the strong interaction interferes with the weak interaction. Therefore by measuring parity-violating observables that occur due to the weak interaction, information can be gained about the strong interaction.

The NPDGamma and n3He experiments are two complementary experiments that measured a parity violating observables in a few nucleon system. They ran on the Fundamental Neutron Physics Beamline at the Spallation Neutron Source.

The NPDGamma experiment measured the parity violating directional asymmetry

in the gamma ray's emission direction after polarized cold neutron capture on a liquid parahydrogen target using an array of 48 CsI detectors.

The n3He experiment measured the parity violating directional asymmetry in the proton emission direction after polarized cold neutron capture on a gaseous ^{3}He target. The capture occurs inside an ionization chamber that measures the proton emission direction.

Both experiments have completed data taking with data analysis in an advanced state. These experiments should be able to be used with a number of already existing experimental results to constrain the models.

I designed and assembled a pair of ^{3}He ionization chambers that were used as beam monitors during the experiments. Using the lessons learned from the beam monitors, I then designed and assembled the ionization chamber that is the combined target and detector for the n3He experiment. The monitors and target chamber were examined to determine their charge collection properties and linearity after installation. One of the monitors was calibrated to determine the neutron flux from the output current.

Contents

List of Tables

List of Figures

Contributions

- I constructed, tested and calibrated a pair of beam monitors (M1 and M2) used on the SNS FnPB beam line.
- NPDGamma Experiment
  - Tested a number of pressure transducers that were to be used on the NPDGamma gas handling system and on other high vacuum applications at the FnPB by comparing them with a known good gauge.
  - Helped assemble and helium leak test part of the hydrogen target fill and vent lines.
  - Tested the linearity of the Artefax preamps that were used to read out the M1 and M2 beam monitors, using a variable voltage source with a series of resistors.
  - Testing NPDGamma DAQ electronics
    - Measured transients at start of 8 step pulse sequence.
    - Aided in spin flipper troubleshooting
    - Tested LED light injection setup that was used to perform systematic tests of the vacuum photodiodes that were used to read out the CsI detector crystal light.
  - Took part in assembly of and data taking with a mock-up hydrogen vessel used to benchmark simulations for neutron scattering from the aluminum in the real hydrogen target vessel.

  - Performed linearity testing of the M3 beam monitor using cadmium collimators of various sizes to vary the neutron flux on the target.
  - Took shifts for several months during NPDGamma data taking.

- n3He Experiment
  - Designed and assembled n3He target frame stack.
  - Designed adapter plug for preamp boards to signal feed throughs
  - Modified preamp board housing design for forced air cooling, and added power and signal cable feed throughs.
  - Leak tested target housing.
  - Bench top testing of the n3He target prior to installation.
  - Took 1 week of shifts monitoring n3He experiment.
  - Analyzed data from target chamber voltage scan.
  - Analyzed run data to examine target linearity.

Acknowledgments

I would like to thank my adviser, Michael Gericke for all of the help he has been to me during my studies. It is with his aide that I have been able to complete my studies.

I would like to thank the members of the NPDGamma and n3He Collaborations whom I worked with at the FnPB. In particular, I would like to thank Seppo Penttilä for his instruction while working at the FnPB. I would also like to thank David Bowman and Geoff Greene for their help during my time there as well. I would also like to thank the other students who were on these collaborations who helped me significantly both with my work, and with transport around Oak Ridge.

I would like to thank my advisory committee for their input and oversight over the years.

I would also like to thank my family for their support during the last several years.

Chapter 1

Introduction

While the fundamental interaction between nucleons has been investigated for decades it has been described as pathologically complicated. While in principle calculable from quantum chromodynamics (QCD), in practice the calculations are not possible, and we are forced to rely on a number of models for different phenomena [1]. These models require experimental input, and this thesis describes the work towards a set of precision measurements of the interactions between nucleons using cold neutrons. As the calculations of the interactions in these experiments cannot be done from descriptions of the basic interactions between the fundamental particles following the interactions described in the so-called Standard Model as would be preferred, other approximate models must be used. Two of these models along with the Standard Model are introduced below.

1.1 Theoretical Motivation

While it is known that the strong force is responsible for binding quarks into hadrons such as protons and neutrons, it is also responsible for binding the individual nucleons into atomic nuclei. There is currently no consistent description of how this happens. The resolution of this problem is currently one of the main experimental and theoretical goals of the international subatomic physics community. The study of the strong interactions at low energy (where binding happens) has been challenging both theoretically and experimentally and many different experimental approaches are being pursued.

The Standard Model of particle physics is a theory that describes the interactions between particles. While since its development in the 1970's it has had enormous success in explaining the results of a wide range of experiments and predicting many new phenomena, it is not a complete picture. Of the four fundamental forces, the electromagnetic, weak and strong forces are included in the Standard Model, but gravity is not. Dark matter and dark energy are also not part of the Standard Model[2]. Due to its broad range of applications, it is a primary effort within the subatomic physic community to verify and extend the Standard Model.

In the Standard Model the fundamental particles are split into three groups: leptons, quarks, and gauge bosons. The lepton group is made up of the electron, muon and tau along with a corresponding neutrino for each. The quark group is comprised of 6 quarks labeled up, down, strange, charm, top, and bottom. There are 5 types of gauge bosons, the gluon, photon, W, Z and Higgs. Each particle has a corresponding antiparticle with the same mass and opposite electric charge. The fundamental parti-

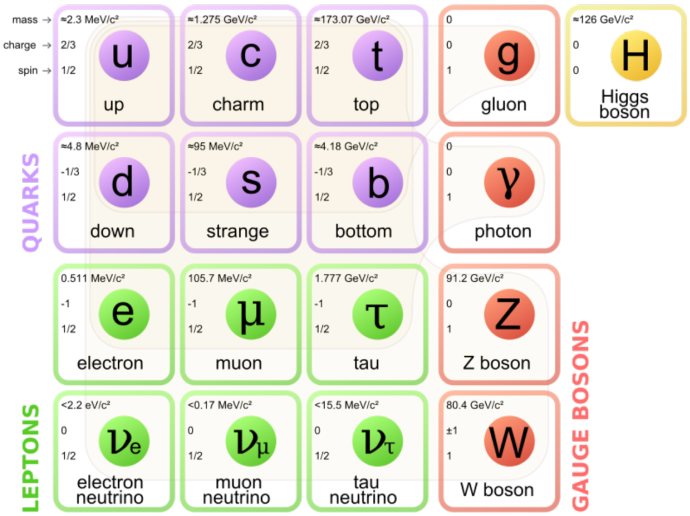

Figure 1.1: The fundamental particles in the Standard Model [3].

cles are believed to have no substructure and are the basis for constructing composite particles. Figure 1.1 lists all of the fundamental particles in the Standard Model.

Interactions in the Standard Model between the fundamental particles are mediated by virtual exchange particles. The gauge bosons are the exchange particles for the fundamental interactions. The electromagnetic interaction is mediated by the massless photon. The weak interaction is mediated by the massive charged $W^{\pm}$ and the neutral Z bosons. The strong interaction is mediated by eight gluons. The Higgs boson plays a special role in the Standard Model and is responsible for mass generation in the theory rather than mediating a force [4](Ch.11). Gravity is currently not part of the Standard Model.

It is the goal of the Standard Model to describe all the observed properties of these fundamental particles and forces such that the properties of composite particles such as neutrons, protons, nuclei, atoms, and molecules can be calculated. It is desired to do this in a way that consistently and properly predicts observed phenomena while

reducing the need for experimental input.

One method of probing the low energy strong interaction is to use the weak interaction. The Standard Model gives a consistent theoretical description of the weak interaction at both the nucleon (neutron and proton) and nuclear level, but in strangeness-conserving neutral current ($\Delta S = 0$) experiments, where ΔS is the change in the number of strange quarks between the initial and final states, the predicted weak interaction effects are not seen as they are in strangeness-changing charged current ($\Delta S = 1$) experiments. It is not known why, but the only possible explanation is that the strong dynamics modify or suppress the weak interaction differently in $\Delta S = 0$, than they do for $\Delta S = 1$ processes, which would require some as of yet unexplained aspect of the strong interaction to be present. As the weak interaction is mediated by massive exchange particles, the W and Z, it is a short-ranged force. Hadronic weak interactions (HWI's) are sensitive to first order to the quark-quark correlations in the interacting hardrons. Measurements of weak effects can provide information about strong dynamics at low energy where the bound nucleons are close together when one compares precision experimental data with various strong interactions models [5].

It is hard to experimentally measure the weak interaction effects in the presence of the much larger strong interaction effects. However, the weak interaction is the only one of the four fundamental forces to violate parity. Thus any measured parity violating signals must arise due to the effect of the weak interaction. This and the fact that the weak interaction acts at short range allows precision measurements of parity violating signals to be used to set the model parameters that determine the

relative strengths of the strong and weak interactions between nucleons. The weak interactions are understood on a fundamental level and any deviation from what might be expected based on the weak interaction can be attributed to strong dynamics.

1.2 Effective Theories

1.2.1 Meson Exchange Models

At low energy, the strong interaction is usually described in terms of nucleons as the fundamental particle rather than quarks, and with mesons as the exchange particles. The weak interaction takes place when one of the quarks in the meson exchanges a $W^{\pm}$ or Z^0 with the quark in the nucleon, while the rest of the quarks interact strongly via gluon exchange. It is the interference between the strong and the weak interaction in these processes that has the potential to tell us something about the models we use for low energy, non-perturbative strong interactions, which cannot currently be calculated from first principles.

One of the meson exchange models for nucleon interactions is the so-called DDH model. This was the first complete theory of this type and was proposed by Desplanque, Donahue, and Holstein [6]. In this model the nucleon-nucleon weak interaction is implemented as a parity-violating weak vertex, a parity-conserving strong vertex, and a meson being exchanged between the vertices. See figure 1.2.

In this approach the theoretically calculated observables are parameterized in terms of seven weak meson-nucleon coupling constants denoted as h_π^1, h_ρ^0, h_ρ^1, h_ρ^2, h_ω^0, h_ω^1, and $h_\omega^{1'}$ where the subscript denotes the exchange meson and the superscript

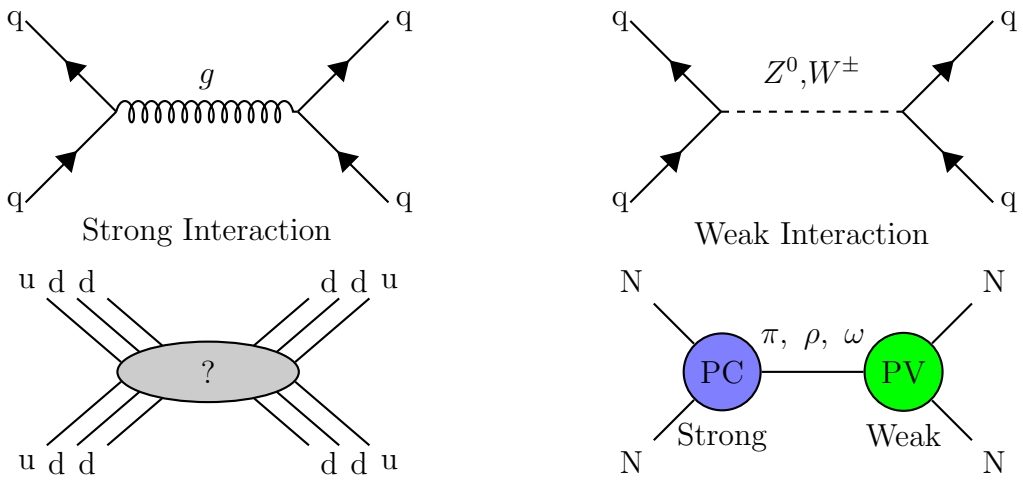

Figure 1.2: Different interactions between the fundamental particles are mediated by different exchange bosons, gluons for the strong interaction or $W^{\pm}$ and Z for the weak interaction. In the DDH model a meson is emitted from the parity conserving (PC) vertex which changes to a massive W or Z boson for the weak interaction at the parity violating (PV) vertex.

indicates the isospin change [7]. Some particles are similar enough in their strong interactions that they can be grouped into isospin multiplets and changes in isospin state change the particle type within that group. Protons and neutrons form one such group. Table 1.1 shows the best value ranges for the DDH coupling constants. The large range in the constants arises due to significant uncertainties in the evaluation of the hadronic matrix elements.

Weak Meson-Nucleon Coupling Constants

Couplings	Cabbibo		Weinberg-Salam	
	Range	Best Value	Range	Best Value
h_π^1	$0 \to 1$	0.5	$0 \to 30$	12
h_ρ^0	$-64 \to 16$	-25	$-81 \to 30$	-30
h_ρ^1	$-0.7 \to 0$	-0.4	$-1 \to 0$	-0.5
h_ρ^2		-58	$-20 \to -29$	-25
h_ω^0	$-22 \to 6$	-6	$-27 \to 15$	-5
h_ω^1	$-2 \to 6$	-1	$-5 \to -2$	-3
$h_\omega^{1'}$	Not Reported		Not Reported	

Table 1.1: DDH "best" value and reasonable range for six of the seven weak meson-nucleon coupling constants. Values are given in units of $1/g_{\pi NN}$ ($g_{\pi NN} = 3.8 \times 10^{-8}$) [8].

1.2.2 Effective Field Theory Models

While a significant discussion of the effective models used to describe the hadronic weak interaction is beyond the scope of this thesis, the basic idea is outlined below, to put the experimental work described here into the broader physics context.

Effective Field Theory (EFT) is an approximation method that can be used to make accurate calculations of problems involving widely separated energy scales. By constructing an effective Lagrangian that includes all possible terms that take into account the symmetries of the assumed fundamental theory, a most general Lagrangian can be constructed. This most general Lagrangian can be expanded in powers of Q/Λ where Q is the energy of interest for calculations and Λ, the scaling factor, is chosen so that $Q \ll \Lambda$, and the leading order terms identified with a method known as power counting. Each term in the expansion has an associated low-energy constant (LEC) that needs to be determined from experiment before calculations can be done.

Reference [1] reviews EFTs for few nucleon systems and their construction.

For parity violation (PV) in nucleon-nucleon (NN) interactions the energy scales of interest are the hadronic scale $\Lambda_{Had} \approx 1\,\mathrm{GeV}$, the pion mass $m_\pi = 140\,\mathrm{MeV}$, the pion decay constant $F_\pi = 93.2\,\mathrm{MeV}$, and the typical momentum Q relevant to a PV hadronic or nuclear process [9]. As QCD is the fundamental theory to describe NN interactions, its symmetries must be incorporated into the EFT and for PV NN interactions so must parity violation and isospin change up to $\Delta I = 2$.

At energies of $Q < 50\,\mathrm{MeV}$ a pionless EFT having 5 LECs and no dynamical pions can be used. A group of six or possibly seven experiments is needed to over-constrain the pionless EFT to determine all of the LECs. As the pion is the lowest-mass meson, as energies increase a long-range pion exchange needs to be incorporated into a pionful theory which has 8 LECs to be determined from experiment. Reference [10] goes into detail on the formulation of the EFTs for nuclear parity violation.

In the $\Delta S = 1$ HWI sector, experiments measuring the effect of the HWI have given rise to a number of mysteries such as the well-known $\Delta I = 1/2$ rule when no apparent symmetry favours the $I = 1/2$ channel over the $I = 3/2$ channel. Anomalously large radiative decay asymmetries of hyperons have also been measured, given what is known of the SU(3) symmetries [9]. With these and other issues, it is hoped information gained about the HWI with new few nucleon experiments in the $\Delta S = 0$ sector can shed more light on the interference of the weak and strong interactions taking advantage of the ability of EFT theories to make calculations in these systems.

1.3 What is Parity?

A parity transformation, P, is a transformation in which the spatial vectors are inverted. That is the vector component x goes to $-x$, y to $-y$ and z to $-z$. An inversion in position also inverts momentum, but angular momentum is unchanged as

$$\mathbf{L} = \mathbf{r} \times \mathbf{p} = P(\mathbf{L}) = P(\mathbf{r}) \times P(\mathbf{p}) = (-\mathbf{r}) \times (-\mathbf{p}) = \mathbf{L}. \tag{1.1}$$

The handedness of a system is then defined by the relative direction of the position or momentum and angular momentum vectors that enter into the process forming either a left or right handed coordinate system. If the observed or measured result has a different value that depends on the relative direction of the position, momentum, and angular momentum vectors, then it is parity violating.

An absolute direction that does not change under a parity transformation is needed. This can be done using two or more detectors fixed in space such that detection of emitted particles corresponds to emission in opposite directions with respect to the location of the decaying particle. The angular momentum of a particle in such an experiment can be fixed by placing the experiment in a magnetic field. The parity violating observable would be the measured number of particles emitted in opposite directions. This was part of the technique used in the discovery of parity violation in the beta decay of ^{60}Co by C.S. Wu and co-workers [11].

Systematic effects usually prevent simple measurements of the number of particles emitted in each direction from being used to extract a parity-violating observable. Additional information is needed. Furthermore, in experiments using accelerators

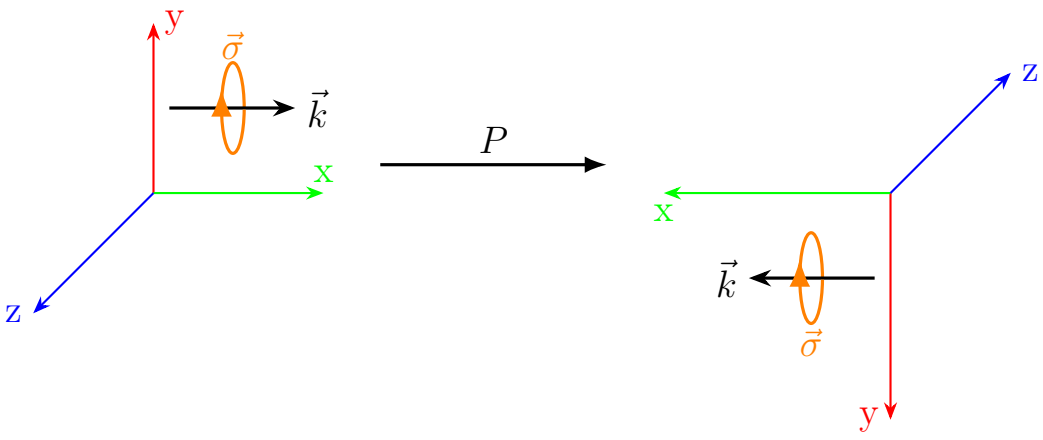

Figure 1.3: Applying a parity transformation to a coordinate system takes a left handed system into a right handed system. A vector such as momentum $\vec{k}$ will change sign under the tranformation, but axial vectors such as spin $\vec{\sigma}$ do not change sign. Applying a second parity transformation will return the transformed state to the untransformed state.

the momentum direction is fixed by the accelerator position relative to the scattering center and detectors. Under these conditions a parity transformation by reversing the position and momentum is not possible. A different method is needed to fix a reference direction that is unchanged by a parity transformation.

The angular momentum or spin of a particle can be used to define a reference direction as these are axial vectors, and axial vectors are unchanged under a parity transformation. The position and momentum can then be defined relative to either the spin or angular momentum of a particle. An effective parity transformation can then be made by reversing the direction of the spin or angular momentum if the position and momentum remain constant and the detectors are not dependent on the spin or angular momentum. NPDGamma and n3He both use this method. The

neutron beam in each experiment is polarized, and a radio frequency spin rotator is used to reverse the neutron spin on a pulse by pulse basis before the capture target. Figure 1.4 illustrates this effective parity transformation using the n3He reaction.

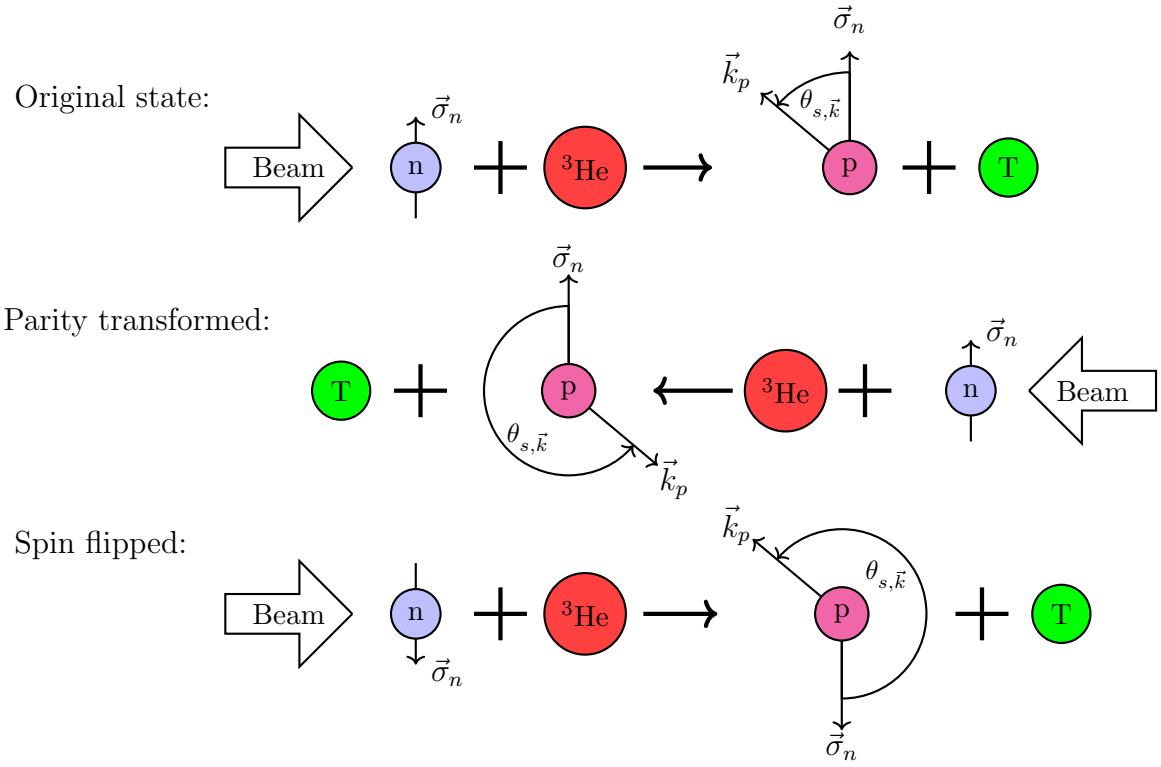

Figure 1.4: Parity transformation illustrated with the n3He reaction. The beam arrow indicates the direction of the neutron beam. As can be seen, the Parity transformed diagram is equivalent to the Spin flipped diagram with a rotation. See section 2.4 for more details on the n3He experiment.

1.4 Experiments

NPDGamma and n3He are two complimentary experiments that are designed to investigate the HWI. They ran consecutively at the Fundamental Neutron Physics Beamline (FnPB) at the Spallation Neutron Source (SNS). Many experiments have been done to study the $\Delta S = 1$ sector of the hadronic weak interaction (charged currents), using non-leptonic kaon and hyperon (excited nucleon) decays. However, for the study of how nucleons and nuclei are formed, the more interesting problem is the study of the strangeness-conserving hadronic weak interaction. NPDGamma and n3He both investigate the $\Delta S = 0$ branch of the hadronic weak interaction, and rely on measuring parity-violating observables to isolate interference effects between the weak and strong interactions.

The presence of the parity-violating signal is due only to the weak interaction effects. The observed HWI parity signal is much smaller than what would be expected based on first-principle calculations from the weak interaction in simple (few nucleon) systems alone, and it is expected that this is primarily the result of some undetected strong interaction dynamics. So if a given model of the strong interaction can predict the modifications to the weak interaction as seen in low energy systems, you can learn something about strong dynamics. Low energy in this context is around the energy levels where nucleon-nucleon binding occurs. Pionless EFT calculations are done for the approximate size of the asymmetries in the NPDGamma and n3He experiments in the references [12] and [13], respectively.

The NPDGamma experiment involves the capture of polarized cold neutrons on protons forming deuterons with the parity-violating emission of a photon in the re-

action $\vec{n} + p \rightarrow d + \gamma$. See section 2.3 for more information on the NDPGamma Experiment. The deuteron is the most loosely bound nuclear system, with a binding energy of 2.224 MeV. This means that the longest-range components of the nucleon-nucleon weak interaction provide the greatest contribution to the asymmetry. The lightest and thus longest-range exchange meson is the pion. The NPDGamma physics asymmetry is calculated in the DDH model as

$$A_{NPDG} = -0.107h_{\pi}^{1} - 0.001h_{\rho}^{1} + 0.003h_{\omega}^{1}.$$

Of these three contributions the pion contribution, h_{π}^{1}, is the most significant one. As the NPDGamma reaction is only a two-body system, its calculation is not complicated by nuclear structure.

The n3He experiment involves the capture of polarized cold neutrons on ^{3}He and the parity-violating emission of a proton and triton in the reaction $\vec{n}+^{3}He \rightarrow^{4} He^{*} \rightarrow p + T$. The star on the ^{4}He* intermediary state indicates it is in an excited state. See section 2.4 for more details on the n3He experiment. For the n3He experiment the interaction is more complicated than for NPDGamma, since the reaction involves more nucleons and a more tightly bound system. The asymmetry is sensitive to the following combination of DDH coupling constants:

$$A_{n3He} = -0.1821h_{\pi}^{1} - 0.1447h_{\rho}^{1} + 0.0267h_{\rho}^{1} + 0.0012h_{\rho}^{2} - 0.1269h_{\omega}^{0} + 0.0495h_{\omega}^{1}.$$

In the DDH framework, the n3He experiment is an important parity-violating measurement because it is an independent probe of the HWI couplings. With NPDGamma, the already existing ^{18}F measurements, the odd-proton nuclear measurements, and p-p scattering at two different energies, there are four different few-body systems. As

the $\Delta I = 1$ coupling constants are small and have a narrow reasonable range, n3He can be used to over-constrain the values of the four coupling constants h_π^1, h_ρ^0, h_ρ^2, and h_ω^0 [14]. This also applies to the more modern effective field theories.

Chapter 2

Experiment Overviews

2.1 Spallation Neutron Source

The SNS is an accelerator-driven, pulsed spallation neutron source located in the Oak Ridge National Lab in Tennessee. For spallation neutron production a high energy particle beam, usually protons, is directed at a thick target of high-mass-number nuclei. After the high-energy particle collides with the target nucleus, a large number of low-mass particles will be ejected. Neutrons tend to be the most common particle created in this process. The number of neutrons produced scales roughly linearly with the mass number of the target nucleus, and with the particle energy up to approximately 1 GeV. [15]

At the SNS, 2.5 MeV H^- bunches are created in an ion source. A linear accelerator is used to increase the energy of these bunches to 1 GeV. Exiting the linear accelerator the H^- ions are passed through a stripper foil to remove the electrons to form H^+ ions, which are bare protons. Proton pulses exiting the foil are stored in an accumulator

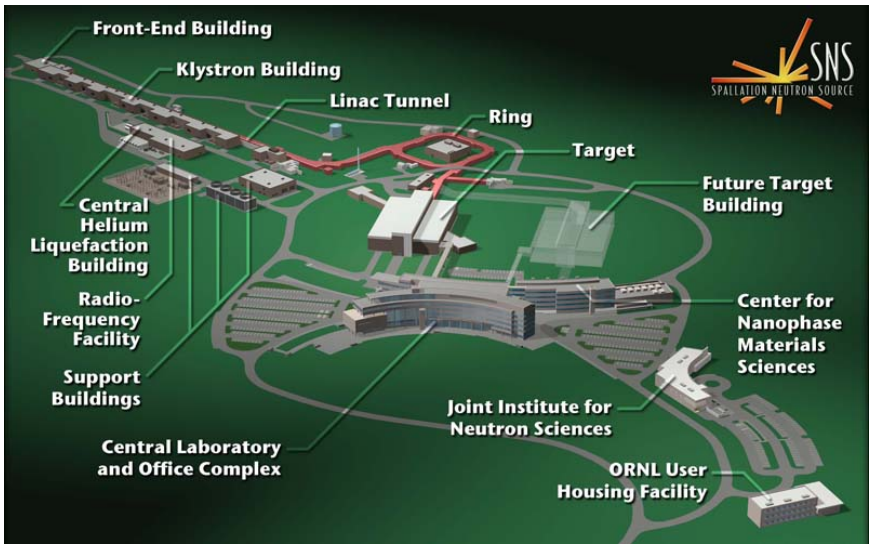

Figure 2.1: Rendering of the Spallation Neutron Source [16].

Figure 2.2: Aerial photograph of the SNS from September 2012 [17].

ring to build up the pulse amplitude and to reduce the pulse width. After sufficient accumulation, proton pulses with a width of less than a microsecond are then released to impact a liquid mercury spallation target with a 60 Hz repetition rate. On average 20-30 neutrons are produced per proton [18][19]. Unlike a continuous neutron source, a pulsed source allows the time structure of the beam to be used during experiments to look at the neutron energy and to examine backgrounds. This is the main advantage of pulsed sources compared to either reactor or continuous accelerator neutron sources. The advantage of reactor sources is that they often provide a higher neutron flux than accelerator sources.

2.2 The Fundamental Neutron Physics Beamline

For the FnPB, the high energy spallation neutrons are cooled through interactions in a 20 K liquid-hydrogen moderator. This produces so-called cold neutrons, with a Maxwell-Boltzmann energy distribution related to the temperature of the moderator. Fig. 2.3 shows a comparison between the measured and simulated neutron flux measured at the end of the beam guide where this pulse shape is evident. In general cold neutrons are considered to be neutrons that have energies of less than 25 meV corresponding to a de Broglie wavelength of 1.8 Å.

The low energy of cold neutrons makes it possible for them to be reflected from so-called neutron supermirror surfaces [20]. The FnPB neutron guide uses a layered supermirror to increase the maximum angle of reflection of neutrons in the guide to minimize the loss of cold neutrons as they are reflected inside the guide. The guide is rectangular, 10 cm horizontal by 12 cm vertical. The guide has a curved bender

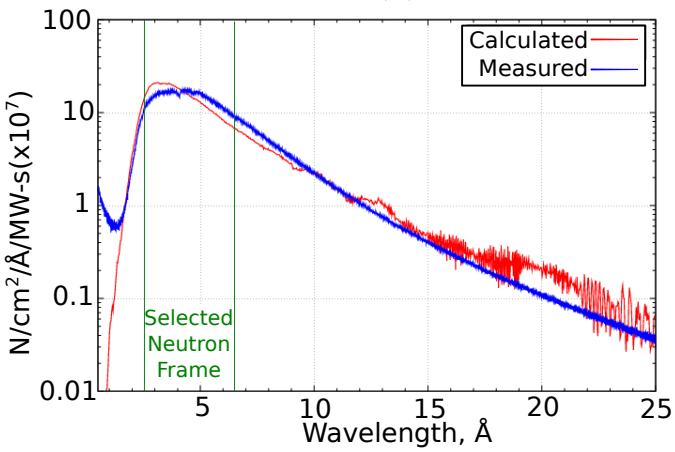

Figure 2.3: SNS unchopped neutron pulse comparison of calculated to measured values. This plot shows the Maxwell-Boltzmann distribution of energies for the neutrons exiting the moderator after thermalization. The upward curve on the left hand side of the measured data is where the end of the previous pulse is overlapping with the start of the next pulse. The green lines show the neutron window that will be selected with the choppers.

shortly after the moderator to remove direct line of sight to the moderator from the cave to reduce backgrounds from the spallation process. The bender is a large radius curved supermirror that is used to change the beam direction with minimal neutron losses. By removing line of sight to the moderator the number of spallation products other than the neutrons reaching the experiments is significantly reduced. Fig. 2.4 shows the layout of the FnPB after the moderator leading up to the experimental cave.

Two shutters are used on the beamline. The shutters are used to block the passage of the neutron beam down the guide to allow access to the experiment cave. The primary shutter is located near the moderator as shown in fig. 2.4. A section of the

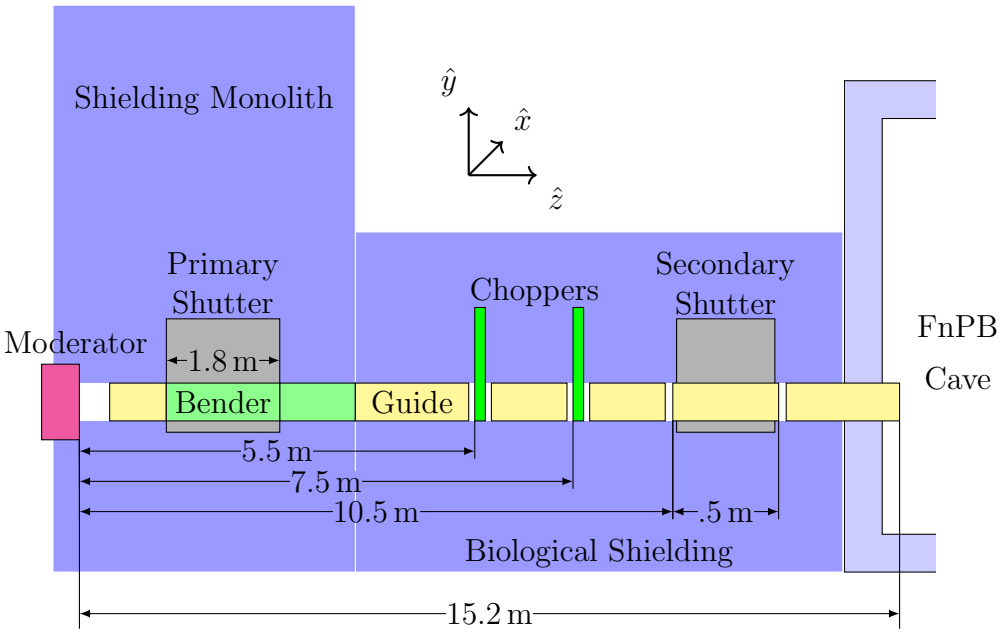

Figure 2.4: Schematic diagram of the FnPB beamline. Dimensions are from reference [21]. Objects are not to scale.

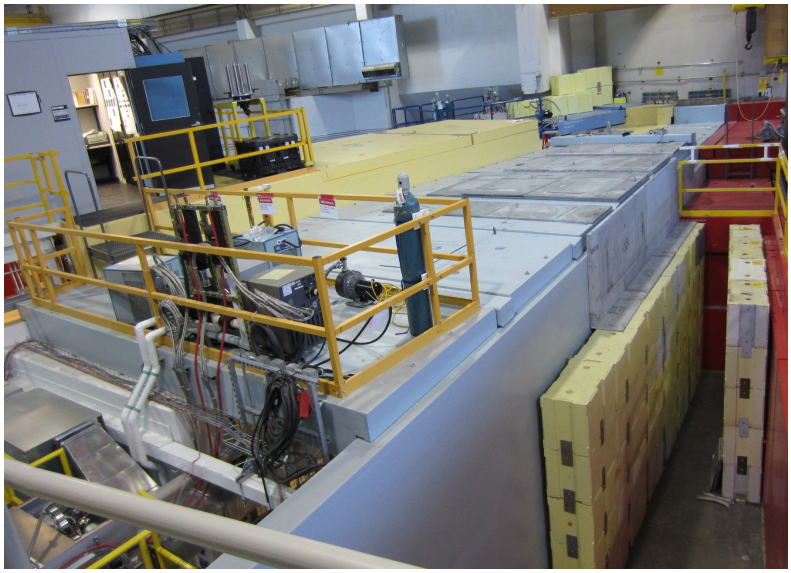

Figure 2.5: The exterior of the FnPB cave. Only the concrete shielding is visible. The FnPB beamline shielding is painted light blue while the adjacent beamlines are yellow and red.

bender passes through the primary shutter and moves with it when the shutter is opened or closed. The secondary shutter is a 0.48 m long cylinder of steel with a ^{6}Li neutron shield absorber on one end. A 0.5 m piece of beam guide passes axially through the shutter and can be rotated out of alignment with the guide to stop neutrons from entering the cave. The secondary shutter is used to block the neutron beam during regular access to the cave.

Two neutron choppers are installed on the beamline. The choppers are used to select the energy window of each neutron pulse that reaches the cave. Each chopper is a large carbon fiber disk coated with ^{10}B to absorb neutrons. Each disk has a single neutron window without the boron coating. When the windows are aligned with the guide, neutrons can pass. The size of the window in each chopper is different and was determined from simulation, based on the neutron spectrum needed for the experiments [22]. The chopper rotation is synchronized with the 60 Hz proton pulse timing such that the choppers complete one rotation per neutron pulse. The width of the window in each chopper determines the length of time it is open per pulse.

The neutrons produced by each proton pulse on the mercury target will exit the moderator at essentially the same time. Because of this, neutrons of different energies from one proton pulse will arrive at the same location at different times. Due to the range of neutron energies exiting the moderator, it is possible for slow neutrons from an earlier pulse to reach the experiment area at the same time as fast neutrons from a later pulse. For the NPDGamma and n3He experiments, it is desired to have a unique neutron energy at each neutron time of flight after a proton pulse. By controlling the phase of the chopper rotation, a selected neutron energy range can be admitted into

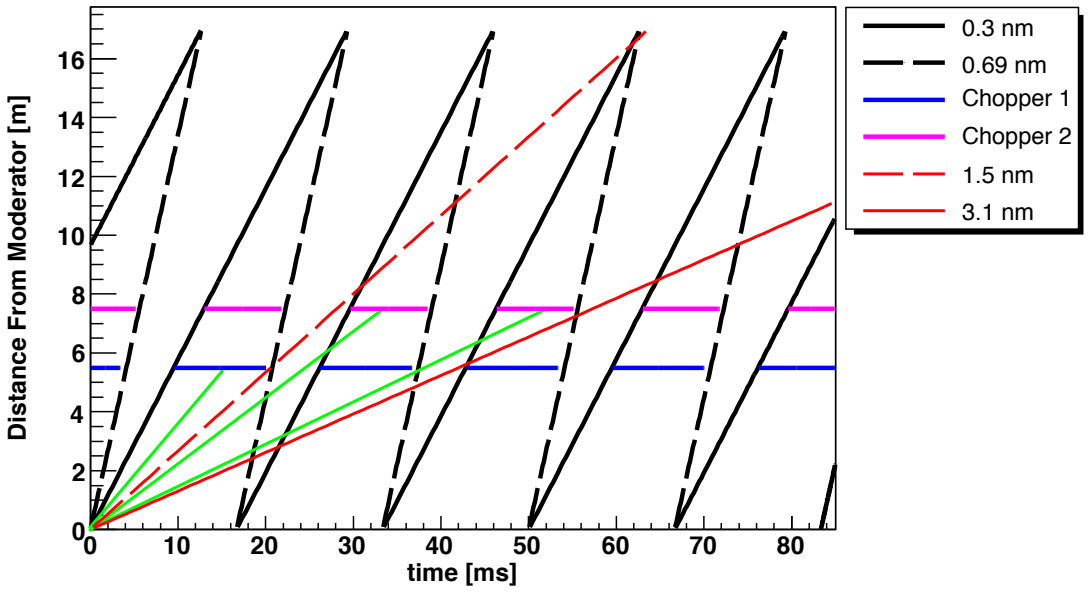

Figure 2.6: For the two choppers, that are located 5.5 and 7.5 meters from the moderator as shown in fig. 2.4, the phasing of the choppers determines the wavelength window that will exit the beam guide. This figure is from reference [8].

the experimental cave while preventing most overlap between pulses.

After a neutron exits the moderator, the time it takes a neutron to travel down the beam guide to the experiment is determined by its velocity. For a non-relativistic subatomic particle the following relations exist between its energy E, wavelength λ, and velocity v:

$$E = \frac{1}{2}mv^2 \quad \rightarrow \quad v = \sqrt{2E/m}, \tag{2.1}$$

$$E = \frac{\hbar^2}{2m\lambda^2} \quad \rightarrow \quad \lambda = \sqrt{2mE/\hbar^2}. \tag{2.2}$$

Fig. 2.6 shows how the choppers can be phased to select the desired energy range for the experiments while preventing overlap between the pulses. The solid horizontal lines for chopper 1 and chopper 2 show the time period for which neutrons are blocked

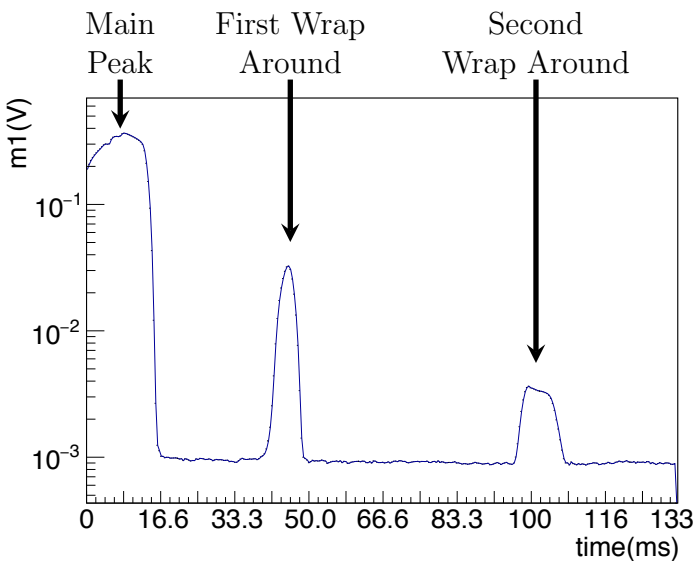

Figure 2.7: Chopped neutron pulse showing main peak and two wrap-around peaks. The data were taken at a 1 Hz pulse rate using the M1 monitor and NPDGamma DAQ. The marked x-axis divisions are for the start times of the 60 Hz pulses with the first pulse at $t = 0$.

from passing through the beam guide for the corresponding positions. The sloped lines show the position of the neutrons along the guide relative to the moderator as a function of time, relative to the time of emission from the moderator. The slope of the lines is proportional to the neutron velocity which is a function of the inverse neutron wavelength. The lines for 0.3 nm and 0.69 nm indicate the extreme neutron wavelength that will make it through to the experimental area, for this particular set of chopper settings. All neutrons with energies corresponding to wavelengths between 0.3 nm and 0.69 nm will also pass the choppers. The 1.5 nm and 3.1 nm lines show how slow neutrons from an earlier pulse can evade the choppers to arrive at the experiment three and four pulses later. Neutrons that originate in one pulse and

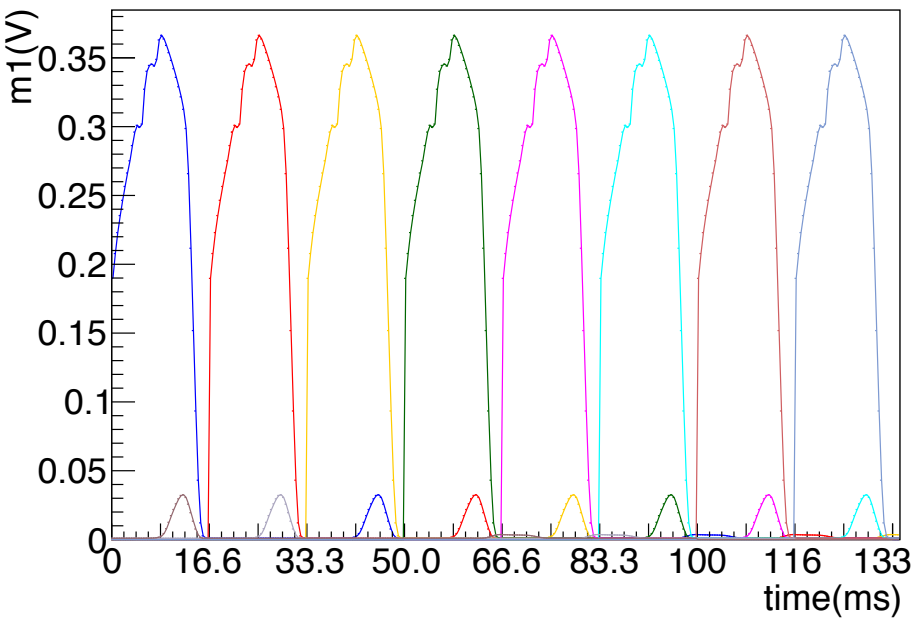

Figure 2.8: The 1 Hz chopped pulse from fig. 2.7 overlayed at 60 Hz repetition rate to show the location of wrap-around neutrons between pulses. Neutrons from each pulse have the same line color. The wrap-around neutrons from the blue pulse can be seen at roughly 47 and 100 ms for example.

arrive in later pulses are called wrap-around or frame-overlap neutrons. The green lines show neutrons with two example energies that would be stopped by the choppers. Fig. 2.3 shows a full, unchopped, neutron pulse, while fig. 2.7 shows a chopped pulse with two wrap-around peaks after the main pulse.

Normally the SNS operates at a 60 Hz, and fig. 2.8 shows a set of 1 Hz pulses overlayed with each other at the 16.66 ms intervals that 60 Hz pulses occur at. The first wrap-around neutron peak is visible two pulses after the main peak. During real 60 Hz running, the neutron signal from all neutrons captured in each time bin will sum together. Fig. 2.9 shows 60 Hz data taken with the M1 monitor where one

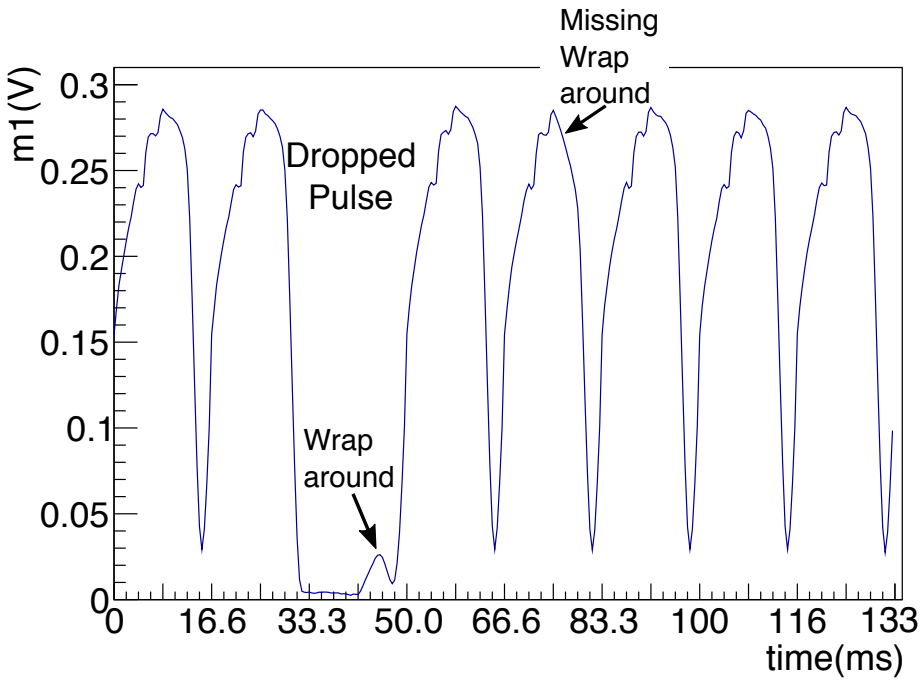

Figure 2.9: For this real 60 Hz pulse data, with the third pulse dropped in the sequence, the first wrap-around neutron peak from two pulses earlier is visible, and two pulses later a deficit is seen in the peak where the wrap-around neutrons are missing.

of the pulses was dropped by the facility. A dropped pulse occurs when the proton pulse is not sent to the spallation target, and no neutrons are produced. The first wrap-around neutron peak is visible from two pulses prior where the missing pulse is and two pulses after the missing pulse there is a deficit in the peak shape on the right-hand side where the first wrap-around peak from the missing pulse would have occurred. The effect of the second wrap-around peak is too small to be easily visible.

Figs. 2.10 and 2.11 show the neutron time of flight (ToF) spectrum as measured in the M1 and M2 monitor, respectively. These plots were taken using the fast DAQ inputs that are normally used for the spin flipper that has 1000 time bins per pulse

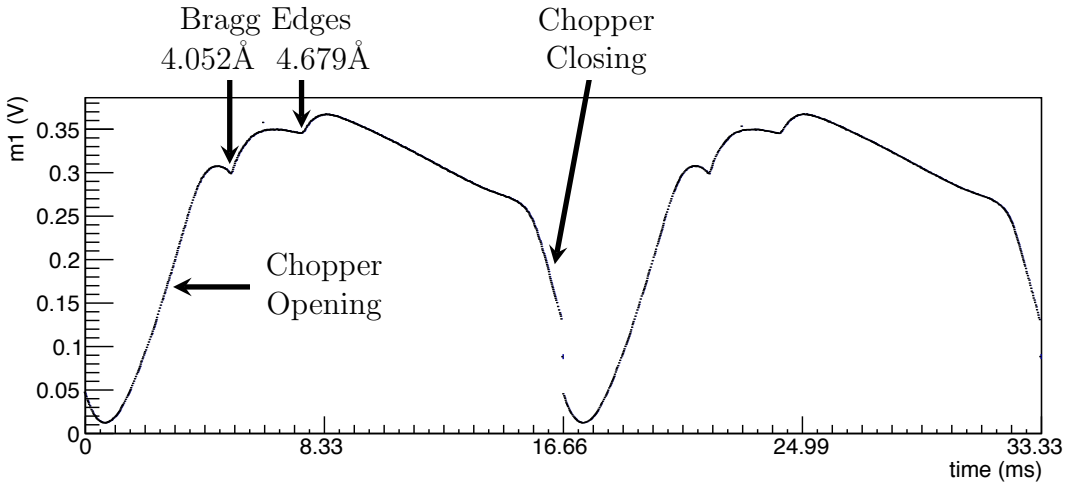

Figure 2.10: 60 Hz neutron pulse spectrum in the M1 monitor taken using high speed DAQ to better the pulse features.

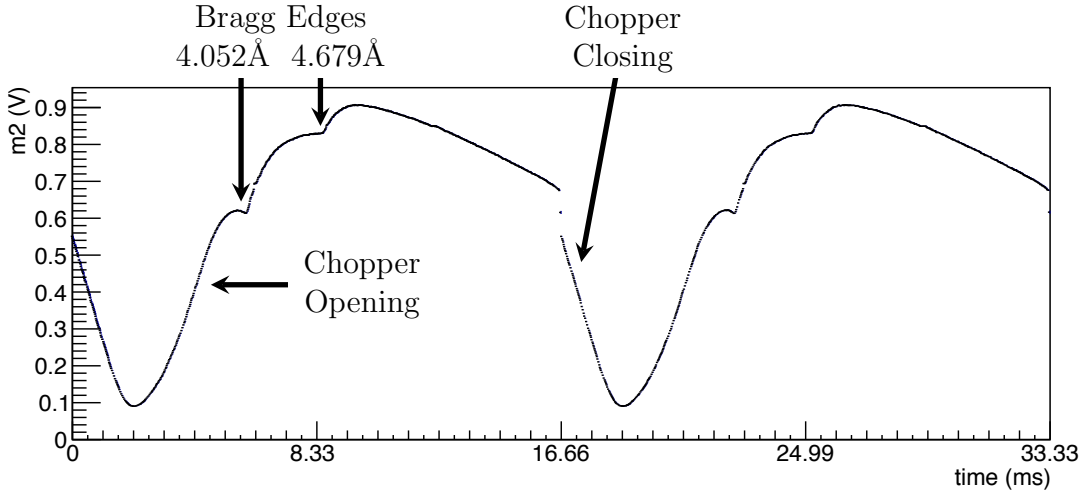

Figure 2.11: 60 Hz neutron pulse spectrum in the M2 monitor taken using high speed DAQ to show better show the pulse features.

rather than the 40 time bins that were used for most data taking to better show the features of the pulse. See section 2.3.1 for information on the NPDGamma DAQ. Visible in the peak are two valleys. These are the Bragg edges where, due to the crystal structure of the aluminum in the beam guide, Bragg scattering removes neutrons at specific wavelengths. The two Bragg edges here are at 4.052 Å, and 4.679 Å[23]. Also visible is the opening and closing of the chopper. Comparing the two plots, it can be seen that the peak features are shifted to later time in the M2 monitor than in the M1 monitor, due to M2 being further from the moderator. The M2 pulse shape is also altered by passing through the supermirror polarizer between the monitors.

The SNS requires less than 0.25 mrem per hour combined neutron and γ-ray radiation outside of an experimental cave. Extensive biological shielding is used around the beam guide and the cave. The beam guide is surrounded first by up to 5 cm of steel and is then encased in 3.96 m high concrete shielding. The cave walls consist of 0.45 cm thick concrete, and a 4.5 m^3 concrete beam stop is placed 6.91 m from the upstream end of the cave. In addition $2.5-5$ cm of A1010 steel are used in the interior of the cave for magnetic shielding from the surrounding area. Fig. 2.5 shows the exterior of the cave and beam guide shielding. There were additional steel plates added to the top of the cave over the supermirror polarizer, and concrete blocks stacked to the right-hand side of the beam line due to higher than anticipated radiation levels at those locations.

2.3 NPDGamma Experiment

The NPDGamma experimental goal is to measure the directional asymmetry in the emission of 2.2 MeV γ-rays, after the radiative capture of polarized cold neutrons on a liquid para-hydrogen target to an uncertainty of 1×10^{-8} [24], in the reaction

$$\vec{n} + p \rightarrow d + \gamma. \tag{2.3}$$

The only experimentally known fact about this asymmetry is that it is smaller than $\sim 2 \times 10^{-7}$ according to the previous NPDGamma measurement at LANSCE [5]. One other measurement was attempted of this observable with the result: $A_{PV} = (0.6 \pm 2.1) \times 10^{-7}$ [25]. The theoretical predictions for the asymmetry are on the order of 5×10^{-8}.

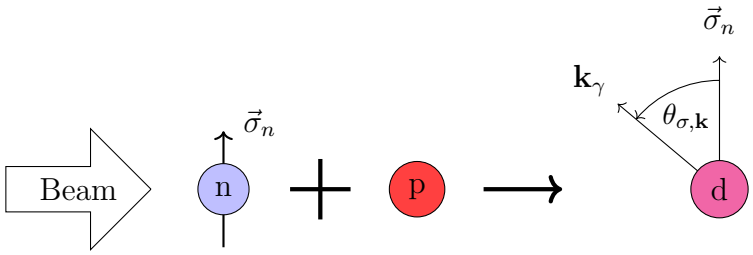

Figure 2.12: NPDGamma reaction schematic.

When the polarized cold neutron captures on a proton in the hydrogen target, the initial capture is an excited ${}^3S_1$ or ${}^1S_0$ state. This will decay by an electromagnetic transition to the final deuteron bound state of ${}^3S_1$. The most probable transition is an M1 transition from the ${}^1S_0$ initial state to the ${}^3S_1$ bound state. The weak interaction can be treated as a perturbation to the strongly interacting system and will introduce a number of possible of P-wave states that can mix with the initial and final S-wave

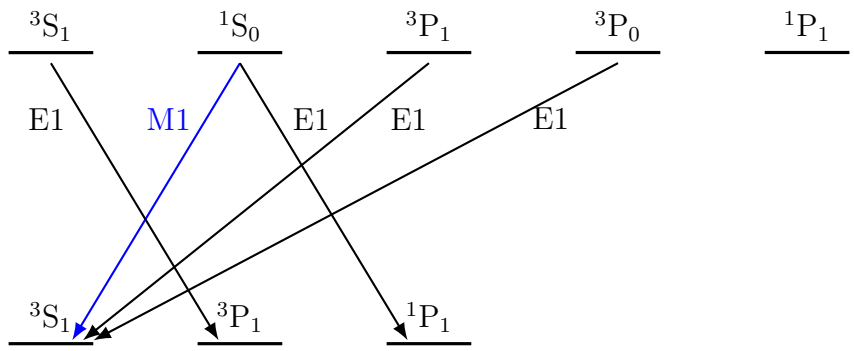

Figure 2.13: Level diagram for initial capture state of the proton and polarized neutron and final deuteron bound states. The mixing of the S and P wave states arises from the weak interaction and the additional E1 transitions to or from P wave states causes the parity-violating γ-ray distribution.

states. The presence of the mixed states allows for E1 transitions as shown in fig. 2.13. It is the interference between the M1 and E1 transitions that gives rise to the parity-violating γ-ray distribution. See reference [26] chapter 2 for more details on calculations of the asymmetry.

2.3.1 Experimental Setup

Fig. 2.14 shows a schematic of the experimental setup, fig. 2.15 shows a CAD model of the installation and fig. 2.16 is a picture of the installed experiment in the FnPB cave.

The data acquisition system (DAQ) for the NPDGamma experiment used a 16-bit analog-to-digital converter (ADC) to measure the output signals from the various experimental components. Using the T0 signal provided by the facility to indicate when a proton pulse was sent to the mercury target, the DAQ would collect data

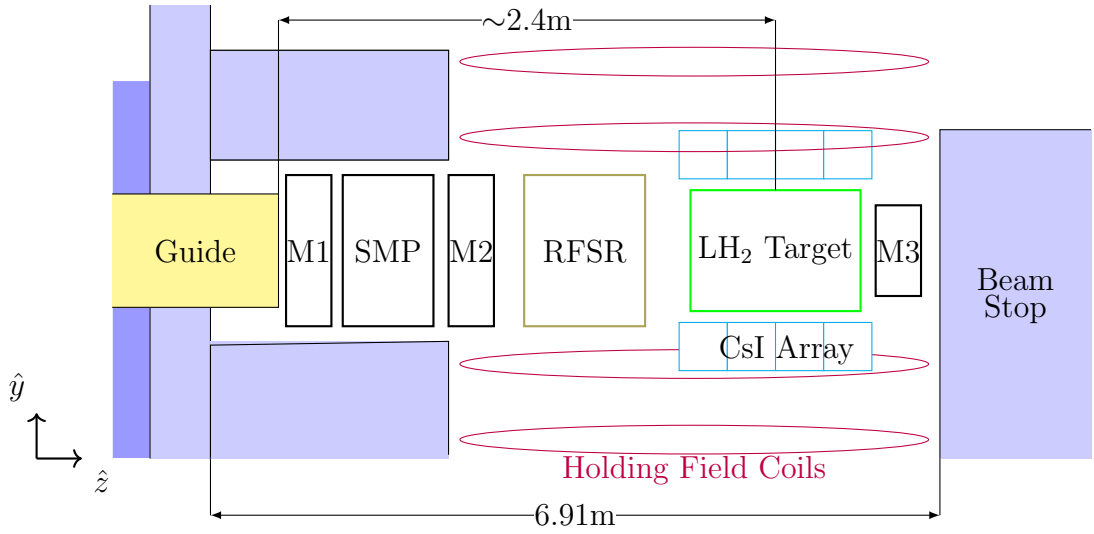

Figure 2.14: NPDGamma schematic diagram. Objects are not to scale.

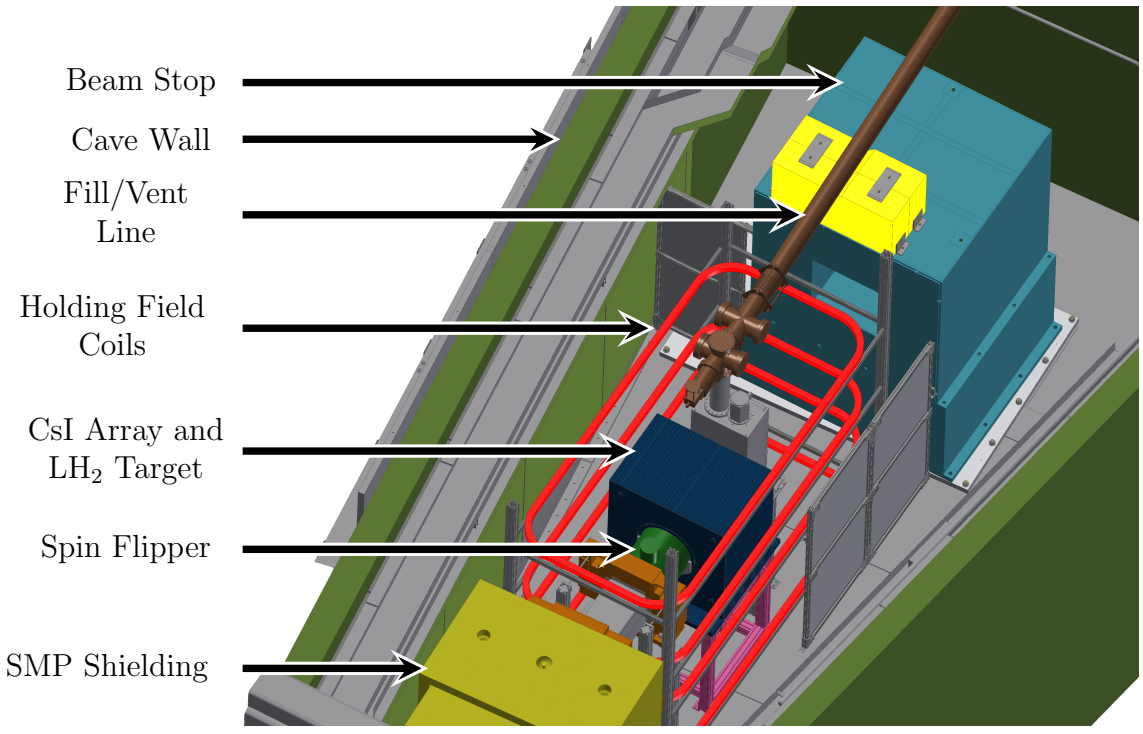

Figure 2.15: NPDGamma in FnPB CAD model.

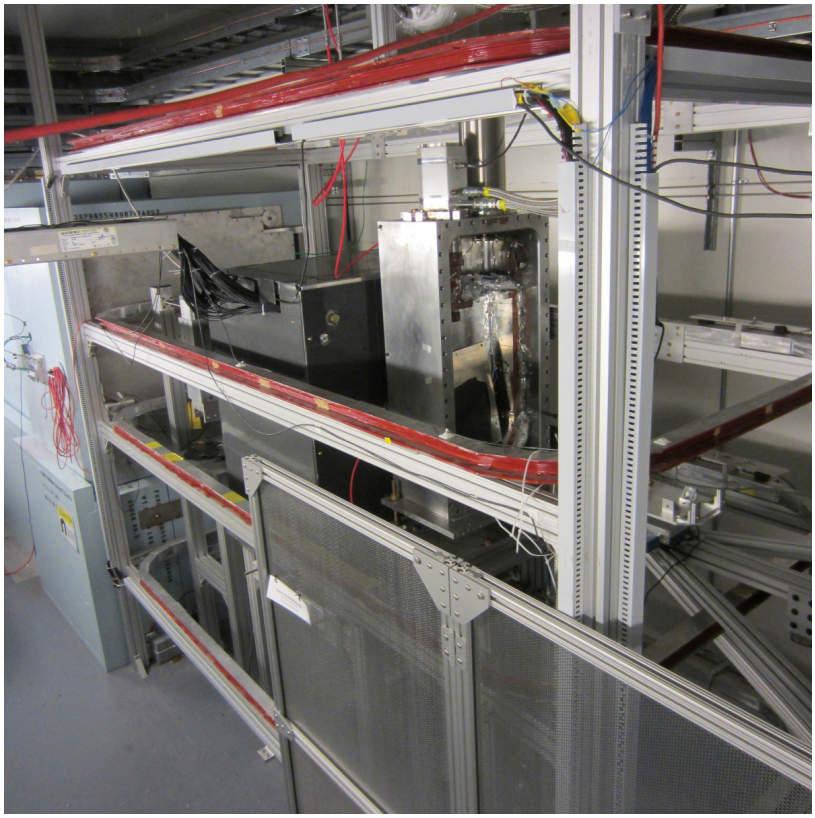

Figure 2.16: NPDGamma installed on the FnPB.

for eight neutron pulses over 133.3 ms. During the ninth pulse, the data is read out from the DAQ to the computer for storage. The signals were over-sampled and then averaged into 40 0.41667 ms time bins per neutron pulse for the three monitors and 48 CsI detectors in the detector discussed below. The spin flipper signals were averaged into 1000 0.01667 ms time bins for each neutron pulse.

The M1 monitor is used to monitor the neutron flux exiting the beam guide. More details are given on basic ionization chamber operation in chapter 3 and on the beam monitor design and construction in chapter 4. The neutron pulse shape and height measured in the M1 monitor was used for a number of different diagnostics during the commissioning, running, and data analysis stages. The M2 monitor was

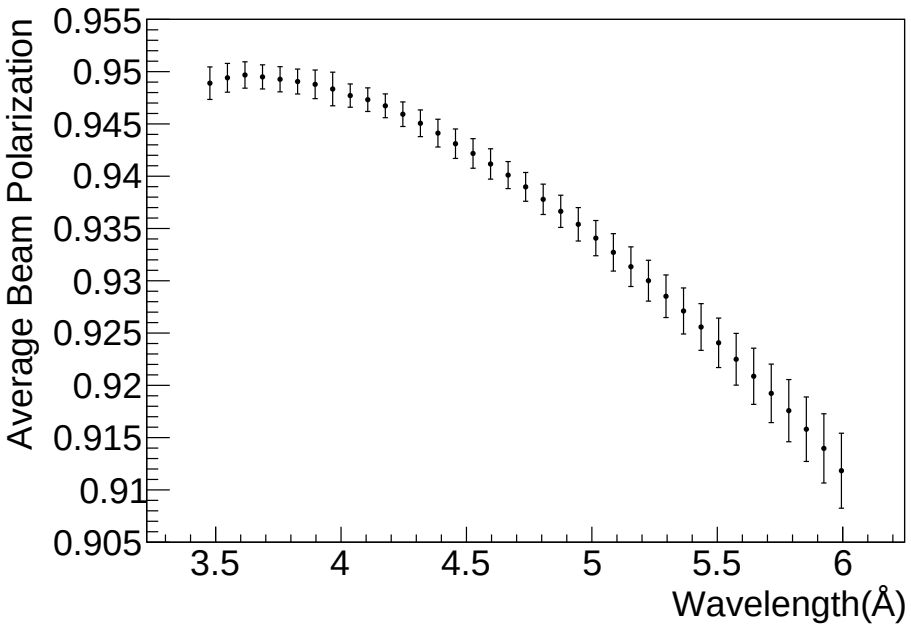

Figure 2.17: Plot of the average neutron beam polarization, measured during n3He polarimetry, determined from 8 polarimetry measurements. Error bars are standard deviation. Data from table A.4 of reference [28].

used for diagnostics during the earlier stages of the experimental commissioning and disconnected during later data taking to simplify the DAQ setup. The M3 monitor has a different design than the M1 and M2 monitors but operates on the same principles and was used to monitor the neutron flux through the hydrogen target.

The neutron beam is polarized through the use of a super-mirror polarizer (SMP) manufactured by Swiss Neutronics [27]. The SMP preferentially transmits neutrons of one polarization while absorbing those with the opposite polarization. The measured beam polarization downstream of the SMP is shown in fig. 2.17.

To maintain the neutron polarization downstream of the SMP, an approximately 10 gauss magnetic holding field is used. The field is produced by the four coils

with the red protective coating in fig. 2.16. As the average neutron polarization will align parallel or anti-parallel to the magnetic holding field, the direction of the field is important. The target, detector array, and magnetic field need to be aligned to better than 20 mrad to prevent mixing of the parity-violating up-down asymmetry and the parity-conserving left-right asymmetry [29].

An inhomogeneous magnetic field will cause spin-dependent Stern-Gerlach steering of the neutron beam inducing a false asymmetry as the steering direction will reverse with the neutron spin. A field uniformity of better than 2.5 mG/cm is required to keep the false asymmetry small compared to the goal statistical uncertainty [29]. A set of trim coils are used to modify the field direction for alignment and gradients.

A radio frequency spin rotator (RFSR) is used to flip the neutron polarization on a pulse-by-pulse basis. The assembled RFSR is shown in fig. 2.18. It uses a cylindrical coil to produce the RF field. The RFSR operates using nuclear magnetic resonance techniques. This can be approximated to a very good degree using a semiclassical model. Assuming neutrons are moving in the $\hat{z}$ direction in a static magnetic field in the $\hat{y}$ direction with magnitude B_0, polarized neutrons will precess at the Larmor frequency,

$$\omega_0 = \frac{\mu_N B_0}{\hbar}, \tag{2.4}$$

where μ_N is the neutron magnetic moment. If there is a time varying field

$$\mathbf{B}(t) = B_1 \cos(\Omega t)\hat{z} - B_1 \sin(\Omega t)\hat{x} \tag{2.5}$$

over a length d in the $\hat{z}$ direction, and if the neutron is on resonance such that $\Omega = \omega_0$,

(a) Side (b) Front

Figure 2.18: The NPDGamma radio frequency spin rotator (RFSR).

and the time in the field is

$$t = n\pi\hbar/\mu_N B_1, \tag{2.6}$$

where $n = 1, 3, 5, \ldots$, the neutron spin will be rotated by $n\pi$ on exiting the spin flipper. This process does not alter the neutron momentum so it will not induce any false asymmetry in the experiment. See reference [30] for more details on the theory and design of the RFSR.

The resonance frequency, Ω, of the RFSR is set by the construction of the spin rotator to be close to the Larmor frequency of a neutron in a 10 G field. After the RFSR was installed, the holding field strength, B_0, was tuned to maximize spin rotation efficiency. Efficient spin flipping also required that the time in the RFSR field and the field strength B_1 be properly related. Since the SNS is a pulsed neutron

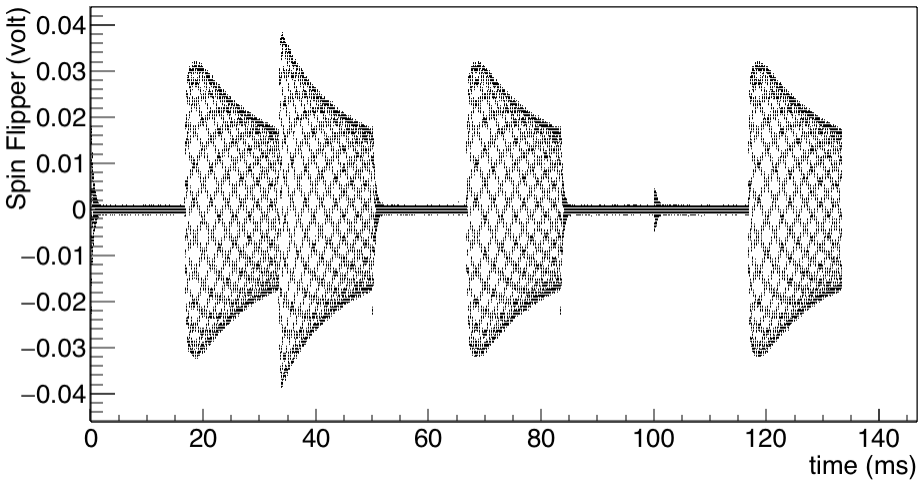

Figure 2.19: NPDGamma RFSR measured voltage over an eight-pulse sequence. While the spin flipper signal is a ramped sine wave, its frequency is approximately 170 kHz, but it is undersampled at 60 kHz so the wave shape is not visible inside the ramp envelope.

source, and the choppers are used to prevent frame overlap, each time of flight has a unique velocity. The length of the RFSR sets the time that neutrons of each energy will remain in the RFSR volume. The B_1 field strength was ramped over a pulse to maximize the spin rotator efficiency at each time of flight. The voltage applied to the RFSR circuit is shown in fig. 2.19 for an eight-step pulse sequence. When the RFSR is active, the neutron spin is rotated from $+\hat{y}$ to $-\hat{y}$.

From polarimetry measurements done at the FnPB, the average spin-flip efficiency during the hydrogen data taking was 0.975 ± 0.002 over the wavelength range 3.7-5.8 Å as given in table 5.6 of reference [31]. Fig. 2.20 shows the spin rotator efficiency over a range of neutron energies as measured during the hydrogen data taking.

NPDGamma used a 16-liter liquid hydrogen target. The target is constructed

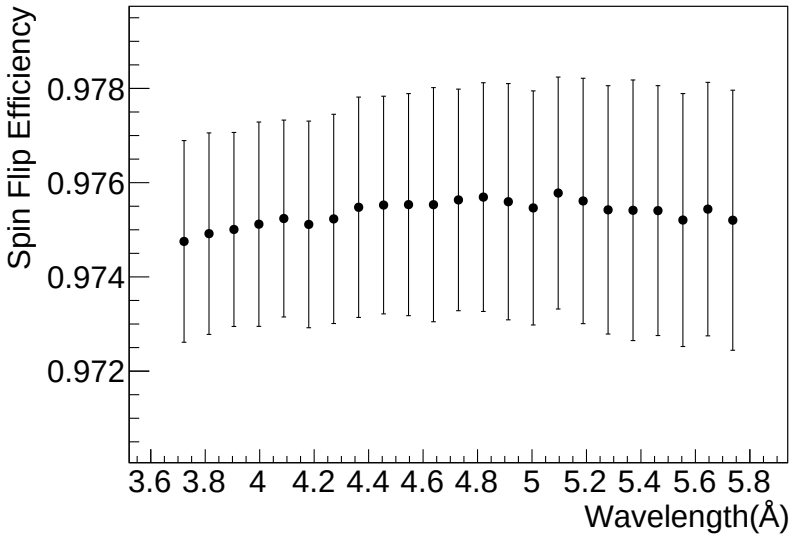

Figure 2.20: Spin rotator efficiency during para-hydrogen data taking. Plot created from data table A.9 in reference [31].

mainly from aluminum because of its low neutron capture cross section. The target was kept at 17 K by two liquid nitrogen cryostats. Molecular hydrogen can exist in either the ortho or para-state. In ortho-hydrogen the two nuclei in a hydrogen molecule have spins in the same direction, and in para-hydrogen the nuclear spins are in opposite directions. As shown in fig. 2.21 para-hydrogen has a much lower scattering cross section than ortho-hydrogen at low energies. A para-hydrogen target is required to prevent beam depolarization due to spin-flip scattering that occurs with a higher cross-section in ortho-hydrogen at low neutron energy. A catalytic converter was used to rapidly convert the target from ortho-hydrogen to para-hydrogen. Reference [35] has more information on the target construction and operation in chapter 4.

At energies over 15 meV spin-flip scattering can occur on para-hydrogen flipping the neutron spin, and one of the protons spins producing ortho-hydrogen [5]. As this

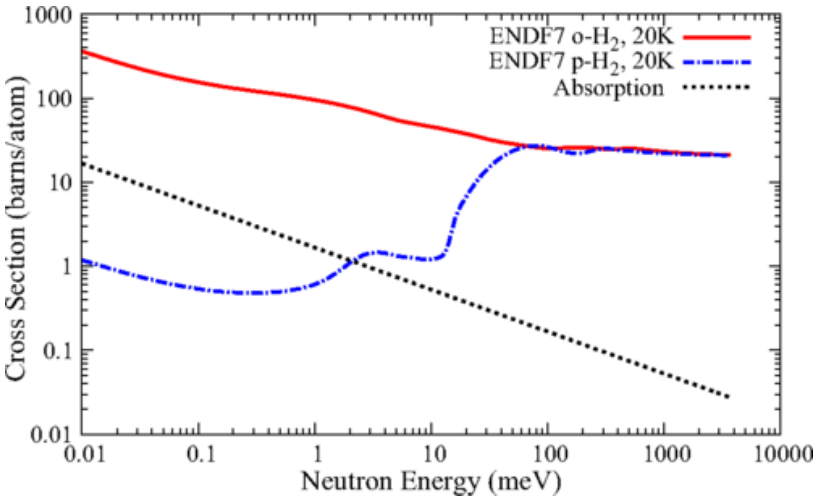

Figure 2.21: Para-hydrogen and ortho-hydrogen scattering cross sections at 2 K from ENDF-VII[32] and the absorption cross section[33]. Figure used with permission from reference [34].

would greatly increase the beam depolarization, the neutron energy is restricted to below 15 meV by the chopper settings.

The target is placed in the center of a CsI(Tl) detector array to measure the direction of γ-ray emission. The detector array consists of 48 cubic crystals of 15 cm per side arranged in four rings of 12 crystals. The size and positioning of the CsI detectors were chosen to satisfy the requirements for spatial resolution, angular resolution, high efficiency, and a large 3π solid angle coverage of the target [36]. Fig. 2.22 shows a CAD model of the array and a picture of it during testing before installation.

To meet the statistical requirements of the NPDGamma experiment, a high neutron flux is needed. The high event rate that this will cause in the detectors makes event mode counting impractical. The light output from the scintillation crystals was integrated using vacuum photodiodes connected to current-to-voltage amplifiers

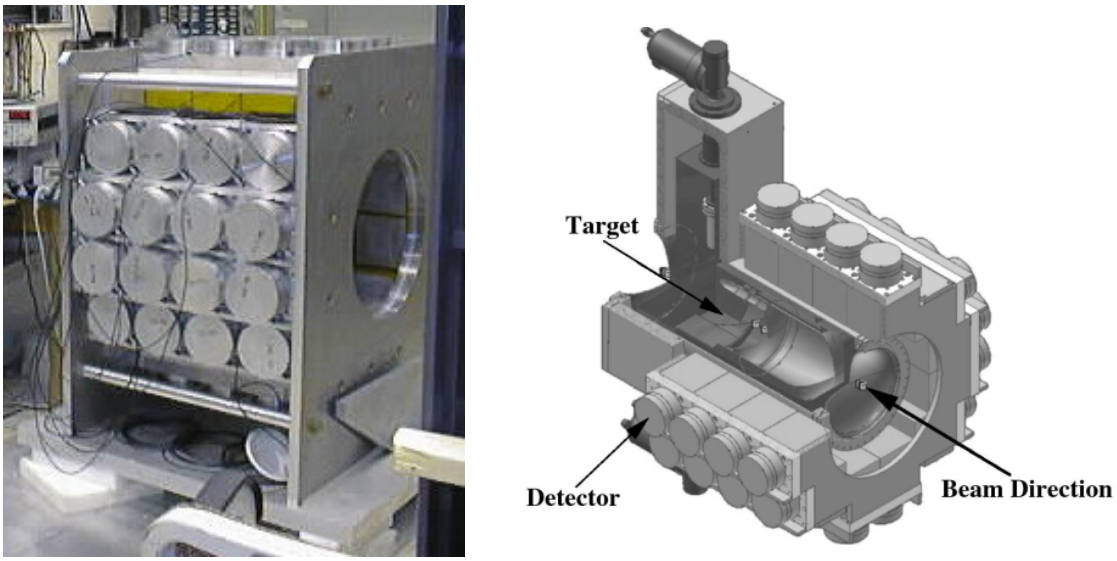

(a) Assembled detector array (b) CAD model. Used with permission from reference [36].

Figure 2.22: CsI detector array.

attached to each CsI detector.

2.3.2 Analysis Overview

To establish some conventions for the analysis, directions will be referenced as follows. As shown in fig. 2.4 and fig. 2.14 the $+\hat{z}$ axis is in the beam direction, and $+\hat{y}$ is in the upward vertical direction. The $+\hat{x}$ direction is then into the page. The directions up and down correspond to the $+\hat{y}$ and $-\hat{y}$ axis directions, respectively, and left and right correspond to the $+\hat{x}$ and $-\hat{x}$ axis directions, respectively. When a neutron pulse is polarized in the $+\hat{y}$ direction, it can be referred to as polarized in the up direction; it will be labeled with an $\uparrow$. Neutron pulses polarized in the $-\hat{y}$ direction can be referred to as polarized in the down direction, and will be labeled with a $\downarrow$. Fig. 2.23 shows the alignment of the CsI detector array to the axis.

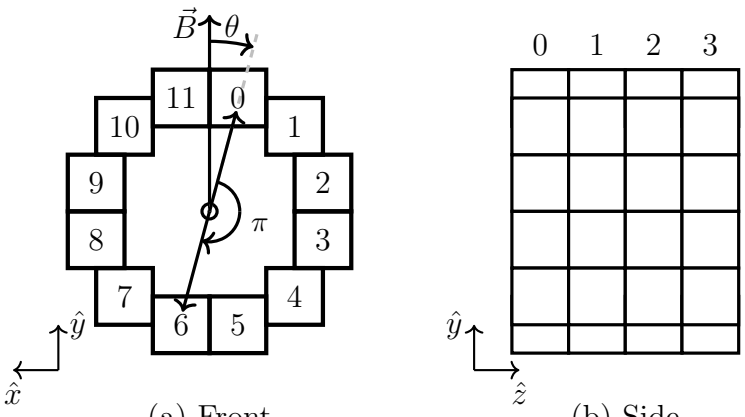

(a) Front (b) Side

Figure 2.23: Schematic diagram of NPDGamma detector array.

The differential cross section for the reaction is

$$\frac{d\sigma}{\Omega} \propto \frac{1}{4\pi}(1 + A_{PV}\cos\theta + A_{PC}\sin\theta), \tag{2.7}$$

where A_{PV} is the parity-violating asymmetry, and A_{PC} is the parity-conserving asymmetry. The PV asymmetry creates an asymmetry in the up-down emission of the γ-rays while the PC asymmetry creates a left-right asymmetry.

For a point target and detectors with perfect spatial resolution the count rate, N, in detector i with neutron pulse polarization up($\uparrow$) or down($\downarrow$) is

$$N_i^{\uparrow/\downarrow} = N_0^{\uparrow/\downarrow}\epsilon_i\,(1 \pm A_{PV}\cos\theta \pm A_{PC}\sin\theta) + p_i \tag{2.8}$$

where $N_0^{\uparrow/\downarrow}$ is the initial neutron flux, ϵ_i is the detector efficiency, the neutron polarization is indicated by the arrow superscript, θ is the angle of the photon emission direction with respect to the polarization axis defined by the magnetic holding field, A_{PV} is the parity-violating asymmetry, A_{PC} is the parity-conserving asymmetry, and p_i is the detector pedestal. The count rate in a detector π radians around the detector

array in the same ring is

$$N_{i+\pi}^{\uparrow/\downarrow} = N_0^{\uparrow/\downarrow}\epsilon_{i+\pi}\left(1 \pm A_{PV}\cos(\theta+\pi) \pm A_{PC}\sin(\theta+\pi)\right) + p_{i+\pi} \tag{2.9}$$

$$= N_0^{\uparrow/\downarrow}\epsilon_{i+\pi}\left(1 \mp A_{PV}\cos\theta \mp A_{PC}\sin\theta\right) + p_{i+\pi}. \tag{2.10}$$

Fig. 2.23 shows the layout of the detector array and an example pair of detectors at θ_i and $\theta_{i+\pi}$.

The raw asymmetry can be isolated from the measured count rate using the ratio

$$A_i^{raw} = \frac{\sqrt{\alpha}-1}{\sqrt{\alpha}+1}, \tag{2.11}$$

where

$$\alpha = \frac{N_i^{\uparrow}}{N_i^{\downarrow}}\frac{N_{i+\pi}^{\downarrow}}{N_{i+\pi}^{\uparrow}}. \tag{2.12}$$

After subtracting the pedestal,

$$\begin{aligned}\frac{N_i^{\uparrow}}{N_i^{\downarrow}} &= \frac{N_0^{\uparrow}\epsilon_i\left(1 + A_{PV}\cos\theta + A_{PC}\sin\theta\right)}{N_0^{\downarrow}\epsilon_i\left(1 - A_{PV}\cos\theta - A_{PC}\sin\theta\right)} \\ &= \frac{N_0^{\uparrow}}{N_0^{\downarrow}}\frac{1 + A_{PV}\cos\theta + A_{PC}\sin\theta}{1 - A_{PV}\cos\theta - A_{PC}\sin\theta}\end{aligned} \tag{2.13}$$

$$\begin{aligned}\frac{N_{i+\pi}^{\downarrow}}{N_{i+\pi}^{\uparrow}} &= \frac{N_0^{\downarrow}\epsilon_{i+\pi}\left(1 - A_{PV}\cos(\theta+\pi) - A_{PC}\sin(\theta+\pi)\right)}{N_0^{\uparrow}\epsilon_{i+\pi}\left(1 + A_{PV}\cos(\theta+\pi) + A_{PC}\sin(\theta-\pi)\right)} \\ &= \frac{N_0^{\downarrow}}{N_0^{\uparrow}}\frac{1 + A_{PV}\cos\theta + A_{PC}\sin\theta}{1 - A_{PV}\cos\theta - A_{PC}\sin\theta}\end{aligned} \tag{2.14}$$

$$\begin{aligned}\alpha &= \frac{N_0^{\uparrow}}{N_0^{\downarrow}}\frac{N_0^{\downarrow}}{N_0^{\uparrow}}\left(\frac{1 + A_{PV}\cos\theta + A_{PC}\sin\theta}{1 - A_{PV}\cos\theta - A_{PC}\sin\theta}\right)^2 \\ &= \left(\frac{1 + A_{PV}\cos\theta + A_{PC}\sin\theta}{1 - A_{PV}\cos\theta - A_{PC}\sin\theta}\right)^2.\end{aligned} \tag{2.15}$$

The initial neutron flux and the detector efficiency cancel in these ratios. Substituting

this back into eqn. 2.11

$$A_i^{raw} = \frac{\left(\frac{1+A_{PV}\cos\theta+A_{PC}\sin\theta}{1-A_{PV}\cos\theta-A_{PC}\sin\theta}\right)-1}{\left(\frac{1+A_{PV}\cos\theta+A_{PC}\sin\theta}{1-A_{PV}\cos\theta-A_{PC}\sin\theta}\right)+1} \tag{2.16}$$

$$= \frac{1+A_{PV}\cos\theta+A_{PC}\sin\theta-(1-A_{PV}\cos\theta-A_{PC}\sin\theta)}{1+A_{PV}\cos\theta+A_{PC}\sin\theta+(1-A_{PV}\cos\theta-A_{PC}\sin\theta)} \tag{2.17}$$

$$= A_{PV}\cos\theta + A_{PC}\sin\theta \tag{2.18}$$

For the real target and detectors with spatial extent and limited spatial resolution, the $\cos\theta$ and $\sin\theta$ factors are replaced by geometric factors, G such that

$$N_i^{\uparrow/\downarrow} = N_0^{\uparrow/\downarrow}\epsilon_i\left(1 \pm A_{PV}\cos\theta \pm A_{PC}\sin\theta\right)$$

$$\rightarrow N_i^{\uparrow/\downarrow} = N_0^{\uparrow/\downarrow}\epsilon_i\left(1 \pm A_{PV}G_{PV,i} \pm A_{PC}G_{PC,i}\right). \tag{2.19}$$

The geometric factors relate the spatial extent and relative position of each of the detectors to the target, and were calculated from simulation [37].

For this experiment, an eight-step spin sequence was used to control for systematic effects. Each sequence consisted of eight neutron pulses with the following spin sequence, $\uparrow\downarrow\downarrow\uparrow\downarrow\uparrow\uparrow\downarrow$. Fig. 2.19 shows the voltage applied to the spin flipper during the pulse sequence to flip the spin from $\uparrow$ to $\downarrow$. To control for systematic effects in the DAQ, every second eight-step sequence was the inverse of the given sequence, and only paired consecutive eight-step sequences that had no dropped pulses within or in the prior eight step sequence were used. A stability cut was also applied such that over an eight-step sequence the beam power was stable to approximately 1% for each pulse in the sequence compared to the sequence average. Each $N_i^{\uparrow/\downarrow}$ is the sum of the integral of pulses with the same neutron polarization direction across an eight-step sequence for the ith detector.

The total signal measured from each detector is the sum of a number of different factors. There exist various backgrounds in the experiment, electronic pedestals, and other systematics effects that had to be measured and accounted for during the data analysis. The main contributions to the signal were γ-rays from neutron capture on aluminum in the target vessel and the liquid hydrogen target. Each of these gamma distributions has an up-down parity-violating asymmetry, and a left-right parity-conserving asymmetry. For each ring of detectors, the asymmetries will mix differently due to the different position relative to the hydrogen in the target vessel and the position of the aluminum that the target vessel is made of.

The raw asymmetry is related to the physics asymmetries by

$$A_i^{raw} = P_{tot}^H f_i^H \times (G_{PV,i}^H A_{PV}^H + G_{PC,i}^H A_{PC}^H) + P_{tot}^{Al} f_i^{Al} \times (G_{PV,i}^{Al,aux} A_{PV}^{Al} + G_{PC,i}^{Al,aux} A_{PC}^H). \tag{2.20}$$

Where $P_{tot}^{H,Al} = \bar{P}_n \epsilon_{SF} \cdot C_{depol}^{H,Al}$ is a factor related to the neutron polarization $\bar{P}_n$, the spin rotator efficiency ϵ_{SF}, and the neutron depolarization $C_{depol}^{H,Al}$ for neutrons that capture in hydrogen, H, or aluminum, Al. f_i is the fraction of the total gamma rays incident on detector i from either hydrogen or aluminum captures.

Three independent analyses of the hydrogen data were performed [38]. The three analyses are in agreement as shown in fig. 2.24. Due to further measurements being required for the aluminum asymmetries, a final hydrogen asymmetry has not been extracted yet.

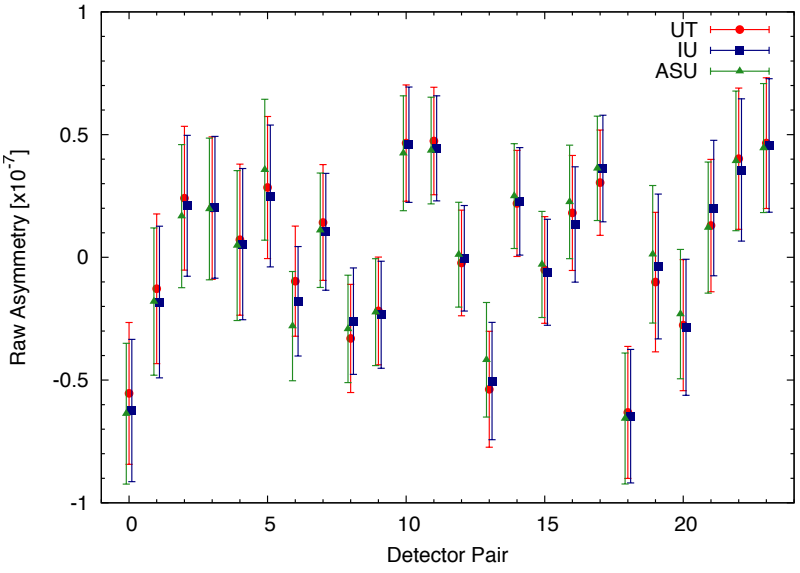

Figure 2.24: Preliminary raw asymmetries from NPDGamma running at the FnPB [38].

2.4 n3He Experiment

The n3He experimental goal is to measure the directional asymmetry in the emission direction of the proton, with respect to the neutron polarization, after capture of cold neutrons on ^{3}He, and the resulting spontaneous breakup:

$$\vec{n} + {}^3He \rightarrow {}^4\text{He}^* \rightarrow p + T + 765\,\text{keV}. \tag{2.21}$$

Using chiral EFT methods, the asymmetry is calculated to be either 1.7×10^{-8} or 3.5×10^{-8} depending on the energy cutoffs used [39]. The goal experimental accuracy is 2×10^{-8} with an estimated 10^7 seconds of beam time required at the FnPB to complete the measurement at the desired accuracy [8].

When the polarized cold neutron captures on the ^{3}He nucleus, it forms an excited ^{4}He compound nucleus. The reaction occurs due to a resonance 20.21 MeV above the

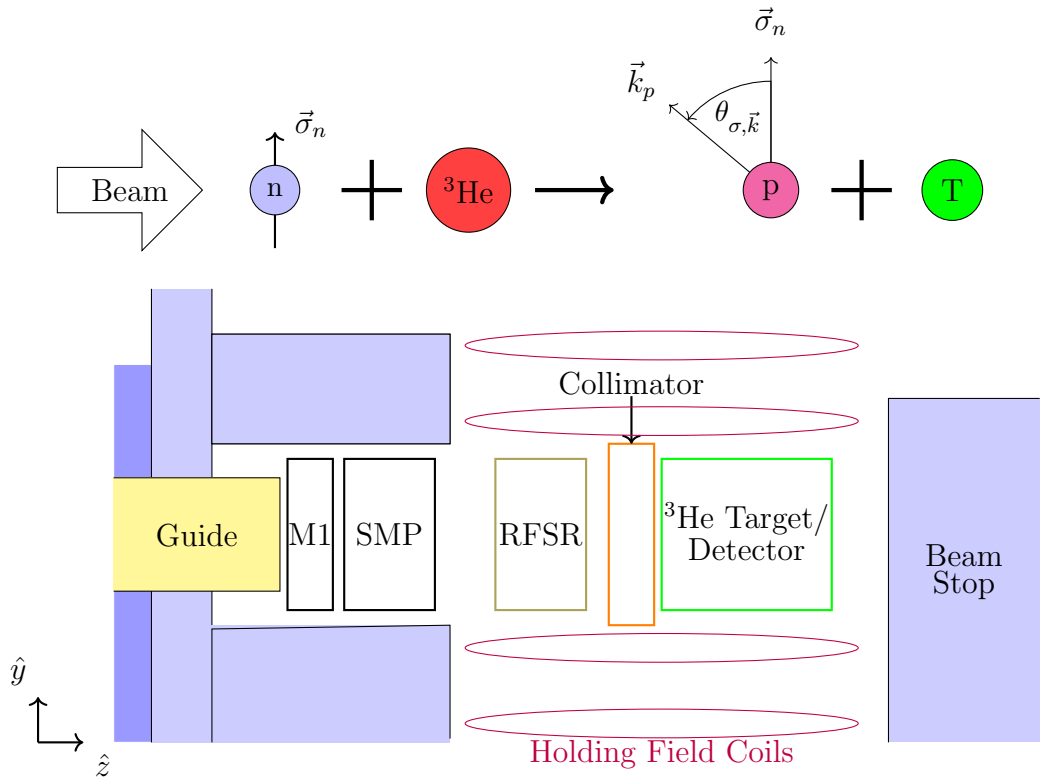

Figure 2.25: Schematic of the n3He experimental layout. Objects are not to scale.

ground state energy of the ^{4}He nucleus. The presence of the weak interaction causes a mixing of states with another resonance at 21.02 MeV that has opposite parity [8]. This mixing of states with opposite parity causes the parity-violating asymmetry that is measured in the n3He experiment, in a similar manner to how the mixing of opposite parity S and P-wave states in the NPDGamma reaction causes the γ-ray asymmetry. For more detailed information on the process, reference [39] presents a detailed chiral EFT calculation of the parity-violating asymmetry.

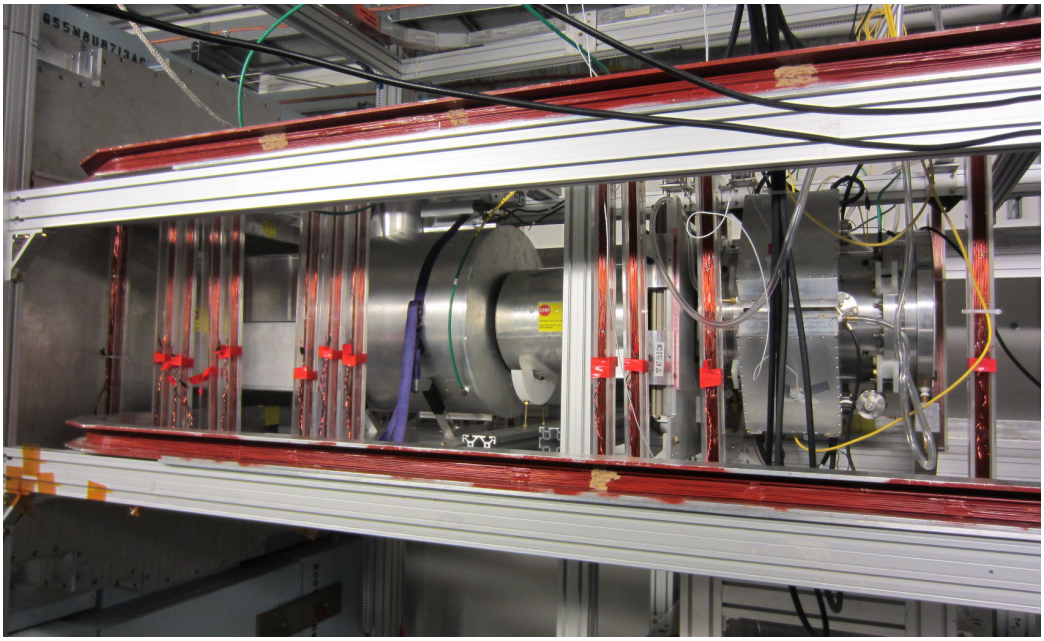

Figure 2.26: The n3He experiment in the FnPB cave.

2.4.1 Experimental Setup

The n3He experiment ran after the NPDGamma experiment and reused the M1 monitor, supermirror polarizer, and holding-field coils. The DAQ, spin rotator, collimator, target-detector and mounting stands were new.

The n3He DAQ setup consists of five 48-channel DAQ modules with 24-bit ADCs. Four of the modules are used to read the signals from the target chamber wires. These DAQ modules over-sampled at 50 kHz and averaged the data into 49 0.32 ms wide time bins per neutron pulse. The remaining DAQ measured the signals from the beam monitors and the spin flipper and was over-sampled at 100 kHz and averaged that into 1624 0.01 ms wide time bins per neutron pulse. The T0 signal provided by the facility is used to coordinate the start of data taking by the DAQs. Data are readout between each pulse so there were no hidden pulses as occurred with the

NPDGamma DAQ.

The spin rotator for n3He operates using the same principles as the NPDGamma spin rotator to rotate the neutron spin by π when active, but has a different winding geometry. The choice of winding geometry was made to minimize fringe fields around the spin rotator to prevent beam steering and depolarization during a spin flip. The same polarizer was used for both NPDGamma and n3He. The n3He spin rotator has a spin-flip efficiency of 0.9979 ± 0.0009 when averaged over all wavelengths in a neutron pulse. Fig. 2.27 shows the assembled spin rotator. Fig. 2.28 shows the spin-flip efficiency as a function of neutron wavelength. Reference [28] has more information on the spin rotator construction and the methods for calculating the spin-flip efficiency.

n3He used an adjustable collimator, located directly in front of the target chamber, to give a well-defined beam area on the target. The collimator had four plates, two horizontal and two vertical that could be adjusted independently. The collimation was set to remove the outer edges of the beam that had diverged from the initial $10\,\text{cm} \times 12\,\text{cm}$ beam cross section set by the neutron beam guide. The aluminum plates had a sheet of cadmium on the front with sufficient thickness to stop the full neutron beam, and a sheet of ^{6}Li loaded plastic on the front to reduce γ-ray production. The collimator was also used to scan the beam over the target to verify the wire readout map, and to vary the beam area and location on the target for systematic studies.

The target for the experiment is a multi-wire ^{3}He ionization chamber with a pure ^{3}He fill gas. Chapter 5 gives more details of the chamber design requirements,

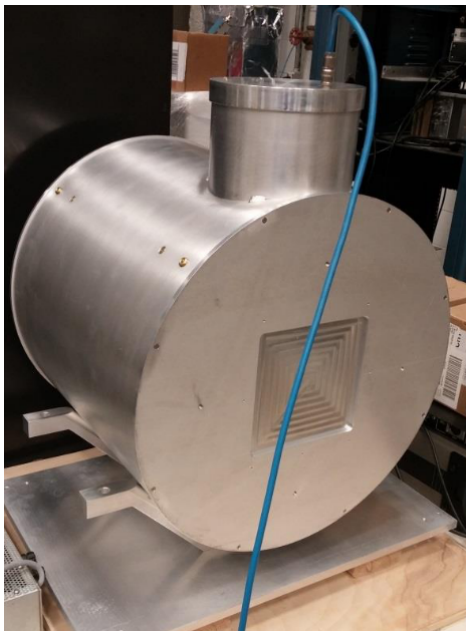

Figure 2.27: The RFSR used for the n3He experiment. Image used with permission from reference [28].

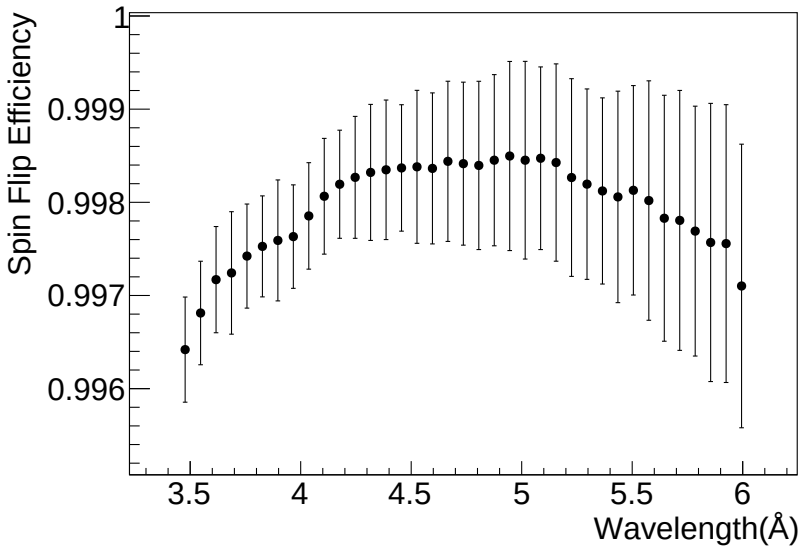

Figure 2.28: Plot of average spin flipper efficiency determined from polarimetry measurements and AFP coils. Data from table A.3 of reference [28].

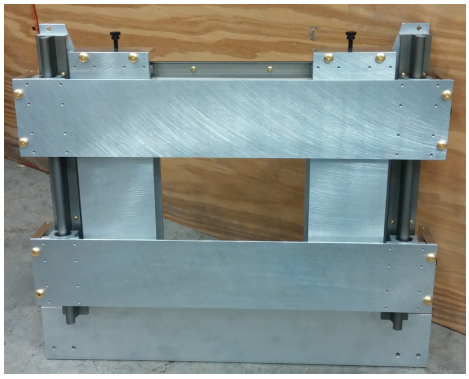

Figure 2.29: The four jaw collimator used for the n3He experiment. The neutron absorbing cadmium and ^{6}Li sheets have not been attached to the movable jaws.

construction, and testing. As shown in fig. 2.30 the target chamber contains 144 signal wires spaced evenly throughout the chamber volume with surrounding high voltage wires that define a volume around each signal wire within which the ionization charge will be collected, as illustrated in fig. 2.35. By reading out each signal wire individually, the position of ionization in the target chamber can be measured in two dimensions. Using simulation, a set of geometry factors can be calculated that relate the target and beam geometry so that the physics asymmetry can be extracted similarly to what was required for the NPDGamma analysis.

Fig. 2.32 shows the wire labeling. Fig. 2.33 shows an example of the early beam data taken with the target. Each cell in this plot corresponds to one signal wire. With the beam entering the target chamber from the left, the intensity falls off exponentially into the chamber. The beam area is not sharply defined despite the use of the collimator due to the proton and triton having several centimeter ranges in the 0.47 atm of ^{3}He fill gas in the target chamber.

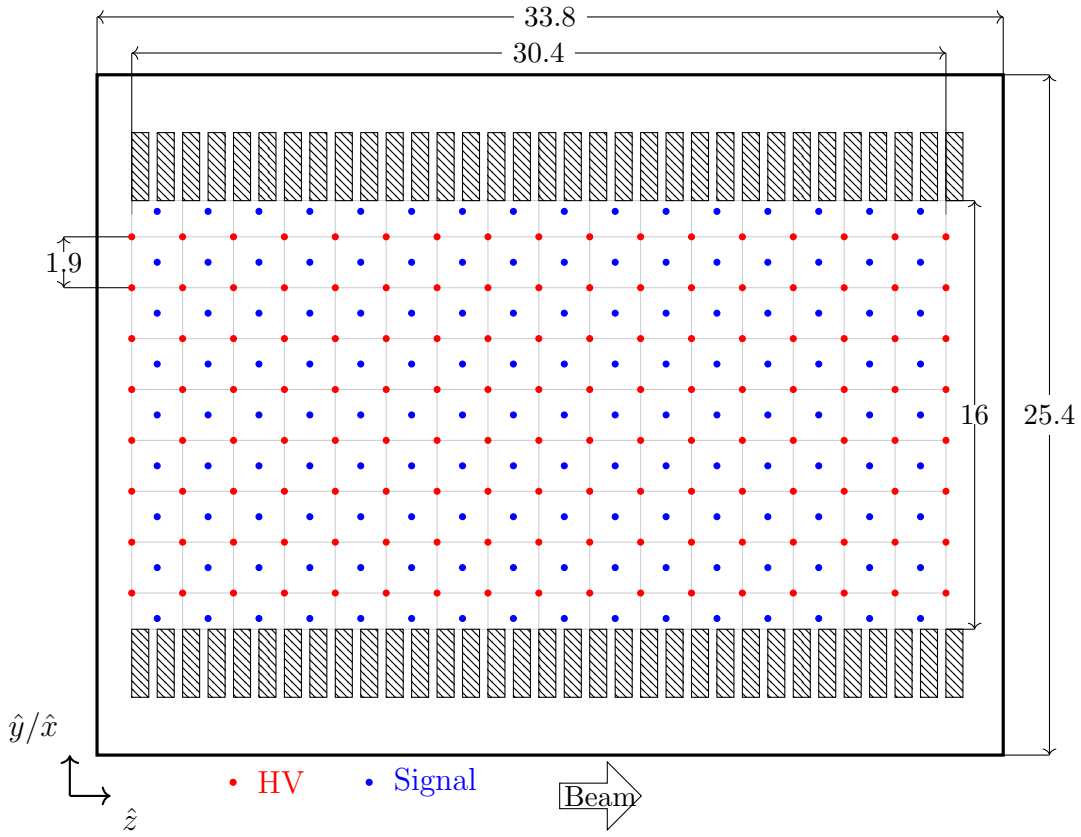

Figure 2.30: Schematic of the wire layout in the n3He chamber, shown in cross section through the chamber's central axis. Each colored point represents one wire. During operation the wires were aligned parallel to either the $\hat{x}$ (horizontal) or $\hat{y}$ (vertical) beam-line axis to measure either PV or PC asymmetries. Linear dimensions are in centimeters.

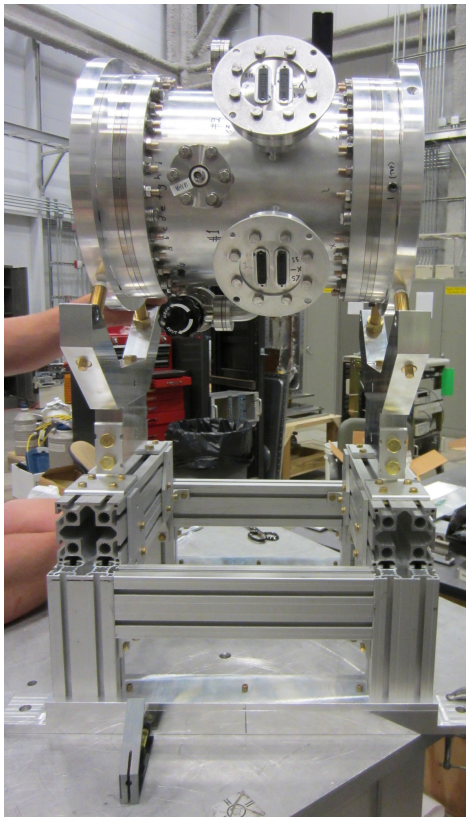

Figure 2.31: n3He target chamber mounted on the adjustable stand. The chamber is mounted on four screws, and by adjusting the height of the screws in pairs the pitch and roll of the chamber can be adjusted.

2.4.2 Systematics and Alignment Requirements

Due to the required high precision of the measurement, systematic effects must be carefully studied and controlled. As discussed in reference [14], the main contribution to the systematic errors is a mixing of the parity-violating asymmetry with the parity-conserving asymmetry that is also present.

The differential cross section for the n3He reaction is to leading order

$$\frac{d\sigma}{d\Omega} \propto (1 + A_{PV} \cos\theta + A_{PC} \sin\theta), \tag{2.22}$$

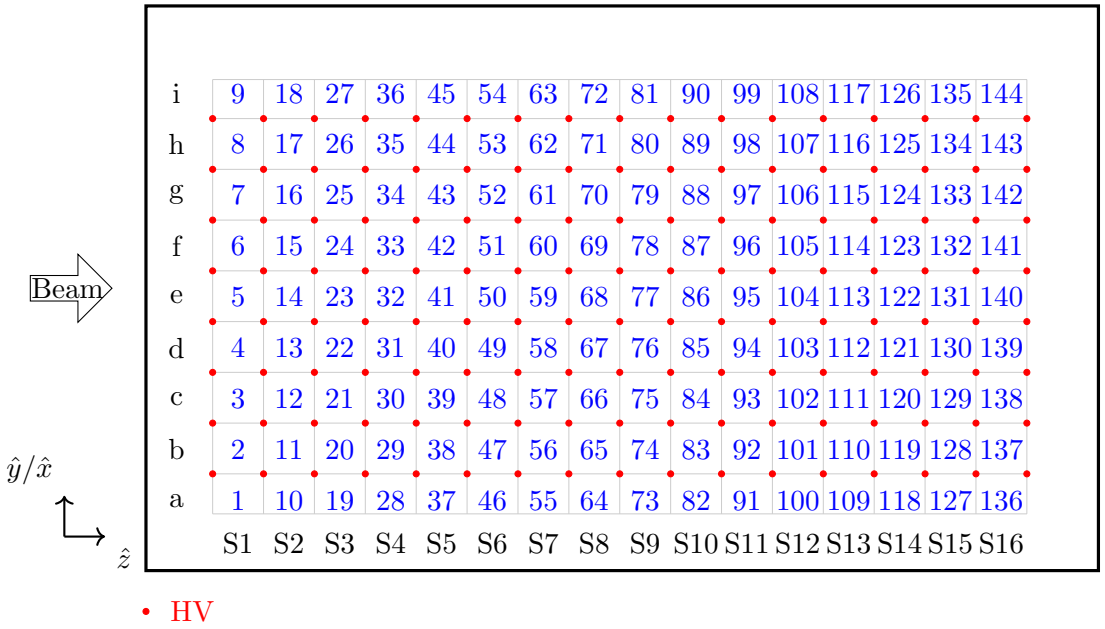

Figure 2.32: The signal wires in the target chamber are indexed in two possible ways, either by a number from 1-144 or by a signal plane number and a letter.

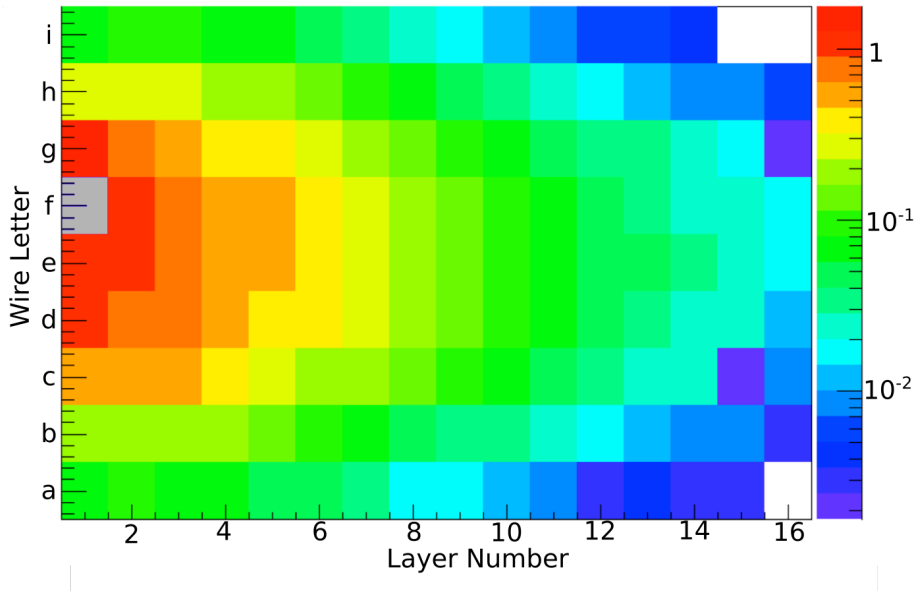

Figure 2.33: Early beam data from the target chamber. Wire 6, in plane 1 row f, is greyed out as it did not function, and the wire 7 signal was also anomalous.

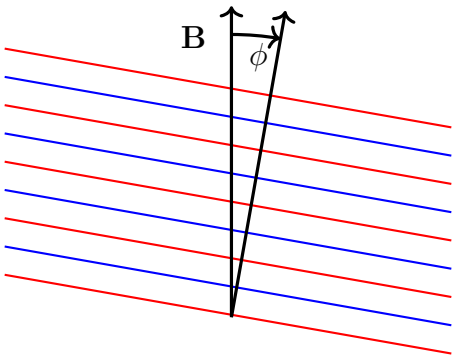

Figure 2.34: B-field and wire alignment angle ϕ.

where A_{PV} is the parity-violating asymmetry, A_{PC} is the parity conserving asymmetry, and θ the angle between the magnetic holding field defining the neutron spin direction and the emission direction of the proton. The magnitude of the parity-conserving asymmetry is estimated at 1.7×10^{-6} [14], and its mixing needs to be controlled to at least an order of magnitude better than the parity-violating asymmetry.

The current induced on a wire is insensitive to initial ionization position within a signal wire's cell as defined by the HV wires and wires frames around it. If the wires are parallel to the x-axis and perpendicular to the neutron spin, then the wire chamber will be sensitive to only the PV asymmetry. If the wire chamber is rotated 90° so that the wires are parallel to the y-axis, then it will be sensitive to only the PC asymmetry for the same reason. If the magnetic holding field, which determines the neutron spin orientation, and the wires in the target chamber are misaligned, then the parity-violating and parity-conserving asymmetry will be mixed.

To have the parity-conserving asymmetry mixing to less than 1×10^{-9}, the fol-

lowing alignment condition needs to be satisfied:

$$\phi < \sin^{-1}\left(\frac{1\times10^{-9}}{1.7\times10^{-6}}\right) = 0.58\,\text{mrad}. \tag{2.23}$$

Due to this, the angular alignment of the wires to the magnetic holding field and thus the neutron spin must be on the order of 1 mrad. This is a fairly strict requirement, and as discussed in section 5.6, the frame stack and assembled target was examined by the the SNS Survey and Alignment Group to fiducialize the target, and to ensure its alignment during data taking.

To determine the neutron beam location, a set of measurements were done with a pair of XY-translation stages and the M3 monitor that was used during NPDGamma and a collimator with a 1 cm square opening centered on the monitor. By scanning these in steps around the beam volume, the beam profile could be determined. After determining the beam profile at two locations along the neutron beam, a laser was aligned to the beam centroid at each position, and the SNS Survey and Alignment Group was brought in to add these positions to their model of the FnPB cave. The laser was used as an initial reference to the beam direction and position during the installation of the experiment components. The Survey and Alignment Group was used to make the final adjustments to the component positions before data taking, and whenever the target orientation had to be changed.

The magnetic field direction and uniformity was measured using a magnetometer on an aluminum sled aligned either parallel or perpendicular to the beam path. The magnetic field was measured to be aligned with gravity. Details of the measurements of the magnetic field, neutron beam position, laser alignment, and target installation are given in reference [40].

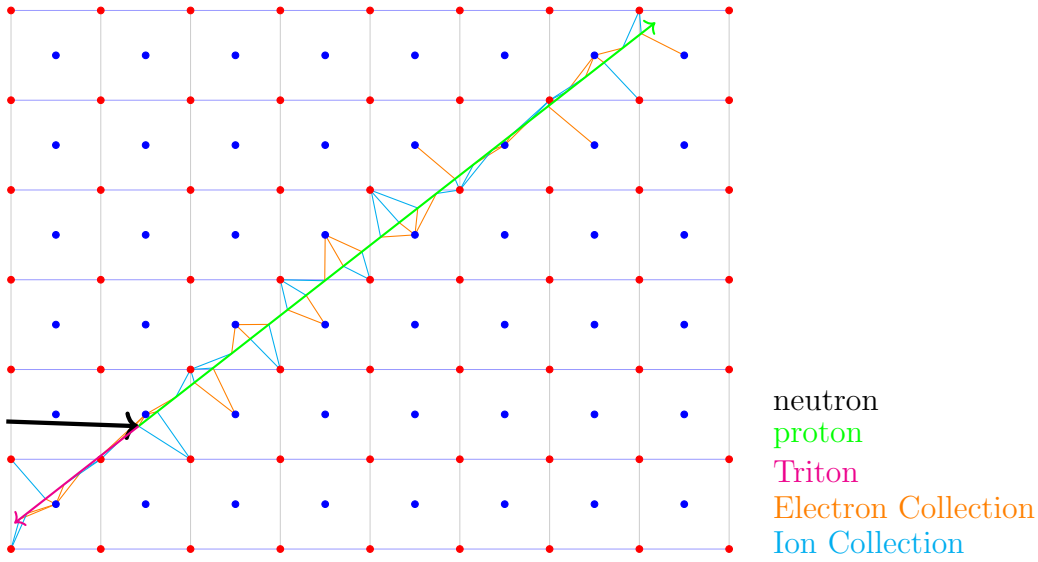

Figure 2.35: Charge collection diagram. Wire spacing and proton and triton distances are to scale. There are thousands more ion-electron pairs created than illustrated here in a real event.

2.4.3 Analysis Overview

When a neutron capture occurs in the ^{3}He gas, the resulting proton and triton will travel through the gas ionizing it. There is 765 keV of kinetic energy shared between the proton and triton. With the small neutron momentum, the proton and triton are emitted essentially back to back. From momentum conservation, the proton will have 571 keV, and the triton will have 194 keV. Fig. 5.10 shows the energy deposition of the proton and triton as a function of distance. Since the proton has the longer range in the target chamber, we will be mostly sensitive to its emission direction.

The proton and triton will ionize the gas mixture as they travel through it, and the ionization electrons will be collected on the signal wires while the positive ions collect on the HV wires. Wires are used instead of plates to allow the protons to range out

over as long as distance as possible. An example neutron capture is shown in fig. 2.35. By measuring the difference in the ionization distribution between the two spin states, the physics asymmetry can be extracted. Both the proton and triton asymmetry are measured simultaneously and have opposite signs, but the triton asymmetry, due to its significantly shorter path length, is small compared to the proton asymmetry.

The yield from the signal wire k in the target chamber can be written as

$$Y_k = I_0 \epsilon_k (1 + P g_k A_{PV} + P g_k A_{PC}) + b, \tag{2.24}$$

where I_0 is the initial SNS beam intensity, ϵ_k is the efficiency of wire k defined as the fraction of the initial ionization charge that is collected, P the beam polarization, g_k is the geometry factor for wire k, A_{PV} the parity-violating asymmetry, A_{PC} the parity-conserving asymmetry, and b the pedestal from the wire and its associated electronics. As with the NPDGamma detector, the $\cos\theta$ and $\sin\theta$ of the ideal detectors is replaced by the geometry factors calculated from simulation that related the beam, target, and wire positions.

A two-step spin sequence, $\uparrow\downarrow$, was used for the n3He experiment. The eight-step sequence used in the NPDGamma experiment was not required as the n3He target and detectors were not expected to have significant drifts in the detector or electronics response over the time scale of a pulse pair. The raw asymmetries for the

n3He experiment can be calculated using a single wire over the two spin states using

$$A_p^s = \frac{Y_k^\uparrow - Y_k^\downarrow}{Y_k^\uparrow + Y_k^\downarrow} \tag{2.25}$$

$$= \frac{I_0^\uparrow \epsilon_k (1 + P^\uparrow g_k A_p) + b_k - I_0^\downarrow \epsilon_k (1 + P^\downarrow g_k A_p) - b_k}{I_0^\uparrow \epsilon_k (1 + P^\uparrow g_k A_p) + b_k + I_0^\downarrow \epsilon_k (1 + P^\downarrow g_k A_p) + b_k} \tag{2.26}$$

$$= \frac{I_0^\uparrow (1 + P^\uparrow g_k A_p) - I_0^\downarrow (1 + P^\downarrow g_k A_p)}{I_0^\uparrow (1 + P^\uparrow g_k A_p) + I_0^\downarrow (1 + P^\downarrow g_k A_p) + 2b_k/\epsilon_k}, \tag{2.27}$$

where A_p is either the parity-violating or parity-conserving asymmetry and the other asymmetry is for simplicity assumed to have a small geometry factor due to the current chamber alignment and is ignored.

As the spin-flip efficiency of the spin rotator is high, $P^\uparrow \approx -P^\downarrow = P$ can be used to further simplify the above equation.

$$A_p^s = \frac{I_0^\uparrow (1 + P g_k A_p) - I_0^\downarrow (1 - P g_k A_p)}{I_0^\uparrow (1 + P g_k A_p) + I_0^\downarrow (1 - P g_k A_p) + 2b_k/\epsilon_k} \tag{2.28}$$

$$= \frac{I_0^\uparrow - I_0^\downarrow + (I_0^\uparrow + I_0^\downarrow) P g_k A_p}{I_0^\uparrow + I_0^\downarrow + (I_0^\uparrow - I_0^\downarrow) P g_k A_p + 2b_k/\epsilon_k}, \tag{2.29}$$

then assuming that $(I_0^\uparrow - I_0^\downarrow) P g_k A_p + 2b_k/\epsilon_k \ll I_0^\uparrow + I_0^\downarrow$, the final simplification can be made to

$$A_p^s = \frac{I_0^\uparrow - I_0^\downarrow}{I_0^\uparrow + I_0^\downarrow} + P g_k A_p. \tag{2.30}$$

In this method, a high pulse-to-pulse beam stability is required to extract A_p. The wire efficiency is divided out, and the pedestal is canceled in the numerator but not the denominator where it is small compared to the sum.

An alternative method is to use two wires in the formula in a ratio and by choosing conjugate pairs. Conjugate wires are wire pairs in a plane that are equally separated from the center of the target. In fig. 2.32 wires in rows a and i, b and h, c and g, d

and f form pairs within a plane. Conjugate pairs are special because the geometric factors are approximately equal, but opposite in sign. As row e is central in the chamber, it has no conjugate wire to be paired with. For this method to work, the pedestal b must be known and subtracted before the ratio is calculated:

$$R_{lm} = \frac{Y_l}{Y_m} = \frac{I_0\epsilon_l(1+Pg_lA_p)}{I_0\epsilon_m(1+Pg_mA_p)} = \frac{\epsilon_l(1+Pg_lA_p)}{\epsilon_m(1+Pg_mA_p)} \tag{2.31}$$

$$A_P^p = \frac{R_{lm}^{\uparrow} - R_{lm}^{\downarrow}}{R_{lm}^{\uparrow} + R_{lm}^{\downarrow}} \tag{2.32}$$

$$= \frac{\epsilon_l/\epsilon_m}{\epsilon_l/\epsilon_m} \frac{\frac{(1+P^{\uparrow}g_lA_p)}{(1+P^{\uparrow}g_mA_p)} - \frac{(1+P^{\downarrow}g_lA_p)}{(1+P^{\downarrow}g_mA_p)}}{\frac{(1+P^{\uparrow}g_lA_p)}{(1+P^{\uparrow}g_mA_p)} + \frac{(1+P^{\downarrow}g_lA_p)}{(1+P^{\downarrow}g_mA_p)}} \tag{2.33}$$

$$= \frac{\frac{(1+P^{\uparrow}g_lA_p)}{(1+P^{\uparrow}g_mA_p)} - \frac{(1+P^{\downarrow}g_lA_p)}{(1+P^{\downarrow}g_mA_p)}}{\frac{(1+P^{\uparrow}g_lA_p)}{(1+P^{\uparrow}g_mA_p)} + \frac{(1+P^{\downarrow}g_lA_p)}{(1+P^{\downarrow}g_mA_p)}} \tag{2.34}$$

using $g_l = -g_m = g$ this further simplifies to

$$A_P^p = \frac{\frac{(1+P^{\uparrow}gA_p)}{(1-P^{\uparrow}gA_p)} - \frac{(1+P^{\downarrow}gA_p)}{(1-P^{\downarrow}gA_p)}}{\frac{(1+P^{\uparrow}gA_p)}{(1-P^{\uparrow}gA_p)} + \frac{(1+P^{\downarrow}gA_p)}{(1-P^{\downarrow}gA_p)}}. \tag{2.35}$$

With the approximation $P^{\uparrow} \approx -P^{\downarrow} = P$ this further simplifies

$$A_P^p = \frac{\frac{(1+PgA_p)}{(1-PgA_p)} - \frac{(1-PgA_p)}{(1+PgA_p)}}{\frac{(1+PgA_p)}{(1-PgA_p)} + \frac{(1-PgA_p)}{(1+PgA_p)}} \tag{2.36}$$

$$= \frac{\frac{(1+PgA_p)^2}{(1-PgA_p)(1+PgA_p)} - \frac{(1-PgA_p)^2}{(1+PgA_p)(1-PgA_p)}}{\frac{(1+PgA_p)^2}{(1-PgA_p)(1+PgA_p)} + \frac{(1-PgA_p)^2}{(1+PgA_p)(1-PgA_p)}} \tag{2.37}$$

$$= \frac{(1+PgA_p)^2 - (1-PgA_p)^2}{(1+PgA_p)^2 + (1-PgA_p)^2} \tag{2.38}$$

$$= \frac{4PgA_p}{2+2(PgA_p)^2} \tag{2.39}$$

$$\approx 2PgA_p, \tag{2.40}$$

assuming $(PgA_p)^2 \ll 1$.

This method has the advantage that the asymmetry extraction is simplified by the cancellation of the beam power variation between pulses that the single wire is sensitive to, but requires that the backgrounds be much more carefully measured than the single wire asymmetry since it does not cancel and must be subtracted before forming the ratios.

While both methods can be used to extract the physics asymmetry A_p, by calculating both and comparing the results, different systematic effects can be examined. As the beam intensity fluctuations are a large source of uncertainty in the single wire asymmetry, the final asymmetry will probably be calculated using a two-wire method. Fig. 2.36 and fig. 2.37 show the parity-violating asymmetry and the parity-conserving asymmetry, respectively, calculated using the two-wire ratio method. The first wire plane has only two good pairs, due to the loss of wires 6 and 7. Data taking is completed but more studies of the data and simulation are required before the physics asymmetry can be extracted.

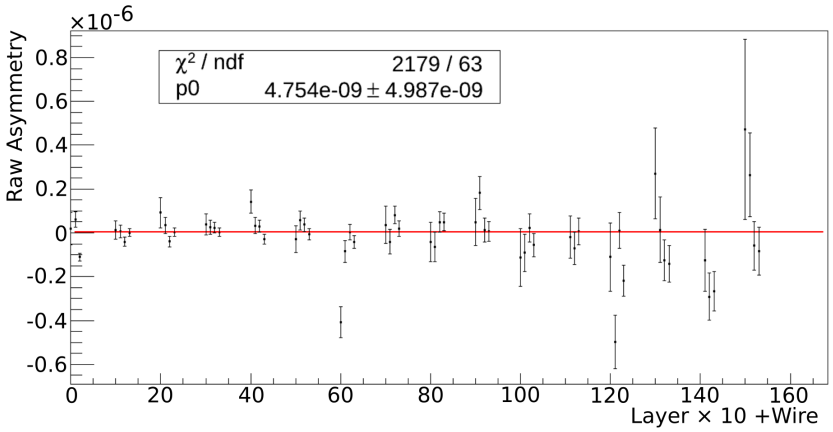

Figure 2.36: Preliminary two-wire parity-violating asymmetry [41]. As most of the neutrons are captured in the front of the chamber, the rear wire planes have worse statistics resulting in much larger error bars than the front wire planes.

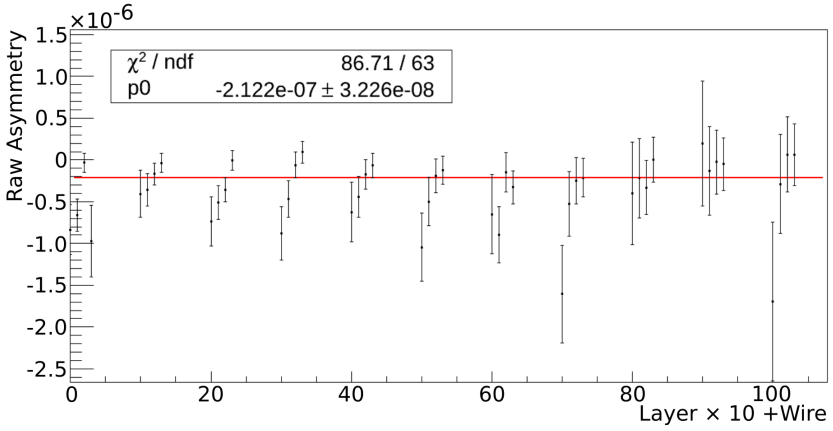

Figure 2.37: Preliminary two-wire parity-conserving asymmetry [41]. The parity-conserving asymmetry is much larger than the parity-violating asymmetry.

Chapter 3

Ion Chambers

The passage of a fast charged particle through a gas can be detected by the ionization trail that the particle creates through interactions with the gas. The energy to ionize the gas is taken from the particle's kinetic energy and the total energy loss by the particle while traversing the medium can be determined by measuring the amount of ionization that occurs. By applying an electric field over the chamber volume, the electron and positive ion pairs can be separated and forced to drift towards the oppositely charged electrodes. The current induced on the electrodes by the motion of the charges can be related to the initial ionization in the gas by factors related to the chamber geometry, gas properties, and the applied fields. Electrons reaching a conducting electrode are absorbed and ions are neutralized.

Many different types of gas ionization detectors have been developed over time to meet the requirements of various applications. Depending on the chamber geometry, applied electric and magnetic fields, and the readout electronics, information about events such as the amount, location, and timing of the ionization in the chamber can

be gathered, or in simpler cases such as Geiger counters, simply that an ionization event occurred somewhere in the chamber at a given time.

3.1 Gas Ionization

As a charged particle passes through a gas, it will interact with the gas in a number of ways. Of main interest in gas detectors are the electromagnetic interactions between the charged particle and the atomic electrons. The electromagnetic interactions will transfer energy from the charged particle to an atomic electron exciting the atomic electron. The atomic electrons can gain enough energy to overcome their binding energy forming an ion-electron pair in the gas. In this way, as a fast charged particle passes through the gas. It will create an ionization trail along its path, and the number of ion-electron pairs is related to the energy lost by the particle.

The Bethe formula [42] gives an average rate of energy lost per unit distance traveled for particles heavier than electron as

$$\left\langle -\frac{dE}{dx} \right\rangle = K\frac{Z}{A}\rho\frac{1}{\beta^2}z^2\left[\ln\frac{2m_ec^2\beta^2E_{Max}}{I^2(1-\beta^2)} - 2\beta^2\right], \tag{3.1}$$

$$K = \frac{2\pi N_A e^4}{m_e c^2}.$$

N_A is Avogadro's number, m_e is the electron mass, A is the atomic mass of the absorber, Z is the atomic number of the absorber. $\beta = v/c$, $c =$ speed of light, v is the velocity of the incident particle, and z is the charge in units of electron charge of the incident particle. E_{Max} is the maximum energy transfer in a signal collision to an electron. I is the effective ionization potential.

The National Institute of Standard and Technology (NIST) maintains a set of

databases for the stopping power of electrons, protons, and alpha particles in different mediums called ESTAR, PSTAR, and ASTAR, respectively [43]. For PSTAR the stopping power is evaluated using the Bethe formula for energies above 500 keV and fitting to experimental data below that energy. The PSTAR database was used to calculate proton and triton ranges in the gas mixtures used in the beam monitors and n3He target chamber. The proton and triton emitted after cold neutron capture on ^{3}He have sufficiently low momentum that the Bethe equation did not apply and all stopping powers were evaluated using the empirical data.

The stopping power, $S(E)$, of a material is defined as the retarding force a charged particle experiences while moving through the material:

$$S(E) = -dE/dx. \tag{3.2}$$

From eqn. 3.1 it can be seen that for a given material, stopping power increases with density.

Not all energy that is transferred from the particle to the gas goes into causing ionization, and different atomic electrons have different binding potentials. Due to this, the effective average energy, W, to create one free electron is used to determine the number of ion pairs produced in the gas from the deposited energy. The value of W needs to be measured for each gas mixture, and can also vary with the incident particle type. W and $\langle dE/dx \rangle$ are related by

$$W\langle N_I \rangle = L \left\langle \frac{dE}{dx} \right\rangle, \tag{3.3}$$

where $\langle N_I \rangle$ is the average number of ionizations created along a path length L [44]. As both the $\langle dE/dx \rangle$, and W are averages, in the case of a thin detector with a small

number of ionizations, there can be large variations in the total energy loss and the number of ions produced by identical particles passing through the detector.

3.2 Charge Collection

To measure the ionization that occurs in a chamber, a voltage is applied over a set of electrodes to create an electric field to separate the ions and electrons before they recombine. In the presence of an electric and magnetic fields, charged particles experience the Lorentz force

$$\mathbf{F} = q\left[\mathbf{E} + (v \times \mathbf{B})\right], \tag{3.4}$$

so that in the absence of a magnetic field, charged particles will undergo continual acceleration in the direction given by the electric field and the sign of the charge.

In a gas medium, the positive ions and electrons produced by ionization will rapidly reach thermal equilibrium with the gas and will spread out due to diffusion. If an electric field is applied, a net movement of the ions and electrons will be seen in opposite directions as they are accelerated by the electric field between collisions with the gas.

Each ion type will have a characteristic drift velocity $\mathbf{v}$ related to the field strength by

$$\mathbf{v} = k\mathbf{E}, \tag{3.5}$$

where k is a constant of proportionality called the mobility, and is characteristic of each ion and the gas it is in. The drift velocity is not the instantaneous velocity of the ions, but the velocity of their net motion superimposed over the thermal diffusion.

The ion mobility is constant for a given E/p value over a wide range of field strengths E and gas pressures p, as the average energy of the ions in the gas is almost unchanged by the electric field, except at high field strengths. Due to their much smaller mass, drifting electrons can substantially increase their energy over the thermal energy between collisions with the gas. The electron drift velocity can be calculated as

$$v_- = \frac{e}{2m_e} E\tau, \tag{3.6}$$

where τ is the mean time between collisions and varies with E. Sections 4.2 and 4.3 of reference [42] provide a more detailed discussion of ion and electron mobility.

Depending on the magnitude of the bias voltage, a chamber can operate in different modes due mainly to the high velocity that the electrons can reach between collision as a function of the electric field. Fig. 3.1 shows how the output signal can vary with the applied bias voltage. The exact voltage over which each mode occurs depends on the electrode shape, spacing, the fill gas type and gas pressure used.

At zero voltage no charge would be collected as the positive ions and electrons will remain adjacent to each other and recombine. As the voltage is increased, charges will start to be separated from each other and an increasing fraction of the initial ionization will be collected before recombination. The recombination mode of operation is not generally used for detectors since the degree of recombination in this range depends on the initial ionization, leading to incomplete information about the signal. The exact voltage at which recombination ends will also vary with the initial ionization density.

If the voltage is increased sufficiently, the charges can be collected without re-

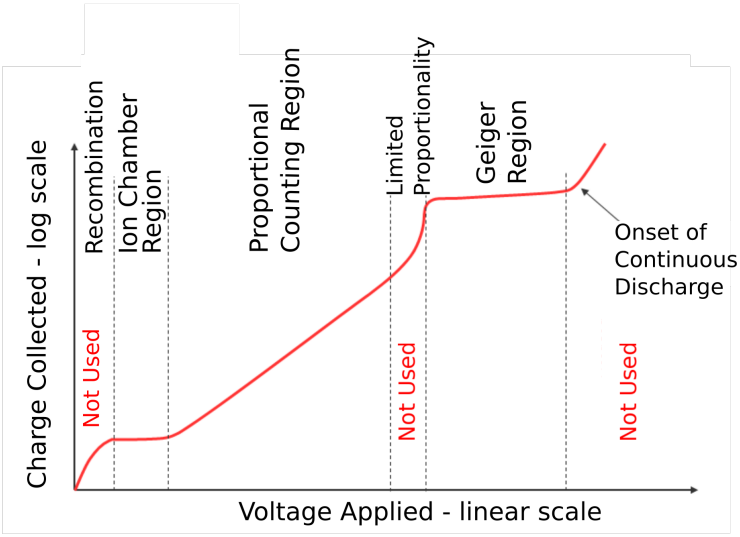

Figure 3.1: Practical ionization detector regions. The charge collected from an ionization chamber is plotted versus the applied voltage for continuous ionization [45].

combination. This mode, where a constant charge is collected as a function of bias voltage, is called the ion chamber region and chambers operated in this mode are called ion or ionization chambers. This is a useful voltage range to operate in, as the measured output charge is equal to the initial ionization charge, and is not altered by changes in the bias voltage so long as it remains in the ionization range. While the total charge collected does not vary, the collection time will increase as the voltage decreases.

As the voltage is increased, the energy of the traveling electrons can become large enough between collisions with the gas to start causing secondary ionizations during collisions. This amplifies the amount of charge that is collected proportional to the initial charge that is ionized. This is called the proportional counting region. The amplification of the initial ionization can be in excess of 10^4 and can make the detection of the initial event much easier than when operating in the ion chamber

region. Chambers operating in this range are called proportional chambers.

The last region of interest is the Geiger region where, whenever an initial ionization event occurs, a large electron avalanche is produced that saturates the chamber. In an electron avalanche, a chain reaction occurs where the initial electrons gain sufficient energy under the effect of the electric field to ionize more atoms or molecules in the gas. Then those ionization electrons cause more ionization, and so forth until all of the electrons are collected. This creates a large signal that is relatively easy to detect, but the signal is not proportional to the initial ionization.

If the voltage is increased beyond the Geiger mode, continuous discharge begins. In this range, once ionization begins, it will continue until the voltage is reduced and no information can be gained on the nature of the initial event.

For the beam monitors and the n3He target chamber, we are primarily interested in the ion chamber mode. This mode is preferred as it will give a very linear signal for a large range of ionization rates in the wire chambers and has the least sensitivity to small variations in the high voltage. The proportional amplification region can also be useful, but at high ionization rates, space charge effects can become more pronounced due to the amplification. Space charges are the ions and electron in the volume of the chamber, and at higher densities can they can significantly distort the electric fields in the chamber.

3.3 Simple Ionization Chamber Model

A simple ionization chamber model can be made considering the charge motion between a pair of infinite parallel plates separated by a distance d. The electric fields

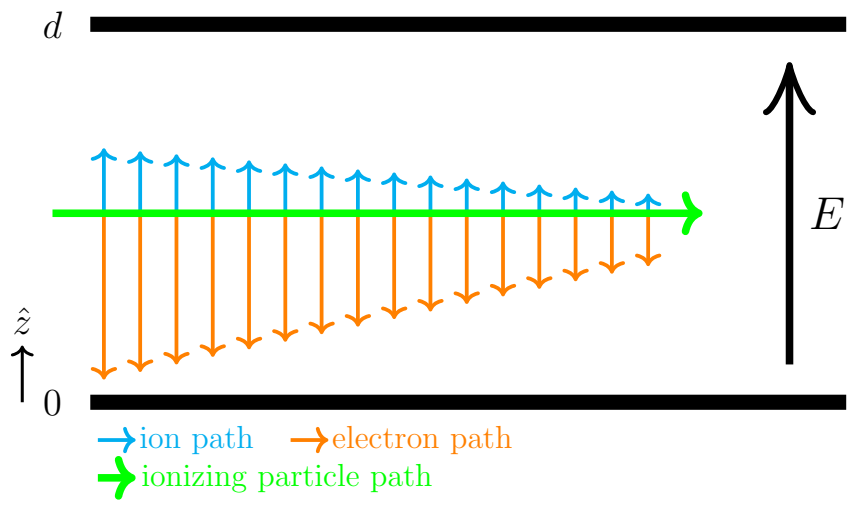

Figure 3.2: A simple parallel plate ionization chamber schematic showing an ionizing particle traveling from left to right. The electrons and positive ions are separated by the electric field E between the plates. Due to the much greater mass of the positive ions compared to the electrons, their mobility is much smaller and they will travel a shorter distance in the same time.

between the infinite plates is uniform, and this simplifies the analysis. Fig. 3.2 shows a simple schematic of this setup.

In an ionization chamber, the positive ions and electrons that are created by ionization in the chamber will drift at a speed proportional to the electric potential across the chamber:

$$v_+ = k_+ E, \tag{3.7}$$

$$v_- = k_- E, \tag{3.8}$$

where k_+ and k_- are the mobility of the ion and electron in the fill gas of the chamber. These mobilities have units of $\mathrm{m}^2/\mathrm{s}\,\mathrm{volt}$. Attachment of electrons to neutral atoms

or molecules to form negative ions is not considered in this model. In general

$$k_+ << k_-$$

due to the large mass difference between the ions and electrons.

To simplify the analysis the effect of space charge will be neglected, so the electric field in the chamber is assumed to be undistorted by the presence of the ionization charges in the chamber. This is a valid assumption so long as the electric field of the space charges is small relative to the applied electric field. This assumption is valid in most cases where large electron avalanches are not occurring during charge collection, the ionization rate is not very large, or the applied fields are not small. It will also be assumed that electrons and positive ions are created at the same rate.

Assuming the chamber is in an equilibrium state with regard to the charge densities over time, the relations between pair production, recombination and charge collection in eqn. 3.9 and 3.10 can be used to calculate the charge collection rate:

$$\frac{\partial \rho}{\partial t} = 0 = I - b\rho\epsilon + v_+ \frac{\partial \rho}{\partial z}, \tag{3.9}$$

$$\frac{\partial \epsilon}{\partial t} = 0 = I - b\epsilon\rho + v_- \frac{\partial \epsilon}{\partial z}. \tag{3.10}$$

Here ρ is the density of the positive ion charges, and ϵ is the density of the electrons in the chamber, b is the rate of recombination of the charges, I is the rate of pair production, and z is the position between the two plates along the axis $\hat{z}$ perpendicular to the lower plate as shown in fig. 3.2.

For a bias voltage V_b, the electric field between the plates is

$$E = \frac{V_b}{d}, \tag{3.11}$$

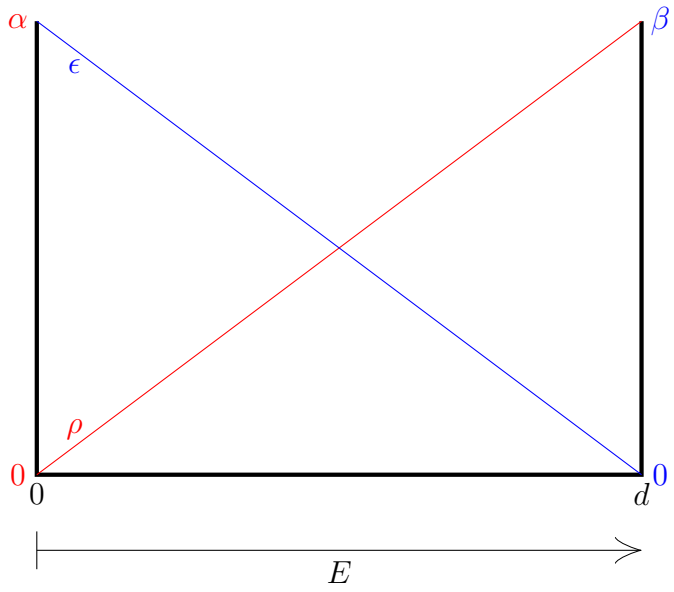

Figure 3.3: Charge density as a function of position in the chamber.

where d is the separation between the plates and E is the electric field. A simple model for the charge density in the chamber at position z between the plates is

$$\rho = \alpha z, \tag{3.12}$$

$$\epsilon = \beta(d - z). \tag{3.13}$$

Subtracting eqn. 3.10 from eqn. 3.9

$$v_+ \frac{\partial \rho}{\partial z} - v_- \frac{\partial \epsilon}{\partial z} = 0,$$

and substituting in eqn. 3.12 and eqn. 3.13

$$v_+ \frac{\partial \alpha z}{\partial z} - v_- \frac{\partial \beta(d - z)}{\partial z} = 0,$$

$$v_+ \alpha + v_- \beta = 0,$$

$$\frac{\alpha}{\beta} = -\frac{v_-}{v_+}. \tag{3.14}$$

Ignoring recombination and substituting eqn. 3.12 and eqn. 3.13 into eqn. 3.9 and eqn. 3.10

$$I + v_+\alpha = 0, \tag{3.15}$$

$$I - v_-\beta = 0, \tag{3.16}$$

and using eqn. 3.14 in the above equations

$$0 = I + v_+\left(-\beta\frac{v_-}{v_+}\right) \rightarrow \beta = \frac{I}{v_-}, \tag{3.17}$$

$$0 = I - v_-\left(-\alpha\frac{v_+}{v_-}\right) \rightarrow \alpha = -\frac{I}{v_+}. \tag{3.18}$$

So then at each z position the rate of charge loss can be calculated to first order from ρ and ϵ:

$$\Delta I = \int_0^d b\rho\epsilon dz \tag{3.19}$$

$$= \int_0^d b\alpha z\beta(d-z)dz \tag{3.20}$$

$$= b\left(-\frac{I}{v_+}\right)\left(\frac{I}{v_-}\right)\int_0^d z(d-z)dz$$

$$= -b\frac{I^2}{v_+v_-}\frac{d^3}{6}. \tag{3.21}$$

For a given rate of pair production I, the rate of collection, I_{col} is then given by

$$I_{col} = I + \Delta I \tag{3.22}$$

$$= I - b\frac{I^2}{v_+v_-}\frac{d^3}{6}$$

$$= I - b\frac{I^2}{k_+Ek_-E}\frac{d^3}{6}$$

$$= I - b\frac{I^2}{k_+k_-}\frac{1}{(V_b/d)^2}\frac{d^3}{6}$$

$$= I - \frac{c}{V_b^2}I^2, \tag{3.23}$$

where $c = bd^5/6k_+k_-$. So for a constant rate of production I, the rate of collection varies as $1/V_b^2$. At low bias voltage potential ($V_b \to 0$) there is little to no charge collection as ($\Delta I \to I$). Note that since eqn. 3.21 was derived with the assumption of no recombination at sufficiently low voltage, this model fails and predicts recombination greater than the initial pair production creating a negative signal, which is unphysical. The assumption that space charge may be ignored also fails with progressively lower ionization rates as the applied field becomes smaller.

At higher bias voltages, the collected charge approaches the produced charge I as ($\Delta I \to 0$). This transition from low to high potential corresponds to the transition from partial recombination to ion chamber region in fig. 3.1. The proportional and Geiger regions do not enter into this model as secondary ionization of the gas is not considered. If space charge effects are considered along with amplification, this will give rise to the limited proportionality region in the model.

3.4 Signal Formation in Ion Chambers

To look at how signals are formed in an ionization chamber, consider a single charged particle with charge q as it moves between the two infinite plates of the simple ion chamber model while the plates are held at a constant voltage. This particle will induce a charge distribution on the plates due to its electric field. To maintain the potential of the plates, charges will have to flow to or from the voltage source. The sum of the charge induced in both plates will be equal to the charge of the particle.

If the charge is half way between the plates, each plate will have half the charge.

If the particle were to start moving towards one of the plates, its electric field will be stronger on that plate and the charge on it will increase. At the same time, the electric field will weaken on the other plate and the charge of that plate will decrease. Due to the motion of the particle between the plates, a current will be induced in each plate to or from the voltage source that maintains the set voltage.

Using the Shockley-Ramo Theorem, the instantaneous current and total charge can be calculated for a moving charge due to the instantaneous change in electrostatic flux lines that end on the electrode [46]. This can be expressed by the following formula:

$$i(t) = -\, q\mathbf{v} \cdot \mathbf{E}_w(\mathbf{r}), \tag{3.24}$$

where $i(t)$ is the induced current at time t, q is the charge and $\mathbf{v}$ is the velocity of the moving particle. $\mathbf{E}_w(\mathbf{r})$ is the weighting field.

The weighting field is calculated like an electric field by setting the potential of the electrode on which the induced current is to be calculated to 1 V and all other electrodes to 0 V. The weighting field is not the electric field of the chamber and is not related to the particle's motion. Using this method greatly simplifies the signal calculations in a semiconductor or gaseous ionization detector.

Chapter 2.5 of reference [47] gives a detailed derivation of the time dependence of the signal in a semiconductor between two parallel plate electrodes. The results for electrons and ions in a gas are identical to those for electrons and holes in a semiconductor as long as one takes into account differences in the mobilities. The electric field is calculated with the plate at $z = d$ at potential V_b while the other plate at $z = 0$ is at ground. To calculate the weighting field, the plate at $z = d$ is chosen

as the signal plate, with the potential there held at 1 V, while the other plate is held at ground.

$$\mathbf{E} = \frac{V_B}{d}\hat{z}, \tag{3.25}$$

$$\mathbf{E}_w = \frac{1}{d}\hat{z}, \tag{3.26}$$

$$i(t) = -q\mathbf{v}\cdot\mathbf{E}_w(\mathbf{r}), \tag{3.27}$$

$$\mathbf{v} = \pm k\frac{V_B}{d}\hat{z} \tag{3.28}$$

where k is the mobility of the particle, and the velocity direction is determined by the charge of the particle and the electric field. Positive ions and electrons will move in opposite directions under the influence of the electric field and have opposite charge, so they will induce currents of the same sign.

For the particle velocity the collection time, t_c, for each member of an ionization pair starting at position z between the plates is

$$t_{c-} = \frac{z}{|\mathbf{v}_-|} = z\frac{d}{k_- V_b}, \tag{3.29}$$

$$t_{c+} = \frac{d-z}{|\mathbf{v}_+|} = (d-z)\frac{d}{k_+ V_b}, \tag{3.30}$$

and the total charge, Q induced by each particle, is a product of the current and the collection time

$$Q_- = i_-(t)t_{c-} = ek_-\frac{V_b}{d^2}\left(z\frac{d}{k_- V_b}\right) = e\frac{z}{d}, \tag{3.31}$$

$$Q_+ = i_+(t)t_{c+} = ek_+\frac{V_b}{d^2}\left((d-z)\frac{d}{k_- V_b}\right) = e\frac{d-z}{d}. \tag{3.32}$$

Due to the specific geometry of this example, the current is constant over time independent of the particle's position between the plates. The total charge collected

is

$$Q_{tot} = Q_- + Q_+ = e\left(\frac{z}{d} + \frac{d-z}{d}\right) = e. \tag{3.33}$$

The total charge induced on the signal electrode by the motion of the two oppositely charged particles, starting at an arbitrary position between the plates, is the same as the charge induced by one particle with an equal magnitude of charge moving along the entire path in the direction of the field. This result for two particles of opposite charge moving along the same path in opposite directions is a general result and is not limited to parallel plates.

For other geometries, the electric field and the weighting field will vary with the position in the chamber. With the varying electric field, the particle velocity will no longer be constant either. With the varying velocity and weighting fields, the induced current $i(t)$ will, in general, no longer be constant over time.

To make use of the current generated in an ionization chamber, one of the electrodes needs to be connected to a device to measure the generated current. As the current is generally fairly small, the device must be very sensitive and amplifiers are frequently utilized.

3.5 Sparking

Sparking occurs in a wire chamber when the voltage difference between two conductors is sufficiently large as to cause breakdown of the separating insulator. This will damage solid insulators burning a trail through them. This can cause mechanical instability and further sparking at lower voltages as the spark's trail remains through

the insulator. When sparking occurs in gases, the gas will form a plasma and new molecular species can be formed.

The breakdown voltage for a gas can be calculated using Paschen's Law:

$$V_B = \frac{Bpd}{\ln(Apd) - \ln\left[\ln(1 + \gamma_{se}^{-1})\right]}, \tag{3.34}$$

where p is the gas pressure, d is the gap distance between the electrodes, γ_{se} is the secondary electron emission coefficient, and the coefficients A and B are experimentally determined variables. A is the saturation ionization at a particular E/p,where E is the electric field, and B is related to the excitation and ionization energies. While A and B vary with E/p, they are relatively constant over restricted ranges of E/p. The gap distance d required for break down to occur also varies strongly with the shape of the electrodes. See section 14.3 of reference [48] for more details on Paschen's Law.

Fig. 3.4 shows a log-log plot of the breakdown voltage plotted against the product pd. There is a pd value for which the breakdown voltage is the minimum and increasing or decreasing either the pressure or the separation d will increase the breakdown voltage. There is a lower limit of $pd = A^{-1}\ln(1 + 1/\gamma_{se)}$ below which breakdown cannot occur.

Usually sparking occurs between some part of the high voltage input or the high voltage electrodes and another part of the chamber that is grounded such as the housing or read out electrodes. In addition to the mechanical damage that sparking can cause to the chamber, it will usually affect the signal readout. The instantaneous current of a spark is usually large enough that it can damage the signal readout electronics. For this reason, the safe range of operation of a chamber without sparking is usually determined without the readout electronics being connected.

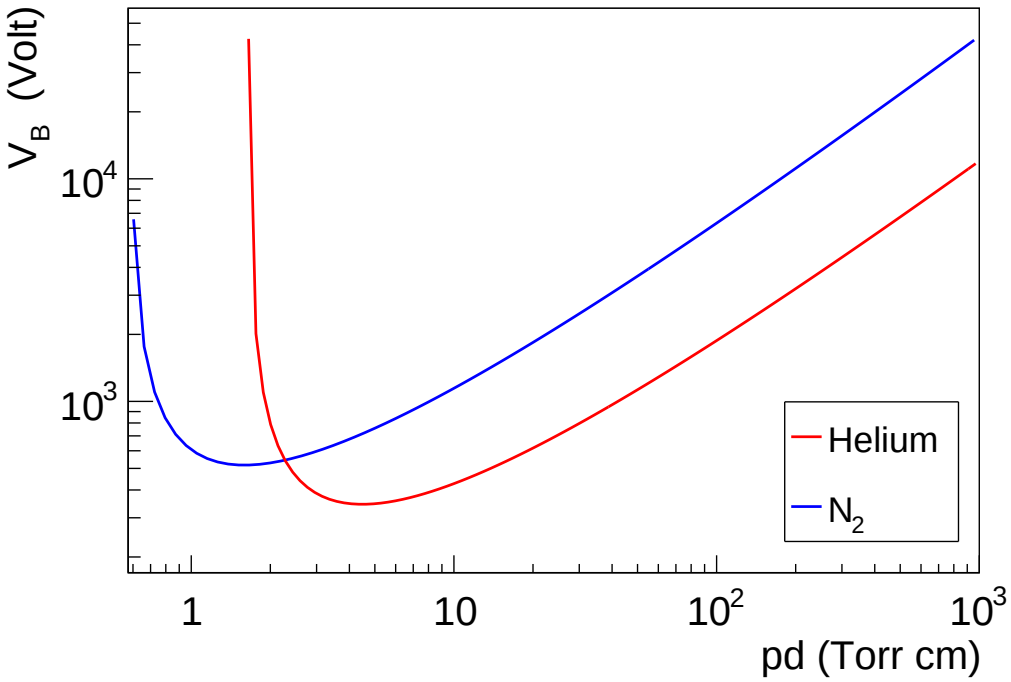

Figure 3.4: Paschen curves for selected gases. A and B values taken from table 14.1 of reference [48].

Chapter 4

Beam Monitor

Two multi-wire proportional chambers (MWPC) were constructed to be used as neutron beam monitors at the FnPB. A multi-wire proportional chamber is an ionization chamber that uses multiple wires as the signal electrodes and operates in either the ionization or proportional charge collection region. A multi-wire chamber design was used for the beam monitors to reduce the total amount of material in the beam to maximize the neutron transmission.

Since wire planes are used, the electric and weighting fields in the chamber are no longer the uniform fields that the parallel plate model in sections 3.3 and 3.4 had. Near the wires, the electric and weighting fields are similar to a wire in a cylinder and have a $1/r$ dependence. Due to this position dependence, there will be a spike in the induced signal when an electron is the near the wire just before it is collected, or an ion is near the signal wire before it drifts away towards a HV wire.

The neutron beam monitors are used to measure the neutron flux and the variation in the neutron flux during experiment data taking. These measurements can be used

to normalize data taken with the main detectors. The monitors were also used to examine the spin flipper efficiency with a polarized ^{3}He cell and for other diagnostics during the experiments. The MWPC beam monitors are labeled M1 and M2 in fig. 2.14. M3 is a monitor of a different design using plates instead of wires and a pure ^{3}He fill gas at 1 atm pressure. Despite these differences, the basic operational principles are the same. Only the M1 monitor was used during the n3He experiment as shown in fig. 2.25.

As a neutron carries no electrical charge, at low energies it will not ionize the chamber gas as it passes through the fill gas. To detect the neutrons, ^{3}He gas is used in the gas mixture in the chamber. Neutrons will capture on the ^{3}He nuclei, which will break up following the reaction $n + {}^3\mathrm{He} \rightarrow {}^4\mathrm{He}^* \rightarrow p + t + 765\,\mathrm{keV}$ where the 765 keV is released in the form of kinetic energy of the proton and the triton. ^{3}He has a large neutron capture cross section of 5333 barns for a neutron velocity of 2200 m/s. As the proton and triton pass through the chamber, they ionize the fill gas and slow down in the process. The proton and triton may either range out, depositing their full energy in the fill gas, or impact the walls or a wire stopping there, only depositing a fraction of their energy in the gas. This causes the total charge collected per neutron event to be variable.

The monitors were designed to remove only a small fraction of the neutron beam to allow the maximum possible neutron flux to continue to the experimental target while providing a measurable signal. The monitors are 3.4 cm thick in the beam direction and only a small fraction of the fill gas is ^{3}He. The rest is nitrogen, which has a small capture cross section of 1.9 barns for a neutron velocity of 2200 m/s.

Nitrogen is added to reduce the distance required for the proton and triton to range out in the fill gas, reducing the number of proton and tritons that impact the walls of the chamber, while not significantly increasing the neutron capture rate. The proton and triton ranges are calculated in section 4.5.1 for the M1 fill gas.

Due to the large neutron beam flux anticipated at the SNS, it was decided to use the beam monitors in current mode instead of counting mode. For a counting mode monitor, each time a neutron is captured the signal pulse can be measured and the energy and timing of the event recorded. The disadvantage of this method is that if a large number of capture events occur in a short time compared to the event time scale, the individual events cannot be resolved. This pile-up of events reduces the efficiency in counting mode. In a current mode monitor for sufficiently rapid events, a continuous output current can be measured that is proportional to the energy deposited in the monitor. By operating in current mode, an increasing event rate does not cause a decrease in efficiency. Different readout electronics are required for each mode of operation, and the current mode electronics are usually inefficient at detecting events at low event rates.

Fig. 4.1 shows a diagram of the chamber with the relative path lengths of the triton and proton in the gas. The monitor is constructed with three wire planes. The outer two planes are the high voltage (HV) planes that provide the bias voltage for charge collection. The center plane is the grounded signal plane that is connected to the readout electronics to measure the currents induced by the charge collection. Due to the negative voltage bias from the signal to HV planes, the positive ions are collected on the HV plane wires, while the electrons are collected on the signal plane

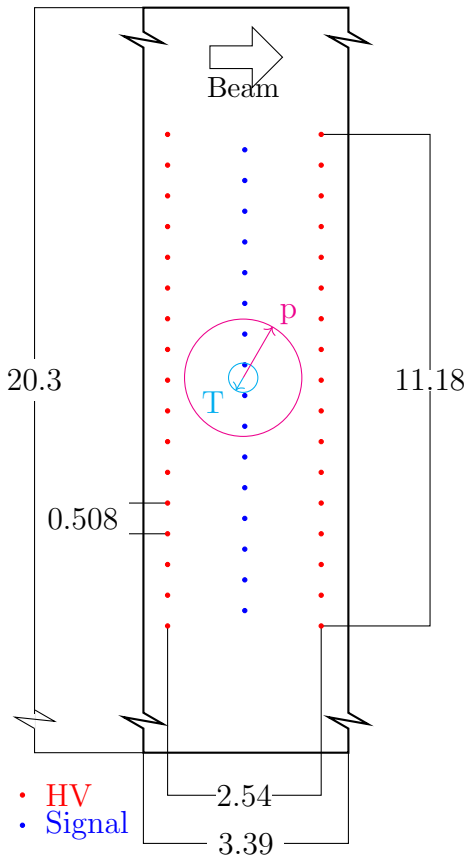

Figure 4.1: Schematic diagram of the beam monitor. Only the interior volume of the housing is shown. The cross section is taken through the center of the beam monitor perpendicular to the wire direction. Each red or blue filled circle is the position of one wire. The proton p and triton T lines in the diagram show the stopping distance of those species for the initial energy they would carry from the breakup of the ^{3}He nuclei after cold neutron capture. Linear dimensions are in centimeters.

wires.

The active volume of the monitor is the space between the HV and signal planes where electrons will be collected towards the signal wires. In the gas volume between the HV plane and the walls of the chamber, any ionization electrons in this region

will go to the grounded chamber wall instead of the signal plane and will not produce any measurable signal.

The FnPB neutron beam pipe has a 10 cm × 12 cm cross section, which sets the cross section of the neutron beam exiting the guide. The beam monitors must cover the full area of the beam, so the interior of the wire frames is a 12 cm × 14 cm rectangle to allow for beam divergence and misalignment during installation. The housing and wire frame dimensions are shown in fig. 4.2.

For the two ^{3}He beam monitors, it is desired to have an absolute wavelength-dependent calibration of the monitors that will allow a given output voltage to be converted into a neutron flux at all neutron flux ranges. This also requires that the linearity of the beam monitors be examined, as the monitor response can vary with the rate of ionization in the monitor following neutron capture. The next sections will describe the design and construction of the beam monitors, their testing, and calibration of one of the beam monitors.

4.1 Wire Frame Stack Design

A prototype monolithic frame design, using macor ceramic constructed from four pieces (top, bottom, and two sides), was constructed at the University of Manitoba. The four sections were joined with a two-part epoxy at the corners of the rectangular frame.

This prototype was tested at the Los Alamos Neutron Scattering Center (LANCSe), beam line FP12, at Los Alamos National Laboratory (LANL) in New Mexico. Initial tests were done to determine the signal-to-noise ratio, γ-ray response, and monitor

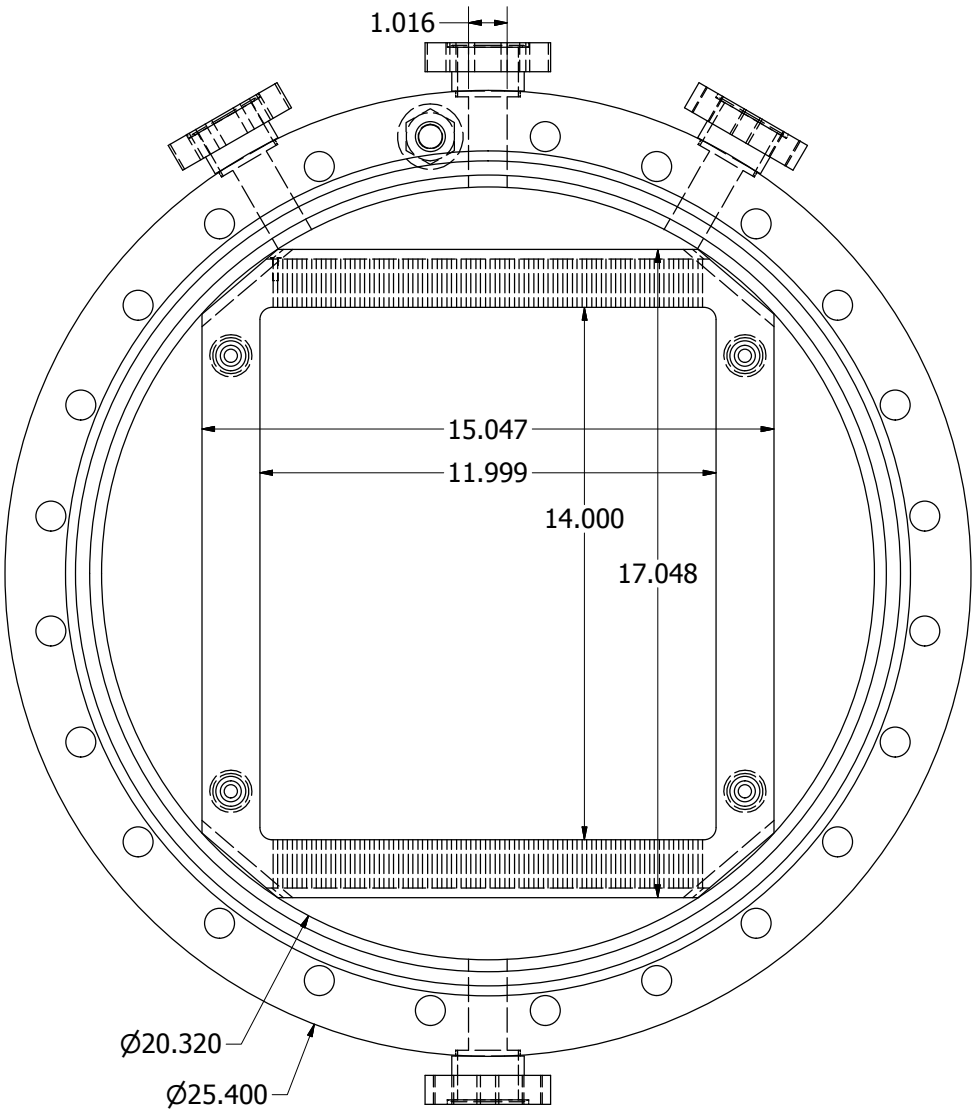

Figure 4.2: CAD drawing of frame stack in housing. Around the edges of the housing are four feedthroughs, three to the top and one on the bottom side. The wires are not shown. Linear dimensions are in centimeters.

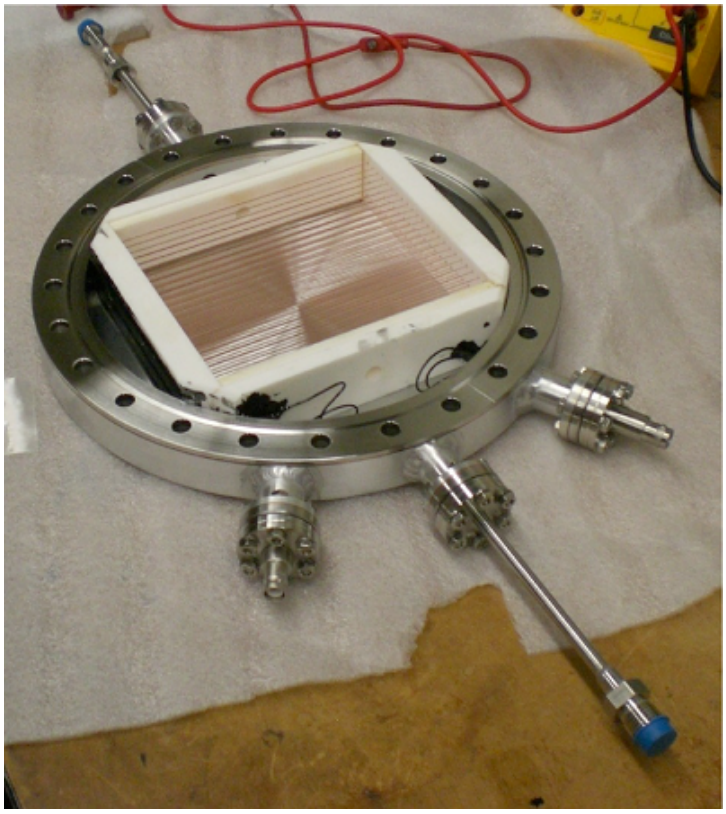

Figure 4.3: Beam monitor prototype with the monolithic frame, shown here during assembly at the University of Manitoba. The black material visible on the white macor ceramic is epoxy used to hold wires in place and to shield the end of the HV and signal wires from sparking. A clear epoxy was used to join the four frame segments.

transmission. The monitor passed these tests, having sufficiently low noise and no measurable response to gamma rays that were created by a cadmium sheet in the neutron beam in front of the monitor. A second test six months later was done to check the monitor's stability, which it passed as well. Several months after that, during testing at the SNS prior to installation, the monitor was found to have developed a very large leakage current of approximately 40 nanoamps for unknown reasons. The

leakage currents were probably surface currents. It was suspected that the epoxy, used to insulate the ends of the wires, was the main cause of the leakage currents given the properties of the macor ceramic the frames were constructed from. After disassembly, there was no visible damage seen on the monitor frame or wires.

A new frame stack design was required after the failure of the prototype. The new frame design was made with the goal of avoiding the problems that occurred with the monolithic macor frame while reusing the same housing, wire geometry, and fill gas. Further requirements were to avoid the use of epoxy and to provide better control of leakage currents. As most leakage currents are surface currents across the insulating frame material that supports the wires, the monolithic frame design was replaced by a new design, using three separate frames with insulating spacers and a drain to ground between the high voltage planes and the signal plane. The drain to ground was used to divert any leakage currents between the high voltage planes and the signal plane to ground before it could be picked up by the signal wires.

Fig. 4.4 shows an exploded CAD drawing of the new frame stack design. The frame labeled BM280 supported the high voltage wires. These were separated from the signal frame (BM281) by four insulating frame spacers (BM286). Each spacer had a hole drilled through the side, to prevent virtual leaks, the trapping of gas during assembly that could leak out later during operation. The grounded rings (BM289) were machined from copper and were used to drain the leakage currents to ground. Machine screws were then used to compress the frame stack together so they could not move relative to each other. The machine screws must be stainless steel to reduce outgassing that is common with other metals and alloys.

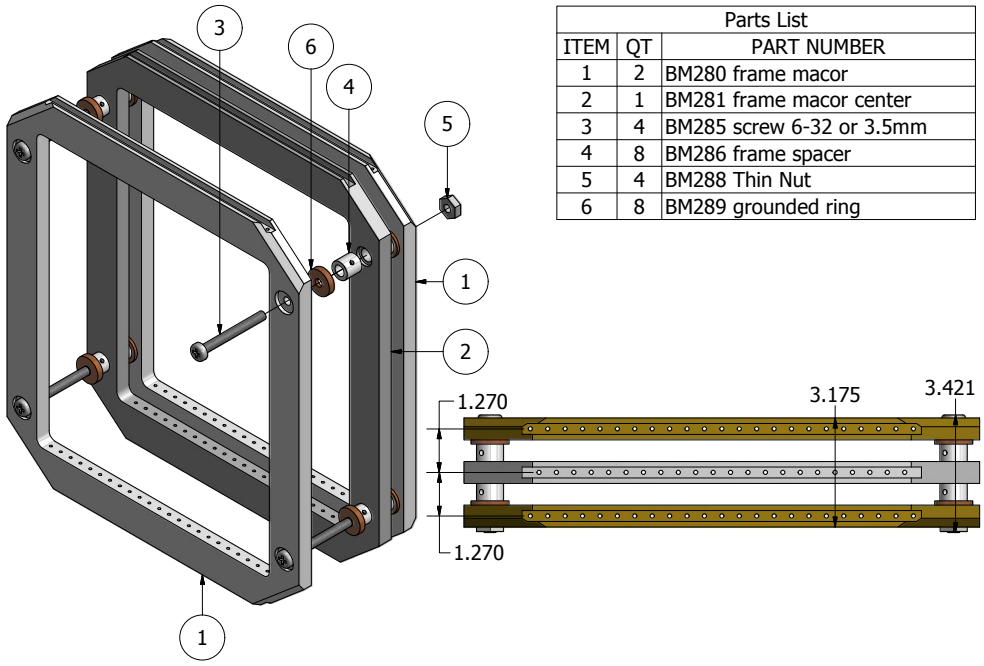

Parts List		
ITEM	QT	PART NUMBER
1	2	BM280 frame macor
2	1	BM281 frame macor center
3	4	BM285 screw 6-32 or 3.5mm
4	8	BM286 frame spacer
5	4	BM288 Thin Nut
6	8	BM289 grounded ring

Figure 4.4: Exploded CAD drawing of the frame assembly for the new frame stack design that was used in the beam monitors. Linear dimensions are in centimeters.

The material for the frame stack parts was restricted to those that would not significantly outgas. Outgassing is a problem in wire chambers since they are sealed systems, because the volume of outgassed vapours in the chamber will increase over time. This can affect the charge transport and breakdown voltage characteristics of the fill gas. Some of the released gases can also attach to the chamber surfaces reducing the efficiency of the chamber by reducing the conductivity of the charge gathering electrodes. Most plastics as they age will outgas organic vapours over time and cannot be used. All materials will absorb gases from the atmosphere with the amount and rate of gas absorption varying with the material and the surface preparation.

The two materials that were investigated for suitability for the frames were macor ceramic and PEEK (poly ether ether ketone) plastic. The criteria for choosing between the materials was the mechanical strength, outgassing, radiation hardness, and cost.

NASA maintains a database of material outgassing [49] that was used as a source of information on the materials. To measure the outgassing from the materials, the total mass loss (TML) after 24 hours in vacuum at 398 K was measured, along with the collected volatile condensable material (CVCM) at the exit port from the heated chamber, and the water vapour regained after 24 hours at 298 K in room air at 50% humidity. All of these values were recorded as a percent of the initial mass of the sample. For PEEK there was a significant outgassing with TML of 0.31%, but low CVCM of 0.01%. The WVR was 0.25% indicating that most of what was outgassed in the vacuum was water rather than organic vapours. For macor, there was low overall outgassing with TML of 0.01%, and 0.00% CVCM, and 0.01% WVR.

The material must also be radiation hard due to the expected gamma ray and neutron flux near the neutron beam. Radiation can damage a material by changing the chemical elements that are present, breaking chemical bonds, or by the formation of reactive chemical species. In crystals, point defects can also be created by atoms being knocked out of a lattice position and into an interstitial region. These changes to the structure of the material can reduce the mechanical strength and increase brittleness. Swelling or densification can also occur due to irradiation.

Most plastics are composed of a combination of carbon, hydrogen, and oxygen with a few other elements present in small quantities, so the relative radiation hardness

of plastics tends to vary with their chemical structure. PEEK is one of the more radiation hard plastics that are commercially available [50] and has been used in many other nuclear physics applications, and so is suitable for use in the beam monitors.

Element	Compound	Approx. % Weight
Silicon	SiO_2	46
Magnesium	MgO	17
Aluminum	Al_2O_3	16
Potassium	K_2O	10
Boron	B_2O_3	7
Fluorine	F	4

Table 4.1: Macor ceramic composition from reference [51].

Element	Capture Cross Section (barns)
Al	0.231
B	767
C	5.551
Cu	3.78
F	0.0096
Fe	2.56
H	0.3326
He	0.00747
^{3}He	5333
K	2.1
Mg	0.063
N	1.9
O	0.00019
Si	0.171

Table 4.2: Selected neutron capture cross sections at 2200 m/s.

Macor is a hard white ceramic composed of 55% fluorophlogopite mica and 45% borosilicate glass [51]. Its chemical composition is given in table 4.1. Its elements all have low neutron capture cross sections compared to other common elements such as

carbon, iron, and copper as shown in table 4.2. Macor is dimensionally stable and maintains its mechanical stability under neutron irradiation [52].

The mechanical deformation and the safety factor of the frames were both investigated under the anticipated maximum loads caused by the wire tension in the frames. The safety factor is the ultimate tensile strength divided by the tensile stress caused by the wire load. If the overall safety factor is less than one through a leg on the frame, then it will rupture as the stress exceeds the material strength. If only a fraction of the frame has a safety factor of less than one, then permanent deformation will remain after the load is removed. A safety factor of greater than one is preferred to offer a margin of safety against mechanical shock and material degradation over time as the M1 and M2 monitors are expected to be used over a series of experiments at the FnPB.

Autodesk Inventor 2008 [53] was used to design the frame stacks for the chamber. Inventor 2008 is a 3D parametric solid modeling program that has a built-in single-part stress analysis that was used to determine the optimal frame design. The stress analysis was performed by applying a force at each of the points where the wire ferrules would contact the surface of the through hole on the top and bottom of each frame. The directions of the forces were set to match the forces required to hold the wires in tension across the frames. This created a balanced set of forces, so the only further constraints that were required was a set of pin constraints on the bolt holes through the frame to keep the frame from sliding in the model.

A 0.0508 cm diameter copper wire manufactured by California Fine Wire was used to string the wire frames. This large diameter wire was chosen to prevent the

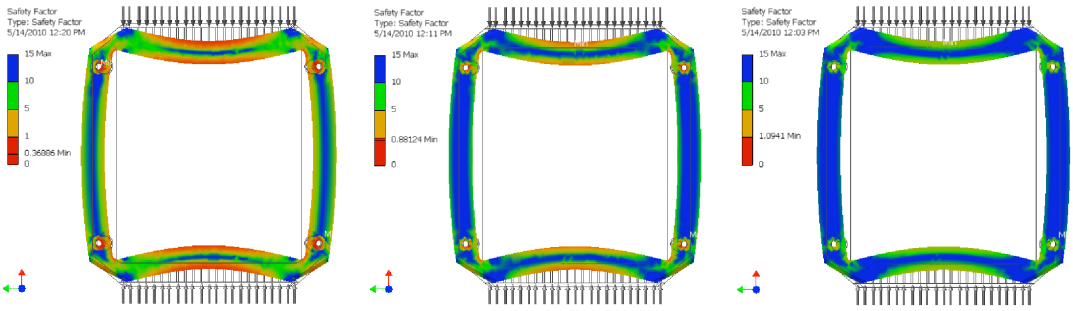

(a) 1/8" Frame (b) 3/16" Frame (c) 1/4" Frame

Figure 4.5: Safety Factors of the three macor frame designs.

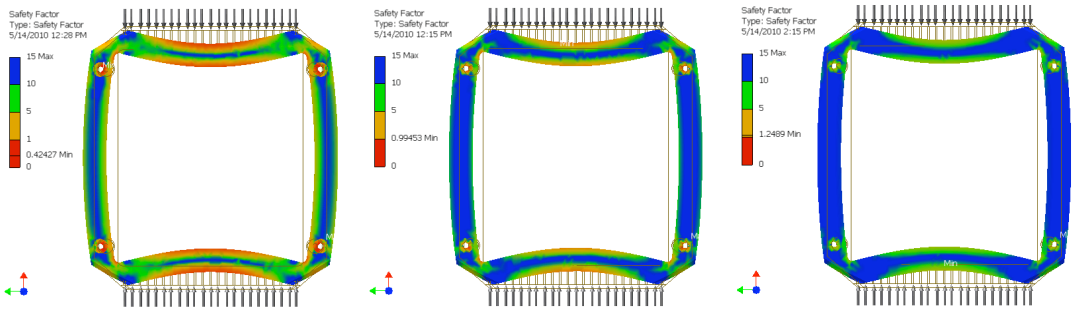

(a) 1/8" Frame (b) 3/16" Frame (c) 1/4" Frame

Figure 4.6: Safety Factor of the three PEEK frame designs.

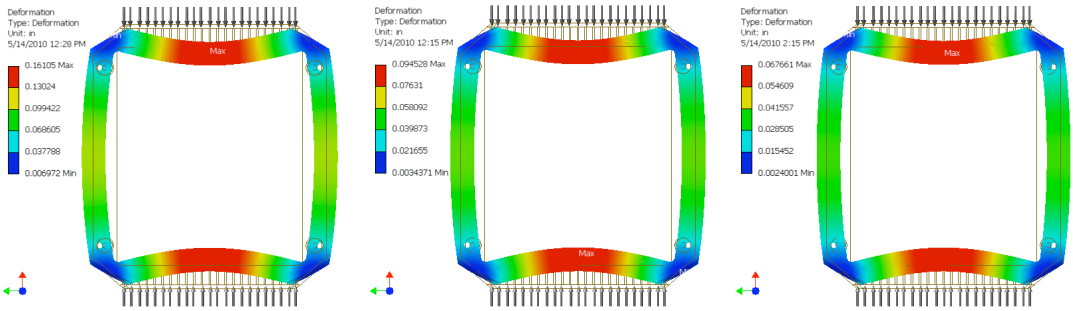

(a) 1/8" Frame (b) 3/16" Frame (c) 1/4" Frame

Figure 4.7: Deformation of the three PEEK frame designs ranges from $0.067 - 0.16$".

electron avalanche the high electric fields near a thinner wire could cause. While this avalanche can cause a large increase in the chamber signal for easier readout, this was not required and can result in nonlinearities at higher event rates, so it was avoided. It was desired to fix the wires to the frames under tension to prevent vibration in the wires as that would increase the noise in the beam monitor signal and to prevent deflection of the wires due to the electric fields in the chamber. The tensile yield strength specified by the manufacturer is 110.8 megapascal(MPa) which for the wire that was used would be reached by a force of

$$F = 110.8\,\mathrm{MPa} \times 0.0020268\,\mathrm{cm}^2 = 22.45\,\mathrm{N}. \tag{4.1}$$

While it was not specified by the manufacturer, the tensile yield strength is usually the stress required to cause a 0.2% permanent elongation after the tension is released. Staying below this limit should keep the wire in its elastic range. The highest possible tension in the wires was preferred to minimize vibration and deflection of the wires. Each arrow in the stress and safety factor figures shows where and in what direction these forces were being applied.

Fig. 4.5 shows the result of the Inventor stress analysis for PEEK and macor frames of varying thicknesses. For both materials, the frame geometry was identical at each thickness. In the stress analysis images, the red sections of the frame show where stresses exceed the tensile limit of the material. If the frame is partially red, it will permanently deform under the load, and if it is completely red, it will break. It was not necessary to investigate the deformation of the macor frames as macor is a brittle ceramic and would break before any significant deformation would occur.

Looking at a set of PEEK frames, the stress analysis shown in fig. 4.6 shows

that a thickness of 1/4 inch (0.635 cm) is required to maintain a sufficient safety factor to prevent the frames from being permanently deformed by the wire load. The deformation of the PEEK frame designs was examined to ensure that the frame would not deform excessively reducing the wire tension after stringing. In fig. 4.7 the red area corresponds to maximum deformation, while the blue areas correspond to minimum deformation. The deformation is exaggerated in the images for visibility.

While macor is much stronger in compression than PEEK, its strength is not much greater in tension. As parts of the horizontal sections of the frames will be in tension, the 1/4 inch thickness was preferred for the macor frames to provide a higher safety factor against shock and vibration that ceramics are more sensitive to than plastics.

For both materials, a frame thickness of 1/4 inch was required to have a sufficiently high safety factor for the design. Due to the higher cost of machining the macor frames compared to the PEEK frames, it was decided to use the PEEK frames for the beam monitors. For PEEK there is a variety of carbon and glass fibre filled PEEK plastics available, but it was thought that the additional strength and creep resistance were not required for this application. Creep, also called cold flow, is the slow deformation that occurs under loads, even below the yield stress. This is an issue in wire frames as it can cause a reduction in the wire tension over time as either the wires stretch or the frames bend inward under the load of the wire tension.

4.2 Monitor Housing

The beam monitor housing is made mainly of aluminum. Aluminum is essentially magnetically transparent, so it will not distort the magnetic fields required for man-

aging the neutron spins in the experiment. Aluminum has a low neutron capture cross section of 0.231 barns at 2200 m/s and scattering cross of 1.503 barns. Aluminum also has an approximately seven minute half-life after neutron capture, so it will not become too strongly activated during continuous beam exposure. Neutron capture on aluminum results in gamma rays, and a beta decay of the ^{29}Al to ^{29}Si. The gamma rays will not create significant ionization in the target chamber. The beta decay electrons have sufficient energy to exit the aluminum window and ionize the fill gas, but due to the short half-life of the beta decay the background will remain small. The short half-life is also useful for radiation safety and reducing wait times after beam exposure before handling. Outgassing from aluminum is also low [54].

The monitor housing is composed of two sides. Each side has a 1 mm neutron window and a eight inch conflat flange. One flange has four mini conflat feedthroughs around the edges for high voltage input, a gas valve, signal readout, and a spare flange. Fig. 4.2 shows a drawing of the frame stack inside the housing.

The conflat flanges on the beam monitor are bimetal flanges [55]. These flanges are created by explosion welding a stainless steel sheet to an aluminum sheet from which the flange is then machined. The knife edges are formed out of stainless steel to make them more resistant to damage while minimizing the amount of steel in the target as it has more problems with neutron activation and a higher magnetic permeability than aluminum.

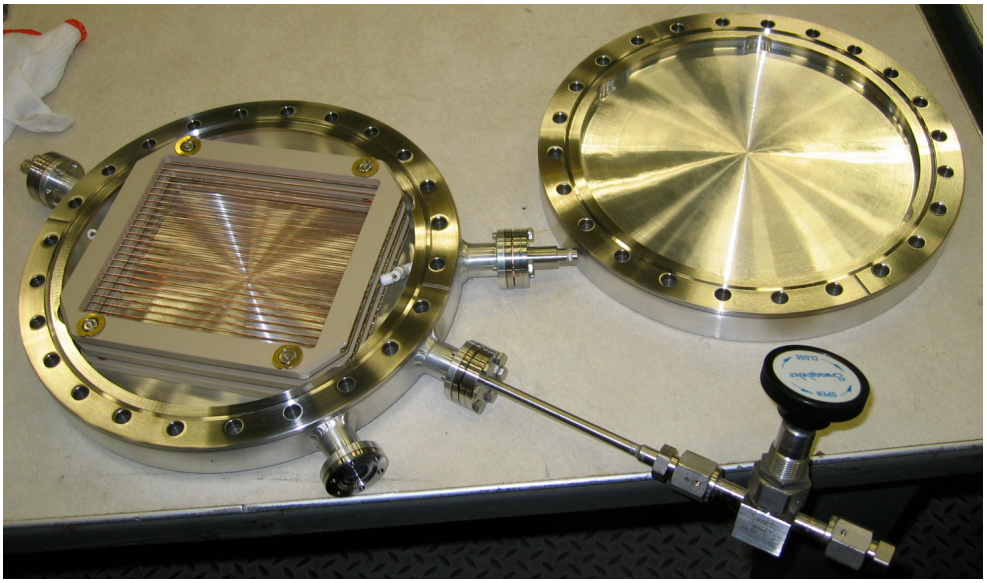

Figure 4.8: M1 beam monitor frame stack in aluminum housing during assembly.

4.3 Frame Wiring

The goal for the frame wiring was to securely fix the wires to the frames under consistent tension to reduce vibration in the wires, which would cause noise in the monitor signal. As the metal wires cannot be glued, crimped, or soldered to the plastic frames, wire ferrules were used. Wire ferrules are tinned metal cylinders with a thin wall, and one flared end. These ferrules were inserted into the through holes in the frames, and the copper wires were soldered under tension to the ferrules. See fig. 4.9 for a picture of the ferrule style that was used and how they sit in the through holes in the frames. The wires were held in place under tension as they could not pull the ferrules through the frame.

Each wire in each plane was electrically connected at both ends by soldering a continuous wire across the wire ferrules. Fig. 4.10 shows this connection along one

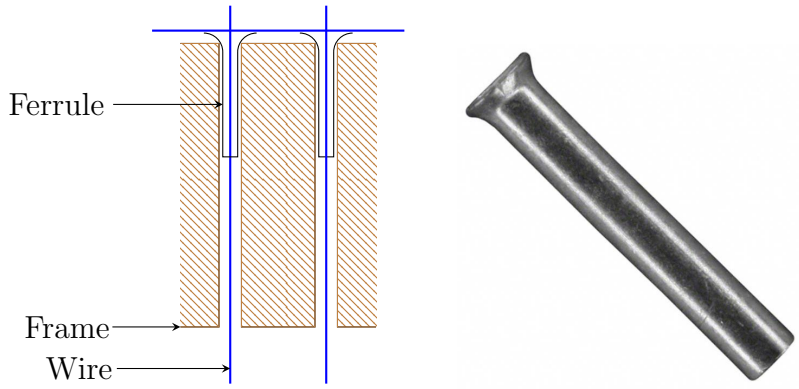

(a) Ferrules in frame cross section (b) Wire ferrule

Figure 4.9: How the wire ferrule is seated in the wire frame.

end of the frame stack. This cross wire summed the currents from the signal plane wires for readout as the beam monitors were not required to be position sensitive and reading all wires gave better statistics from the monitor. By joining all of the wires in the HV frames, each frame could be connected to the HV feedthrough by one wire. The wire ends are visible in fig. 4.10 with the continuous joining wire and the thicker wires that lead to the signal and HV feedthroughs.

Fig. 4.11 shows the aluminum jig that was used to hold the wire frames while the wires were soldered onto the frame.

The initial frame-wiring procedure used at the University of Manitoba consisted of the following steps: Copper wire was cut to length from the manufacturer delivered spool, and cleaned with ethanol soaked kim wipes. If any kinks or nicks were found in the wire, it was discarded. The wire was pushed through the holes on the frame and a ferrule was placed over each end. The wires were held at one end by the set screws along the left hand side of the plate in fig. 4.11. The wires were tensioned with a 2 kg weight hung over a pulley that provided $2\,\mathrm{kg} \times 9.81\,\mathrm{m/s^2} = 19.62\,\mathrm{N}$ tension

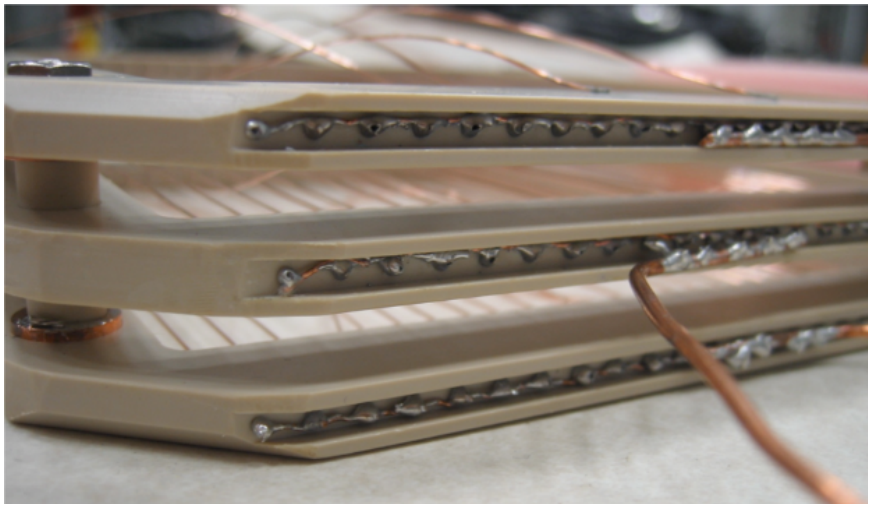

Figure 4.10: Shown here is one the end of the frame stack as assembled at the University of Manitoba. Loose wires whose solder joints broke can be seen above the wire frame in the top of the image. The cross wire joining each wire in a plane is visible as well.

on the wire, somewhat below the calculated tensile yield force. The left hand wire ferrules (as the frame is oriented in fig.4.11) on the side of the frame opposite the weights were soldered into place. A single connecting wire was soldered across the wire ends to electrically join the wires at that end. A heavier 16 gauge wire was also soldered to 5 adjacent frame wires, to form a strong mechanical joint, to connect to the feedthroughs. This was allowed to cool for an hour before the screws were released to begin pre-creeping the frame and wires. A basic tin-lead solder was used for all solder joints.

The frame and wires were allowed to pre-creep 24 hours before the ferrules were soldered to the wires on the right hand side of the frame. The 24 hour pre-creep was done to minimize wire relaxation after the weights were removed. Another connecting

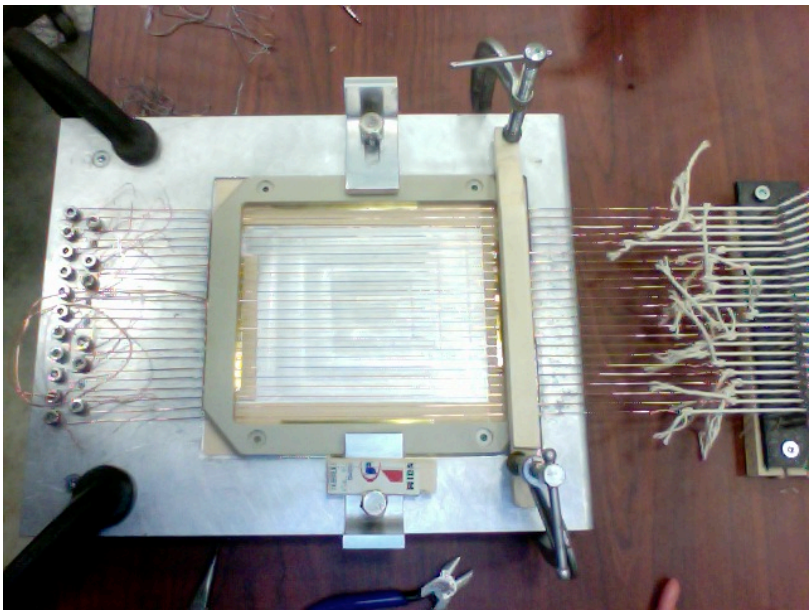

Figure 4.11: For wiring the frames, an aluminum jig was used to hold the frame in place with two L brackets and a wooden bar used to prevent the frame from lifting out during soldering. On the left hand side are a set of screws used to hold the wires in place during the initial stages of soldering, and the strings on the right hand side of the image go out to the weights used to tensions the wires.

wire was soldered to the wire ends on that side of the frame as well. This was then allowed to cool for one hour before the weights were released.

This procedure resulted in cold solder joints from which the wires eventually broke. This was first noticed during final assembly of the wire chambers at the SNS. Fig. 4.10 shows the wire frame stack with some of the loose wires visible above the frame stack. This required rewiring the frames.

During the restringing of the frames, the 2 kg weights used at the University of Manitoba were replaced with lighter weights to give a higher safety factor on the

solder joint strength. The setup was otherwise identical. The soldering operations were changed with the left hand wire ferrule (as the frame is oriented in fig 4.11) being soldered to the wire before it was strung through the frame so that the soldering temperature was not limited by the PEEK safe temperature range. The connecting wire and the 16 gauge wire were soldered in place before the weights were added. Instead of using the set screws to the hold the wire while the weights were added, the already attached ferrule was used to hold the wire.

The right hand ferrule on each wire ferrule was soldered to the wire with the same procedure as before, but with a second soldering iron held to the side of the wire inside the frame to heat the wire faster. Since this soldering iron was not held as close to the PEEK as the iron soldering at the outside groove, it was operated at a higher temperature.

The M1 Monitor frames were soldered first, using the modified procedure. The wires were tensioned using 0.5 kg weights. After establishing success with the M1 frames, the M2 frames were soldered using 1 kg weights. No significant difference was noticed during operation with the difference in the wire tension.

4.4 M1 Monitor Assembly and Bench Top Testing

4.4.1 Maximum High Voltage Test

After wiring the frames for the M1 monitor, Accu-Glass Inc. high temperature UHV compatible epoxy [56] was applied to both ends of the HV wires in the frame grooves in an attempt to prevent sparking. 20 hours of presetting were required to

cover the wires due to the low initial viscosity of the epoxy.

A high voltage test was performed with the chamber fully assembled and exposed to the atmosphere. During this test, sparking was observed in the 500 to 750 V range, between the housing and the corners of the frame assembly, even through the epoxy. The sparking damaged the epoxy insulation, and that resulted in a significant decrease of the maximum high voltage before sparking. The gas breakdown occurred between the wire nearest to the wall of the chamber at the frame corners and the chamber housing.

Assuming that a few percent ^{3}He in the ^{3}He-N_2 gas mixture does not significantly affect the dielectric characteristics of the gas, the required distance between the wires and the housing to stop sparking was calculated using the dielectric strength of nitrogen. The voltage required to cause breakdown varies strongly with the electrode shape. Air has a breakdown voltage of 3000 V/mm between two plane electrodes, and 400 V/mm for a needle electrode discharging to a plane. Helium has a relative dielectric strength of 0.15 to air, and N_2 gas has a relative dielectric strength of 0.97 to air [57]. Using the needle to plane breakdown voltage of air as the reference, a 3 kV operating voltage requires at least a

$$d = \frac{V}{V_B} = \frac{3000\,\mathrm{V}}{0.97 \times 400\,\mathrm{V/mm}} = 7.73\,\mathrm{mm} \tag{4.2}$$

gap between the wire ends and the housing for the chosen fill gas mixture in the monitors.

In the end, it was decided to machine a groove into the vacuum housing, as shown in fig. 4.12 to increase the distance from the HV wire solder joints in the frame to the grounded housing. An arc, 3 mm deep and 1.905 cm radius, was cut into the side of

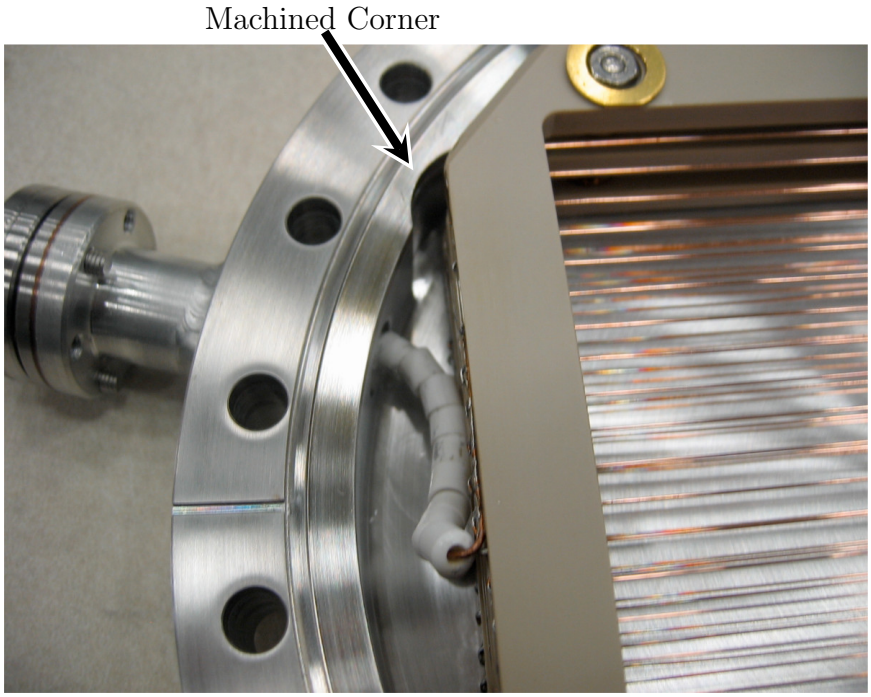

Figure 4.12: The assembled frame stack in the housing with the machined groove. The read out wire going to the feedthrough is shown, covered with insulating ceramic beads to prevent the wire from grounding to the frame or housing.

the housing as shown in fig. 4.12. With this modification, it was found the chamber could be raised to 3 kV without any sparking, twice the the anticipated operating voltage of 1.5 kV.

4.4.2 Effectiveness of Drain Rings

The effectiveness of the drain rings, labeled BM289 in fig. 4.4, were tested by assembling the beam monitor with room air as a fill gas, applying a bias voltage, and measuring the output current from the signal plane. A current to voltage amplifier was used to amplify the output current, and an oscilloscope was used to measure the

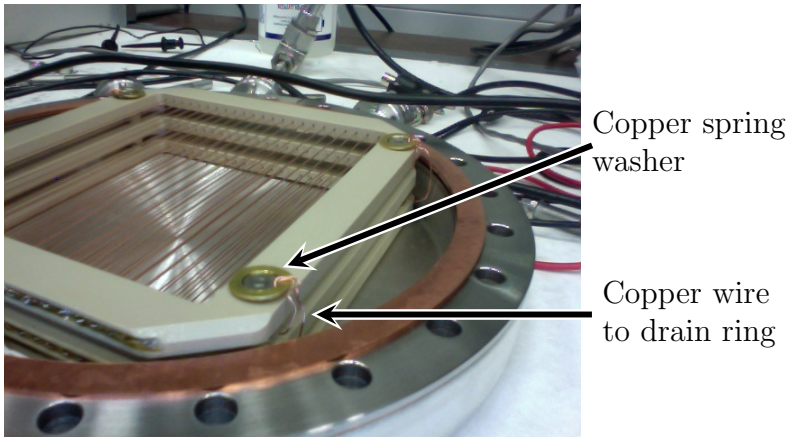

Figure 4.13: The drain rings were connected to ground using soldered copper wires connected to copper spring washers between the frame stack and the housing.

voltage. The preamp output is given by

$$V = (I \times R) \times 2.4,$$

where I is the current drawn from the signal plane, $R = 30M\Omega$ is the preamplifier gain. The leakage current is calculated by taking the measured voltage and feedback resistor value multiplied by 2.4. Fig. 4.14 shows the preamp circuit diagram and the board. No ionization source was used during this testing.

The leakage current was measured first without the drain rings between the frames connected to ground. This was compared with a copper wire soldered to each of the drain rings that was then connected to the spring washers between the frame stack and window as shown in fig. 4.13. The leakage current as a function of applied high voltage is shown in fig. 4.15. The leakage current was significantly reduced with the drain rings connected to the spring washers so that the leakage current could be drained to ground through the housing. This was the configuration used for the final

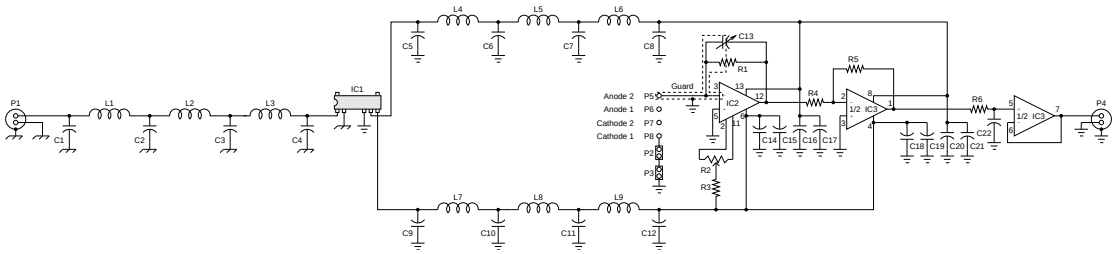

(a) Preamp Diagram

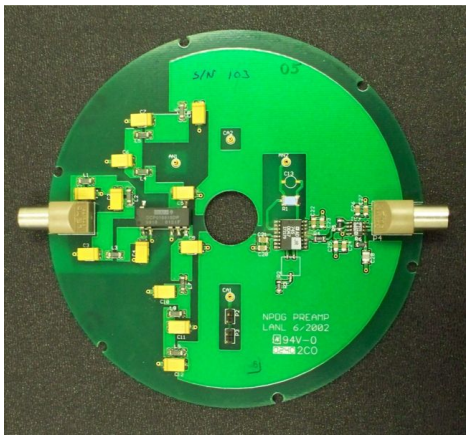

(b) Preamp board

Figure 4.14: Current mode preamp used for the M2 monitor during testing and operation at the FnPB.

assembly of both monitors.

4.4.3 Helium Leak Checking

The M1 monitor chamber was leak checked in the SNS vacuum lab, using a He leak checker. The monitor chamber was found to be leak tight to a sensitivity of 10^{-9} Torr liter/s. The chamber was then pumped 24 hours with a dry pump to a sub mTorr vacuum and at about 60°C temperature. The heating allows some additional cleaning of the chamber by increasing the rate of outgassing from the surfaces of the

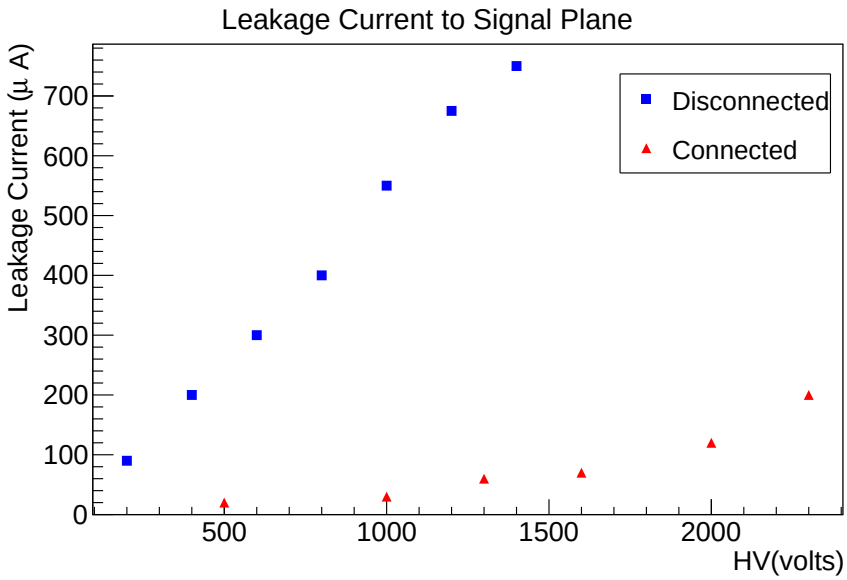

Figure 4.15: This plot shows the leakage current measured during bench top testing of the M1 beam monitor with the drain rings connected to ground or disconnected from ground.

chamber. The temperature had to be kept low due to the thermal properties of the PEEK frames. After cooling down, the chamber was leak checked again and found to have remained leak tight to the same sensitivity as before.

4.5 Fill Gas Calculations

The requirement for the beam monitor is that it gives a clear and detectable signal while absorbing a minimal amount of the neutron beam. While estimates could have been made, the noise and background levels for the monitor were not known before operation. Due to this, a useful partial pressure of ^{3}He in the fill gas was estimated based on the neutron transmission of the aluminum windows, so that the signal from

the neutron capture in the ^{3}He gas would be larger than the background from the windows. The transmission of neutrons through a material can be calculated from

$$I = I_0 \exp\left\{-\rho l \left[\sigma_{Abs}\frac{v_{ref}}{v} + \sigma_{sct}\right]\right\}, \tag{4.3a}$$

$$T = I/I_0. \tag{4.3b}$$

Here I_0 is the original intensity of the beam, I the intensity after passing through the monitor, ρ is the areal density of the material, l its thickness in the beam direction, σ_{Abs} the absorption cross section at $v_{ref} = 2200\,\mathrm{m/s}$, σ_{sct} the scattering cross section for the material the beam interacts with, and T is the transmission. The factor v_{ref}/v parameterizes the $1/v$ dependence of the absorption cross section that arises from the energy dependence of the neutron nucleus absorption cross section at low energies. From eqn. 2.1 $2200\,\mathrm{m/s} = 25.3\,\mathrm{meV}$. The scattering cross section has a comparatively weak energy dependence as seen in fig. 4.16.

For the two 1 mm thick Al windows on the chamber, the density of aluminum, $2.7\,\mathrm{g/cm^3}$, is used to calculate the areal density using the atomic weight of 27. Aluminum has an absorption cross section of 0.231 barns for a neutron velocity of 2200 m/s [59]. Al has a scattering cross section of 1.503 barns. The FnPB neutron chopper wavelength window of 3Å to 6.9Å corresponds to an energy window of 9 to 1.7 meV with the peak neutron flux around 4 meV. Using these numbers in eqn. 4.3 with a neutron energy of 4 meV, one finds the transmission of 1 mm of aluminum, $T_{Al,1mm}$, is 98.8%, or equivalently, 1.2% of the beam is absorbed or scattered after passing through 1 mm of aluminum.

The number density of the ^{3}He in the chamber can be calculated from the ideal

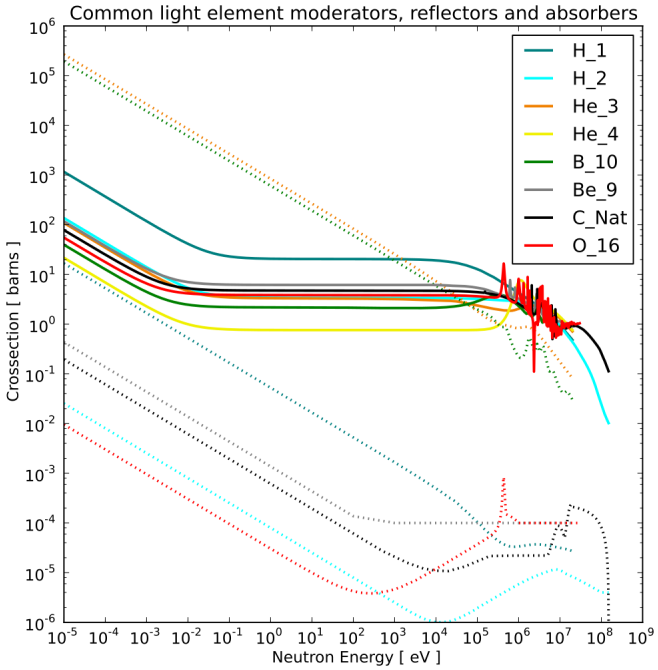

Figure 4.16: Scattering (solid line) and absorbtion (dotted) cross sections of light elements, the data was obtained from the database NEA N ENDF/B-VII.1 using JANIS software [58].

gas law:

$$n/V = \frac{P}{kT}. \tag{4.4}$$

The absorption cross section for ^{3}He is 5333 barns at 2200 m/s, and the scattering cross section is 6 barns. For the beam monitors, the gas volume is approximately 3.4 cm in the beam direction. Using eqn. 4.3 one finds that 2.2% of a neutron beam with an energy of 4 meV would be absorbed by 15 Torr ^{3}He gas in the beam monitor.

The M1 monitor was filled with a mixture of ^{3}He and nitrogen gas. The vacuum gauge read a pressure of 0.3 Torr initially while the chamber was under vacuum. It then was filled to 15.1 Torr with ^{3}He gas, followed by nitrogen up to 750 Torr. A

small volume of helium gas was lost into the nitrogen lines when the valves were opened. After filling, when the valves to the chamber from the fill lines were closed, the pressure gauge read 751.9 Torr.

For an accurate calculation of the number of neutrons capturing in the ^{3}He gas in the detector, the neutron scattering and absorption rate for each material needs to be calculated in the order it is encountered by the neutron beam. Scattering from the aluminum windows also needs to be included more carefully, since some of the neutrons are scattered into the chamber and some of them are scattered out of the chamber.

Treating the 1 mm window as negligibly thick, the solid angle to the interior of the detector, with respect to the aluminum window, is 2π. Dividing this by the solid angle of a sphere, $2\pi/4\pi = 1/2$, gives the fraction of the neutrons that will scatter into the detector. Thus for isotropic scattering of neutrons from either of the windows, 1/2 of the scattered neutrons will be scattered into the detector.

$$\begin{aligned} T_{Al,scatt,1mm} &= \exp\left\{-\frac{(2.7g\,cm^{-3})\times(6.022\times10^{23}mol^{-1})}{(27g\,mol^{-1})}(0.1\,cm)\right. \\ &\qquad \left.\times\ 1.503\times10^{-24}cm^2\right\} \\ &= 0.9909. \end{aligned} \tag{4.5}$$

For the M1 fill gas mixture:

$$\begin{aligned} \frac{n_{^3He}}{V} = \frac{P}{kT} &= \frac{14.8\,\text{Torr}\times133.32\,\text{Pa/Torr}}{(1.38\times10^{-23}\,\text{J/K})(300\,\text{K})} \\ &= 4.766\times10^{23}\,\text{m}^{-3}, \end{aligned}$$

while for nitrogen

$$\frac{n_N}{V} = 2.373 \times 10^{25}\,\mathrm{m}^{-3}.$$

Using the above information in eqn. 4.3 the transmission after absorption and scattering in the gas is

$$T_{gas} = T_{^3He} T_{N2} = 0.976, \tag{4.6}$$

and the transmission due to only neutron capture in the gas is calculated using eqn. 4.3 with $\sigma_{sct} = 0$ resulting in:

$$\begin{aligned} T_{gas,abs} = \exp &\left\{ \frac{-4.766 \times 10^{23}}{10^6 cm^3} (3.4\,\mathrm{cm}) \right. \\ &\left. \times \left[(5333 \times 10^{-24}\,\mathrm{cm}^2) \sqrt{\frac{25.3\,\mathrm{meV}}{4\,\mathrm{meV}}} \right] \right\} \\ &\times \exp \left\{ \frac{-2.369 \times 10^{25}}{10^6\,\mathrm{cm}^3} (3.4\,\mathrm{cm}) \right. \\ &\left. \times \left[(1.9 \times 10^{-24}\,\mathrm{cm}^2) \sqrt{\frac{25.3\,\mathrm{meV}}{4\,\mathrm{meV}}} \right] \right\} \\ &= 0.9781. \end{aligned}$$

For the purpose of calculating the transmission of the neutron beam through the monitor, the scattered neutrons will be considered to be removed from the beam as the fraction of the scattered neutrons reaching the experimental target approximately 2.4 m distant will be small. The monitor transmission is the product of the transmission of the two Al windows, $T_{Al,1mm}$, and the transmission of the gas mixture, T_{gas} including scattering and absorption:

$$T_{M1} = T_{Al,1mm} \times T_{gas} \times T_{Al,1mm} = 0.988 \times 0.976 \times 0.988 = 0.952. \tag{4.7}$$

The monitor will remove approximately 4.8% of 4 meV neutrons from the beam. The average transmission over a FnPB neutron pulse energy range is 0.953.

Of the neutrons removed from the beam by the monitor, only a fraction are absorbed in the ^{3}He fill gas of the monitor to create a signal. Neutrons absorbed in the windows will not contribute significantly to the signal, but as given above 1/2 of the neutrons scattered by the Al windows will be scattered into the monitor and a fraction of those will then be absorbed by the gas. The main contribution to the signal comes from neutrons that pass through the first windows into the gas, $T_{Al,1mm}(1 - T_{gas,abs})$. Half of the neutrons scattered from the first window can also capture in the gas $0.5T_{Al,scatt,1mm}(1-T_{gas,abs})$. From the neutrons transmitted through the first window and the gas, 1/2 of the neutrons scattered by the second window will be scattered back in to the gas, $T_{Al,scatt,1mm}T_{gas} \times 0.5T_{Al,scatt,1mm}(1 - T_{gas,abs})$ for a total capture fraction of

$$\begin{aligned} f_{cap} &= T_{Al,1mm}(1 - T_{gas,abs}) + 0.5T_{Al,scatt,1mm}(1 - T_{gas,abs}) \\ &\quad + T_{Al,1mm}T_{gas} \times 0.5T_{Al,scatt,1mm}(1 - T_{gas,abs}) \\ &= 0.022. \end{aligned} \tag{4.8}$$

So 2.2% of 4 meV neutrons incident on the monitor will capture in the fill gas between the HV planes. Due to the small amount of copper in the wires, the transmission and scattering of the wire planes has been ignored in this analysis.

4.5.1 Proton and Triton Range

While the partial pressure of the ^{3}He component of the fill gas is determined by the desired neutron capture rate in the monitor, the nitrogen partial pressure was chosen

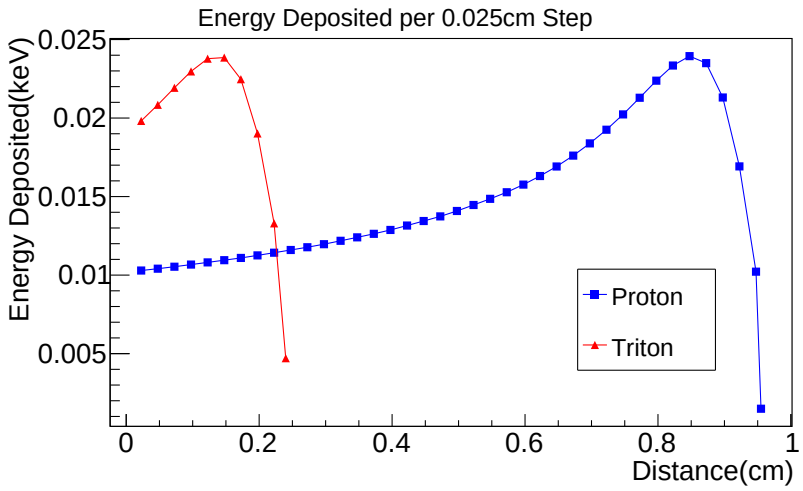

Figure 4.17: The energy deposited per 0.025 cm step in the gas mixture for the M1 monitor.

to limit the range of the protons and tritons in the beam monitor. The distance the proton and triton will travel in the gas is determined by their initial energy and how quickly the particle's energy is transferred to the gas. Section 3.1 discusses energy deposition in a gas.

From the capture of a cold neutron on a ^{3}He nuclei, there is 765 keV of kinetic energy shared between the proton and triton after break up. Using conservation of momentum, it can be calculated that the proton starts with 562 keV energy and the triton starts with 203 keV.

Using the PSTAR data for the stopping power of the fill gas, the energy deposition per unit length was calculated for the proton in the gas mixture for the M1 monitor. The stopping power was taken in 50 keV increments from $1 - 600$ keV from the database. Linear interpolation was used between the points to determine the stopping power at energies between the tabulated values. Using Bragg's rule of stopping

power additivity, that the stopping power of a mixture is the sum of the stopping powers of the components weighted by their relative abundances, from appendix A of reference [60], the stopping power for a mixture of gases was calculated from the PSTAR stopping powers by adding the weighted interpolated stopping powers.

While triton stopping powers were not available, the proton values were used for the triton calculations since stopping powers vary mainly with charge rather than the mass of the ion. Due to the high pressure of the nitrogen in the fill gas, the stopping distance of the proton was just under 1 cm. Fig. 4.1 shows the stopping distances to scale with the wire frame spacing.

4.6 M1 Final Testing and Installation

After the assembly, pumping and filling, and HV testing of the beam monitors was completed, testing of the beam monitors was done using a thermal neutron source, a low intensity monochromatic cold neutron source, and a calibrated neutron beam.

4.6.1 Californium Source

As an initial test, the M1 monitor function and the suitability of the chosen ^{3}He thickness was tested with a californium source. Californium emits 2.1 MeV neutrons as a spontaneous fission product. The source had a collimated and moderated flux of approximately 3100 neutrons per second. The source was moderated using room temperature plastic moderators surrounding the californium source with approximately 85% of the neutrons at thermal energies. For thermal energies, the energy at the peak of the Maxwell-Boltzmann energy distribution is 25.3 meV corresponding to a

(a) Californium source

(b) M1 monitor data taking setup

Figure 4.18: M1 monitor during testing at the californium neutron source.

velocity of 2200 m/s. The low flux of this source, compared to the FnPB beam line at the SNS, required the operation of the detector in counting mode instead of current mode. Fig. 4.18 shows a picture of the source and the beam monitor during data taking.

The preamp used with the detector in the standard operating mode (current mode) is too slow for use in counting mode. A set of Cremat amplifiers were used instead. The first stage was a charge sensitive preamplifier model number CR-110. The second amplification stage was a CR-200 shaping amplifier with a 2 microsecond shaping time. The use of the shaping amplifier filtered out a great deal of the noise that was present in the signal reducing the RMS of the intrinsic noise from the amplifiers from 40 mV to 10 mV. Fig. 4.19 is a diagram of the test setup. To reduce the noise added

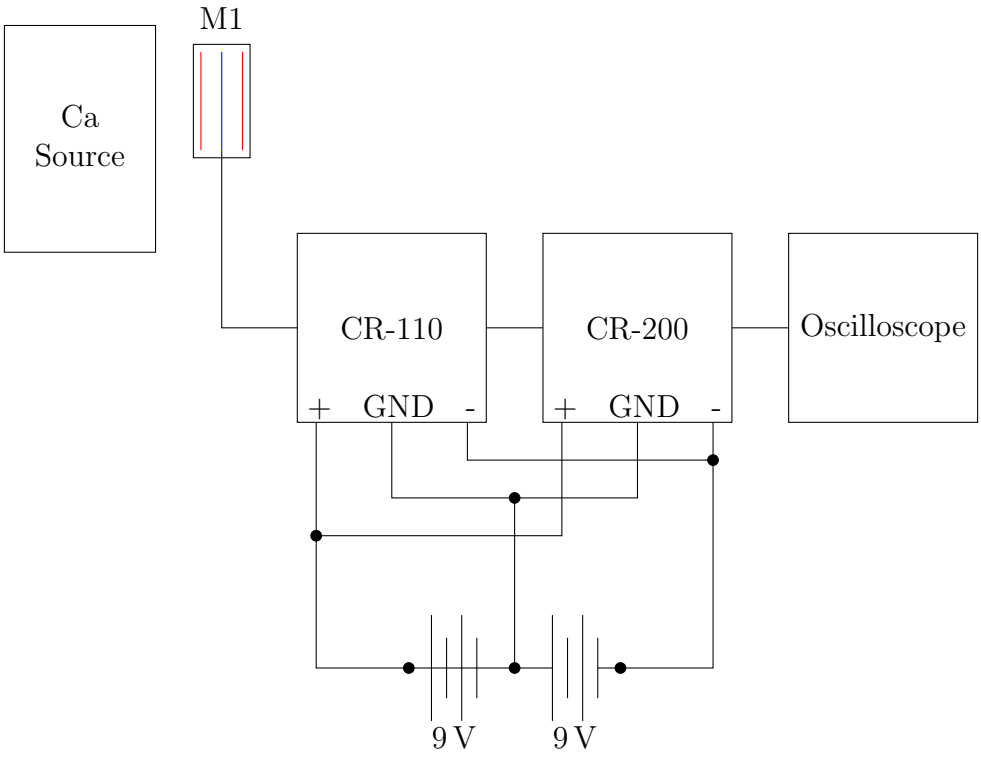

Figure 4.19: Schematic of the M1 Monitor setup used during testing at the californium neutron source.

by the amplifiers, a pair of 9 V batteries was used to power the amplifiers instead of a DC power supply, since this would decrease the noise and prevent ground loops.

This setup was then used to find a way to reduce the noise in the system. While observing the output of the CR-200 amplifier on the oscilloscope, the available NIM bin and HV power supplies were used to apply the bias voltage to the beam monitor. Of the available combinations, the one that showed the lowest peak height in the signal on the oscilloscope was chosen to be used. No other notable optimizations were performed.

The monitor was moved to the californium source once all noise sources were

minimized. By setting the trigger on the oscilloscope above the noise floor, and by observing when the oscilloscope was triggered, clear neutron pulses were observed with an approximate height of 60 mV. It was confirmed that it was neutron pulses causing the triggers rather than noise as, when the shutter was closed on the source, peaks higher than 45 mV were no longer seen.

In one minutes an average of 0.9 neutron captures per second were seen. Using equation 4.8 redone for 25.3 meV neutrons, the approximate energy at the peak of the neutron flux from a thermal source, and the given source flux, the approximate capture rate in the beam monitor was calculated at 28 neutrons per second. Due to the dead time after each event trigger while the oscilloscope paused to display the waveform, the full event rate could not be counted. The neutron event peak height is also variable, so some fraction of the neutron events would not have been triggering the oscilloscope, and may have had peak heights lower than the electronics noise.

Reducing the HV bias to 1.5 kV, 1 kV, and 0.5 kV, neutron events could still be seen, but at 0.5 kV the count rate was reduced to 0.7 per second. Below 0.5 kV the oscilloscope trigger had to be reduced to 23.6 mV as the event peak height was reduced. With the lower trigger the noise was beginning to trigger the oscilloscope. Comparing this with the more precise voltage scan done at the FnPB discussed in section 4.9.1, it is apparent that the recombination region had been entered for the monitor at bias voltages of 0.5 kV and lower.

4.6.2 Calibrating M1 Monitor at HFIR

After determining the basic working condition using the californium source, the monitor was taken to the High Flux Isotope Reactor (HFIR) beamline HB-D2 for calibration. The CR-110 CSP and CR-200 2 microsecond shaping amplifier powered with two 9 V batteries, that were used during testing with the californium source, were used again in the same configuration. The bias voltage was set at 2 kV. Fig. 4.20 shows the setup during pulse counting in the M1 monitor.

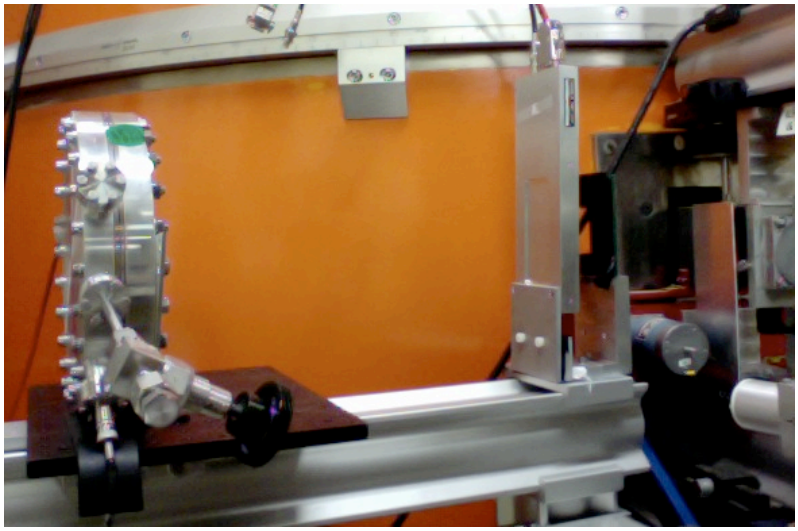

Figure 4.20: The HB-D2 beam line with the M1 monitor on the left and the HFIR monitor on the right as setup during the counting measurements.

The HB-D2 beam line has a flux of 350000-380000 neutrons per second as measured using the calibrated beam monitor provided at the beam line. The calibrated monitor has an efficiency of $\epsilon_{HFIR} = 0.01$, so for each count from the monitor 100 neutrons have passed through it. The neutron wavelength from this beam line is nearly monochromatic with a neutron energy very close to 4.5 meV = 4.26 Å. Due

to the neutron energy filtering method used at the beamline, some half wavelength neutrons, 18 meV = 2.13Å, will also be present at a low intensity level in the beam. The beam pipe is 1.5 cm in the horizontal direction and 2 cm in the vertical direction. This is significantly smaller than the 10 cm × 12 cm beam pipe at the FnPB where the monitor is intended to be used, so even as the beam diverges after exiting the beam pipe, it will all still be captured in the active area of the monitor.

To start with, an oscilloscope was used to verify that neutron pulses could be observed above the electronic noise. An increased noise level was seen as compared to when the monitor was setup at the californium source. Sources of additional noise included the increased number of electronics in the area that were not part of the setup but that the longer cables between the HV power supply and the beam monitor and the cable between the CR-200 amplifier and the readout electronics had to pass over between the beamline and the NIM crate.

Using the calibrated monitor provided by the beam line, transmission measurements were made of the M1 monitor and a piece of aluminum. Data was taken in 3-6 consecutive approximately 1 minute intervals for each configuration. The data was taken in intervals so that any variation over time in the measured flux, such as changes in the background caused by adjacent beam lines, could be seen, but the neutron flux and backgrounds were steady over time.

4.6.3 M1 Transmission

Measurements of the flux through the HFIR monitor were made with the M1 monitor between the HFIR monitor and the neutron beam source, and with the

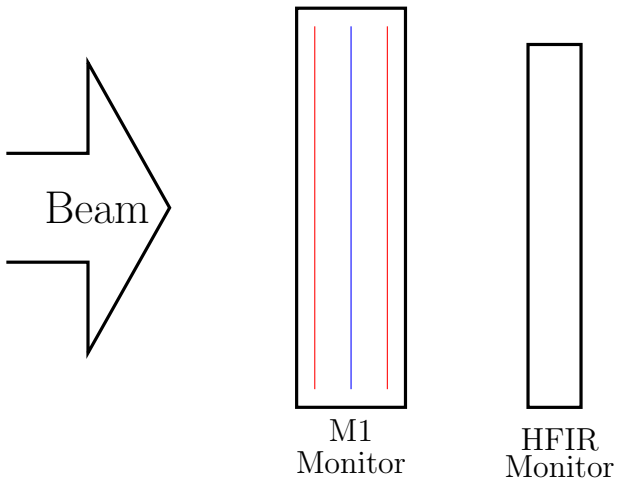

Figure 4.21: Schematic diagram of the setup used for measuring the transmission of the M1 monitor. Drawing objects are not to scale.

M1 monitor removed from the beam. Background measurements were made in each configuration with the shutter closed on the beam path. Fig. 4.21 shows the setup. Table 4.3 shows the results of these measurements.

The standard deviation of the average of the N measured count rates, x, for a configuration was calculated from

$$\sigma = \sqrt{\frac{1}{N}\sum_{i}^{N}(x_i - x_{avg})^2}. \tag{4.9}$$

Monitor In, Beam On		
Time(s)	Counts	Counts/s
63.49	212522	3347.33
64.91	216820	3340.32
62.56	210147	3359.13
64.35	214249	3329.43
86.74	289260	3334.79

Monitor In, Beam Off		
Time(s)	Counts	Counts/s
60.98	144	2.36
61.22	138	2.25
61.05	401	6.57
61.37	507	8.26
64.84	506	7.8
61.44	335	5.45

(a) Monitor in measurements

Monitor Out, Beam On		
Time(s)	Counts	Counts/s
60.98	213435	3500.08
60.8	211737	3482.52
61.29	214291	3496.35
60.76	212195	3492.35
73.85	257937	3492.71

Monitor Out, Beam Off		
Time(s)	Counts	Counts/s
70.92	388	5.47
61.01	305	5
63.7 3	61	5.67

(b) Monitor out measurments

	Avg. Counts/s	Std. Dev.
Monitor In, Beam On	3344.05	11.56
Monitor In, Beam Off	5.45	2.396
Monitor Out, Beam On	3492.8	5.35
Monitor Out, Beam Off	4.47	1.133

(c) Averages and standard deviations

Table 4.3: Transmission measurements for the M1 monitor.

The M1 transmission was calculated from:

$$\begin{aligned} T &= \frac{I_{in}}{I_{out}} = \frac{\epsilon_{HFIR} R_{in}}{\epsilon_{HFIR} R_{out}} \\ &= \frac{3344.05 - 5.45}{3492.8 - 4.47} = \frac{3338.6}{3488.33} = 0.957, \\ \Delta T &= \sqrt{\left(\frac{\sigma_{in}}{R_{in}}\right)^2 + \left(\frac{\sigma_{out}}{R_{out}}\right)^2} \\ &= \sqrt{\left(\frac{11.56 + 2.396}{3338.6}\right)^2 + \left(\frac{5.35 + 1.133}{3488.33}\right)^2} \\ &= 0.00456. \end{aligned}$$

This gives a measured transmission through the active area of the M1 monitor of $95.7 \pm 0.5\%$ at 4.5 meV. Fig. 4.25 compares the calculated and measured M1 monitor transmissions using modified aluminum cross sections using measurements detailed in the next section.

4.6.4 Aluminum Neutron Transmission

As the cross section values given in reference [59] are for Al atoms, and the binding between the atoms in the aluminum alloy windows can alter the cross sections, a transmission measurement was made through a sample of aluminum metal. The goal of this measurement was to determine the actual scattering and absorption cross sections closer to our energy range of interest. The aluminum cross sections are important for, as discussed in section 4.5, the transmission and scattering of the Al monitor windows will effect the number of neutrons capturing in the beam monitor.

The aluminum sample had a smaller surface area than the HFIR detector face, so a boron loaded aluminum collimator was placed between the aluminum block and HFIR

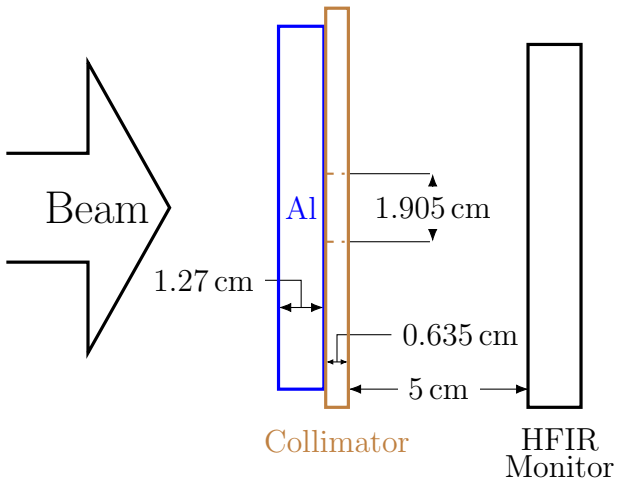

Figure 4.22: Schematic diagram of the setup used for measuring the transmission of the aluminum sample. Objects are not to scale. The opening in the collimator was 1.27 cm horizontal by 1.905 cm vertical.

monitor to reduce the beam size. See fig. 4.22 for the setup details. This required the calculation of the solid angle of the aluminum block with respect to the collimator opening to determine the number of neutrons scattering from the aluminum block that would pass through the collimator to enter the monitor.

Using the formula for the solid angle of an offset rectangle from reference [61], the average solid angle was numerically calculated. The solid angle was calculated for approximately 25000 points in the volume of aluminum intersected by the rectangular beam profile of 1.5 cm × 2 cm. The Al sample was 1.27 cm thick in the direction of the beam. The collimator and HFIR monitor were attached on the beam line rail which aligned them to each other and to the neutron beam. The aluminum block was placed by hand between them. The alignments were verified by eye. The solid angle was calculated relative to the downstream opening of the 1.27 cm wide by 1.905 cm

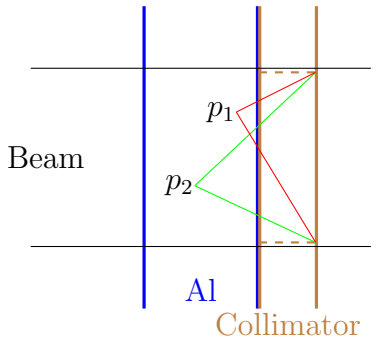

Figure 4.23: Schematic of the solid angle calculation for aluminum scattering through collimator. Two example points, p_1 and p_2, are shown in the intersection volume of the neutron beam and the collimator opening with the lines going to the points on the collimator opening the solid angle was calculated to.

tall by 0.635 cm thick collimator. The solid angle has a maximum of 2.516 steradians at the front center of the aluminum sample and a minimum of approximately 0.1 at the back corners of the beam intersection volume. From the calculations, the average value of the solid angle is 0.88 steradians. Approximately $0.88/4\pi = 7.0\%$ of neutrons scattered from the Al block would pass through the collimator opening.

From the NIST cross section for neutrons scattering from aluminum, the transmission of the Al sample due to scattering alone can be calculated as

$$\begin{aligned} T_{sc} &= \exp\left\{-\frac{(2.7g\,\mathrm{cm}^{-3}) \times (6.022 \times 10^{23}\,\mathrm{mol}^{-1})}{(27\,\mathrm{g\,mol}^{-1})}\right. \\ &\quad \left. \times \quad (1.27\,\mathrm{cm})1.503 \times 10^{-24}\,\mathrm{cm}^2\right\} \\ &= 0.8914. \end{aligned}$$

The intensity of the scattered fraction of the beam that reaches the HFIR monitor

was therefore

$$I_0 \times 0.07 \times (1 - T_{sc}) = 0.0076 I_0,$$

where I_0 is the initial intensity of the beam entering the Al block.

For the Al sample, a calculation of the expected transmission was done using the same method that was used for the M1 monitor in section 4.6.3. The results are shown in table 4.4. To take into account the fraction of the scattered beam that reaches the monitor, one can use the measurements without the aluminum sample as a reference measurement. The number of counts coming from the scattered fraction of the beam is then

$$I_{sct} = 0.0076 I_0 = 0.0076(2076.75 \pm 2.24)\text{c/s} = 15.78 \pm 0.017\text{c/s}.$$

Subtracting that from the measurements with the sample in the beam, with the background subtracted, one finds

$$I_{Al,Trans} = (1843.281 \pm 6.15)\text{c/s}(15.78 \pm 0.017)\text{c/s} = 1827.5 \pm 6.167\text{c/s}.$$

From this and the sample out beam on measurement a transmission for the Al sample was calculated as

$$T_{Al,meas} = \frac{1827 \pm 6}{2076 \pm 2} = 0.880 \pm 0.003.$$

Using the NIST neutron cross section library, the calculated transmission through

Al In, Beam On

Time(s)	Counts	Counts/s
60.59	112325	1853.85
77.17	141750	1836.85
60.87	112641	1850.52
60.82	112213	1845
60.71	112313	1849.99

Al In,Beam Off

Time(s)	Counts	Counts/s
60.72	188	3.1
75.51	273	3.62
60.67	218	3.59

(a) Al block in measurements

Al Out,Beam On

Time(s)	Counts	Counts/s
60.63	126162	2080.85
60.6	125902	2077.59
60.63	126125	2080.24
61.94	128642	2076.88
60.6	126177	2082.13

Al Out,Beam Off

Time(s)	Counts	Counts/s
61.23	186	3.04
61.2	155	2.53

(b) Al block out measurements

Al Sample Measurements

	Average cnts/sec.	St. Dev.
Beam On, Al Sample In	1847.24	5.92
Beam Off, Al Sample In	3.43	0.24
Beam On, Al Sample Out	2079.54	1.99
Beam Off, Al Sample Out	2.79	0.25

Background Subtracted

Sample In	1843.81	6.15
Sample Out	2076.75	2.24
Transmission	0.888	0.003

Scattering Subtracted

Sample In	1830.4	6.18
Sample Out	2076.75	2.24
Transmission	0.880	0.003

(c) Averages and Calculation Results

Table 4.4: Average of counts taken with the Al sample in place with the HFIR nitrogen monitor and configuration shown in fig. 4.22.

1.27 cm of Al is

$$\begin{aligned} T_{Al,NIST} = \exp\Bigg\{ & -\frac{(2.7g\,\mathrm{cm}^{-3}) \times (6.022 \times 10^{23}\mathrm{mol}^{-1})}{(27\mathrm{g/mol})} \\ & \times \quad (1.27\,\mathrm{cm}) \left(1.503 \times 10^{-24} cm^2 + 0.231 \times 10^{-24} cm^2 \sqrt{\frac{25.3\,\mathrm{meV}}{4.5\,\mathrm{meV}}} \right) \Bigg\} \\ & = 0.8548. \end{aligned}$$

From the single energy measurement of the transmission through the aluminum sample done at HFIR, the NIST calculated transmission can be rescaled for use at other energies using

$$T_{Al,NIST}(E) = \exp\left[-\rho l (\sigma_{sct} + \sigma_{abs} \sqrt{E_{ref}/E}) \right] \tag{4.10}$$

$$\ln(T_{Al,NIST}(E)) = -\rho l (\sigma_{sct} + \sigma_{abs} \sqrt{E_{ref}/E}). \tag{4.11}$$

Rescaling the NIST value to the measured value at 4.5 meV gives

$$\ln(T_{Al,NIST}(E)) \frac{\ln(T_{Al,NIST}(4.5\,\mathrm{meV}))}{\ln(T_{meas}(4.5\,\mathrm{meV}))} \tag{4.12}$$

$$\Rightarrow \ln(T_{Al,scaled}(E)) = \frac{\ln(T_{meas}(4.5\,\mathrm{meV}))}{\ln(T_{Al,NIST}(4.5\,\mathrm{meV}))} \left[-\rho l (\sigma_{sct} + \sigma_{abs} \sqrt{E_{ref}/E}) \right], \tag{4.13}$$

with a numerical value of the scaling factor given by

$$\frac{\ln(T_{meas}(4.5\,\mathrm{meV}))}{\ln(T_{Al,NIST}(4.5\,\mathrm{meV}))} = \frac{\ln(0.880)}{\ln(0.855)} = 0.81965. \tag{4.14}$$

In general for a function, $f(x, y)$, of two variables with standard deviations s the error of the function, Δf may be calculated as

$$\Delta f(x, y) = \sqrt{\left(\frac{\partial f(x, y)}{\partial x} \right)^2 s_x^2 + \left(\frac{\partial f(x, y)}{\partial y} \right)^2 s_y^2} \tag{4.15}$$

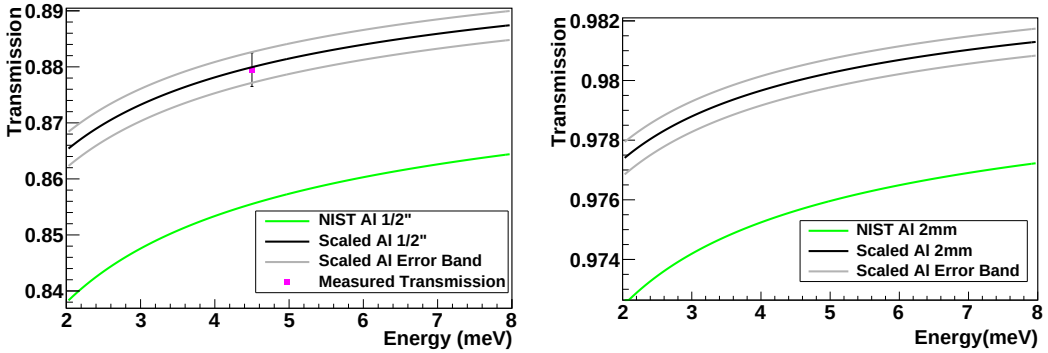

(a) 1.27 cm Al transmission

(b) 2 mm Al transmission

Figure 4.24: Plot (a) shows a comparison of the measured Al transmission compared to the NIST calculated Al transmission, $T_{NIST,AL}(E)$, for a range of energies and the rescaled transmission, $T_{scaled,Al}(E)$. Plot (b) shows $T_{NIST,AL}(E)$ and $T_{scaled,Al}(E)$ at the combined thickness of the two 1 mm monitor windows.

and apply this to scaling factor calculation with the assumption that the error in $T_{Al,NIST}(4.5\,\text{meV})$ is negligible to that of $T_{meas}(4.5\,\text{meV})$, it can be calculated as

$$\Delta\frac{\ln(T_{meas}(4.5\,\text{meV}))}{\ln(T_{Al,NIST}(4.5\,\text{meV}))} = \sqrt{\left(\frac{\partial}{\partial T_{meas}}\frac{\ln(T_{meas}(4.5\,\text{meV}))}{\ln(T_{Al,NIST}(4.5\,\text{meV}))}\right)^2\sigma^2_{meas}} \tag{4.16}$$

$$= \sqrt{\left(\frac{1}{T_{meas}(4.5\,meV)\ln(T_{Al,NIST}(4.5\,meV))}\right)^2\sigma^2_{meas}} \tag{4.17}$$

$$= \sqrt{\left(\frac{1}{(0.880)\ln(.0.855)}\right)^2 0.003^2} \tag{4.18}$$

$$= 0.0217. \tag{4.19}$$

Fig. 4.24 shows the results of the calculations for a range of neutron energies comparing the calculated transmission, using the NIST cross section values, with the

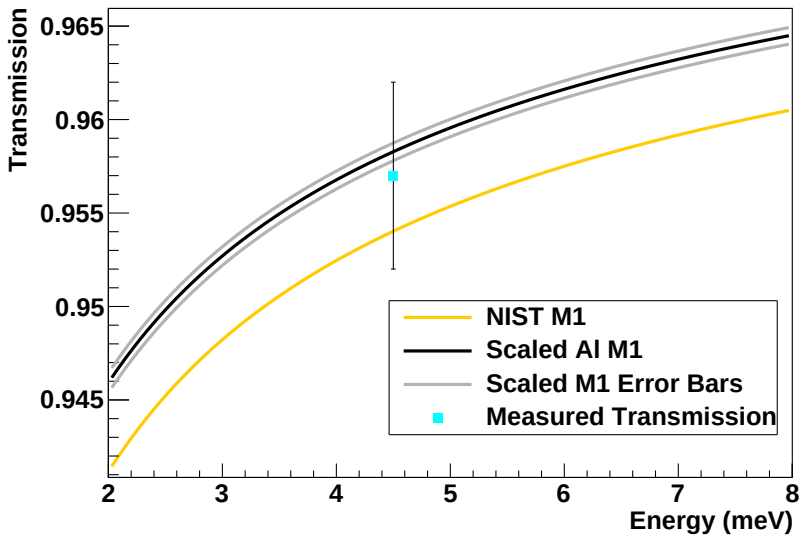

Figure 4.25: Comparison of the measured monitor transmission at 4.5 meV with the calculated monitor transmission using the NIST cross section values for the Al windows and fill gas mix, and the rescaled Al values with NIST values for the fill gas.

measured sample transmission at 4.5 meV, and the rescaled transmission.

Fig. 4.25 shows a comparison of the M1 monitor transmission calculated from the NIST cross section values with the measured transmission, and the effect of using the rescaled aluminum cross sections for the monitor windows. Both the scaled and unscaled calculated transmissions, using the NIST database, are consistent with the measured transmission at 4.5 meV to within the measurement error.

4.6.5 M1 Calibration with HFIR Monitor

To determine the number of neutrons capturing in the active area of the monitor, a counter was used along with a discriminator to measure the number of pulses for 100 seconds with the neutron beam on and off. The difference in these measurements

should give the number of neutrons captured in the monitor.

A Phillips Scientific 705 Discriminator and an Ortec 974 Counter were used with a Phillips Scientific 794 Gate needed to convert the discriminator NIM pulse to the TTL pulse required by the counter. The pulse from the discriminator had a width of 200 ns. This would allow a maximum of 5 million counts per second so the dead time effect in the measurements should be minimal with a maximum of 1.2 million counts per 100 seconds. Counts were taken for 100 seconds at a time. The threshold was reduced in steps from 45 mV to 10 mV.

While the majority of the counts at the lower discriminator settings should occur due to the low amplitude electronic noise in the system, the noise should not change with the beam on or off. By taking two sets of measurements at each discriminator setting, one with the beam on and one with the beam off, and taking the difference between those counts, the difference should be the number of neutrons counted during a given time period. When the difference in the measurements stops changing as the discriminator setting is lowered, then all of the neutron events are being counted.

From the image shown in fig. 4.20, it was estimated that there was about 30 cm between the M1 and the nitrogen monitor. The solid angle from a point centered on the HFIR monitor face 30 cm away is calculated as

$$\Omega = 4 \arctan\left(\frac{\alpha\beta}{2d\sqrt{4d^2+\alpha^2+\beta^2}}\right) \tag{4.20}$$

$$= 4 \arctan\left(\frac{3\,\text{cm} \times 9\,\text{cm}}{2(30\,\text{cm})\sqrt{4(30\,\text{cm})^2+(3\,\text{cm})^2+(9\,\text{cm})^2}}\right) \tag{4.21}$$

$$= 0.029 \tag{4.22}$$

$$\frac{0.029}{4\pi} = 0.00235. \tag{4.23}$$

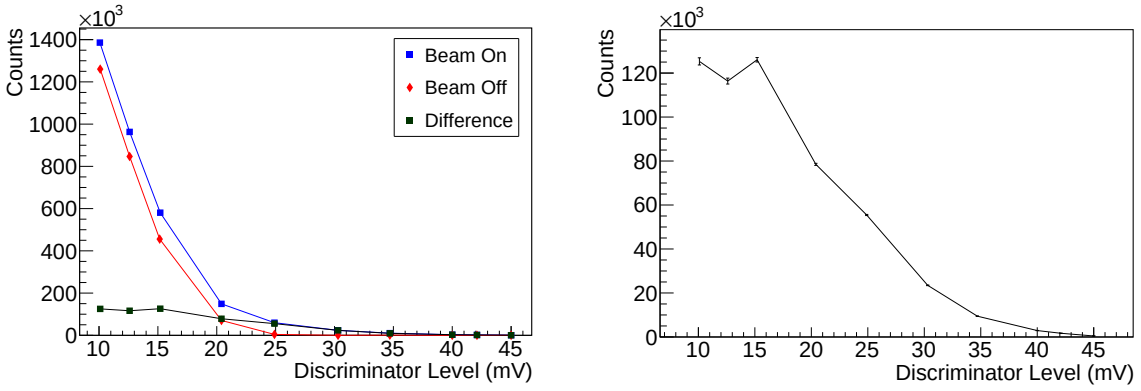

(a) (b)

Figure 4.26: Neutron pulse counting with the monitor M1 at HFIR with a discriminator. Number of pulses recorded on the counter in 100 seconds for the given discriminator setting. Uncertainties on each value are $1/\sqrt{N}$ where N is the number of counts taken at that discriminator setting.

From eqn. 4.5 the 1 mm Al window will scatter 0.009 of the initial beam flux. The fraction of this that will reach the HFIR monitor can be calculated as

$$0.00235 \times 0.009 I_0 = 0.000021 I_0, \tag{4.24}$$

so the number of reflected neutron from the M1 to the HFIR monitor is negligible compared to the HFIR monitor counting rate.

In fig. 4.26 the three discriminator settings 15.2 mV, 12.6 mV, and 10.1 mV, form an approximate plateau. The average of these is 1220 ± 20 counts/s. Using the HFIR monitor during these measurements, an average count rate of 3696 ± 3 counts/s was obtained for the 100 s time intervals. For the HFIR monitor, the neutron flux is 100 times the count rate. The fraction of incident neutron capturing in the M1 monitor

is

$$\frac{(1220 \pm 20)\text{n/s}}{(3696000 \pm 300)\text{n/s}} = 0.0033 \pm 0.00005. \tag{4.25}$$

Comparing this with the calculation done in eqn. 4.8, recalculated for an energy of 4.5 meV, a capture rate of 0.021 or roughly 7760 n/s is estimated from theory based on the HFIR monitor count rate. The counting rate is lower by a factor of 6.4 than estimated based on the ^{3}He fill gas pressure. It is possible that another higher plateau in the beam-on/beam-off count difference could have been found, if it had been possible to lower the discriminator threshold further revealing more neutron counts. It is also possible that the ^{3}He fill gas pressure was lower than recorded during filling, but the monitor transmission measured in section 4.6.3 is consistent with the 14.8 Torr pressure so that is unlikely.

4.6.6 Mounting the M1 Monitor in the FNPB Neutron Guide

After testing at HFIR, the beam monitor was mounted to the vacuum window of the FnPB guide in front of the supermirror polarizer, as seen in fig.4.27. Plastic insulating spacers were used to electrically isolate the monitor from the beam line. This was done despite the uncertainty in the helium gas pressure in the monitor as the required concrete radiation shielding over the supermirror polarizer needed to be put into place to keep on schedule for the NPDGamma experiment installation.

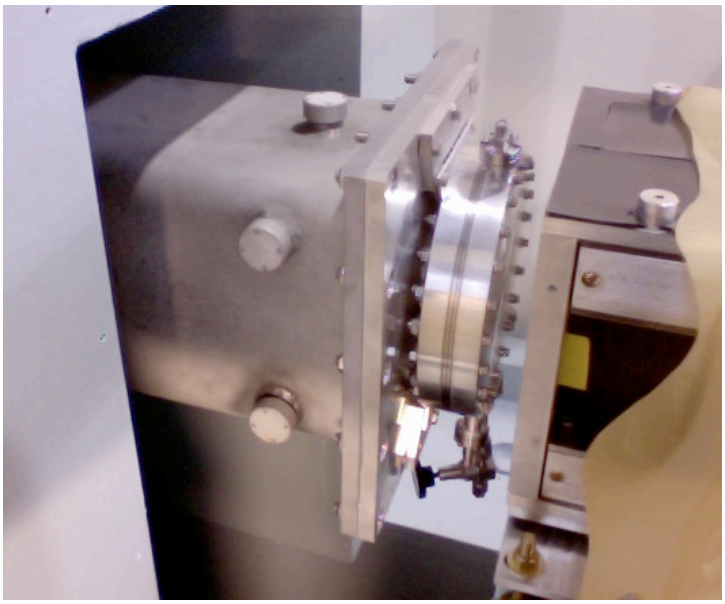

Figure 4.27: Monitor M1 mounted on the beam pipeline. To the right of the monitor can be seen part of the supermirror polarizer.

4.7 M2 Monitor Assembly

The M2 monitor was assembled using the same procedure used for M1, except that the wire tension was increased to 1 kg from the 0.5 kg that was used for the M1 monitor frame wiring in section 4.3. M2 did not have epoxy applied to the frame as the housing was machined to prevent sparking.

During HV testing of the filled M2 monitor, the power supply tripped immediately when it was turned on. After opening the monitor housing, it was found that the wires were bowing outward and touching the housing. It is likely that the bake out temperature was too high during vacuum pumping to remove impurities. As PEEK plastic has a higher rate of thermal expansion than the copper wires, the frames would stretch the wires at sufficiently high temperatures. Consequently after cooling, the

stretched wires bowed out and some of the HV wires then came into contact with the housing, causing a short to ground. As a result, the M2 monitor had to be restrung. After being pumped with a turbo pump for two days, the M2 monitor filled again with a final fill gas mixture of 10 Torr of ^{3}He and 766.9 Torr of N_2 .

4.8 M2 Calibration

To calibrate the M2 beam monitor for use at the FnPB, it was taken to the High Flux Isotope Reactor (HFIR) cold beam line CG1. CG1 is a 40 Hz chopped cold neutron source providing neutrons with wavelengths from approximately 1 Å to 16 Å with the peak of the spectrum at approximately 3 Å. This allowed the M2 monitor to be calibrated for a wider range of energies than was the case for the attempted M1 monitor calibration.

Using a provided calibrated nitrogen monitor to measure the neutron flux, a conversion factor can be calculated to convert the output current from the M2 monitor to the number of incident neutrons on the monitor. Fig. 4.28 shows the setup at the beamline used during data taking. The nitrogen and M2 monitors each had separate DAQs. The M2 monitor current was read out in current mode through the same current to voltage preamp used in section 4.4.2.

One long run, which ran overnight and accumulated data from 1868962 chopper frames, was taken with the provided calibrated nitrogen monitor to determine the location of the Bragg edges. Due to the crystal structure of the aluminum in the beam guide, Bragg scattering will remove neutrons at specific wavelengths. This results in visible valleys in the neutron pulse that can be used to identify the neutron

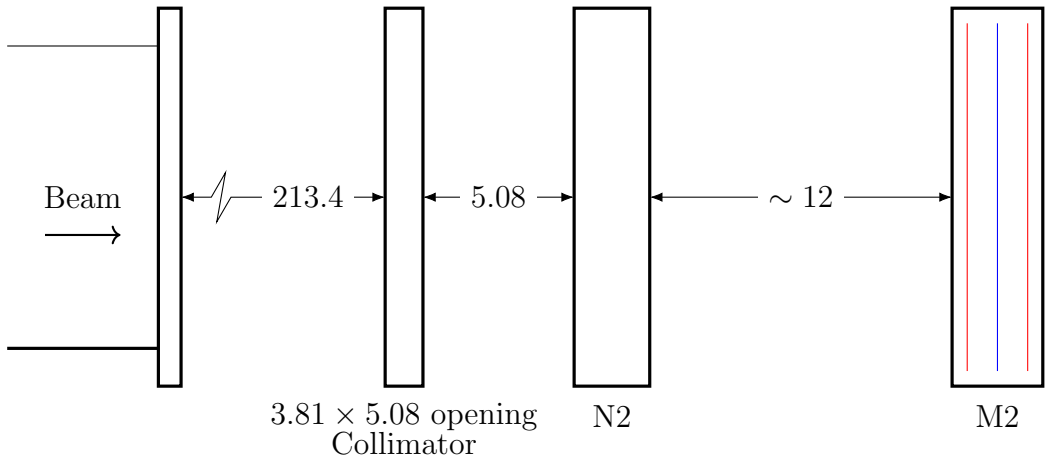

Figure 4.28: Schematic of the calibration setup used at the CG1 beam line. Linear dimensions are in centimeters. Drawing is not to scale.

wavelength at those DAQ time bins. With the neutron wavelengths known at two times, the wavelength of the neutrons in all time bins can be calculated. Fig. 4.29 shows the measured neutron spectrum for the long run compared with a second shorter run during which the M2 monitor was operated simultaneously. In section 4.8.2 this run is used to locate the Bragg edges in the nitrogen monitor and to determine the time of flight to wavelength conversion.

A second run was taken with the M2 and nitrogen monitors operating simultaneously. Data was recorded for 97119 chopper frames. Fig.4.28 shows a schematic of the setup used for the calibration measurement. All measurements were done with the collimator in place upstream of both detectors.

For the calibration of the M2 monitor, counts were accumulated for 97119 chopper frames with the nitrogen monitor. Data runs were taken simultaneously on a separate DAQ for the M2 monitor voltage.

4.8.1 Nitrogen Monitor Counting Rate

The calibrated nitrogen monitor provided at the beam line is a very thin counting mode monitor. Defining the efficiency of a beam monitor, ϵ, as the number of detected neutrons divided by the number of incident neutrons, the nitrogen monitor has a reference efficiency of $\epsilon_{Nr} = 0.000012$ for neutrons with a wavelength of $\lambda_r = 1.798\,\text{Å}$. For other wavelengths, the efficiency is given by

$$\epsilon_N(\lambda) = \epsilon_{Nr}\frac{\lambda}{\lambda_r}. \tag{4.26}$$

The counting rate for the HFIR nitrogen monitor is

$$R_N(\lambda) = \epsilon_{Nr}\frac{\lambda}{\lambda_r}\frac{dn}{dt}, \tag{4.27}$$

where R_N is the counts per second, and dn/dt is the number of neutrons incident on the nitrogen monitor per second.

The HFIR nitrogen monitor DAQ system stored the total number of neutron counts per time bin and the number of chopper frames over which the counts were taken. Each chopper frame was 1/40 s wide and was divided into 1000 time bins. To convert the counts, N_n, stored in the data file into neutrons per second per time bin, the following conversion was used

$$R_N = N_n \times \frac{40}{\text{Frames} \times 0.025s}, \tag{4.28}$$

$$\sigma_{R_N} = \sqrt{N_n} \times \frac{40}{\text{Frames} \times 0.025s}. \tag{4.29}$$

4.8.2 Time Offset

The crystal structure of aluminum in the beam guide and path will create its first two Bragg edges at 4.052 Å, and 4.679 Å [23], as can be seen in fig. 4.29. The time

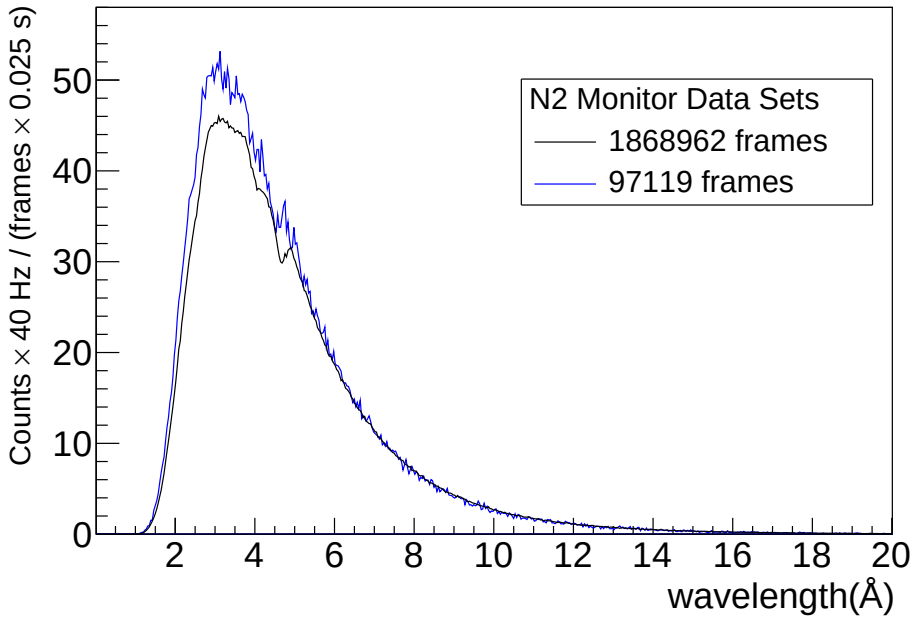

Figure 4.29: Comparison of the two data sets taken with the HFIR nitrogen monitor. The counts are for each of the 25 microsecond time bins.

bins for wavelengths $20-35$ Å are not shown as the neutron flux was essentially zero that far from the peak.

Using the long run for the nitrogen monitor, the 4.052 Å and 4.679 Å Bragg edges are found in the time bins corresponding to 3.7 ms and 4.15 ms, respectively. Using this information, the distance of the monitor from the chopper can be determined as follows.

The neutron velocity and wavelength are related by

$$\lambda(t) = \frac{h}{mv} = \frac{h(t - t_{offset})}{md}, \tag{4.30}$$

where m is the mass of a neutron, h is Planck's constant, d is the distance the neutrons has traveled, in time $t - t_{offset}$, t is the time for that DAQ bin, and t_{offset} is

the difference between the recorded and actual time of flight. t_{offset} can be calculated

$$t_{offset} = \frac{v_1 t_1 - v_2 t_2}{v_1 - v_2} = \frac{t_1 \lambda_1 - t_2 \lambda_2}{\lambda_1 - \lambda_2} \tag{4.31}$$

$$= 0.000956\,\text{s}. \tag{4.32}$$

Using the known neutron velocity at the Bragg edges, the distance to the chopper is

$$d = v_1(t_1 - t_{offset}) = 976.32\,\text{m/s}(0.00372\,\text{s} - 0.000956\,\text{s}) = 2.7\,\text{m}. \tag{4.33}$$

Since the nitrogen monitor was not moved between the runs, the same time offset and distance can be used for all runs.

4.8.3 M2 Monitor Data

For the M2 monitor data set shown in fig. 4.30, the Bragg edges are observed at 3.7 ms and 4.18 ms. Using the same method as was used for the nitrogen monitor run, the time offset and time bin to wavelength conversion can be calculated for the M2 monitor. Since the position and DAQ setup of of the two monitors are different, their time offset will be different as well. The M2 time offset is then found to be

$$t_{offset,M2} = 0.000792\,\text{s}, \tag{4.34}$$

with the corresponding error found found to be

$$\sigma_{t_{offset,M2}} = \sqrt{\left[\frac{v_1 \sigma_{t_1}}{v_1 - v_2}\right]^2 + \left[\frac{v_2 \sigma_{t_2}}{v_1 - v_2}\right]^2} \tag{4.35}$$

$$= \sqrt{\left[\frac{976.32\,\text{m/s} \times 0.000025s}{976.32\,\text{m/s} - 845.07\,\text{m/s}}\right]^2 + \left[\frac{845.07\,\text{m/s} \times 0.000025\text{s}}{976.32\,\text{m/s} - 845.07\,\text{m/s}}\right]^2} \tag{4.36}$$

$$= 0.0002\,\text{s}. \tag{4.37}$$

The uncertainty in the time offset arises primarily from the difficulty in determining the exact time bin where the Bragg minimum occurred. The uncertainty in the time bin was taken as the width of one time bin. Higher statistics for a run would allow for a more precise determination of the Bragg minimum, but for this work, the uncertainty stated above was deemed to be sufficiently small. Fig. 4.31 shows a plot of the M2 current with the time bins converted to wavelength.

The distance from the chopper to the M2 monitor can be calculated as

$$d_{M2} = v_1(t_1 - t_{offset}) = 976.32\,\mathrm{m/s}(0.00368\,\mathrm{s} - (0.000792 \pm 0.0002)\,\mathrm{s}) = 2.82 \pm 0.2\,\mathrm{m}. \tag{4.38}$$

The separation between the nitogen and M2 monitor was not accurately measured, but the 12 cm separation calculated from eqn. 4.33 and eqn. 4.38 is consistent with the records that were made.

While data was taken for a 25 millisecond time window for each chopper frame corresponding to wavelengths up to approximately 35 Å, there are very few neutrons past 16 Å, and many of the plots are truncated at lower wavelengths.

4.8.4 Monitor Comparison

To compare the monitor signals, a plot was made with each monitor signal normalized to have a peak height of 1, as seen in fig. 4.32. If the conversion from time to wavelength was done correctly, the Bragg edges in each monitor's spectrum should line up, as is seen.

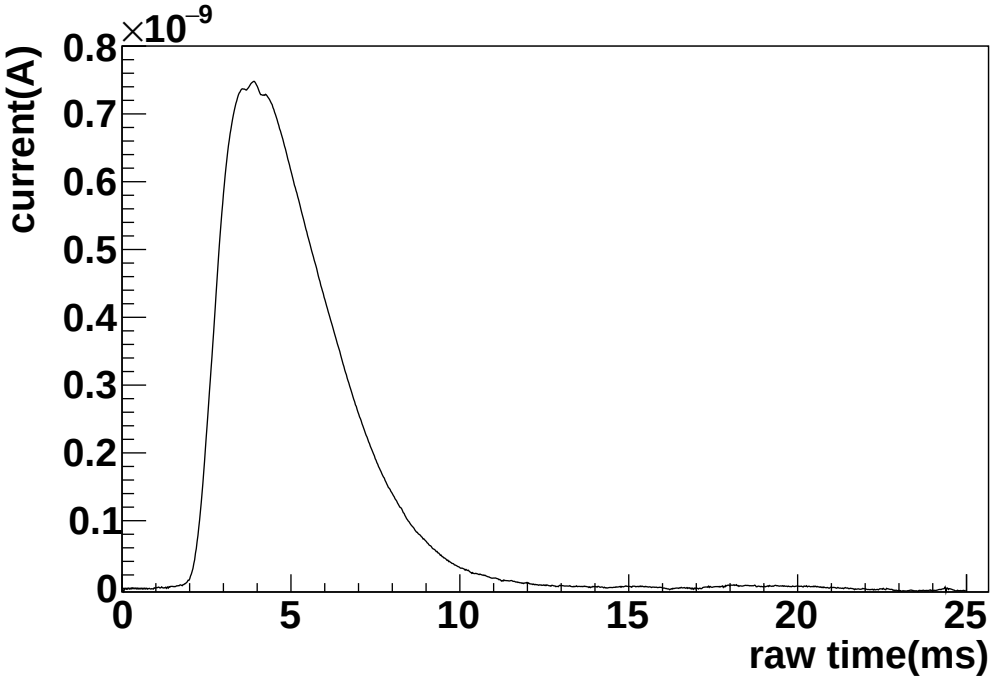

Figure 4.30: Monitor M2 raw time bins converted to ms with no corrections.

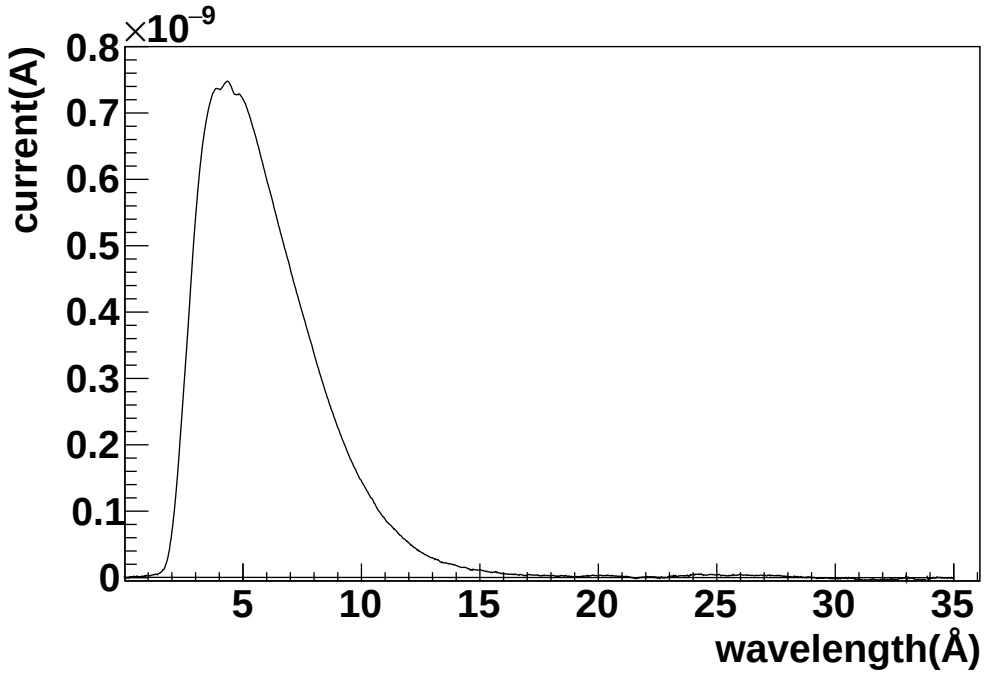

Figure 4.31: Monitor M2 plotted against the calculated wavelength.

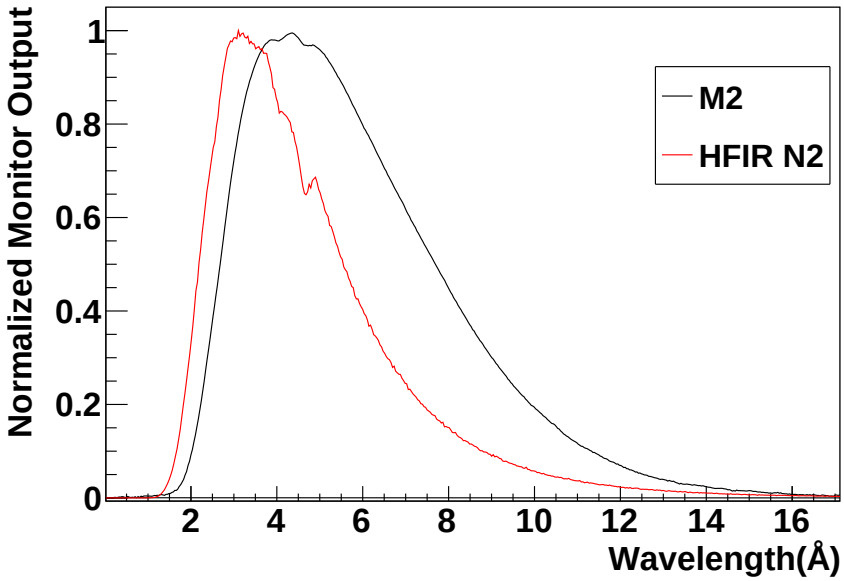

Figure 4.32: Comparison of the HFIR nitrogen and M2 monitor wavelength conversion. The monitor spectrum's peaks are both scaled to 1.

4.8.5 Calibration Method

The nitrogen monitor can be used to measure the number of neutrons entering the M2 monitor at a given neutron wavelength. By comparing the neutron flux into the nitrogen monitor at a given wavelength with the current output of the M2 monitor, the M2 monitor can be calibrated.

The analysis presented here follows the procedures outlined in references [62] and [63]. The current mode output voltage for the M2 monitor can be calculated as follows:

$$V(\lambda) = \epsilon_{M2}(\lambda) G \frac{dn}{dt}, \tag{4.39}$$

$$I(\lambda) = \epsilon_{M2}(\lambda) \frac{dn}{dt}, \tag{4.40}$$

where $V(\lambda)$ is the measured voltage, G is the gain of the M2 monitor preamp, $I(\lambda)$ is

the output current, $\epsilon_{M2}(\lambda)$ is the efficiency of the monitor at the wavelength λ, and dn/dt is the rate of neutrons entering the monitor.

Due to the low neutron capture rate in the nitrogen monitor, the incident flux and the transmitted flux are nearly equal. Dividing $I(\lambda)$ by $R(\lambda)$, the nitrogen monitor count rate in time bin λ, one finds

$$\begin{aligned}\frac{I(\lambda)}{R_N(\lambda)} &= \frac{\epsilon_{M2}(\lambda)\frac{dn}{dt}}{\epsilon_{Nr}\frac{\lambda}{\lambda_r}\frac{dn}{dt}} \\ &= \frac{\epsilon_{M2}(\lambda)}{\epsilon_{Nr}\frac{\lambda}{\lambda_r}} \\ \epsilon_{M2}(\lambda) &= \epsilon_{Nr}\frac{\lambda}{\lambda_r}\frac{I(\lambda)}{R_N(\lambda)}. \end{aligned} \tag{4.41}$$

The associated uncertainty is given by

$$\begin{aligned}\sigma_f &= \sqrt{\left(\frac{\partial f}{\partial x}\sigma_x\right)^2 + \left(\frac{\partial f}{\partial y}\sigma_y\right)^2} \\ \sigma_{\epsilon_{M2}} &= \epsilon_{Nr}\frac{\lambda}{\lambda_r}\sqrt{\frac{1}{R_N^2(\lambda)}\sigma_{I(\lambda)}^2 + \frac{I^2(\lambda)}{R_N^4(\lambda)}\sigma_{R_N}^2} \\ &= \epsilon_{Nr}\frac{\lambda}{\lambda_r}\frac{I(\lambda)}{R_N(\lambda)}\sqrt{\frac{1}{I^2(\lambda)}\sigma_{I(\lambda)}^2 + \frac{1}{R_N^2(\lambda)}\sigma_{R_N}^2}. \end{aligned} \tag{4.42}$$

For the measured M2 current in wavelength bin i, the error was taken to be the root mean square width of the bin signal over all chopper frames:

$$\sigma_{I(\lambda),i} = \sqrt{\frac{1}{N_f}\left[\sum_{j=1}^{N_f} I^2(\lambda_j) - \left(\frac{1}{N_f}\sum_{j=1}^{N_f} I(\lambda_j)\right)^2\right]}, \tag{4.43}$$

where N_f is the number of chopper frames. For the HFIR nitrogen monitor the error in the counts was taken as the square root of the number of counts divided by the counting time.

The neutron flux incident on the M2 monitor can be calculated as

$$F(\lambda) = \frac{I(\lambda)}{\epsilon_{M2}(\lambda)}. \tag{4.44}$$

The M2 efficiency is plotted in fig. 4.33.

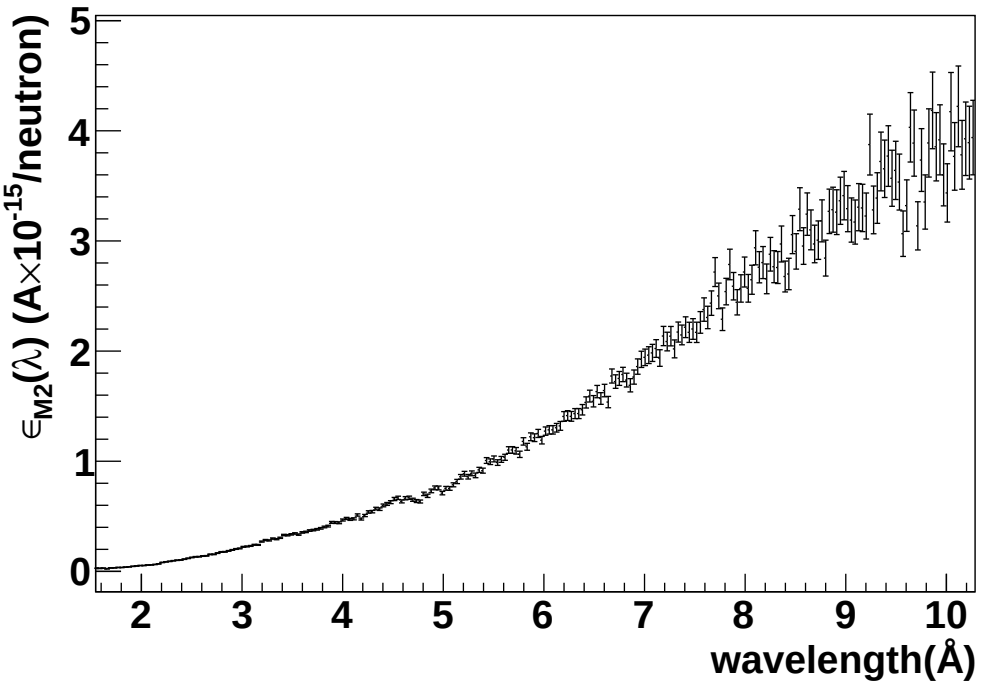

Figure 4.33: Graph of efficiency of the M2 monitor calculated using equations 4.41 and 4.42. The $\epsilon_{M2}(\lambda)$ is a conversion from the output current of the M2 monitor to the number of incident neutrons and has units of A/neutron.

4.8.6 Conversion to SNS Time Binning

The data acquisition systems used for the experiments at the FnPB and HFIR CG1 beam lines use different time binning that is related to the different beam time structures. The SNS uses a 60 Hz pulse rate with each pulse having a wavelength

range of 2.6-6.5 Å. At the FnPB, each pulse is divided into 40 time bins by the NPDGamma DAQ. The time bin width is 0.42 ms as compared to the 0.0244, ms bin width used at the HFIR beam line. Details of the NPDGamma DAQ are given in section 2.3.1. The efficiency for the ith SNS time bin is taken to be the error weighted average of the range of efficiencies calculated for the n HFIR time bins that fit in the SNS time bin:

$$\epsilon_{M2,SNS}(\lambda) = \frac{\sum_{j=1}^{n} \epsilon_{M2}(\lambda_j)/\sigma^2_{\epsilon_{M2},j}}{\sum_{j=1}^{n} \frac{1}{\sigma^2_{\epsilon_{M2},j}}}, \tag{4.45}$$

$$\sigma_{M2,SNS}(\lambda) = \sqrt{\frac{1}{\sum_{j=1}^{n} \sigma^2_{\epsilon_{M2},j}}}, \tag{4.46}$$

where $\epsilon_{M2,SNS}(\lambda)$ is the ampere to incident neutrons conversion for the NPDGamma time bin λ, and $\sigma_{M2,SNS}(\lambda)$ the error. 3-4 HFIR bins were averaged together for each SNS time bin.

4.8.7 Comparison to Boron Flux Measurement

A neutron flux measurement at the FnPB was made in July 2011 using a boron plate positioned at the center of the NPDGamma CsI detector array [64]. Boron-10 has a neutron capture cross section of 3835 barns for neutrons at 2200 m/s and the boron plate had a sufficient thickness to stop the full neutron beam. After a neutron captures on boron, it can decay by one of two paths,

$$^{10}\mathrm{B} + n \rightarrow ^{7}\mathrm{Li} + \alpha$$

with 6% probability, or

$$^{10}\mathrm{B} + n \rightarrow ^{7}\mathrm{Li}^{*} + \alpha + \gamma(0.48MeV)$$

with 94% probability. When there is a gamma ray produced its energy is consistently 0.48 MeV. A fraction of the gamma rays will deposit energy in the surrounding CsI array and, with the aid of simulation, the energy deposited in the CsI array can be used to calculate the total number of neutrons captured in the boron plate.

The center of the detector array is 242 cm from the center of the beam monitor. The spin flipper is also located between the M2 monitor and the boron plate. To calculate the neutron flux entering the monitor, the neutron flux measured at the boron plate needs to be corrected by the transmission of the 242 cm path through the air, the spin flipper transmission, and the beam monitor. The transmissions were calculated for the materials in the beam path using the NIST Neutron Scattering Lengths and Cross Sections web page [59], and eqn. 4.3.

Table 4.5 gives the composition that was used for air. The partial pressure and partial volume for each element in a volume of gas can be found using Amagat's law of additive volume

$$\frac{V_x}{V_{Tot}} = \%V = \frac{P_x}{P_{Tot}},$$

where V_{Tot} and P_{Tot} are the total volume and pressure. A total pressure of 760 Torr was used. The partial volume, V_x, of a particular element in the gas is the volume that the element would have occupied if it were a monoatomic gas, with unchanged pressure and temperature. P_x is the partial pressure. Using this relation for the partial pressure, the molecular density of the gases was calculated. The total transmission through 158 cm of air was then

$$T_{air}(\lambda, d) = T_{O2}(\lambda, d) \times T_{N2}(\lambda, d) \times T_{CO2}(\lambda, d) \times T_{Ar}(\lambda, d).$$

From the MCSTAS simulation detailed in reference [64], an estimated 0.5% of the

Gas	% Volume
O_2	20.95
N_2	78.09
CO_2	0.03
Ar	0.93

Table 4.5: Composition of air used in transmission calculations.

beam would capture on the Li cover of the spin flipper at the window edges and 0.5% of the neutron beam would not hit the boron plate. The two spin flipper windows were considered to be of 1 mm of pure Al and have a transmission designated $T_{sf}(\lambda)$. The total transmission was then

$$T(\lambda) = T_{air}(\lambda) \times 0.995 \times 0.995 \times T_{sf}(\lambda)$$

The flux was measured using the neutron beam on the boron target in a separate run. The beam power was known to be 0.601148 MW and the binning of the data, converted to wavelength, corresponded to a bin width of 0.09 Å. The flux measurement, therefore, had units of $n/s/$Å.

The M2 monitor preamp was changed between HFIR and the setup at the SNS during these measurements. The preamp used at the FNPB for M2 had a $0.5\,M\Omega$ resistor and 2.43 voltage multiplier. The preamp at HFIR had a $30\,M\Omega$ resistor and, while not recorded, it is standard to have a 2.43 voltage multiplier on the preamp. Both voltages were converted to current by dividing by the preamp amplification factors,

$$I(\lambda) = \frac{V(\lambda)}{2.43 \times R}. \tag{4.47}$$

The neutron flux through the beam monitor was then calculated as

$$F(\lambda) = \frac{I(\lambda)}{\epsilon_{M2,SNS}(\lambda)}, \tag{4.48}$$

with an uncertainty of

$$\sigma_F = \frac{\lambda_r}{\lambda}\frac{I(\lambda)}{\epsilon}\sqrt{\left(\frac{\sigma_I}{I(\lambda)}\right)^2 + \left(\frac{\sigma_{\epsilon_{M2,SNS}}}{\epsilon}\right)^2}.$$

Fig. 4.34 shows the plot of the boron flux measurement compared with the M2 monitor flux, and the values are in good agreement. Fig. 4.35 shows an M2 current plot. It can be seen that the shape of the pulse for the neutron flux and current are different. This is due to differences in the capture cross section of the neutrons at the different energies.

4.9 Monitor Linearity

To make use of the calibration of the monitors, it is required to measure the linearity of the beam monitors to ensure that at the higher flux of the SNS compared to the CG1 beamline that the monitor response is the same. The first check is a voltage scan to determine which region of the charge collection curve the monitors are operating in as shown in fig. 3.1. The second is a beam power scan to ensure the monitors are operating in a region in which the signal is proportional to the accelerator beam current over a large range of beam powers.

4.9.1 Voltage Scans

As discussed in section 3.2 the amount of charge collected can vary with the bias voltage applied to the monitors. It is desired for the monitors to operate in the ion

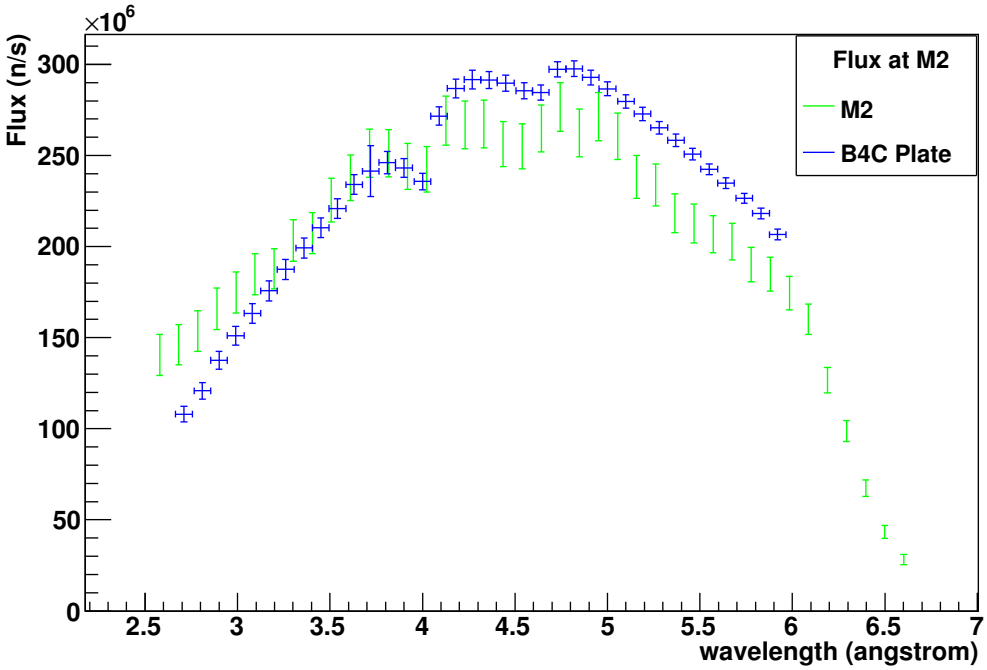

Figure 4.34: M2 neutron flux from HFIR calibration compared with boron plate flux. Horizontal error bars are bin widths.

chamber region as variations in the bias voltage and the ionization rate will have the least effect there.

Bias voltage scans were done for the M1 and M2 neutron beam monitors. The monitors were scanned in increments of 100 volts from 0-500 volts and in increments of 200 volts up to 1800 V. Each monitor was scanned independently while the other was held constant at 1600 V. The monitor held at constant bias was used to normalize the signal of the scanned monitor during analysis to remove neutron beam fluctuations.

The output voltage from the power supply was measured using a Fluke 77 Series II multimeter and a voltage divider. The voltage divider reduced the voltage by a factor of 0.1011 to reduce the applied voltage to within the operating range of the

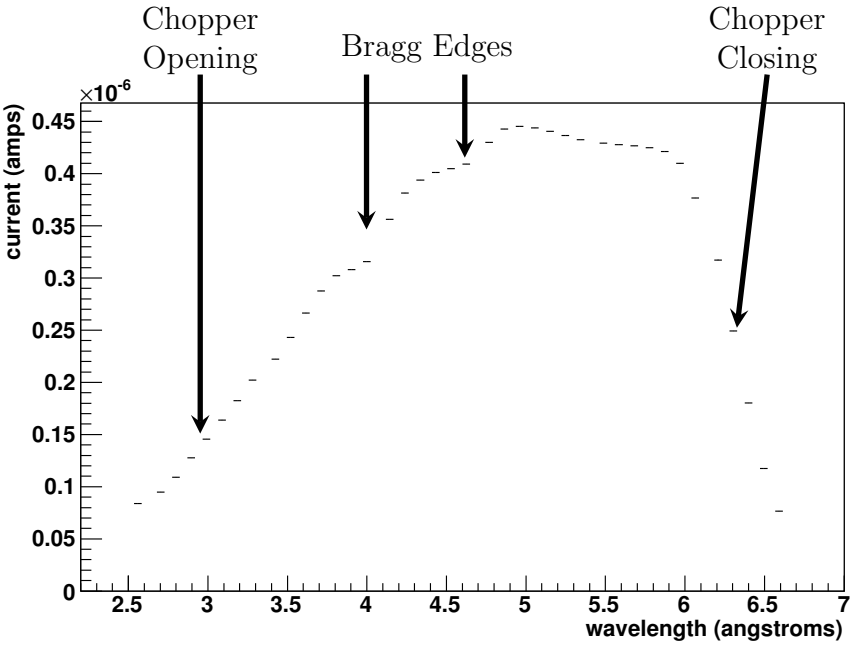

Figure 4.35: M2 60 Hz Time-of-flight spectrum from SNS FnPB.

multimeter.

For the M2 amplifier a gain of 1215 kΩ was recorded, and the M1 amplifier had a gain of 100 kΩ. These measurements were taken during the NPDGamma experiment commissioning using the NPDGamma DAQ, with each neutron pulse divided into 40 time bins.

Figs. 4.38 and 4.39 show the ratio of the monitor signals as a function of bias voltage. To establish the data for these plots, a run was taken containing 800 neutron pulses for each bias voltage. A profile histogram was created for the 40 time bins of each pulse. If a pulse was significantly lower than average or completely missing, it was excluded. A small number of time bins from each monitor were combined in an error weighted average over the 800 pulses. While the same number of time bins were averaged for each monitor, the bin range was offset by 2 time bins in M2, compared

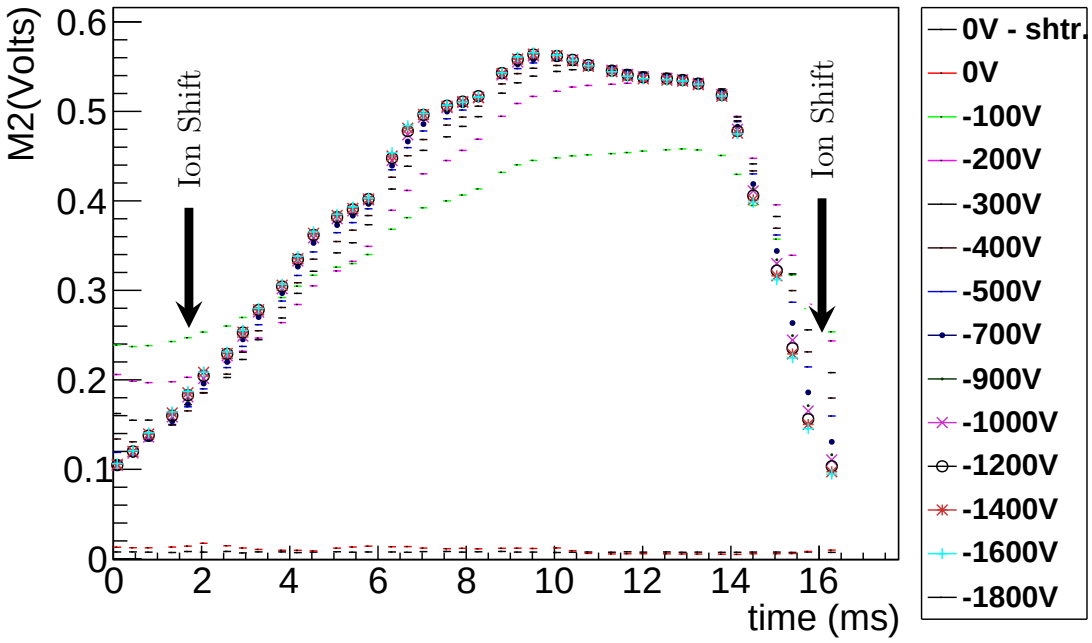

Figure 4.36: Pulse profile histogram plots for M2 scan.

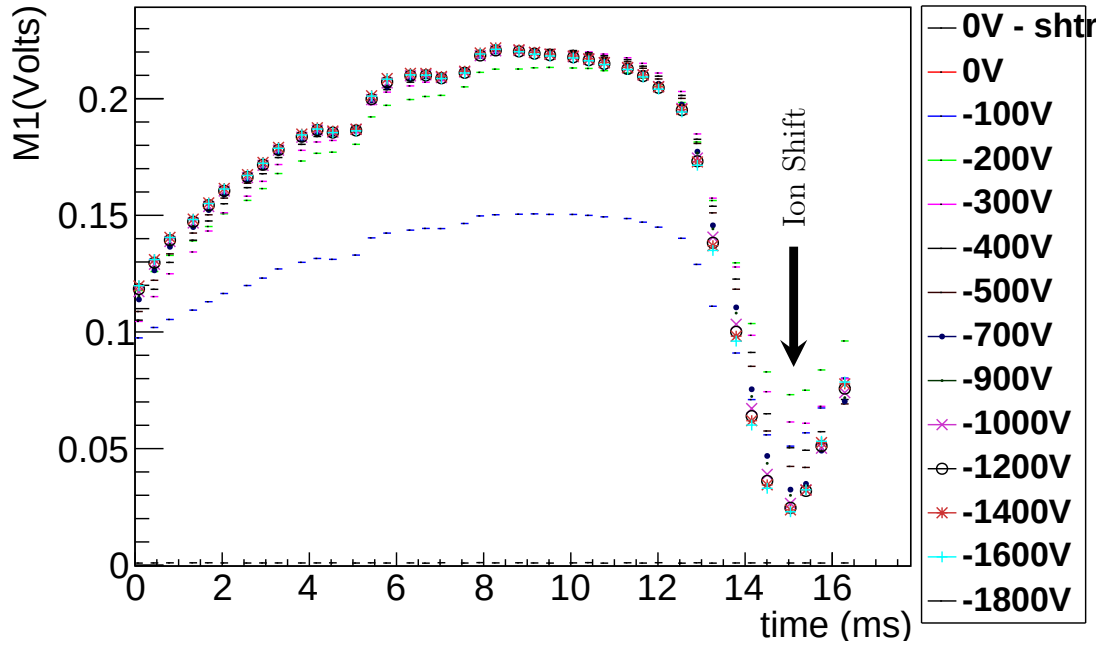

Figure 4.37: Pulse profile histogram plots for M1 scan.

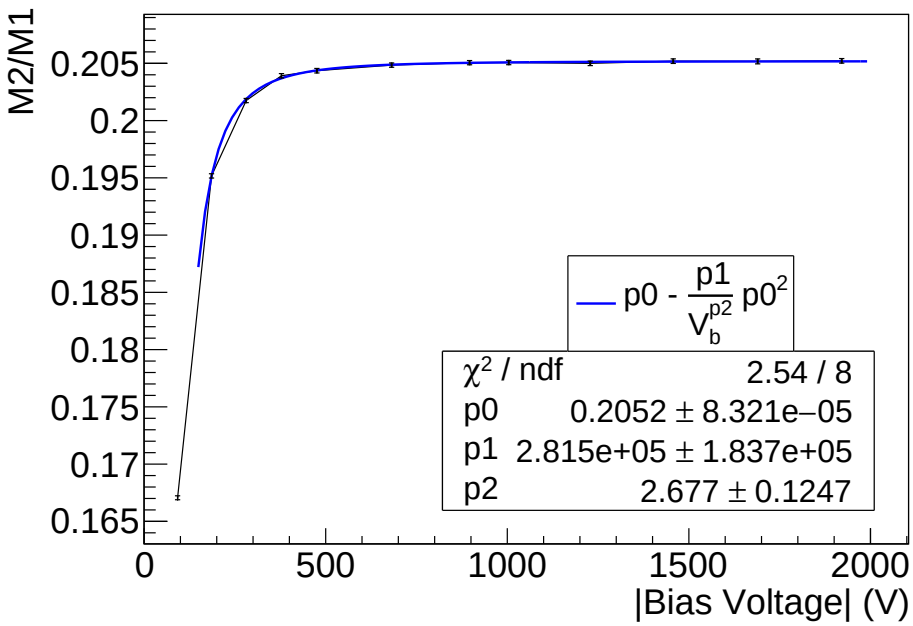

Figure 4.38: The ratio of the error weighted average of time bins 21-24 of M2 divided by time bins 19-22 of monitor M1 plotted vs. bias voltage.

to M1 due to the difference in the position of the beam monitors, so that the ratio could be calculated for neutrons of the same energy.

To compare the measured values with the simple charge collection model from section 3.3, the curve in equation 3.23 was fit to the data. The fitting parameters $p0$ and $p1$ correspond to I and c respectively, while $p2$ is the power to which the bias voltage V_b will be raised.

The parameter $p2$ was unexpectedly different in the fit for each monitor. The M2 monitor produces a value of 2.7 ± 0.1 for the $p2$ parameter, but M1 was found to come on much faster with 5.5 ± 0.1 for the $p2$ parameter. The two monitors have nearly identical wire geometries, so that could not cause the difference. The M1 monitor has a lower overall fill gas pressure and a higher fraction of ^{3}He to N_2, which would

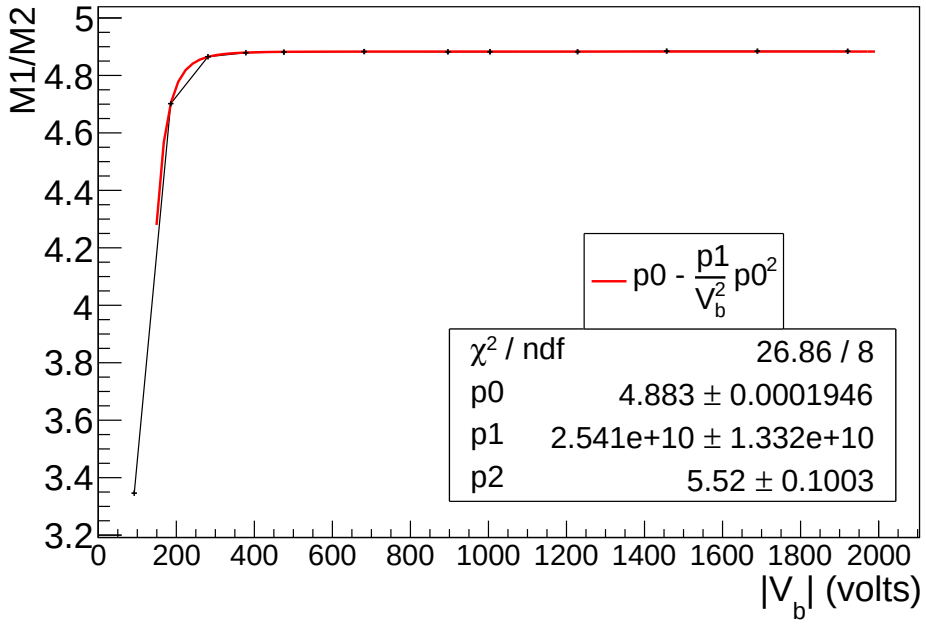

Figure 4.39: The ratio of the error weighted average of time bins 19-22 of monitor M1 divided by time bins 21-24 of M2 plotted vs. bias voltage.

allow for higher electron and ion mobilities in the gas. This would allow faster charge separation and a reduction in $p1$ as $c \propto 1/k_+k_-$, not the increase in $p1$ and $p2$ that is seen. The cause of this difference in behavior is not understood, but so long as the applied bias voltage on each monitor is over $-800\,\mathrm{V}$, the monitors should behave as expected with complete and rapid charge collection.

Since the supermirror polarizer is located between the monitors, the M1 monitor has roughly three times the neutron flux of the M2 monitor. In section 4.9.2 variations of a factor of ~ 4 in the neutron flux don't seem to impact the monitor linearity so that is not likely the cause of the difference either.

4.9.2 Beam Power Scan

Since the purpose of the beam monitors is to provide a measurement of the instantaneous neutron flux during operation, it is important that the monitors operate with the same efficiency at all beam powers. To test this, the output voltage of the monitors was compared to the average proton power on the mercury spallation target for runs in which the proton power was relatively constant. The monitor signals should be linear to the proton power.

The first step was to find a series of runs for which the proton beam power on the mercury spallation target was relatively constant and to average the beam power over the length of the run. This was made possible by access to the beam history kept by the facility. Data can be accessed in time intervals as short as 0.1 second increments, covering six proton pulses. By using the time stamp stored for each data file, obtained during NPDGamma data taking, the proton beam power for the same time period can be found and compared with it.

After candidate runs over a range of beam powers were identified, the beam monitor data was examined for stability and dropped pulses. This was done by comparing the peak bin in each pulse in the run and by seeing that its value remained within approximately 90% of the run average. As the pulse height is different for each proton power, the pulse height cutoff was determined individually for each run.

These measurements were done with the NPDGamma DAQ setup using the eight step spin sequences shown in section 2.3.1. If a pulse in an eight step sequence or the last two pulses of the previous eight step sequence was below the cutoff, the entire eight step sequence was discarded. Approximately 2% of pulses were dropped from

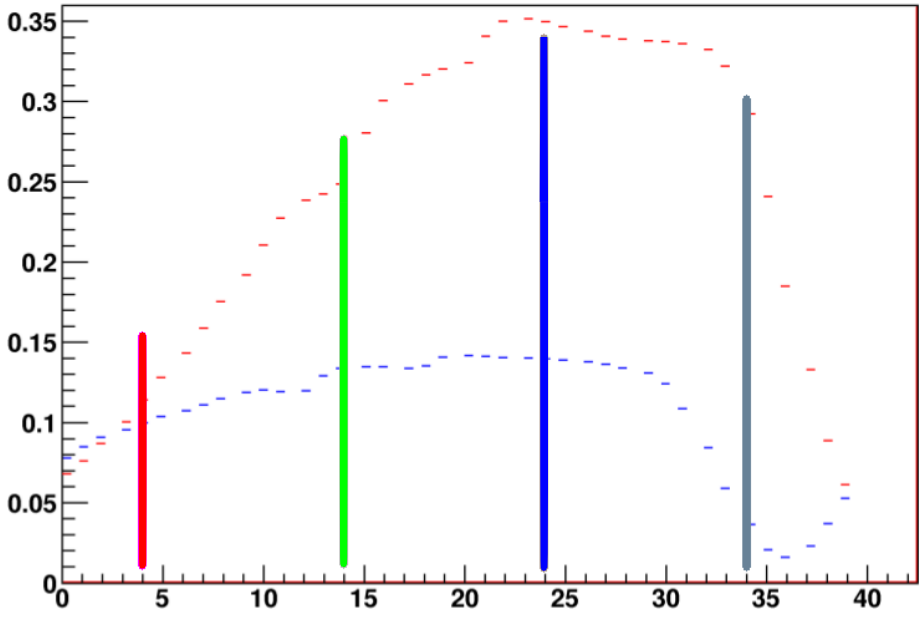

Figure 4.40: For the comparisons to be done later, the marked time bins, 4 (red), 14 (green), 24 (blue), and 34 (blue) for the monitors show where in the profile the monitor voltage was being sampled.

each run. The remaining pulses were then averaged for each time bin in a pulse. Most runs had 2500 entries, so with eight pulses per entry, this gives on average approximately $20000(1 - 0.02) = 19600$ pulses being averaged together for each time bin.

A total of 52 runs were chosen for the analysis, with proton beam powers ranging from approximately 200-900 kW. Appendix A.2.2 lists the run numbers and beam powers for the runs that were used.

Fig. 4.41 shows a graph of the average M1 signal for the chosen time bins marked in fig. 4.40, as a function of beam power. Based on the fit to the data, the M1 monitor response to the changes in the beam power are linear within error. Fig. 4.43

shows the same for the M2 monitor. The fitting equation for each line is a first order polynomial of the form $a + bx$.

For both monitors, there are ten runs in the 460 to 550 kW range that are anomalously low compared to the other runs. Removing those runs has the effect seen in fig. 4.42 and fig. 4.44. Removing these runs from the fits gives an improved χ^2. The removed runs occurred in the same 22 hour period. It is possible that during this period there was a problem with the facility, reducing the efficiency with which neutrons were produced by the proton beam. Fig. 4.45 and 4.45 show the fit for all time bins with the low runs removed. From this and the voltage scan measurement, it can be concluded that the beam monitors are linear over the examined neutron flux.

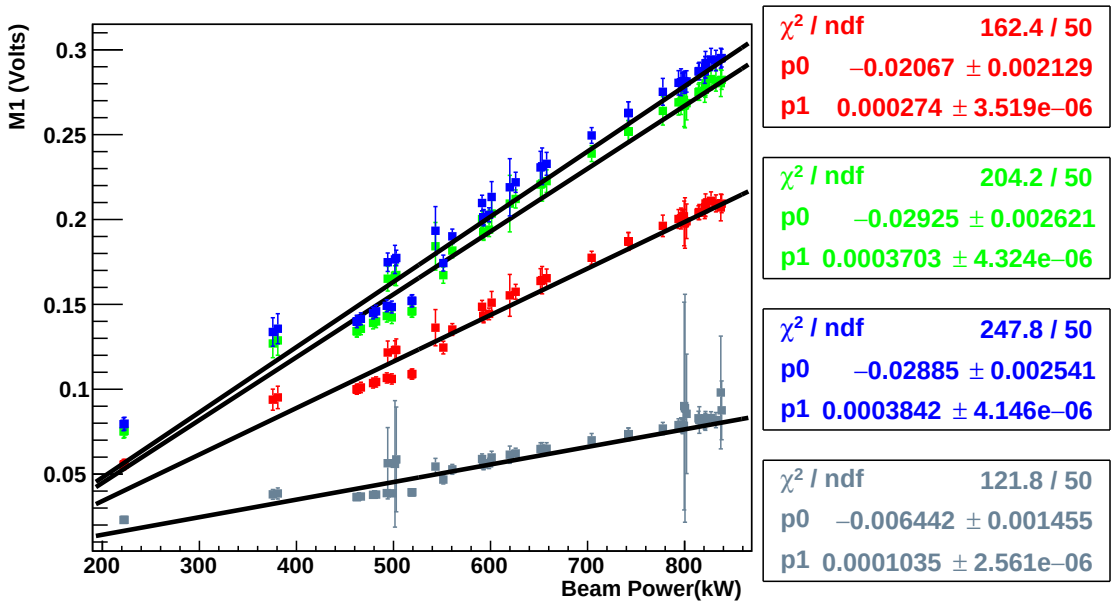

Figure 4.41: Comparison of time bins 4 (red), 14 (green), 24 (blue), and 34 (grey) for the M1 monitor. The error bars are the standard deviation in the monitor voltage.

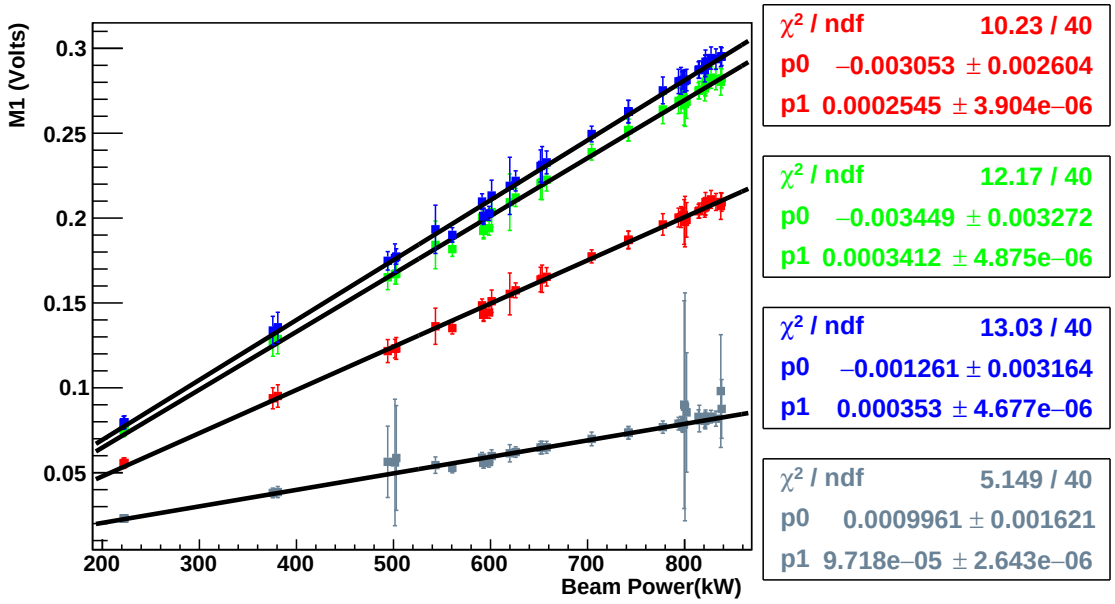

Figure 4.42: Comparison of time bins 4 (red), 14(green), 24 (blue), and 34 (grey) for the M1 monitor with the low runs removed.

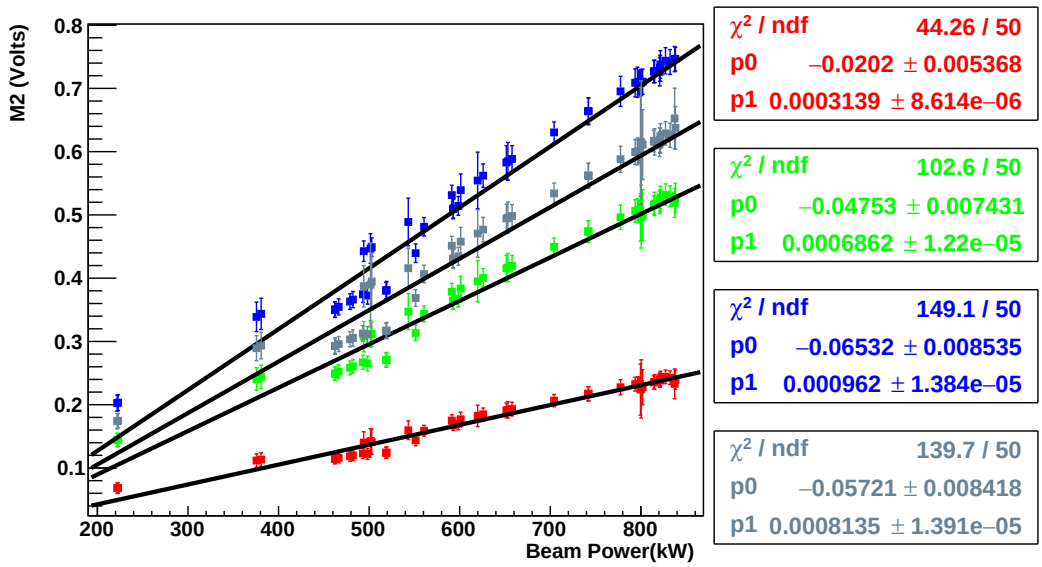

Figure 4.43: Comparison of time bins 4 (red), 14 (green), 24 (blue), and 34 (grey) for the M2 monitor. The error bars are the standard deviation in the monitor voltage for the time bin over the run.

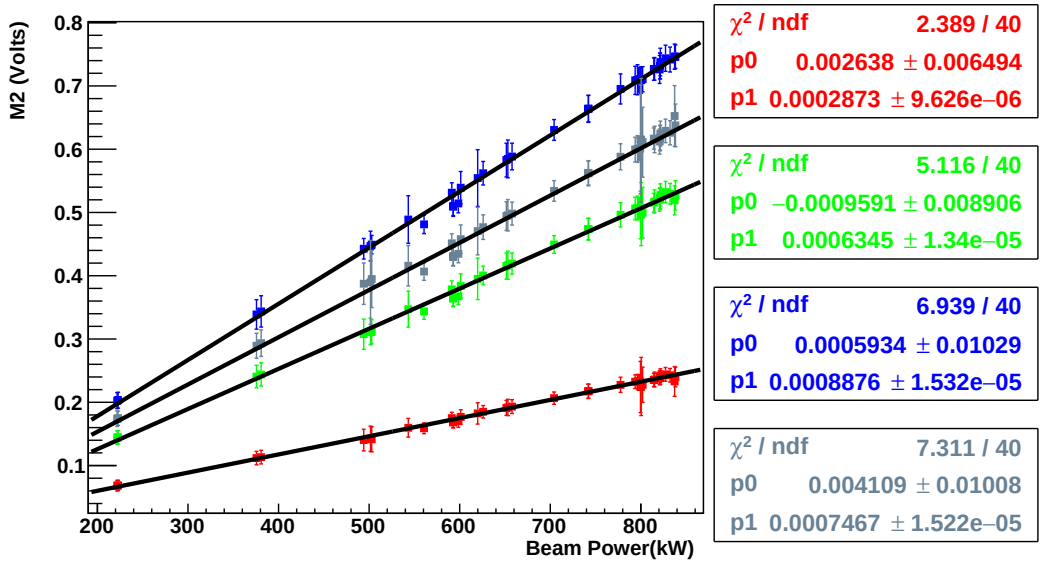

Figure 4.44: Comparison of time bins 4 (red), 14 (green), 24 (blue), and 34 (grey) for the M2 monitor with the low runs removed. The error bars are the standard deviation in the monitor voltage for the time bin over the run.

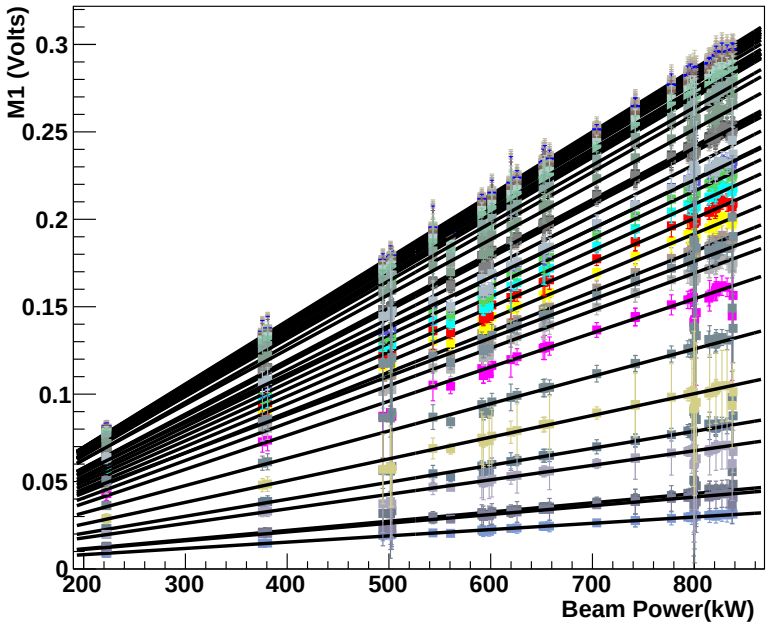

Figure 4.45: M1 time bins plotted vs. beam power for all time bins. The error bars are the standard deviation in the monitor voltage for the time bin over the run.

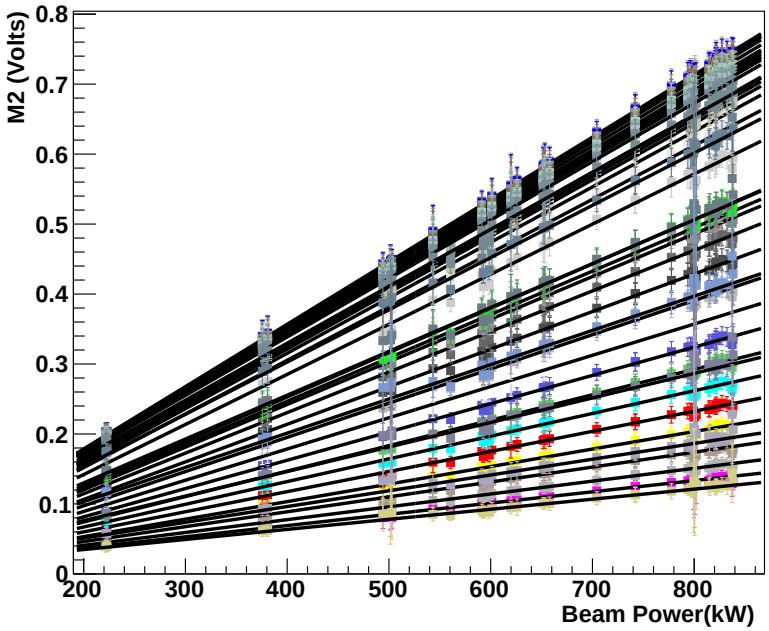

Figure 4.46: M2 time bins plotted vs. beam power for all time bins. The error bars are the standard deviation in the monitor voltage for the time bin over the run.

Chapter 5

n3He Target Chamber

The target chamber for the n3He experiment is a multi-wire proportional chamber using a pure ^{3}He fill gas. By using a pure fill gas, the chamber can act as the ^{3}He target for the experiment as well as the ionization detector for measuring the ionization distribution. While the use of a gas mixture could have improved the HV characteristics of the target chamber, the neutron capture signals from the additional fill gasses would have complicated the ^{3}He asymmetry extraction.

To minimize variation in the signal from each capture event, it is important that most of the protons and tritons can range out in the target chamber. For this reason, wires are used instead of plates for the HV and signal electrodes.

As discussed in section 2.4.2 there are two possible measurement modes for the target chamber: one for the PV asymmetry and one for the PC asymmetry. To measure the PV asymmetry, the target chamber must have finite resolution in the direction parallel to the magnetic field. To measure the PC asymmetry, the target chamber must have finite resolution in the direction perpendicular to the magnetic

field. The target chamber must also be able to be changed between these modes periodically during running. The target chamber will also benefit from finite resolution along the axis of the target chamber.

To maximize statistics, the full neutron beam needs to be stopped within the target chamber. This sets limits on the minimum chamber length and the gas pressure. The transverse area of the target chamber also needs to be larger the than the beam profile at the target.

How these requirements and the lessons learned from the beam monitors are incorporated into the target chamber design will be discussed below.

5.1 Housing

The target chamber housing was made by Atlas Technologies [65]. As with the beam monitors, the target chamber has an aluminum body with bimetal conflat flanges. The aluminum body has a low magnetic permeability, low neutron capture cross section, and short beta decay half-life after neutron capture. The bimetal conflat flanges provide a durable knife edge while minimizing the amount of magnetic material in the target chamber.

The target chamber body is an aluminum cylinder with a 25.4 cm interior diameter and 0.635 cm thick walls. The end flanges are 12 inch conflat flanges. Two pairs of 4.5 inch conflat feedthroughs on opposite sides of the chamber were used with Lesker 2×25 pin Dsub vacuum feedthrough to read out the signal wires. Two 2.75 inch feedthroughs on opposite sides of the target chamber between the signal feedthroughs were used for the HV supply. One of the two 90° feedthroughs was used for the gas

Figure 5.1: The aluminum target housing and end windows for the the n3He target.

fill. Fig. 5.1 shows the target housing with the two end windows. Fig. B.9 shows the dimensions of the target chamber.

5.1.1 Leak Testing

Prior to assembly, the target chamber was examined with a helium leak checker to ensure the target chamber was helium tight for the experiment. The leak test setup schematic is shown in figure 5.2.

During the first leak check, a leak was found in one of the 90° feedthroughs. The ORNL machine shop inspected the feed-through, but as the leak was so close to the conflat knife edge, it was not possible to weld there without risk of distorting the flange. Instead, the feedthrough was closed off with a blank flange for the duration of the experiment, and the leak sealed with epoxy. The epoxy was allowed to set for a few days, and the helium leak check was repeated. This fix is shown in fig. 5.3a

The target chamber was then wrapped in heat tape and aluminum foil insulation to be heated and pumped for two days. After this, a second leak was found in one of

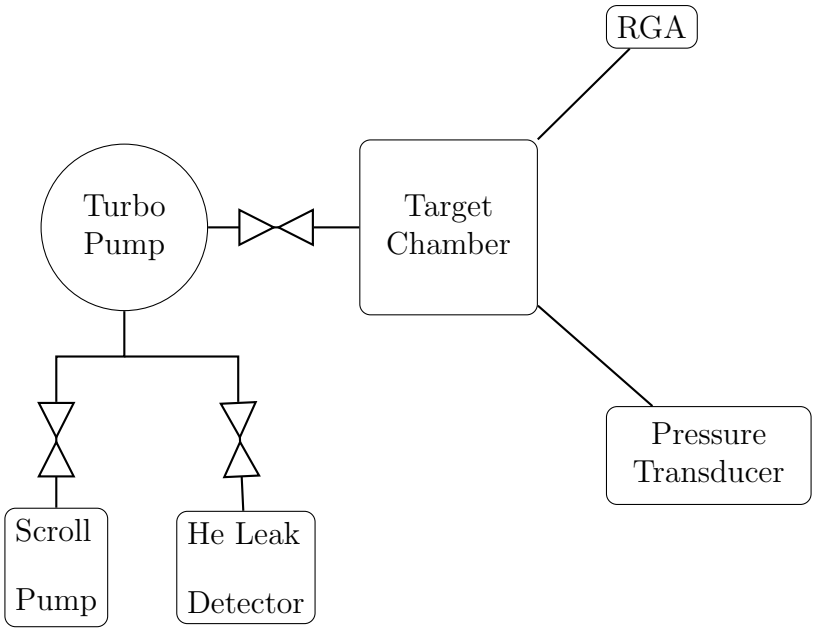

Figure 5.2: Target chamber housing leak check setup schematic.

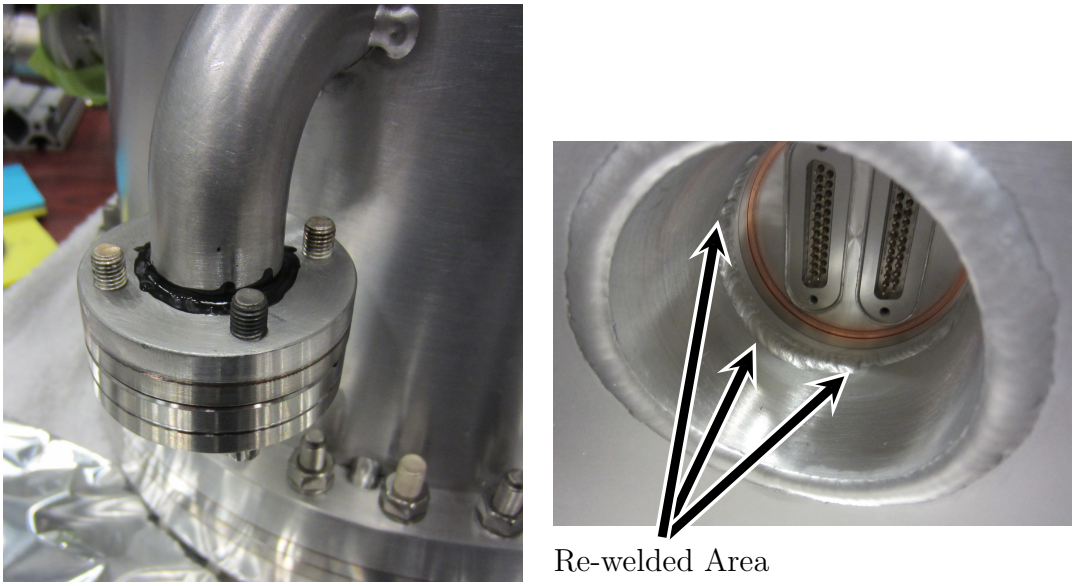

(a) Epoxied Gas Flange

(b) Welded signal Flange

Figure 5.3: Two leaks in the chamber flanges were fixed during the leak check process.

the signal feedthrough flanges. This larger feedthrough was welded to seal the leak at the ORNL machine shop. Fig. 5.3b shows the welded flange. After welding, the chamber was thoroughly cleaned with kim wipes and ethanol before a second bake out and a successful leak test.

5.2 Frame Stack

The design for the frame stack was done by myself, at the University of Manitoba, with input from my adviser Michael Gericke and the collaboration at key points. Using the information and experience gained in the construction and operation of the M1 and M2 beam monitors, I used Autodesk Inventor to create a 3D model of the target chamber frame stack design that would meet the requirements for the target chamber operation. Appendix B.2 has a selection of CAD drawings for the target chamber and its parts.

For the n3He experiment, it was required to measure the distribution of ionization in the chamber. To do this, each signal wire in the target chamber was read out individually. This allowed the location of ionization to be determined in the chamber in two dimensions, along the chamber axis, and one direction perpendicular to the chamber axis. For the wire spacing requirements, the simulation results given in table 3 of reference [8] indicated only a small increase in the error dilution going from 5 mm to 20 mm wire spacing so that a wire spacing anywhere in that range would be usable. The wires also had to be held under tension similar to the beam monitor wires to prevent vibration.

The minimum interior opening size of the wire frames was taken to be the size of

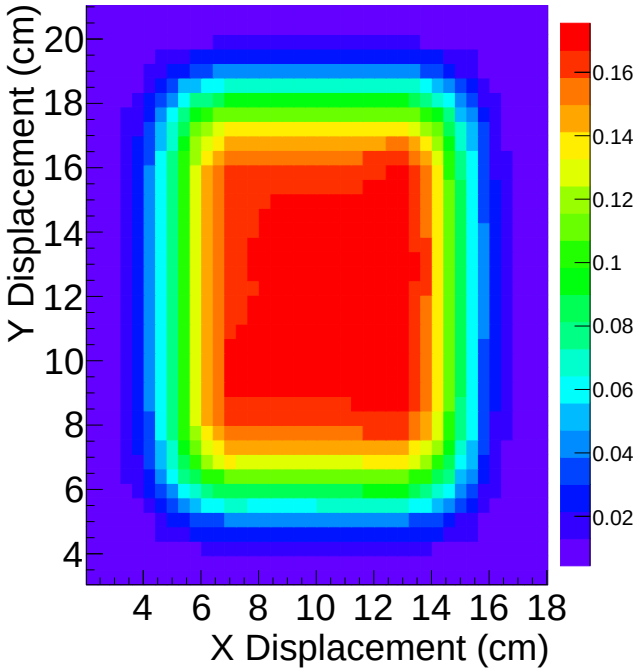

Figure 5.4: FnPB beam profile measured during n3He comissioning in 1 cm steps at an unrecorded point between the target mount location and SMP shielding.See references [66] and [40](ch.4:Beam Scanning), for more details.

the neutron beam after two meters of beam divergence in air, an estimated 14 cm × 16 cm, from the initial 10 cm × 12 cm beam cross section at the exit of the beam guide. Fig. 5.4 shows a scan of the beam profile made during the experiment commissioning. The overall size of the frames was limited by the target chamber interior diameter.

The design goal of the n3He target is to be able to align the wires in the target to order of 1 mrad angular alignment with respect to each other and the magnetic holding field that determines the average beam polarization to control systematic effects as discussed in section 2.4.2. For the wires on a frame, machining tolerances of better than 0.2 mm were required for alignment, which was achievable.

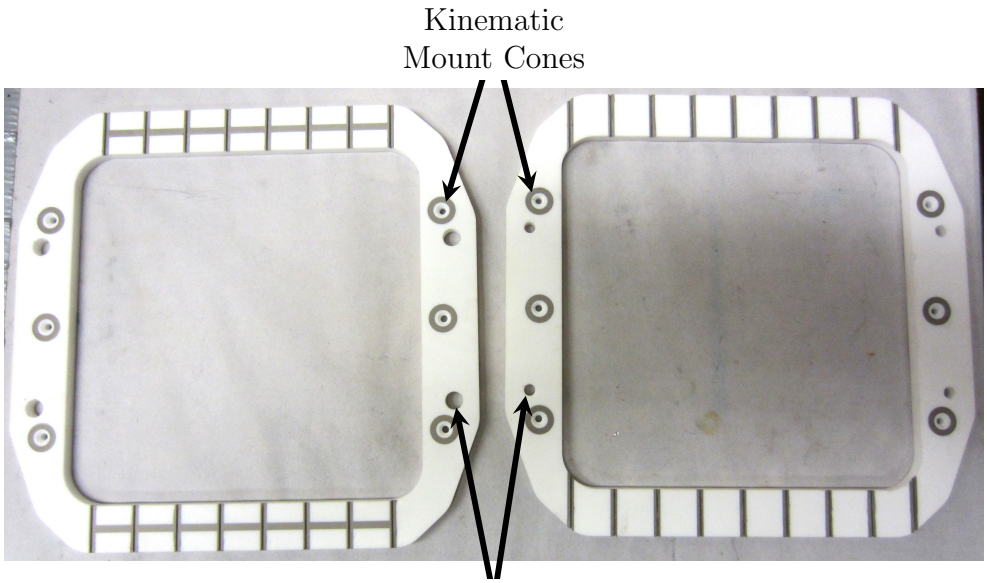

(a) HV Frame (b) Signal Frame

Figure 5.5: Unstrung macor wire frames.

For the frame construction, macor ceramic and PEEK plastic were the primary materials considered. Macor was chosen primarily for alignment concerns since the significant bowing that occurred in the PEEK beam monitor frames during stringing would prevent the precise alignment of the wire frames in the target chamber. The use of macor required a significantly different design than the PEEK beam monitor frames used. Instead of using through holes and ferrules for mounting the wires, grooves were ground onto the frame surface for locating the wires. Thin film metallization was used to create conductive traces that could be soldered to for attaching the copper wires to the frames. Fig. 5.5 shows an unstrung HV and signal frame. Fig. D.1 shows a strung HV frame.

More difficult to achieve is this degree of alignment between the wire planes. A kinematic mount consisting of three ball and cone joints was used as this kind of

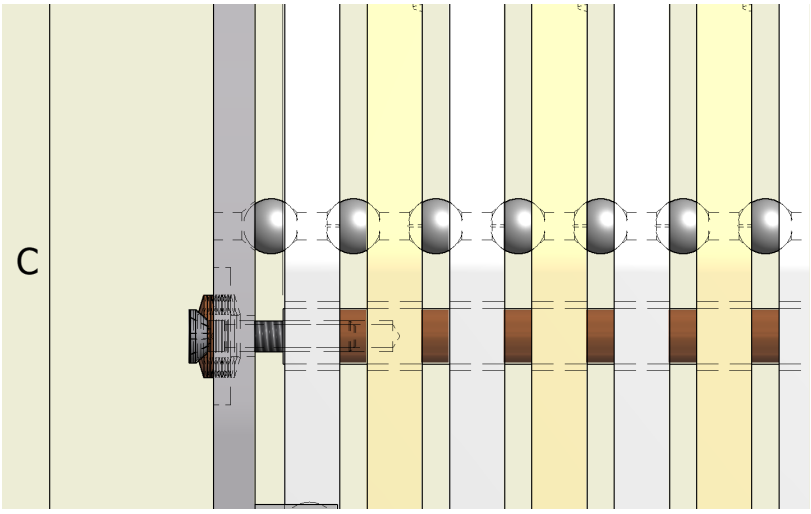

Figure 5.6: CAD model of the ball in cone joint that was used between the wire frames. One of the compression rods is also visible with the screw and spring washers used to set the pre-tension in the rod.

mount can provide accurate and repeatable alignment between surfaces. A set of six cones were machined into the surface on each side of the frame, three of which were used for the mount. The wire frames were stacked with a set of three ceramic beads between the frames, and this gave a reliable and consistent positioning between the frames. Fig. 5.6 shows a CAD model of the of the frame stack with hidden lines showing the ceramic ball in the cones between the frames.

With macor chosen as the preferred material and the basic frame design determined, Autodesk Inventor single part stress simulations were performed using different frame thicknesses and wire spacings. Thinner frames would allow a closer wire spacing, but also require more wires per frame increasing the stress on the frame and the cost of the read-out electronics. The selection criteria was that the safety factor should not go below two in the results of the stress analysis. Using the results of

these simulations, a minimum frame thickness of 3/16 inch was chosen with a 1.9 cm wire spacing. 1/4 inch thick frames were chosen as the cost difference was minimal compared to 3/16 inch frames. Fig. 2.30 shows the arrangement of wires inside the target chamber in a simplified cross section. See appendix C for details of the stress calculations and simulations.

The frame stack was mounted to one of the end windows of the target chamber using an aluminum mount plate. The mount plate had an interior opening larger than the wire frames' interior opening so that it would not interfere with the neutron beam. The mount plate was split on one side which allowed a set screw to be used to expand the plate to hold it securely in the end window without touching the thin neutron window or the conflat knife edge. The frame stack was mounted to this plate using the same ball and cone kinematic mount as the wire frames used to each other. Four threaded holes in the mount plate were used to hold the phosphor bronze rods for the compression plate discussed below. Fig. D.3 shows the mount flange in the end window with the four bronze rods and three ceramic balls for the kinematic mount.

To hold the frame stack together while in the horizontal position, a spring loaded compression plate was used to control the total compression force on the frames and to allow a limited range of thermal expansion and contraction in the frame stack without damaging the frames. Fig. D.7 shows the frame stack with the compression plate on top and fig. D.8 shows the stack of Belleville spring washers under the bolt head that was used to set the spring pre-load. Fig. 5.7 shows the assembled frame stack just before insertion in the housing.

To read out the 144 signal wires, two printed circuit boards (PCBs) were used

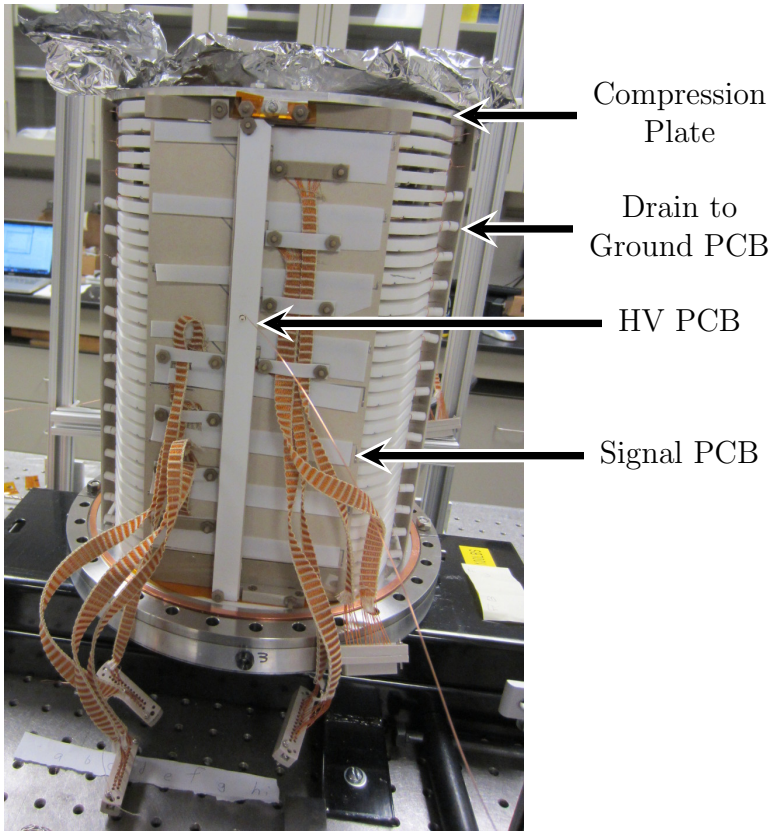

Figure 5.7: Assembled target frame stack mounted on lift jack prior to insertion into housing. White telfon shielding is over the HV and signal board traces to protect against sparking.

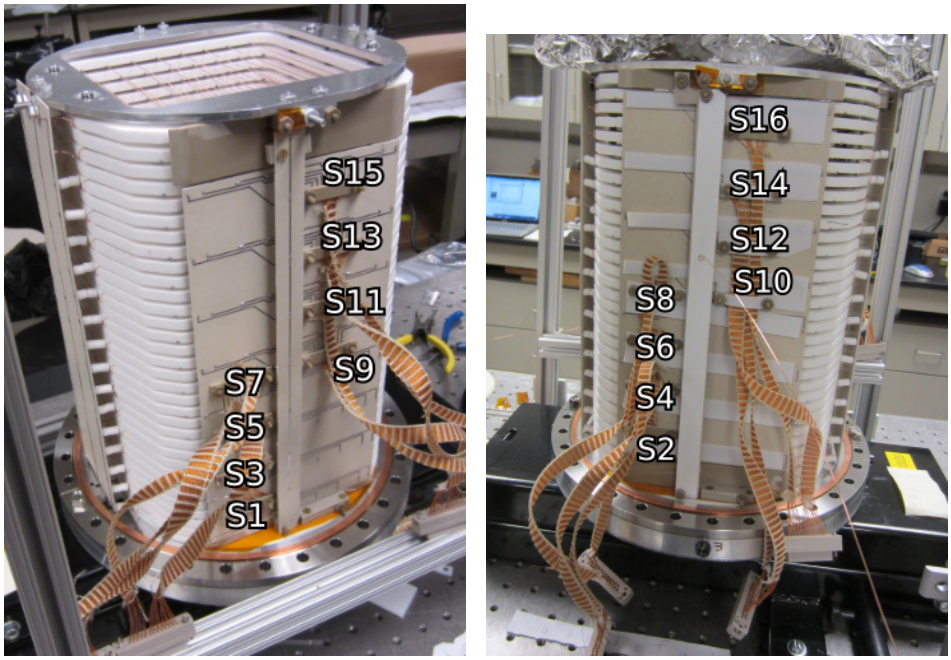

(a) PCB with even numbered wire frames.(b) PCB with odd numbered wire frames.

Figure 5.8: Signal Read out PCBs. Each PCB did carried one half of the frames.

with D-Sub plugs connected to the PCBs by Kapton ribbon cables. Fig. D.9 shows the layout of the signal PCBs. Each signal wire was soldered to one trace on a PCB, and then the traces connected to wires from one signal plane were gathered into one place for the Kapton ribbon cables to be soldered to as shown in fig. D.11. Each 25 pin D-Sub plug had two ribbon cables. Each cable carried signals from one signal wire frame. Two D-Sub plugs were connected to each signal feedthrough for a total of 36 wires. One PCB was connected to all of the even numbered signal planes and the other PCB the odd numbered signal planes as shown in fig. 5.8. Appendix D.2 has more details on the wire to feedthrough and wire to ADC mapping.

The PCBs were made from Rogers' Duroid material [67] as it is suitable for use in UHV. As Duroid is a Teflon glass composite, it is fairly radiation hard. The main

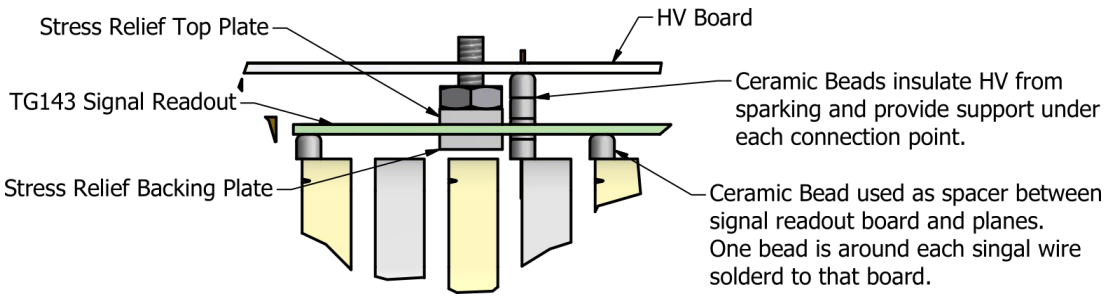

Figure 5.9: CAD model of the ceramic beads used to space the signal and HV PCBs from the wire frames. The stress relieving plates are used to clamp the Kapton ribbon cables to the signal PCBS to prevent damage to the solder joint and traces during installation.

effects of radiation exposure are an increase in brittleness and a reduction in tensile strength [68]. The boards were spaced away from the HV planes with ceramic beads placed over each signal wire on the backside of the board that also served to shield the signal wires from the HV as shown in fig. 5.9.

5.3 Fill Gas Calculations

To meet the statistical requirements for the experiment, it is desired to stop the full neutron beam in the target chamber. There was a large range of gas pressures it was possible to operate the target chamber at due to the high neutron capture cross section of 5333 barn at 2200 m/s. An approximate low end to the pressure can be set at 0.43 atm, where the neutron transmission through the target length is 1%.

The range of the protons and tritons in the fill gas is also important. The longer it takes the protons and tritons to range out the more likely it is that they will impact

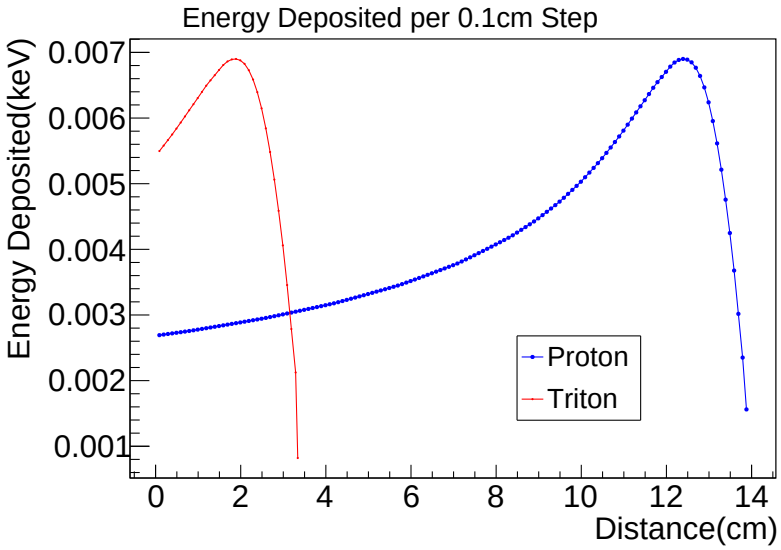

Figure 5.10: Calculated energy deposited per 0.1 cm step in 0.47 atm He. The same methods and ^{3}He data set were used for the this calculation as the beam monitor proton and triton range calculations in section 4.5.1.

a wall before depositing all of their energy giving a more variable signal per event. The ranges change linearly with the fill gas pressure. Fig. 5.10 shows the ranges at the 0.47 atm fill gas pressure. As the ranges increase in the gas, the changes in the ionization distribution due to the asymmetries will also increase, but so will the fraction of protons and tritons that impact the walls of the target chamber.

The optimal pressure was found using Monte Carlo simulations to examine how varying the gas pressure would alter the neutron capture locations and the energy deposition by the protons and tritons. Fig. 5.11 shows the results of the fill gas calculations done using Geant4 by Michael Gericke for the fill gas and different collimation widths. A minimum can be seen at approximately 0.1 atm. The error dilution, σ_D, is the increase in the asymmetry measurement uncertainty over counting statistics. Fig.

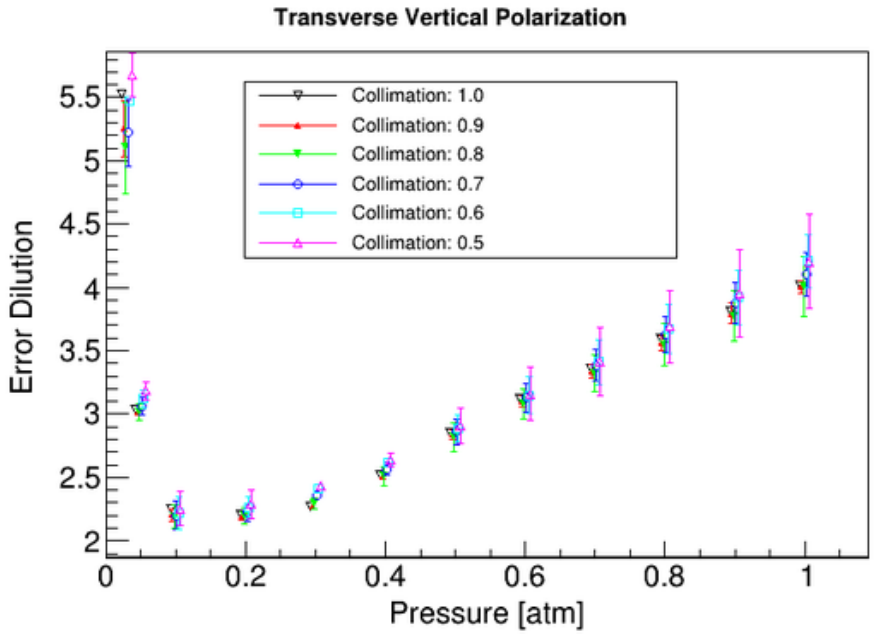

Figure 5.11: Changes to dilution factor with fill gas pressure and collimation changes as a fraction of 12 cm vertical beam height [69].

5.12 of a similar simulation done using mcstas and TRIM by Chris Coppola shows a minimum at approximately 0.4 atm. Based on these simulations and the HV requirements, a gas pressure of 0.47 atm was chosen to allow sufficiently high bias voltage for efficient charge collection, while attempting to minimize the error dilution.

5.4 Target Assembly

The target chamber was assembled in the lab space at the SNS. The frame stack was built up on the mount plate attached to one of the end windows. A scissor jack was used to lift the frame stack into the housing. A Kapton sheet was placed around the interior of the housing to prevent sparking from the HV to the housing during

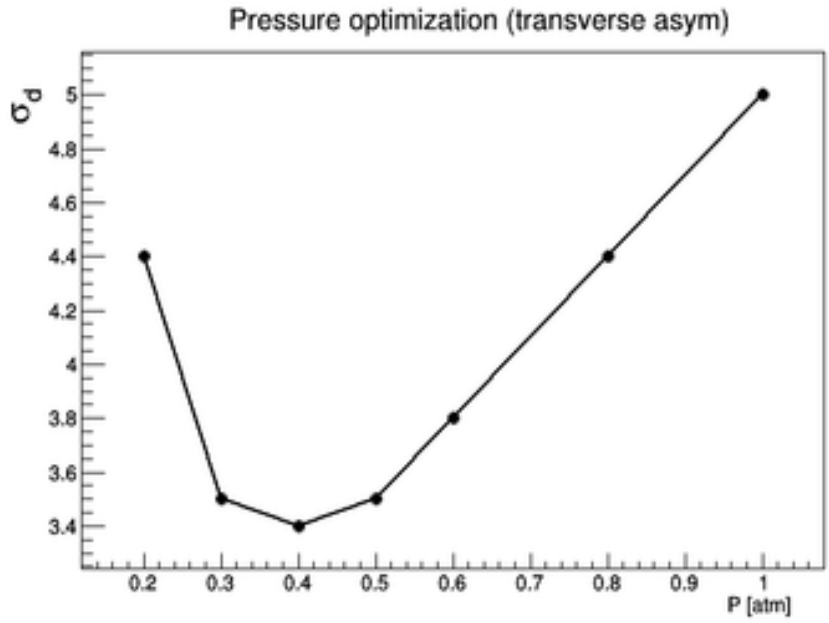

Figure 5.12: Changes to dilution factor with fill gas pressure [70].

operation, as shown in fig. D.15. Fig. 5.13 shows the frame stack inside the housing after assembly.

5.5 Bench Top Testing

The initial high voltage testing in room air was successful at 600 V applied to the HV. Further testing on the sealed chamber pumped down to vacuum allowed 2500 V to be reached. After filling with 1 atm ^{4}He gas, only $500 - 600$ V could be reached before sparking started. Using a clear plexiglass end flange on the target chamber, the sparking was found to be occurring in the HV feedthroughs. Inspecting the feedthrough, the sparking appeared to be occurring between the HV pin and the grounded body of the flange. A cylindrical Teflon shield was placed around the pin

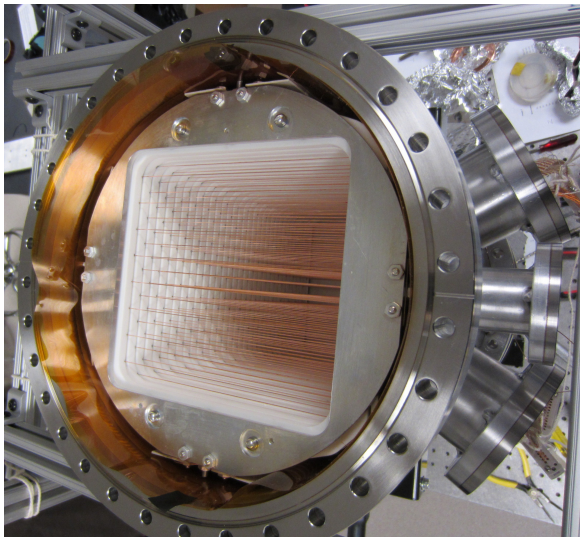

Figure 5.13: n3He frame stack inside the the housing.

to stop the sparking as shown in fig. 5.14.

As given in section 3.5, the breakdown voltage will vary with the gas pressure. Using the shielded HV feedthrough, the breakdown voltage in the target chamber at two ^{4}He fill gas pressures. At 0.88 atm pressure sparking occurred at 940 V, and at 0.41 atm sparking occurred at 800 V. From the beam monitor voltage scans in section 4.9.1 a bias voltage of -800 V should be sufficient to operate the target chamber.

5.6 Target Chamber Fiducialization

To reach the required alignment sensitivity, the frame stack was fiducialized by the Survey and Alignment Group at the SNS using a 3D coordinate measuring machine to measure the frame stack position relative to the mount flange and gluing four fiducial markers on the exterior of the flange. The location of the measurement points and fiducial markers are shown in fig. 5.15.

Figure 5.14: One of the HV feedthroughs being fit with the teflon shielding to block line of site between the pin and the grounded flange. The zip tie was used to help form the teflon and removed during installation.

Since the wires could not be measured directly by the coordinate measuring machine, the outside edge of each frame was measured to determine their angular alignment. The angular alignment of the frames to the first frame in the stack is shown in fig. 5.16. This measurement found an approximate 25 milliradian twist from the first frame to the last frame.

This twist will have a significant effect on the measured asymmetry by mixing the PV and PC asymmetries as given in eqn. 2.22. Since the statistics are highest in wire planes closest to the entrance windows, where most neutrons will capture, it is preferred to minimize the mixing at the front of the target chamber by aligning the first wire plane to the magnetic field. The twist and alignment to the magnetic field need to be taken into account in the geometry factor simulations.

The coordinate measurement machine must be able to reach at least three fiducial

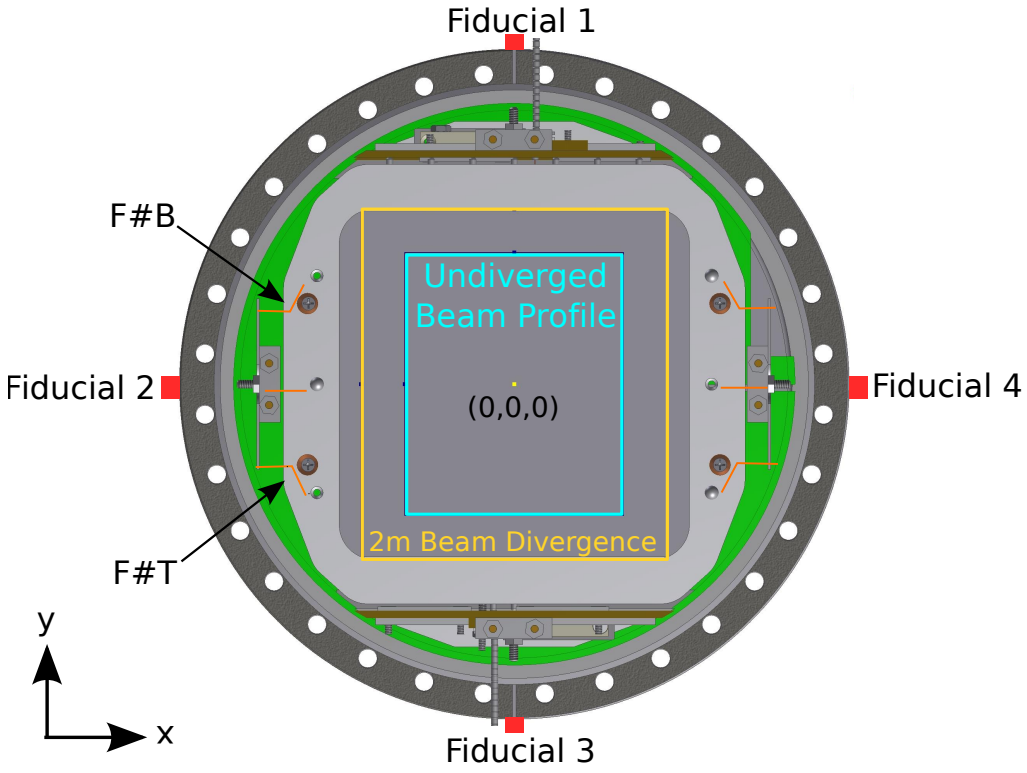

Figure 5.15: Fiducials 1-4 were placed on the outside of the mount flange at the indicated locations. The wires are not shown in this image but would be parallel to the y-axis. The wire frame twist was measured along the flat side of each frame at approximately the points marked by F#T and F#B.

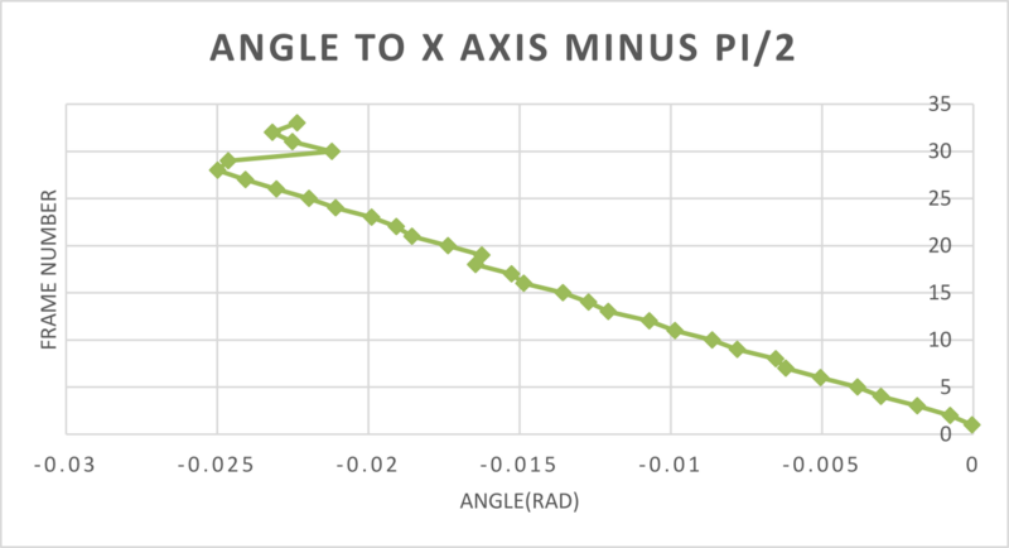

Figure 5.16: Measured angle of the wire frames to the first HV frame on the stack.

markers to determine the chamber orientation. To ensure at least three markers were always reachable by the coordinate measurement machine when the target chamber is installed in the beamline, additional fiducial markers were glued to the exterior of the housing and located relative to the initial four reference points before installation on the beamline.

A flat level block was glued to the top of the chamber aligned parallel to the first wire frame to serve as an external reference surface. This level block was used with a digital protractor to make an initial rough alignment with the beam after installation and angle operating mode changes before Survey and Alignment would be called in to make the final alignment using the coordinate measuring machine. Fig. 5.17 shows the level block location on top of the target chamber.

To make precise alignment of the target chamber possible, a four point adjustable stand was used. Fig. 2.31 shows the target chamber on its stand. Fig. 5.18 shows the

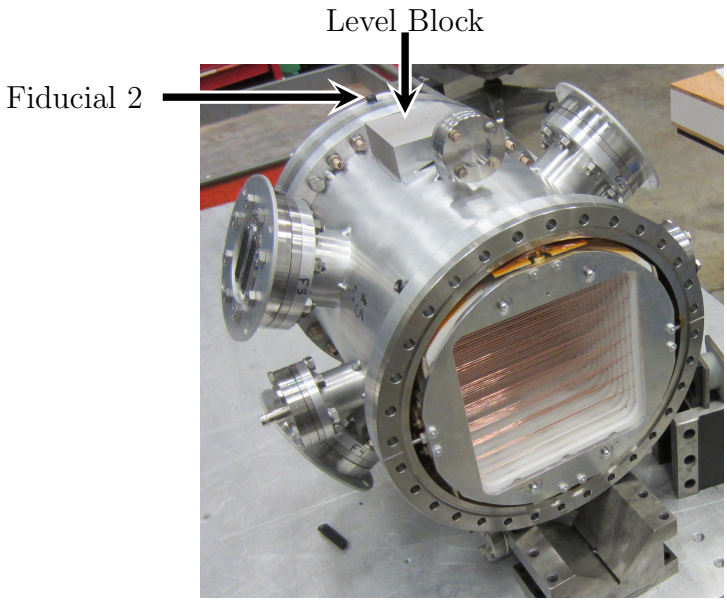

Figure 5.17: Target chamber with level block being placed during fiducialization. The level block was placed on the same side of the target chamber as Fiducial 2.

top of the target chamber stand inside the field coils. The mount rings on the outside of the target chamber make contact with the stand. On one of the mount rings that were bolted to each end of the target chamber, there are four cones machined at 90-degree intervals used to set the initial rotation position to one of the ceramic balls as shown in fig. 5.19b.

By adjusting the height of all four screws simultaneously, the height of the target chamber can be changed. Angle adjustments can be made by moving pairs of screws as shown in fig. 5.20. Adjusting the height of the front or back pair can change the pitch of the target chamber, and adjusting left or right-hand pairs can change the roll of the target chamber. The stand sits on a flat table and can be translated to change the chamber position in the $\hat{x}$ and $\hat{z}$ directions. The yaw of the chamber can also be changed by rotating the stand on the table surface.

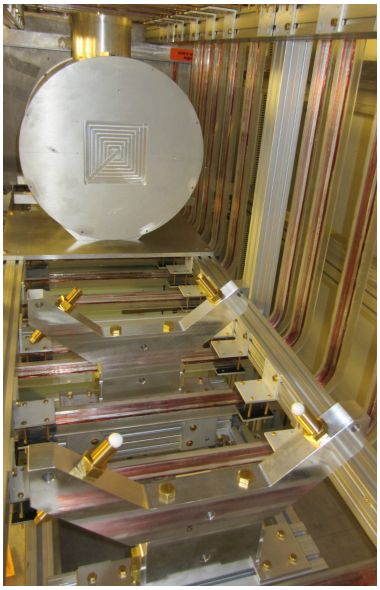

Figure 5.18: Target chamber adjustable stand inside the field coils. The brass screws are topped with sockets that will hold the ceramic balls that electrically isolate the stand from the target chamber.

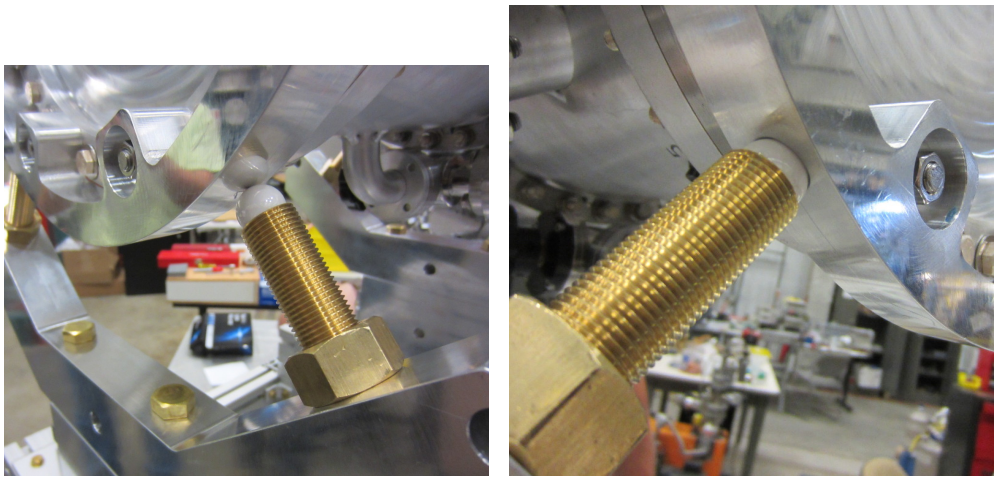

(a) Ball on Surface (b) Ball in Cone

Figure 5.19: The target chamber has four points of contact with the stand and rests on the ceramics beads on top of each brass screw.

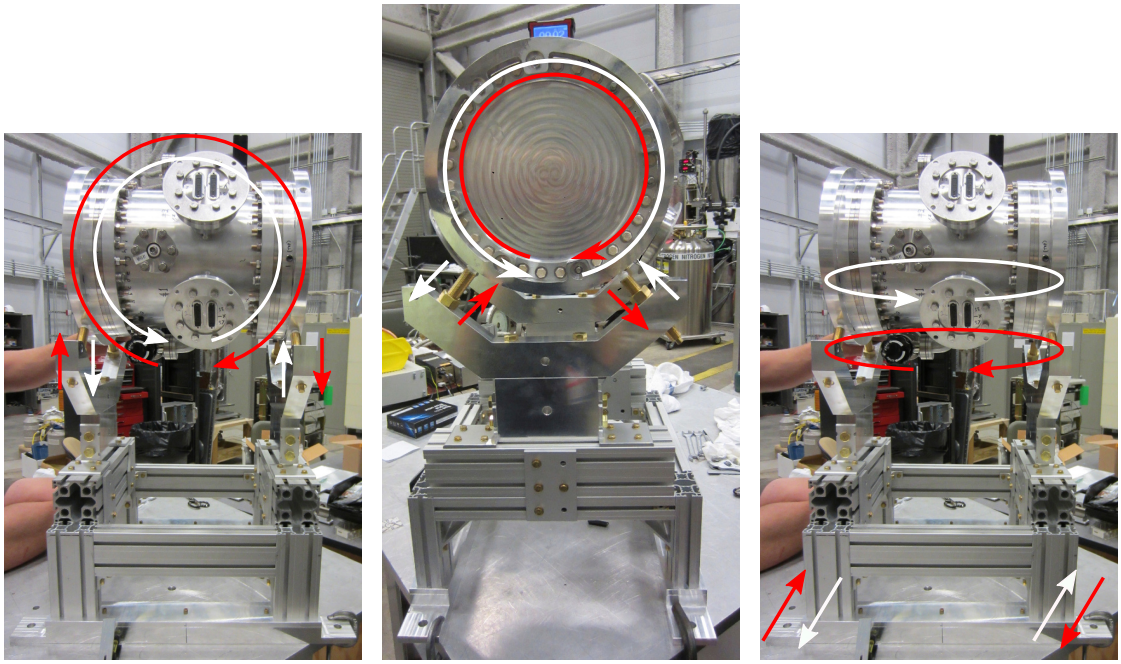

(a) Pitch (b) Roll (c) Yaw

Figure 5.20: Target chamber angle adjustments.

5.7 Voltage Scan

As discussed in section 3.2 depending on the applied bias voltage, an ionization chamber can collect some, all, or a multiple of the initial ionization that occurs in the chamber. To determine the range the n3He target chamber was operating in, two voltage scans were done with the target chamber a few weeks apart near the end of running. One scan covered a short range near the operating voltage; the second covered an extended range and is the subject of most of the following analysis.

The target chamber power supply is a Spellman Bertan, PMT-30C-3N and it was scanned in a range from 0 to -552 V with 18 different voltages being examined during the scans. The M1 monitor was used as a reference to account for any neutron beam

intensity changes during the voltage scan.

5.7.1 Calculation Method

To compare the voltage scans, the average of the integrated pulse value for each wire and the beam monitor was used. For wire x the integral $x_{j,i}$ is formed for pulse i in run j from the measured signal as

$$x_{j,i} = \frac{1}{60 \times N} \sum_{k=1}^{N} s_{j,i}(k), \tag{5.1}$$

where N is the number of time bins per pulse, 49 for the target chamber wires and 1624 for the beam monitor, $1/(60 \times N)$ is the bin width in seconds for N time bins per 60 Hz pulse, k is the time bin index, and $s_{j,i}(k)$ is the recorded signal in time bin k. The run average $\langle x_j \rangle$ of the pulse integrals is then calculated for all M pulses in the run j that pass the stability cut discussed below using

$$\langle x_j \rangle = \frac{1}{M} \sum_{i=1}^{M} x_{j,i}. \tag{5.2}$$

The standard deviation $\sigma(x_j)$is calculated at the same time as the average using

$$\sigma(x_j) = \sqrt{\langle x_j^2 \rangle - \langle x_j \rangle^2}, \tag{5.3}$$

with the standard error,

$$SE(x_j) = \frac{\sigma(x_j)}{\sqrt{M}} \tag{5.4}$$

being taken as the uncertainty in the run average. The beam monitor run average is designated $\langle m_j \rangle$ for run number j.

2000 neutron pulses were taken for each run. A beam stability cut was made to exclude pulses from the run average that were low or dropped by examining time

bin 600 near the neutron pulse peak in the M1 monitor. A pulse integral would be excluded from the run average if the value of time bin 600 was less than 90% of the average of that time bin for the run.

To determine the pedestal in each signal, a constant offset in the measured signals, a run with the beam off and the HV on (designated run 0) was also averaged using the above procedure to determine the pedestal for each wire, $\langle x_0 \rangle$, and the beam monitor, $\langle m_0 \rangle$. The pedestal was then subtracted before dividing the wire run average by the beam monitor run average to form the ratio

$$R_{x_i} = \frac{\langle x_i \rangle - \langle x_0 \rangle}{\langle m_i \rangle - \langle m_0 \rangle}. \tag{5.5}$$

Error propagation was done in two steps using the following formula. The error in the pedestal subtracted signal for all signals was calculated from

$$\sigma\left(\langle A_i \rangle - \langle B_0 \rangle\right) = \sqrt{SE(A_j)^2 + SE(B_0)^2}, \tag{5.6}$$

where A_i and B_i are the signal and pedestal respectively for the chamber wire or monitor. The error in the ratio of the chamber signal to monitor signal for each wire was then calculated using

$$\sigma(R_{x_i}) = R_{x_i}\sqrt{\left(\frac{\sigma(\langle x_i \rangle - \langle x_0 \rangle)}{\langle x_i \rangle - \langle x_0 \rangle}\right)^2 + \left(\frac{\sigma(\langle m_i \rangle - \langle m_0 \rangle)}{\langle m_i \rangle - \langle m_0 \rangle}\right)^2}. \tag{5.7}$$

5.7.2 Voltage Scan Results

The ratio discussed in the preceding section was then plotted against the absolute value of the bias voltage measured for that run. The absolute value was used to simplify the plots. Fig. 5.21 shows a fairly typical wire result. There is a recombination region from 0 V to approximately −200 V followed by the ion chamber region

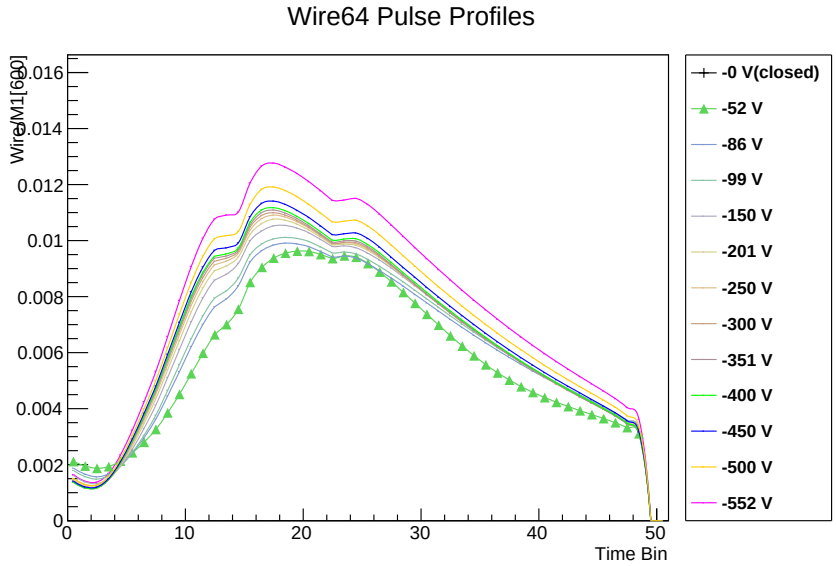

(a) Wire 64 pulse profiles for each run overlayed in one plot.

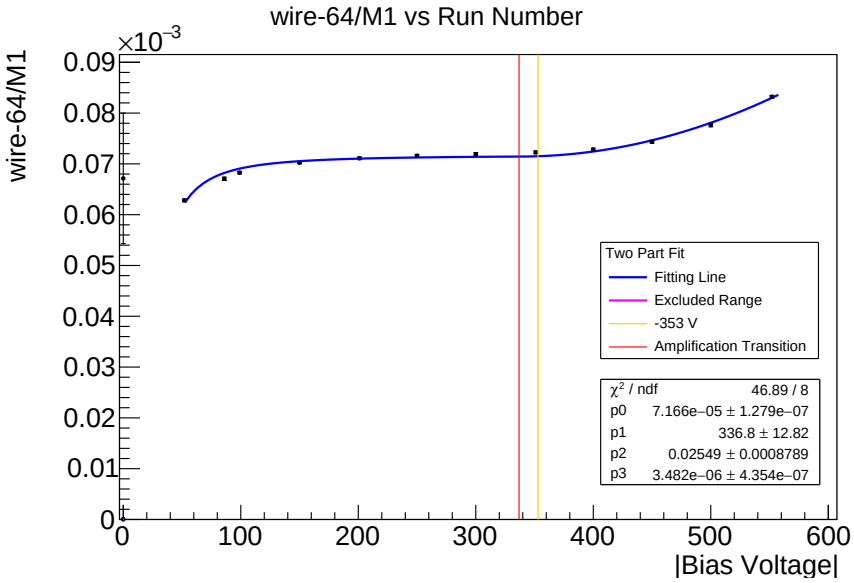

(b) Wire 64 integrated signal divided by M1 integrated signal plotted vs. applied bias voltage.

Figure 5.21: Wire 64 Voltage Scan

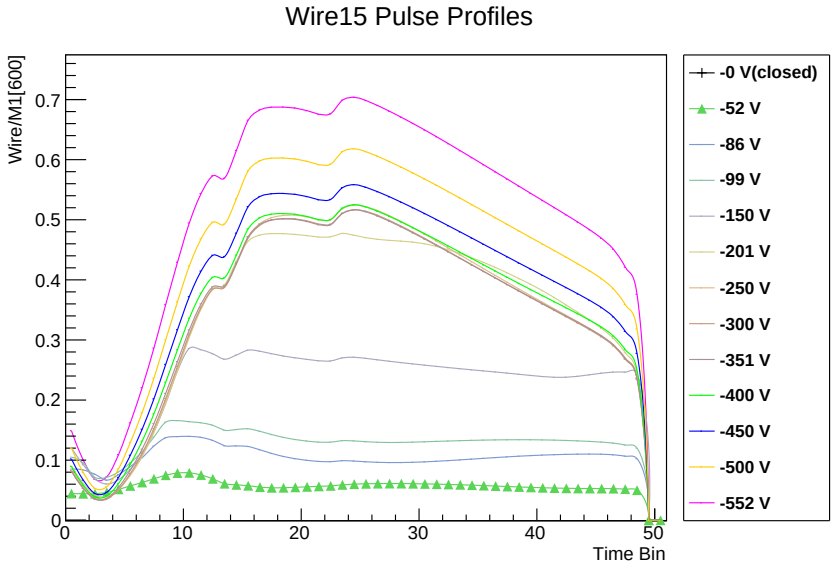

(a) Wire 15 pulse profiles for each run overlayed in one plot.

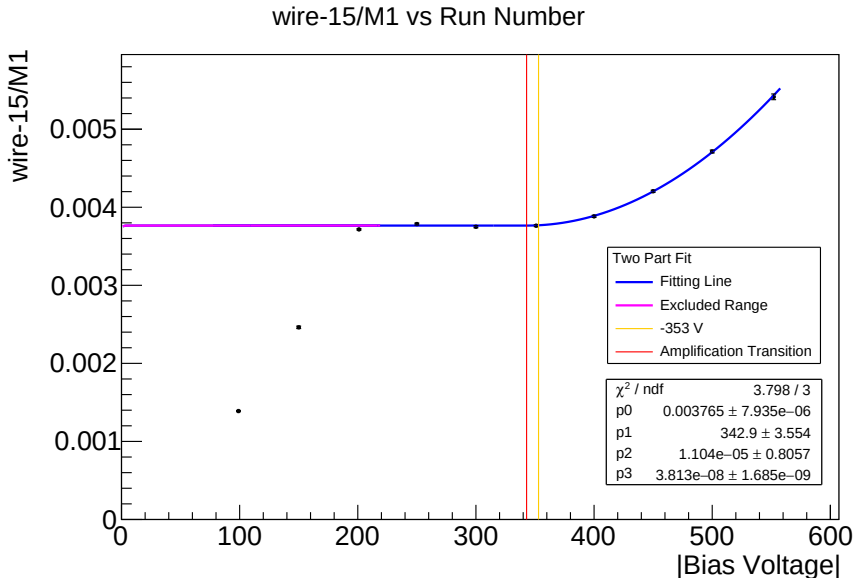

(b) Wire 15 integrated signal divided by M1 integrated signal plotted vs. applied bias voltage.

Figure 5.22: Wire 15 Voltage Scan

up to approximately $-340\,\mathrm{V}$, with the onset of amplification and the beginning of proportional counting region beyond that.

To fit the data, a modified version of the simple ion chamber charge collection eqn. 3.23 was used with an added quadratic amplification term,

$$f(V_b) = \begin{cases} I - \frac{C}{V_b^2} & \text{if } V_b < V_{trans} \\ I - \frac{C}{V_{trans}^2} + I \times A \times (V_b - V_{trans})^2 & \text{if } V_b > V_{trans} \end{cases}, \tag{5.8}$$

where I is the initial ionization, C is the recombination factor, V_b is the applied bias voltage, V_{trans} is the transition voltage recombination to amplification.

For an unknown reason, at low voltages some of the wires show anomalously high signals on some of the $-52\,\mathrm{V}$ to $-200\,\mathrm{V}$ data points. Fig. 5.22 shows an example this behavior. From the charge collection model, there is no physical reason that a lower bias voltage could create a higher collected current than a higher bias voltage. A probable cause of these variations is a resonance between the wires and the power supply at the lower voltage setting, but a confirmation of that hypothesis was not pursued.

To deal with these anomalous points, excluded voltage regions were designated for the wires as determined from visual inspection. If the value of a point at a lower bias voltage was higher than at a higher bias voltage, that point was excluded. These excluded voltage ranges are shown in magenta on the fit line when it was used. If too much of the low range was excluded then instead of fitting eqn. 5.8, the following equation that did not include an recombination term was used:

$$f(V_b) = \begin{cases} I & \text{if } V_b < V_{trans} \\ I + I \times A \times (V_b - V_{trans})^2 & \text{if } V_b > V_{trans} \end{cases}. \tag{5.9}$$

This was done because when the low voltage region was unconstrained, then the uncertainties on the fit parameters would become large. This fitting equation was also used for some of the wires in the back planes of the detector that did not have a visible recombination region.

Not all anomalous points were as high as shown in fig. 5.22. In cases where the chi squared for the fit was over 150, another point in the low voltage region could be excluded by removing the point further from the fit line. Fig. 5.23 shows an example of this, where after initially excluding the 180 to 220 V range, the exclusion was expanded to the 120 to 220 V range.

As the target chamber was operated at −353 V during data taking and two voltage scans performed a few weeks apart showed stable behavior in the −200 to −350 V range, it is not believed that these deviations had any effect on the target chamber operation.

The outer wires in rows a and i, as shown in fig. 2.32, have a different high voltage operation than the inner wires, in rows b-h, transitioning almost directly from recombination to amplification. The outer wires are in half sized cells that only have two HV wires to one side and the edge of the wire frames to the other side. The reduced number of field wires creates a different field configuration around these wires than the inner wires with four HV wires, which will affect how charge collection occurs.

From the voltage scan, we can conclude that the target chamber was operating mostly in the linear amplification region. Fig. 5.24 shows the ionization to linear amplification transition voltage from the fits to the data. As can be seen, the transition

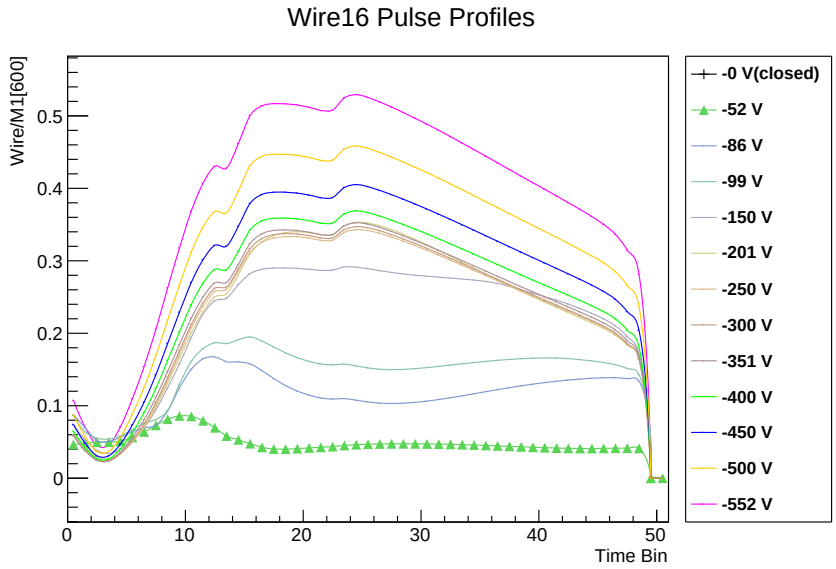

(a) Wire 16 pulse profiles for each run overlayed in one plot. Points below −240 V show anomalous peak shapes and heights.

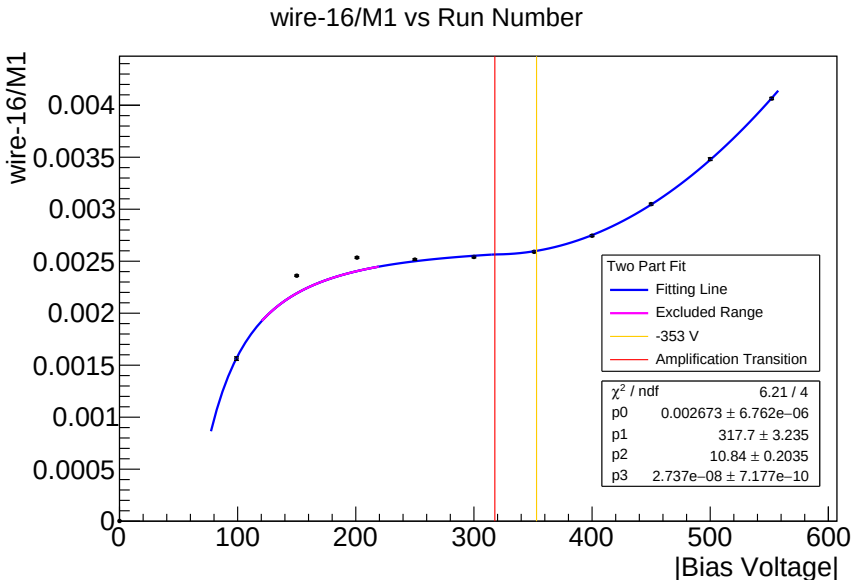

(b) Wire 16 integrated signal divided by M1 integrated signal plotted vs. applied bias voltage.

Figure 5.23: Wire 16 Voltage Scan

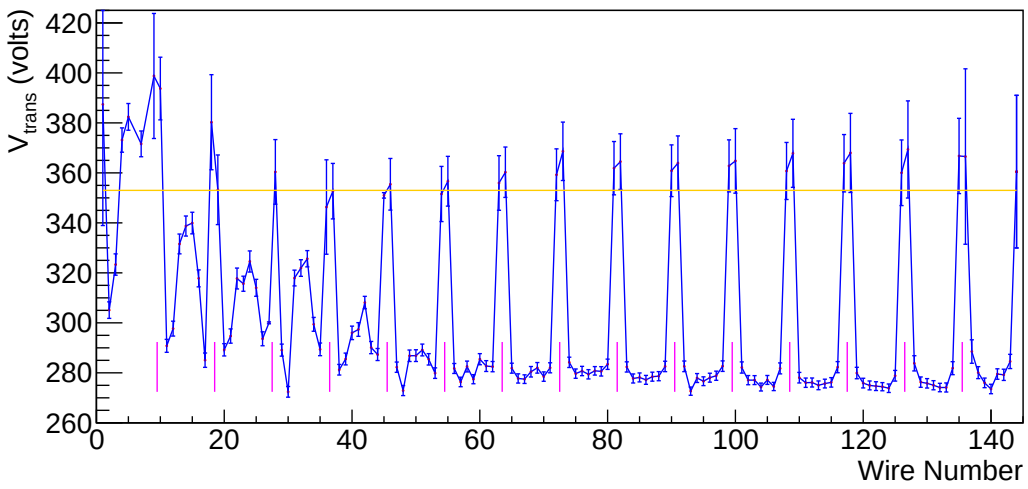

Figure 5.24: Transition voltage from ionization region to amplification region for each wire based on the voltage scan curve fitting. The purple lines indicate the transitions between wire planes.

voltage for most wires is below the operating voltage of −353 V. While the ionization chamber region is preferred as it is less sensitive to power supply voltage variations, operating at the low end of the amplification should still be usable. Appendix E has more curve fitting results.

5.8 Target Linearity

It is important that the target chamber output signal is linear with respect to the neutron flux. As the ionization density increases in an ionization chamber, the required voltage to prevent recombination also increases and the amplification factor can also decrease.

During previous testing, as discussed in section 4.9.2, the beam monitors were

found to be linear over a wide range of neutron fluxes. The M1 monitor was used as a reference to compare the chamber to. A number of runs were selected over the n3He experimental run time that would cover the full range of the proton beam power seen on target during data taking from 850 kW to 1400 kW.

To determine the linearity of the target response, the same pulse integral run average calculation method as was used for the voltage scan in the previous section was used for the new set of runs, but these values were divided by the error weighted average of all runs being plotted. The error weighted average and its error were calculated using the following formula:

$$\langle x \rangle_{avg} = \frac{\sum \langle x_j \rangle / SE(x_j^2)}{\sum 1/SE(x_j^2)}, \tag{5.10}$$

$$\sigma(\langle x \rangle_{avg}) = \left(\frac{1}{\sum 1/SE(x_j^2)} \right)^{1/2}. \tag{5.11}$$

The beam monitor signal was also divided by its average over the runs, $\langle m \rangle_{avg}$, with the associated uncertainty $\sigma(\langle m \rangle_{avg})$ calculated using the same method as was used for the wires. This made both values unitless for the linearity calculation to follow. Plotting $(\langle x_j \rangle / \langle x \rangle_{avg}) / (\langle m_j \rangle / \langle m \rangle_{avg})$ vs. $(\langle m_j \rangle / \langle m \rangle_{avg})$ should give a horizontal line if the target chamber is linear. If the target chamber is non-linear, the target chamber is more likely to loose efficiency at higher neutron fluxes so a negative slope is expected. The reason for this is that as the ionization rate increases the space charge density in the gas volume also increases. Particularly the positive ions, due to their long collection times, can build up near the collecting electrodes. This can result in charges in the target chamber being shielded from the HV reducing the effective field, increasing collection times, and allowing for more recombination.

The non-linearity of each wire is then the slope of the fitted line divided by the

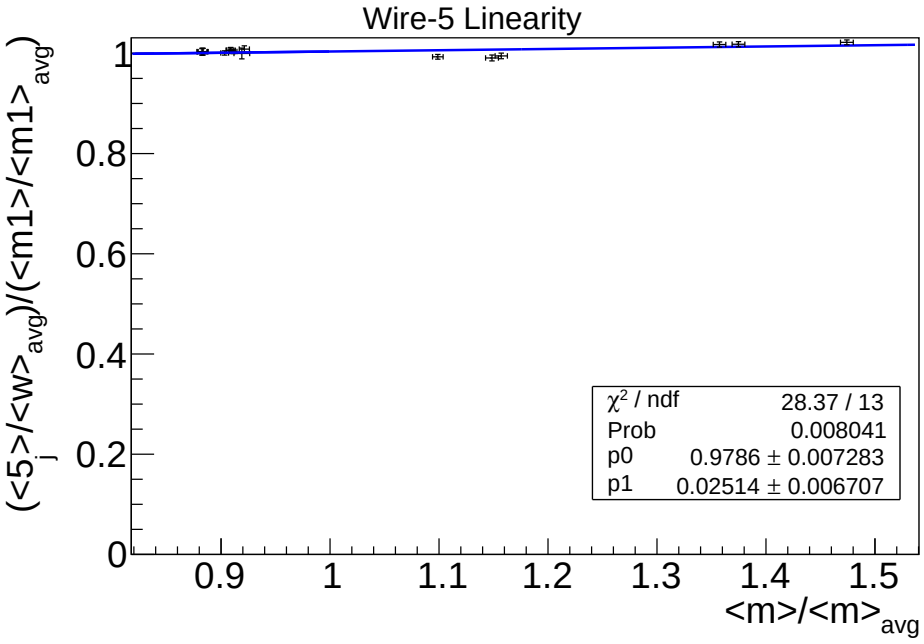

Figure 5.25: Linearity plot for wire 5.

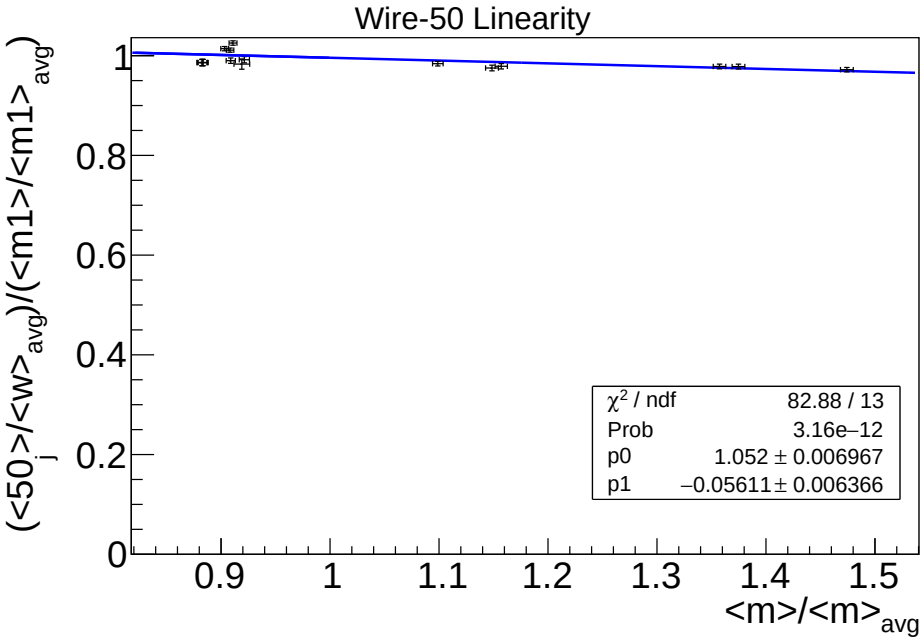

Figure 5.26: Linearity plot for wire 50.

intercept. As seen in fig. 5.27 the wire linearities are in the 4 to −6% range. From this it can be concluded that the target chamber was operating sufficiently linearly that the effects on the uncertainty of the asymmetry measurements will be less than the goal statistical uncertainty. See appendix F for plots of the fit values and other wire data plots.

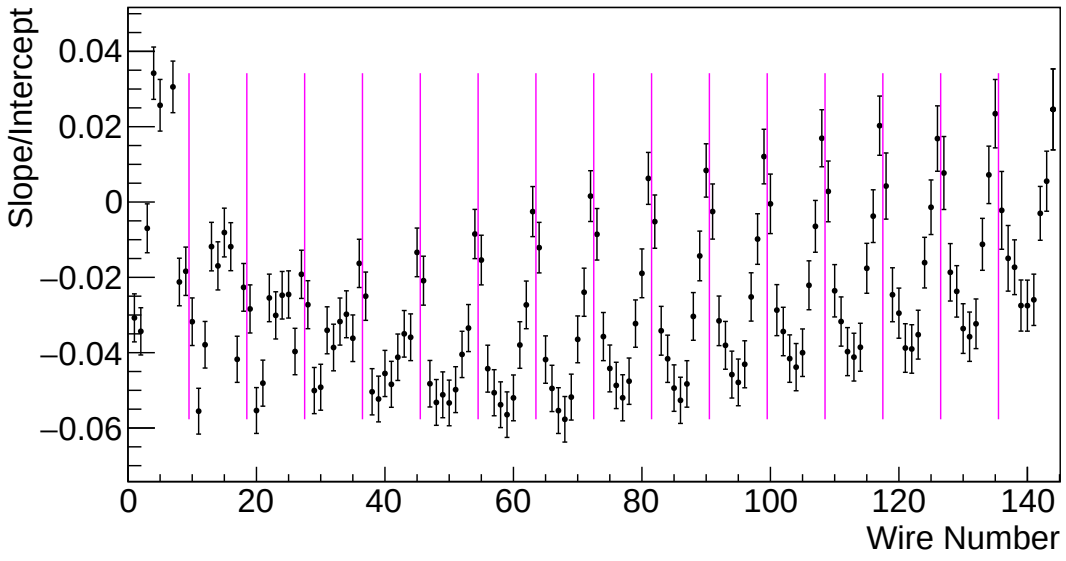

Figure 5.27: Slope over intercept from target chamber linearity curve fitting.

5.9 Garfield++ Simulations

After ionization occurs in the target chamber, it takes time for the charge to be collected. To calculate the charge collection times in the target chamber geometry, Garfield++ was used. It is an object-oriented toolkit for the detailed simulation of particle detectors which use a gas mixture or a semiconductor material as sensitive medium [71]. Garfield++ uses the Shockley-Ramo theorem to calculate the current

induced on an electrode by the motion of a charge.

For the n3He target chamber, the charge collection times were examined for both ions and electrons starting in different positions within the cells. The current induced on a signal wire was examined both for charges starting within a cell defined by the HV wires and for cross talk between the cells.

5.9.1 Field Map Calculation

It was decided to use a 3D dimensional target model for the simulation to examine the effect of being near the end of the wires. While Garfield++ can be used to calculate fields for some 2D geometries containing only wires, cylinders, and flat planes, a 3D field map requires the use of third-party programs.

Gmsh was used to create the 3D geometry for the simulation. Gmsh is a free 3D finite element grid generator [72][73]. It works by first specifying the points for an object that are then used to create directed lines or arcs between the points which are joined to make surfaces. Multiple surfaces can be joined or a single surface extruded to create 3D shapes. It can then generate a finite element tetrahedral mesh from the geometry.

The mesh is then processed using Elmer [74], an open source multiphysics simulation engine maintained by CSC IT Center for Science, which calculates the electric and magnetic fields for the mesh geometry using a set of boundary conditions set on the mesh surfaces and permittivities of the volumes as defined in the Elmer input file.

Detailed instructions and examples for how to setup this kind of simulation are in the open source finite element analysis section of the Garfield++ website [75].

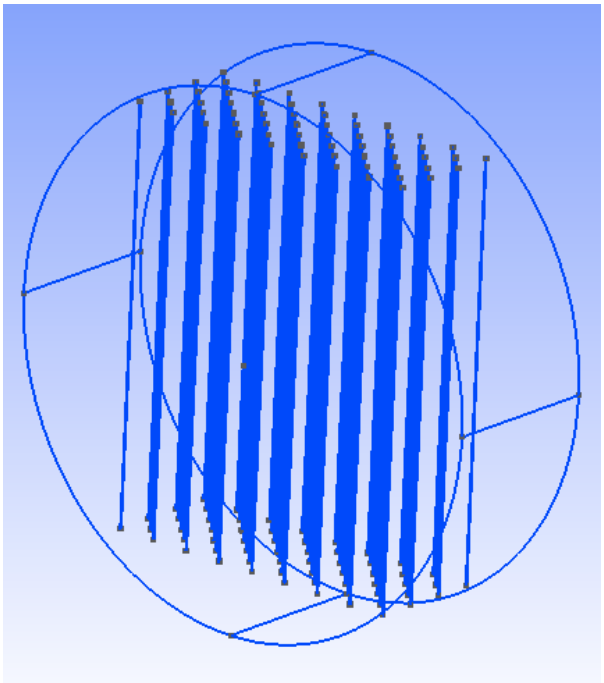

Figure 5.28: Reduced geometry model of n3He target chamber.

5.9.2 Simulation Details

A reduced geometry and length model is used to reduce processing time and memory requirements. Features such as the wire frames and PCBs are omitted while the housing interior, HV, and signal wires are included. The total number of wire frames is also reduced. These changes should not affect the accuracy of the simulation. The chamber housing is modeled as a simple cylinder of zero thickness as the presence of the feedthroughs should have minimal effect on the fields in between the wires. The wire frame model of the chamber is shown in fig. 5.28. The finite element mesh composed of tetrahedra generated from the wire frame is shown in fig. 5.29.

For the field boundary conditions, the housing cylinder was grounded at 0 V as were the signal wires. The HV wire surfaces were at −350 V, close to the measured

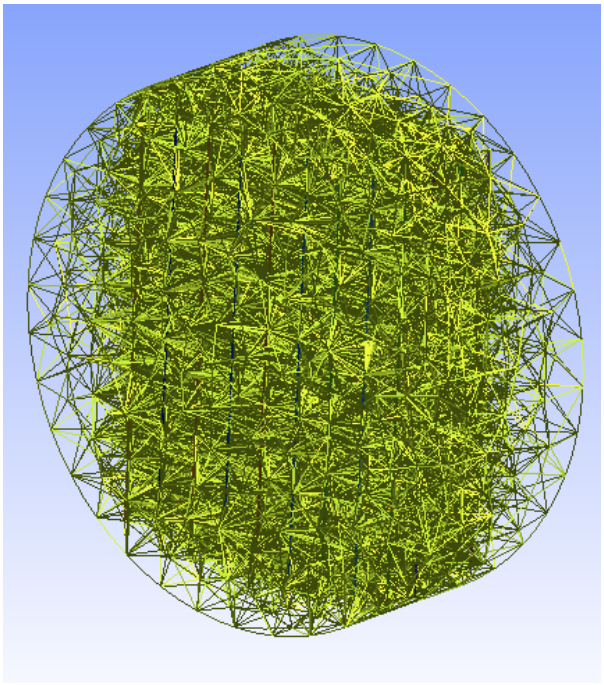

Figure 5.29: Finite element mesh generated from the specified geometry.

−353 V bias voltage used during data taking. A 2D slice of the field map through the center of the target chamber is shown in fig. 5.30.

In Garfield++ gas properties are calculated using Magboltz, a program for the calculation of electron transport properties in gas mixtures using semi-classical Monte Carlo simulation, for the electron transport properties of the fill gas. Ion mobilities are loaded from a user provided text file. Information for the ^{3}He ion mobilities was taken from reference [76].

5.9.3 Collection Times

To examine the charge collection times and the total induced signal from both ionization within a cell and from adjacent cells in the target chamber, an ion and

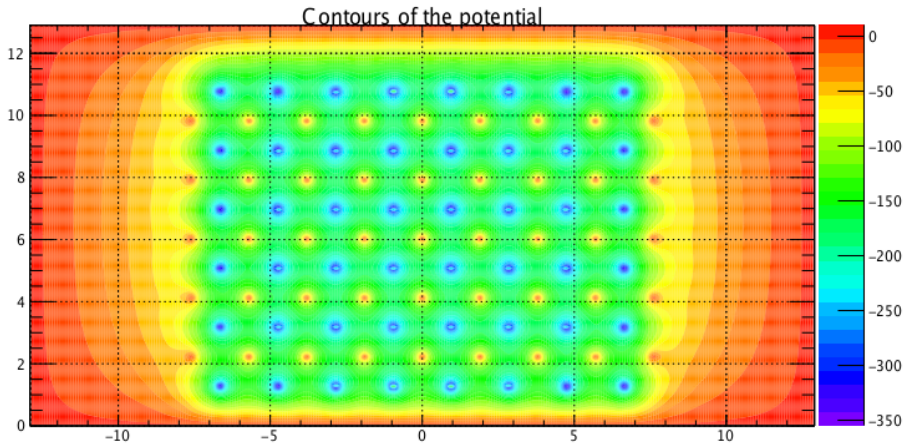

Figure 5.30: Electric field for cross section through central axis of cylinder with the wires perpendicular to the page.

electron pair were drifted from 30 points located in a diagonal line across the target chamber and 30 points in a straight line across the chamber. Fig. 5.31 shows the layout of points. For the diagonal, there are six evenly spaced points in each half cell. In both cases the induced signal is calculated for the wire at the lowest right of the line marked with the black circle. This will allow a representative value for the signal induced on that one wire for charge collection both inside and outside the cell to be calculated.

Fig. 5.32 and fig.. 5.33 show how the collection times of the ions and electrons change with the position in the cell along the diagonal. The red and blue lines in the plots indicate the position of the HV and signal wires along the diagonal. Since ions collect towards HV wires, they have the shortest collection time when starting near an HV wire, and similarly electrons have the shortest collection time when starting near a signal wire.

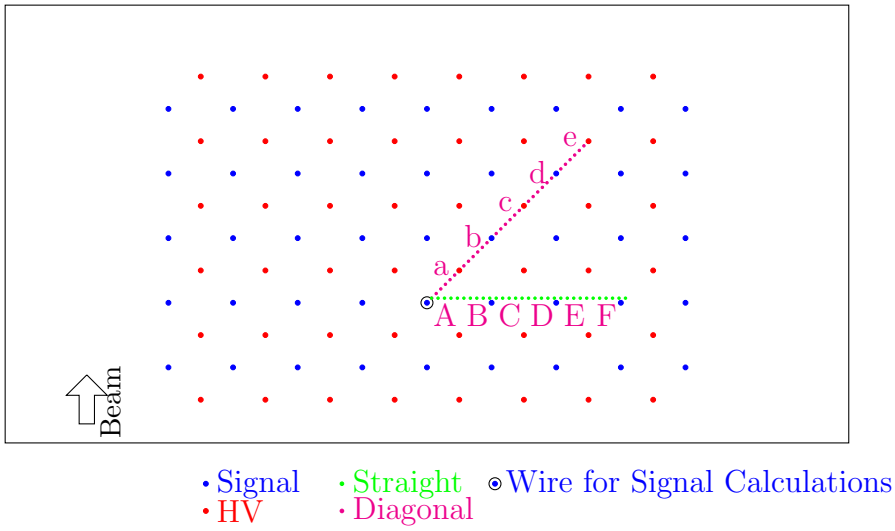

Figure 5.31: Location of ion-electron pair origins for simulations. All signals in the simulation were calculated relative to the signal wire marked with the black circle. Each half cell that the simulation lines pass through is identified with an alphabetical label.

For the n3He experiment, the width of a target chamber time bin is 0.32 ms = 0.32×10^6 ns. All of the electron collection times are significantly shorter than the bin width. The longest ion collection times are on order 1.05×10^6 ns. Due to this, some of the longest ion collection times will occur over multiple time bins in the DAQ, but there is no significant space charge build up between pulses as the collection times are small compared to the total pulse length.

Fig. 5.34 and fig. 5.35 show the average integrated induced signal on the signal wire from the 100 events. The further the ion or electron traveled before collection on a wire, the larger the integrated signal. Summing the ion and electron signals yields a consistent signal for ion and electron pairs for each quarter cell independent of where the pair started in the cell. This confirms that the signal induced by charge

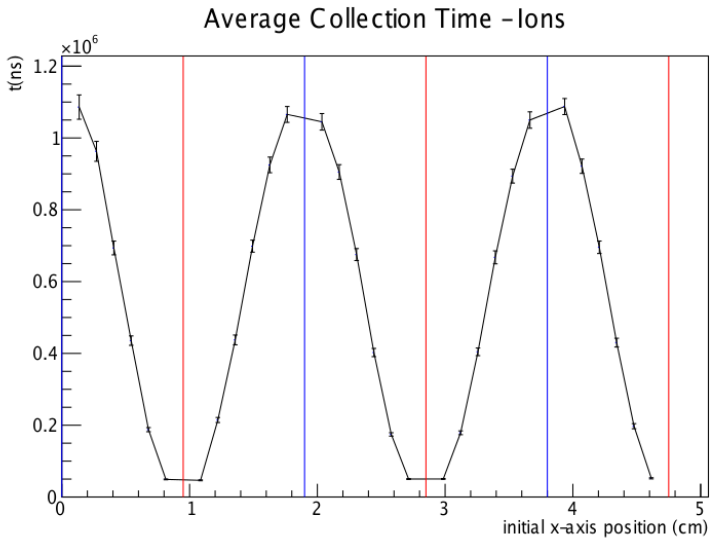

Figure 5.32: Diagonal line average ion collection times. Error bars are standard deviation. The red lines show where the diagonal line crossed the HV wires, and the blue lines the signal wires.

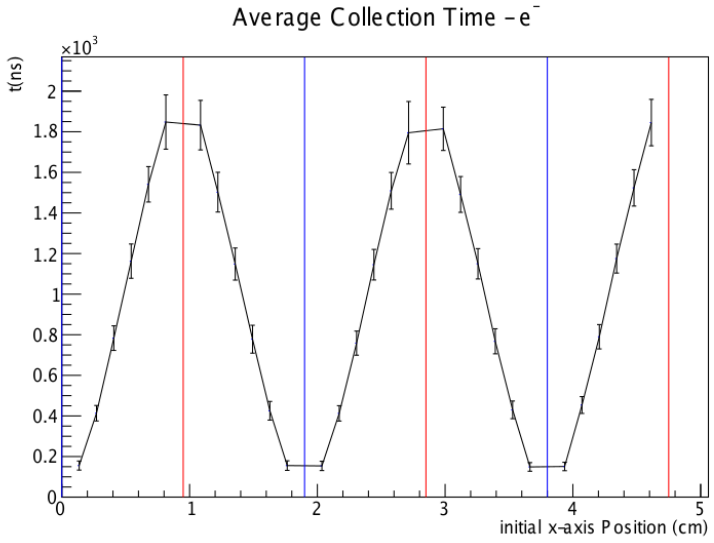

Figure 5.33: Diagonal line average electron collection times. Error bars are standard deviation. The red lines show where the diagonal line crossed the HV wires, and the blue lines the signal wires.

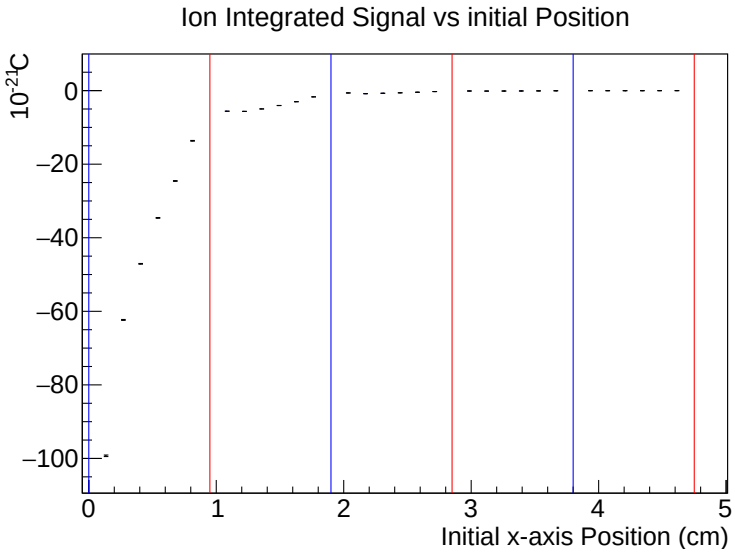

Figure 5.34: Diagonal line average integrated ion signal. Error bars are standard deviation. The red lines show where the diagonal line crossed the HV wires, and the blue lines the signal wires.

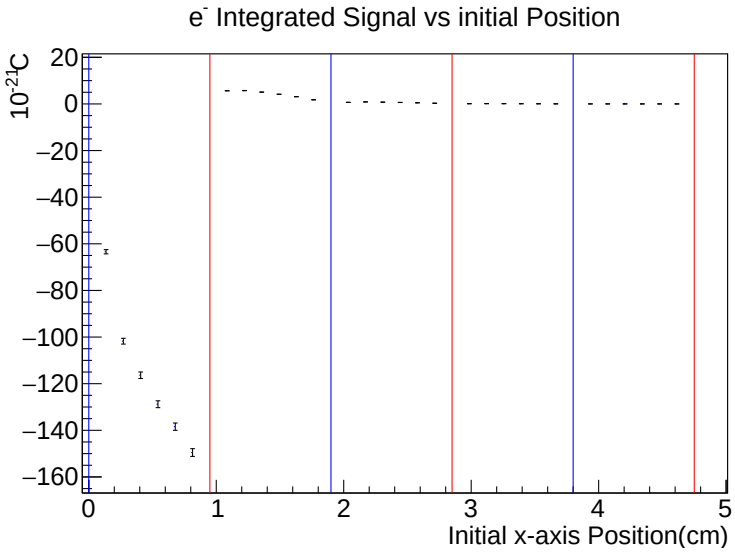

Figure 5.35: Diagonal line average integrated electron signal. Error bars are standard deviation. The red lines show where the diagonal line crossed the HV wires, and the blue lines the signal wires.

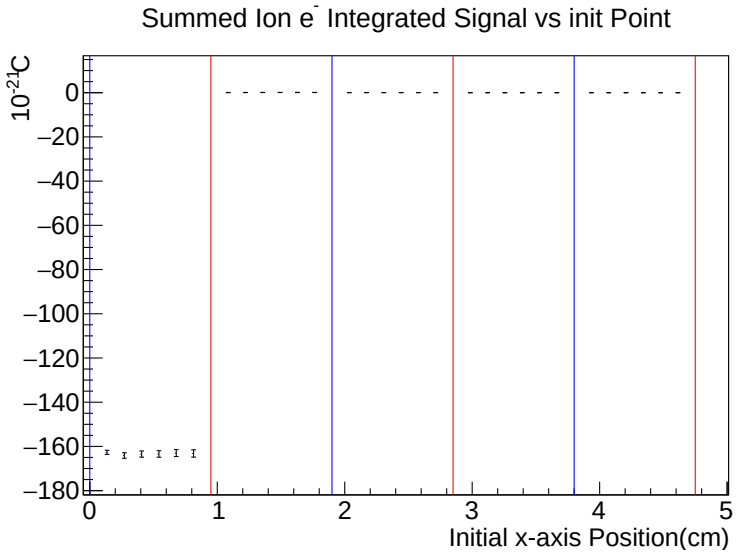

Figure 5.36: Diagonal line sum of average electron and ion signals. The red lines show where the diagonal line crossed the HV wires, and the blue lines the signal wires.

collection after ionization is independent of the location of the initial ion-electron pair formation. The in cell group has a average signal of $(-163 \pm 0.5) \times 10^{-21}$ C. The charge of an electron is $e = -160.2 \times 10^{-21}$ C. The simulated charge collection values are close to the expect charge collection for two particles of charge $\pm e$.

Charge collection was also examined for a straight line across multiple cells. The electrons behaved similarly to how they behaved for the diagonal line case. The ion collection times and signals show the greatest change The average integrated charge from the five points inside the cell with the signal wire is $(-161 \pm 1) \times 10^{-21}$ C. Table 5.1 summarizes the results of the two simulations.

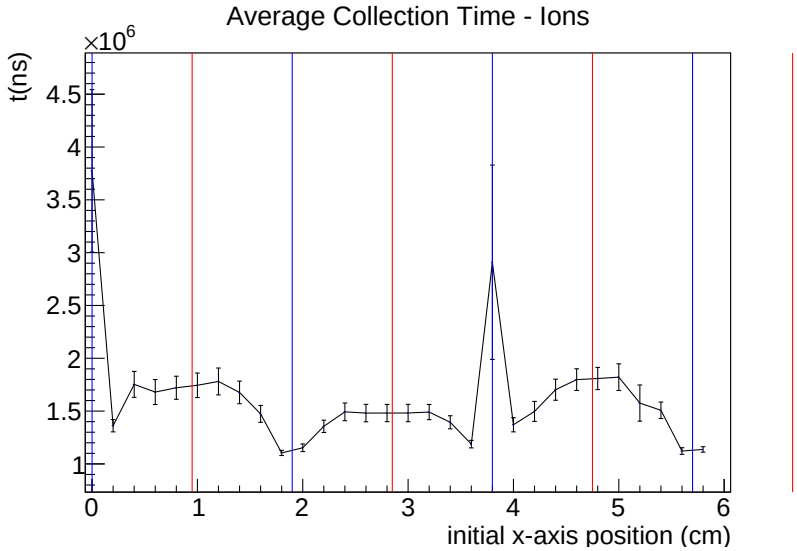

Figure 5.37: Straight line average ion collection times. Error bars are standard deviation. The reason for the large collection times at the 0 cm and 3.8 cm locations has not been investigated at this time.

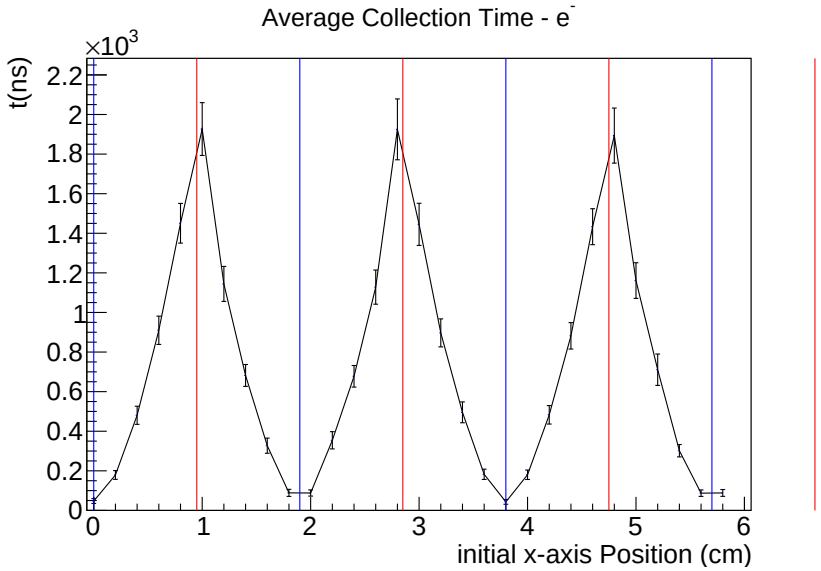

Figure 5.38: Straight line average electron collection times. Error bars are standard deviation. The blue lines show where the signal wires were crossed, and the location along the x-axis of the HV wires.

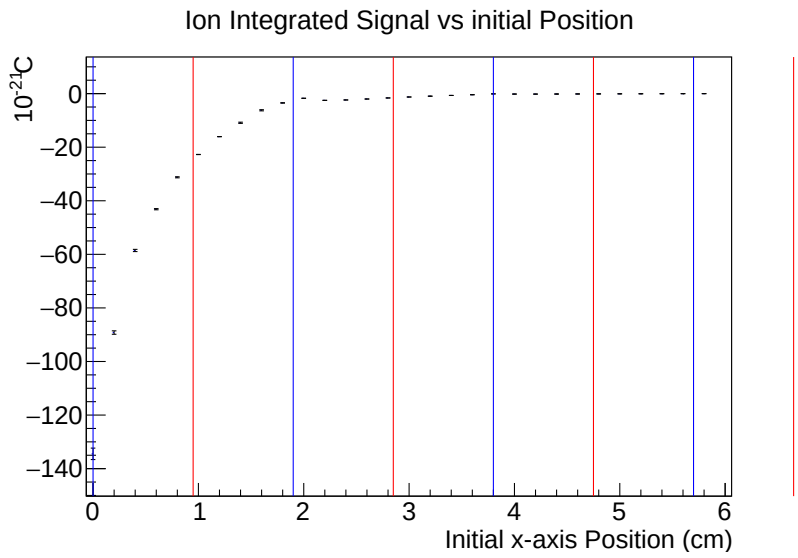

Figure 5.39: Straight line average integrated ion signal. Error bars are standard deviation. The blue lines show where the signal wires were crossed, and the location along the x-axis of the HV wires.

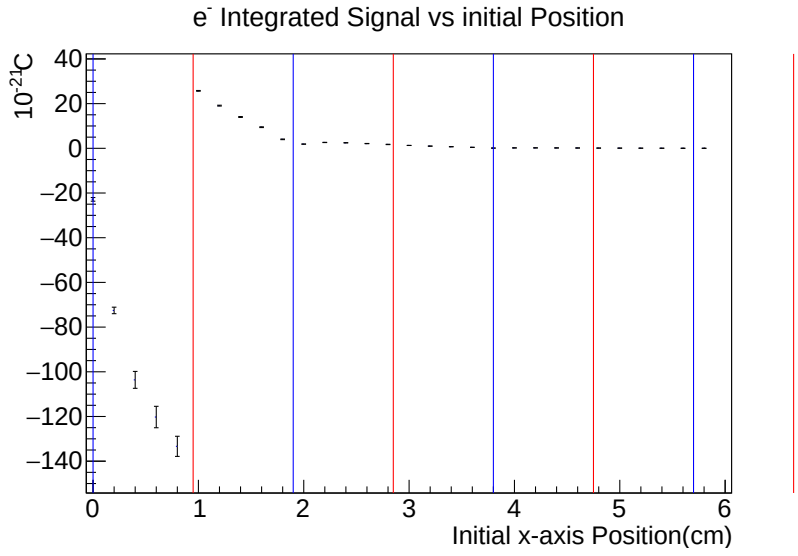

Figure 5.40: Straight line average integrated electron signal. Error bars are standard deviation. The blue lines show where the signal wires were crossed, and the location along the x-axis of the HV wires.

Diagonal	1/2 Cell Avg. of Int. Signal	Uncertainty.	fraction of in cell
a	-162.2	0.5	
b	0.09	0.02	1847
c	0.042	0.007	3904
d	0.0022	0.0004	73929
e	0.0010	0.0005	157394
Str. Line			
A	-161	1	
B	2.28	0.09	70
C	0.128	0.018	1257
D	0.010	0.004	15688
E	0.019	0.002	8448
F	0.0028	0.0003	56746

Table 5.1: Summary of charge collections times and average induced total signals.

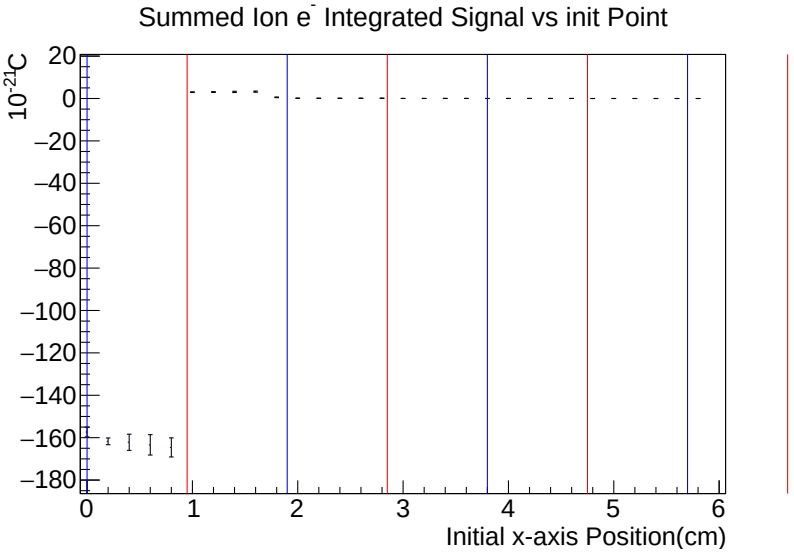

Figure 5.41: Straight line sum of average electron and ion signals. The blue lines show where the signal wires were crossed, and the location along the x-axis of the HV wires.

Chapter 6

Summary

The study of the strong interaction at low energies has been both experimentally and theoretically difficult. The strong interaction is responsible for binding quarks in nucleons, as well as nucleons in nuclei, but currently there exists no consistent description of how this occurs. Due to the difficulty in making low-energy calculations with QCD, a number of different approximation models are used to describe the different interactions. The models created for this purpose, such as the DDH meson exchange model and the EFT models, require experimental input.

The NPDGamma and n3He measure parity-violating observables in few nucleon systems. These observables arise due to the presence of the weak interaction, the only one of the fundamental interactions to violate parity. The weak interaction is described consistently at the quark and nucleon levels in the Standard Model, but in $\Delta S = 0$ experiments, the expected weak interaction effects are not seen. The only explanation for this is that the strong interaction is interfering with the weak interaction. Because of this interference, by measuring parity-violating observables,

it is possible to probe the strong interaction at low energy. By combining the results of the NPDGamma and n3He experiments with other experiments, the experimental parameters of the relevant models can be over-constrained.

The NPDGamma experiment measures the parity-violating directional asymmetry in the γ-ray emission from polarized cold neutron capture on a liquid para-hydrogen target in the reaction

$$\vec{n} + P \rightarrow d + \gamma. \tag{6.1}$$

Para-hydrogen is used as ortho-hydrogen has a higher scattering cross section that would depolarized the neutron beam. The γ-ray emission direction is measured by an array of 48 CsI detectors that cover a 3π solid angle around the target.

The measured signal in each detector is the sum of a number of different factors. Due to the high precision required for the experiment, the backgrounds and the electronic pedestal had to be measured and accounted for. The main contributions were γ-rays from neutron captures on the aluminum in the hydrogen target and the liquid hydrogen. While hydrogen and aluminum target data taking has been completed, further analysis of the aluminum target asymmetry is still required before the hydrogen asymmetry can be extracted.

I designed and assembled a pair of ^{3}He MWPCs to be used as neutron beam monitors during experiments at the FnPB. The beam monitors consist of a signal wire plane sandwiched between two HV wire planes in an aluminum housing. The fill gas is mainly nitrogen with a small partial pressure of ^{3}He added. The ^{3}He is used as it has a high neutron capture cross section and, after neutron capture, it consistently breaks up into a proton and a triton sharing 765 keV of kinetic energy. The proton

and triton will ionize the fill gas as they pass through it. Due to the effect of the negative applied bias voltage on the HV wires the electrons will collect on the signal wires, and the ions on the HV wires. This motion of the charges will create a current in the wires that will be read out from the signal wires to measure the amount of ionization inside the beam monitors.

As discussed in chapter 3, depending on the bias voltage applied to an ion chamber, the charge collection can occur in different modes. Charge collection in the monitors was examined by varying the bias voltage from 0 to −2000 volts. From this, the minimum required operating voltage of −800 V was determined to ensure rapid and complete charge collection. The beam monitor's response was examined at various neutron flux as indicated by the average proton power on the spallation target over the course of a run during NPDGamma data taking. Plotting the monitor current output vs the proton power, it was determined that the monitors response was linear. The M2 monitor was also calibrated to determine the neutron flux for a given output current. The details of the beam monitor design and testing are discussed in chapter 4.

The n3He experiment measures the directional asymmetry in the emission of a proton and triton after capture of polarized cold neutrons on an unpolarized ^{3}He target in the reaction

$$\vec{n} + {}^3\mathrm{He} \rightarrow {}^4\mathrm{He}^* \rightarrow p + T. \tag{6.2}$$

To measure the emission direction, a MWPC is used as combined target and detector with a pure ^{3}He fill gas. A MWPC is used to allow the protons and tritons to range out over as large of a distance as possible in the target chamber to minimize the

variation in the signal from each neutron capture caused by the proton or triton stopping prematurely on a surface in the chamber.

By analyzing the changes in the ionization distribution between neutron pulses polarized in the the up and down directions, the asymmetries can be extracted. In the PV asymmetry measurement mode, the wires in the target chamber are perpendicular to the magnetic field and the chamber is sensitive mainly to changes in the ionization distribution in the up-down direction. In the PC asymmetry measurement mode, the wires in the target chamber are orientated parallel to the magnetic field and thes chamber is mainly sensitive to changes in the ionization distribution in the left-right direction. Data taking has been completed for both asymmetries and analysis is in progress.

A voltage scan was done with the target chamber from 0 to -552 volts to determine in what charge collection mode the target chamber was operating. This scan determined that the wires in the target chamber were operating in the ion chamber to the start of the amplification region at the $-353\,\mathrm{V}$ bias voltage. The ion chamber mode is preferred as it is the least sensitive to any variations in the power supply performance, and the higher the amplification, the greater risk of non-linearities at higher initial ionization rates as well. The voltage scan indicates no problems with the operation of the target chamber.

It is required that the target chamber response be linear to changes in the neutron flux. To check the target chamber response to changes in the neutron flux, a selection of runs were made from the data taking cycle where the proton power on target ranged from approximately $850\,\mathrm{kW}$ to $1400\,\mathrm{kW}$. The M1 monitor was used as the reference

for beam power having previously been determined to be linear over a wide range of neutron fluxes. Plotting the wire output voltage vs the M1 monitor output voltage for the selected runs, it was found that the target chamber was linear for all wires. Having passed both of these tests, the target chamber was determined to be working in an acceptable range to make the required measurements of the asymmetries.

Appendix A

Run Number Tables

A.1 HFIR Data Taking

run#	Shutter
23	open
24	open
25	open
26	open
27	open
28	open
29	open
30	closed
31	closed
32	closed
33	closed

(a) Set 1

run#	Shutter
54	closed
55	closed
56	closed
57	closed
60	open
61	open

(b) Set 2: Faraday Cage

Table A.1: HFIR Run numbers and shutter positions for M2 data taking.

run#	Shutter
54	closed
55	closed
56	closed
57	closed
60	open
61	open

Table A.2: Set 2: HFIR Run numbers and shutter positions for second M2 data taking with faraday cage on power supply.

A.2 NPDGamma Data Runs

A.2.1 Beam Monitor Voltage Scans

Run	Nominal Voltage(V)	Measured Voltage(V)	Supply Voltage(V)	HV Supply Current(mA)	Proton Power(kW)
66390	0	0	0	0	655.7
66391	0	0	0	0	655.12
66392	500	48.1	475.8	0.16	
66393	100	9.32	92.18	0.03	
66394	200	18.77	185.7	0.06	653.
66395	300	28.42	281.1	0.09	
66396	400	38.24	378.2	0.12	
66397	700	68.9	681.5	0.22	
66398	900	90.6	896.1	0.28	653.82
66399	1000	101.5	1003.9	0.31	
66400	1200	124.2	1228.5	0.38	653.35
66401	1400	147.3	1456.9	0.44	
66402	1600	170.8	1689.4	0.51	653.
66403	1800	194.2	1920.8	0.57	

Table A.3: M2 voltage scan run numbers with recorded values and calculated applied bias voltage.

Run	Nominal Voltage(V)	Measured Voltage(V)	Supply Voltage(V)	HV Supply Current	Proton Power (kW)
66420	0	0	0		
66421	100	9.32	92.18		
66422	200	18.78	185.8		646.30
66423	300	28.44	281.3		
66424	400	38.2	377.8		
66425	500	48.1	475.8		
66427	700	69	682.5		
66428	900	90.7	897.1		
66429	1000	101.5	1003.9		
66430	1200	124.3	1229.4		644.7
66432	1400	147.5	1458.9		
66433	1600	170.7	1688.8		644.8
66434	1800	194.1	1919.8		

Table A.4: M1 voltage scan run numbers with recorded values and calculated applied voltage.

A.2.2 Beam Monitor Linearity

Run #	Beam Pwr.	Date and Time	Activity
66099	221.804	Wed Jun 22 05:07:14 2011	Chlorine
66100	222.869	Wed Jun 22 05:07:14 2011	Chlorine
66103	375.65	Wed Jun 22 05:07:14 2011	Chlorine
66104	380.792	Wed Jun 22 05:07:14 2011	Chlorine
65747	494.051	Sun Jun 19 14:57:19 2011	Aluminum
65757	501.535	Sun Jun 19 16:37:26 2011	Aluminum
65758	502.876	Sun Jun 19 14:57:19 2011	Alumunum
66089	543.25	Wed Jun 22 03:58:03 2011	Chlorine

Table A.5: Runs used for beam monitor linearity testing. Table continued in table A.6.

Run #	Beam Pwr.	Date and Time	Activity
66537	560.632	Wed Jun 22 03:58:03 2011	Chlorine ring 2
66305	591.284	Thu Jun 23 12:12:09 2011	Chlorine Target, Second Ring
66490	592.837	Sat Jun 25 00:58:02 2011	Cl Production, ring 2
66491	592.841	Sat Jun 25 01:04:57 2011	Cl Production, ring 2
66593	598.52	Sat Jun 25 12:52:23 2011	Cl Production, ring 2
66281	601.148	Thu Jun 23 09:25:38 2011	Chlorine Target, Second Ring
66292	619.858	Thu Jun 23 10:42:13 2011	Chlorine Target, Second Ring
66293	625.902	Thu Jun 23 10:49:08 2011	Chlorine Target, Second Ring
66277	651.535	Sat Jun 25 18:30:25 2011	Cl production, ring 2
66279	653.174	Thu Jun 23 09:11:48 2011	Chlorine Target, Second Ring
66276	657.805	Thu Jun 23 08:51:01 2011	Chlorine Target, Second Ring
66180	704.212	Wed Jun 22 20:56:52 2011	Chlorine Production
66135	742.093	Wed Jun 22 15:44:18 2011	Chlorine Production
66130	742.137	Wed Jun 22 15:09:42 2011	Chlorine Production
66122	777.587	Wed Jun 22 14:14:21 2011	Chlorine Production
65148	793.753	Wed Jun 22 17:14:38 2011	Chlorine Production
65145	796.324	Wed Jun 22 16:53:29 2011	Chlorine Production
67284	797.687	Wed Jun 29 23:50:47 2011	Chlorine Target, centered
67286	798.13	Thu Jun 30 00:04:38 2011	Chlorine Target, centered
67306	798.337	Thu Jun 30 02:23:06 2011	Chlorine Target, centered
67296	799.287	Thu Jun 30 01:13:55 2011	Chlorine Target, centered
65582	799.599	Sat Jun 18 11:20:01 2011	Al Production Data
65652	800.402	Sat Jun 18 11:20:01 2011	Al Production Data
65827	802.016	Sat Jun 18 11:20:01 2011	Al Production
63521	814.334	Thu Jun 2 00:12:54 2011	Aluminum Data, Shutter Open
63529	815.183	Thu Jun 2 01:33:22 2011	Aluminum Data, Shutter Open
65180	820.788	Wed Jun 15 14:10:03 2011	Aluminum Target
66062	821.29	Wed Jun 22 00:50:52 2011	Chlorine production data
66063	821.369	Wed Jun 22 00:57:47 2011	Chlorine production data
64340	821.551	Thu Jun 9 02:28:07 2011	Al production data series run
64407	827.252	Thu Jun 9 13:39:47 2011	Al production data series run
66083	832.283	Wed Jun 22 03:16:33 201	Chlorine production data
63629	837.314	Thu Jun 2 22:39:41 2011	Al Runs, shutter open

Table A.6: Runs used for beam monitor linearity testing.

Run #	Beam Pwr.	Date and Time	Activity
66896	462217	Mon Jun 27 07:00:35 2011	Cl ring 3
66895	462308	Mon Jun 27 06:53:40 2011	Cl ring 3
66880	466388	Mon Jun 27 05:09:27 2011	Cl ring 3
66852	478940	Mon Jun 27 01:55:45 2011	Cl ring 3
66839	482099	Mon Jun 27 00:25:49 2011	Cl ring 3
66814	493098	Sun Jun 26 21:32:52 2011	Cl ring 3
66804	498256	Sun Jun 26 20:23:40 2011	Cl ring 3
66766	518639	Sun Jun 26 15:48:28 2011	Cl ring 2
66764	519433	Sun Jun 26 15:34:38 2011	Cl ring 2
66716	551364	Sun Jun 26 09:58:06 2011	Cl production

Table A.7: A list of the low points removed from plots of the beam power. The date and time is for the start of the run. Approximately 8 minutes of beam data were taken per run.

A.3 n3He Data Runs

	Run Number with Shutter	
Bias Voltage (V)	open	closed
0 (Power off)	57181	57178-79
-253	57185	57183
-303	57187	57189
-337	57177	
-355	57193	
-397	57195	57198
0 (power off)	57201	

Table A.8: Run numbers, shutter and voltage setting during the first voltage scan.

Bias Voltage (V)	Run Number with Shutter	
	open	closed
0V(off)	59815	59816
-52V	59817	59818
-86V	59819	59820
-99V	59821	59822
-150V	59823	59824
-201V	59825	59826
-250V	59827	59828
-300V	59829	59830
-351V	59831	59832
-400V	59833	59834
-450V	59835	59836
-552V	59837	59838
-500V	59839	59840
-400V	59841	59842
-350V	59843	59844
-200V	59845	59846
-150V	59847	59848
-100V	59849	59850
-49V	59851	59852
0(off)	59853	

Table A.9: Run numbers, shutter and voltage setting during the second voltage scan.

Run Number
19484
18014
22014
26014
29914
34014
38024
41914
46014
48012
48014
48015
50014
52014
54014
57014

Table A.10: Run numbers for n3He target linearity testing.

Appendix B

CAD Diagrams

B.1 Beam Monitor CAD Drawings

All linear dimensions are centimeters.

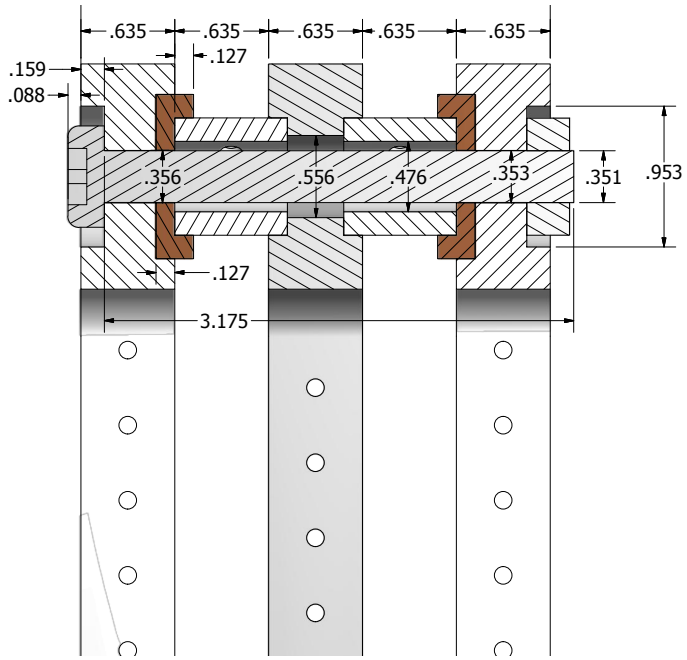

Figure B.1: Beam Frame Stack

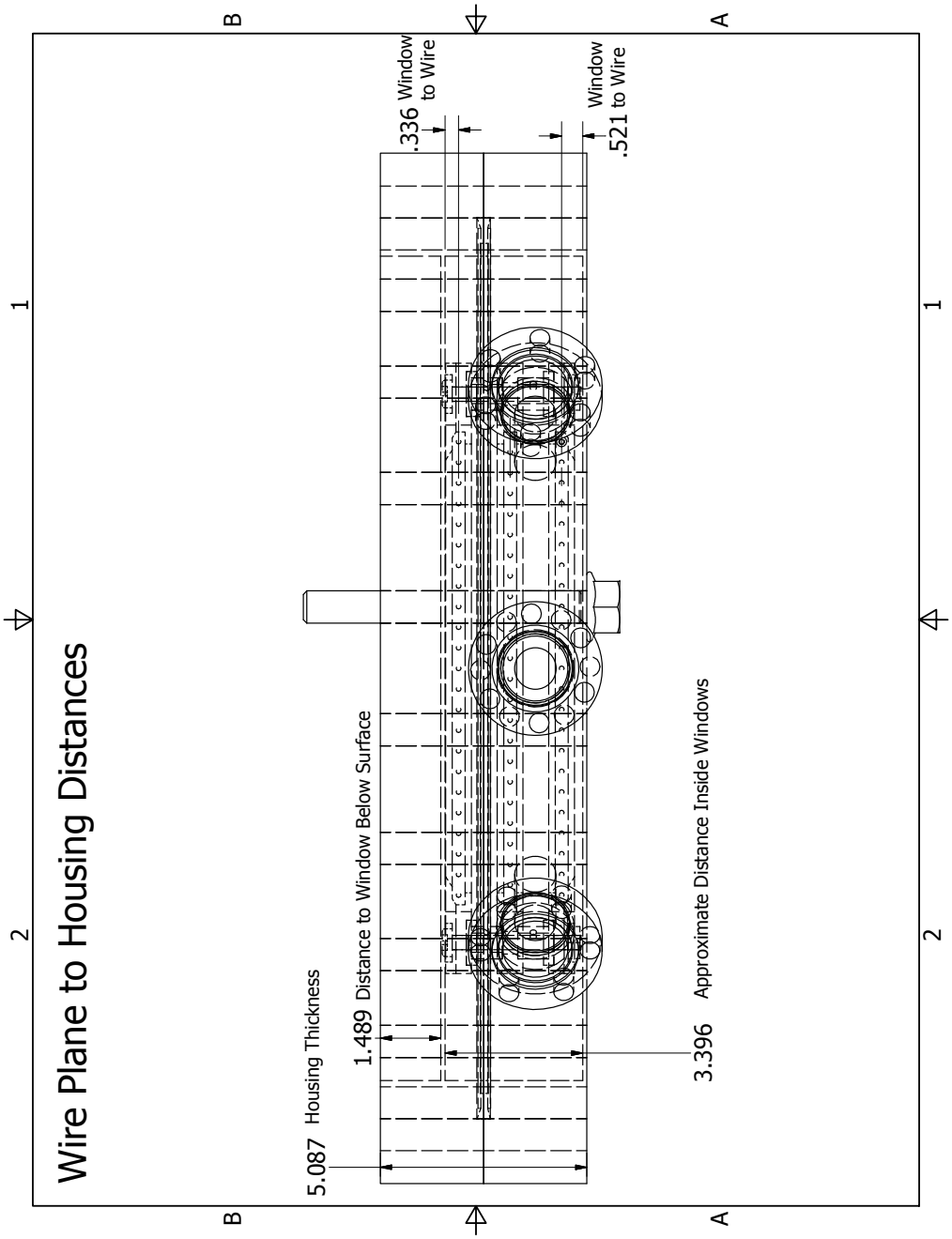

Figure B.2: Beam monitor end view.

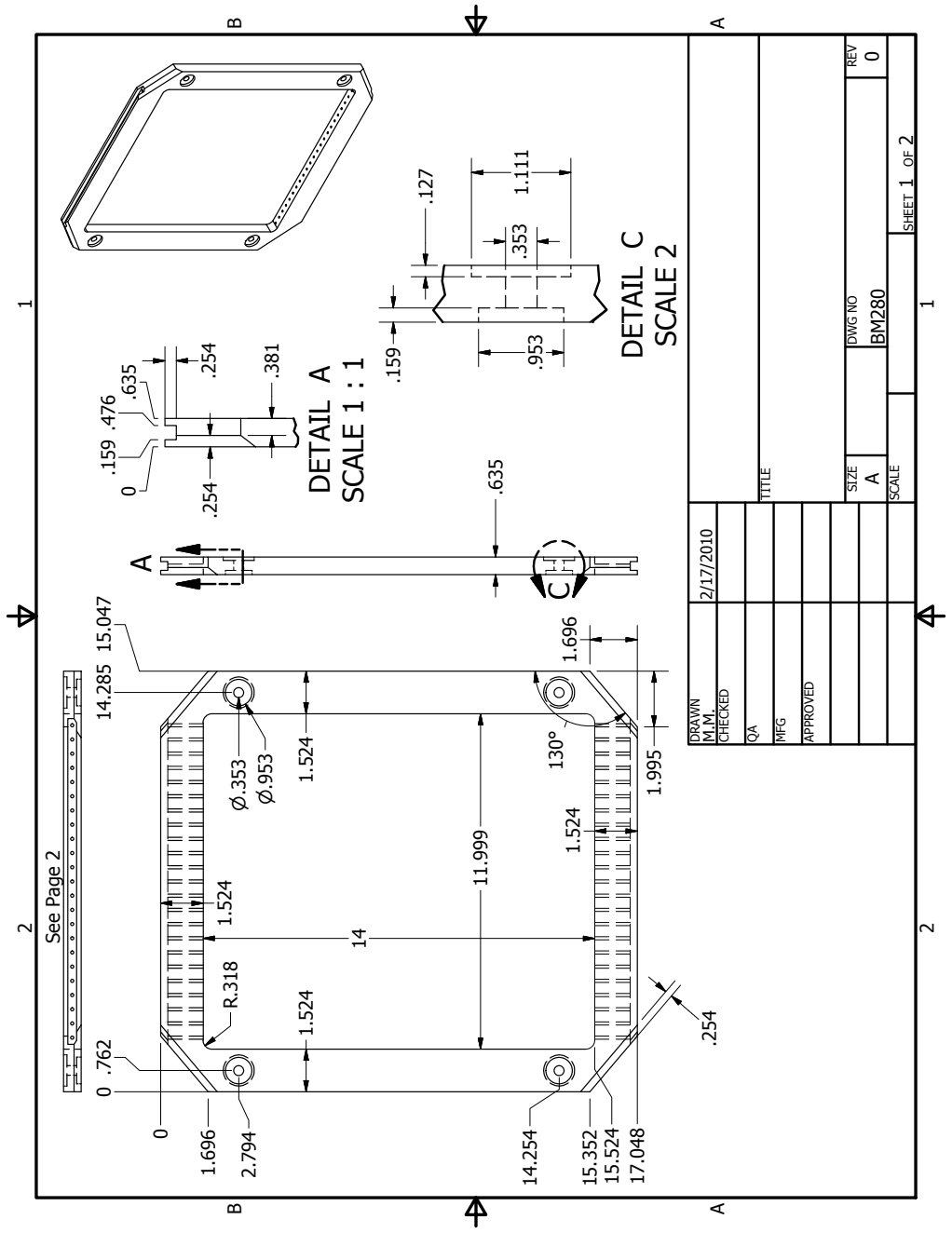

Figure B.3: Beam Monitor Signal Frame. While macor is the specified material in the drawing PEEK was used.

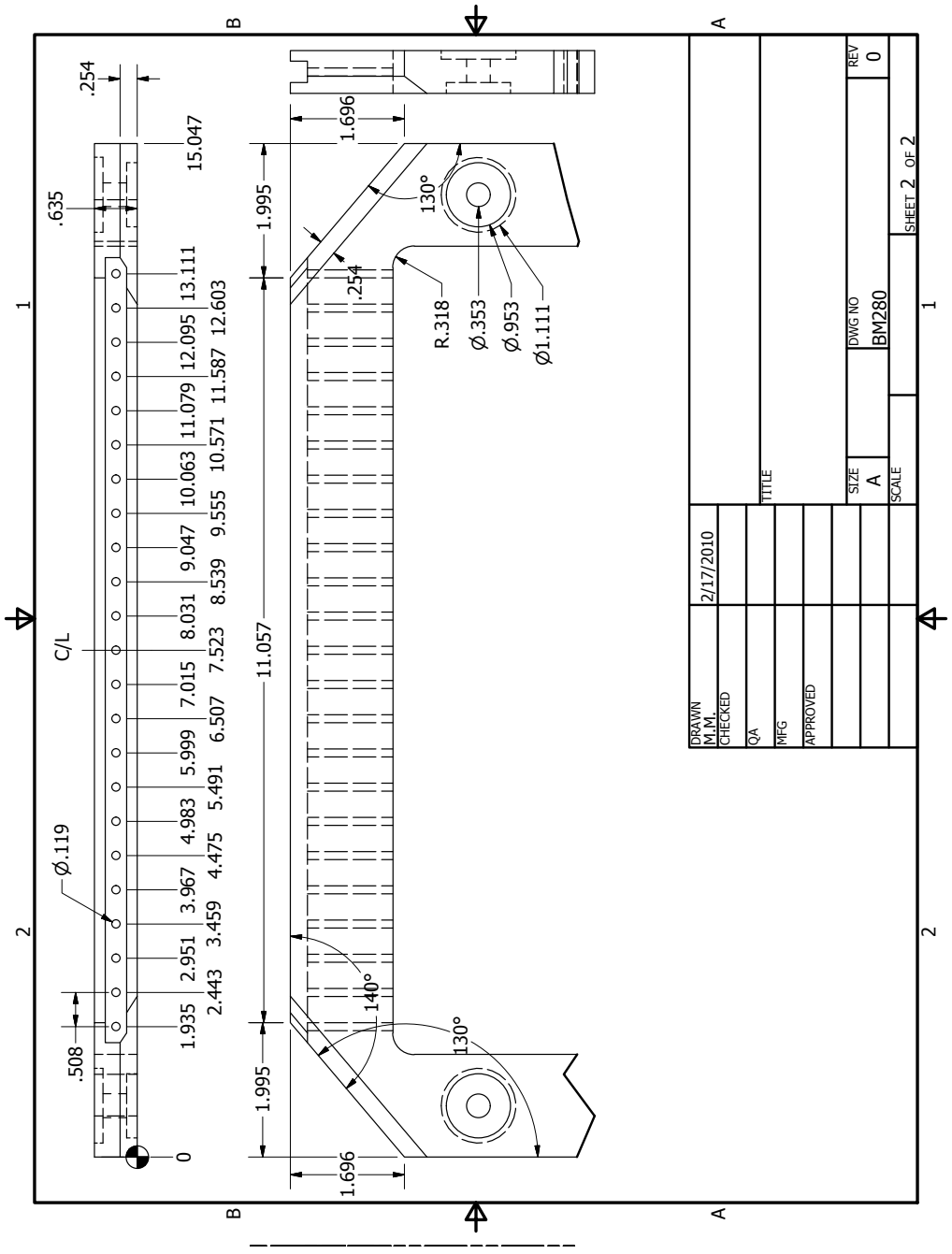

Figure B.4: Beam Monitor Signal Frame. While macor is the specified material in the drawing PEEK was used.

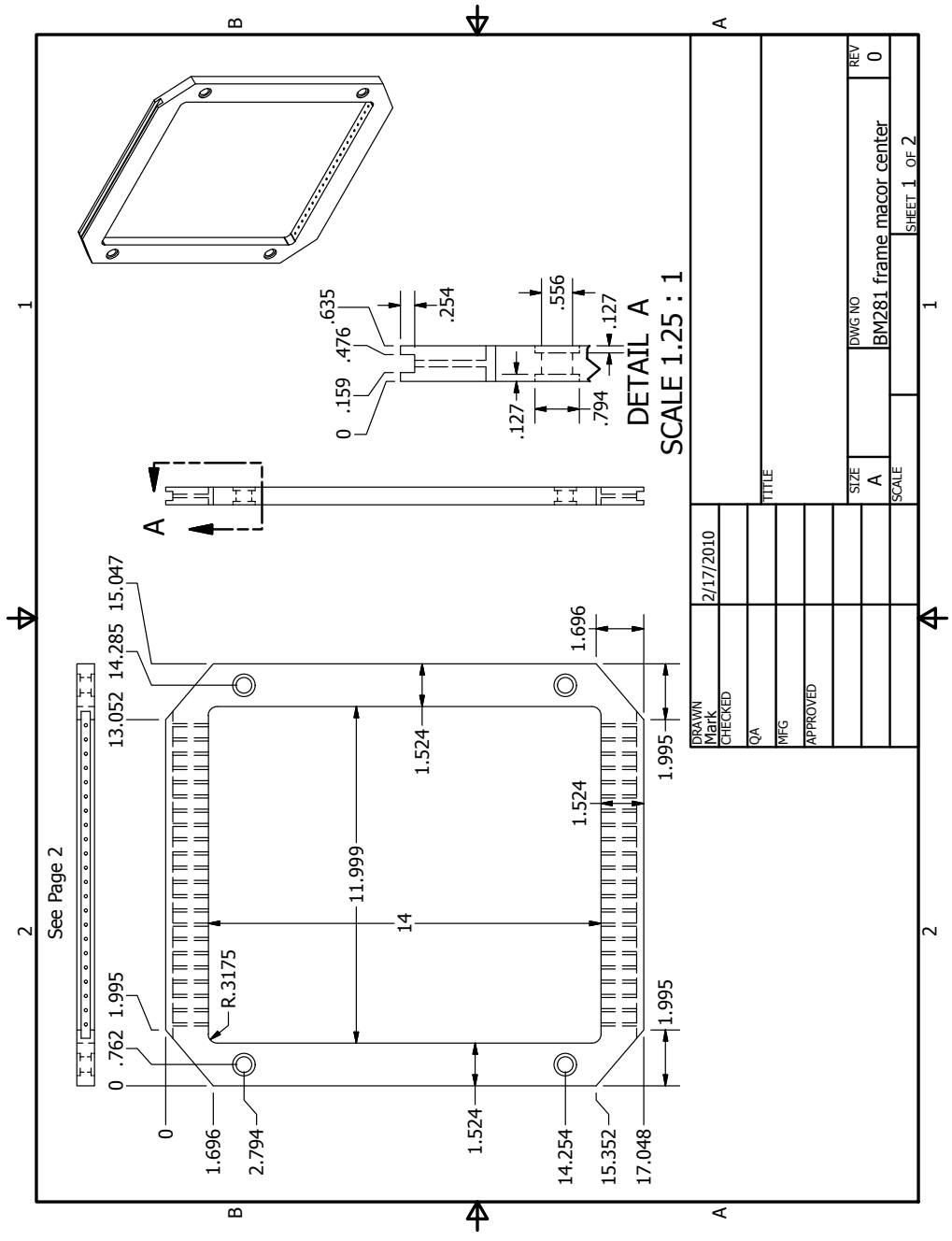

Figure B.5: Beam Monitor HV Frame. While macor is the specified material in the drawing PEEK was used.

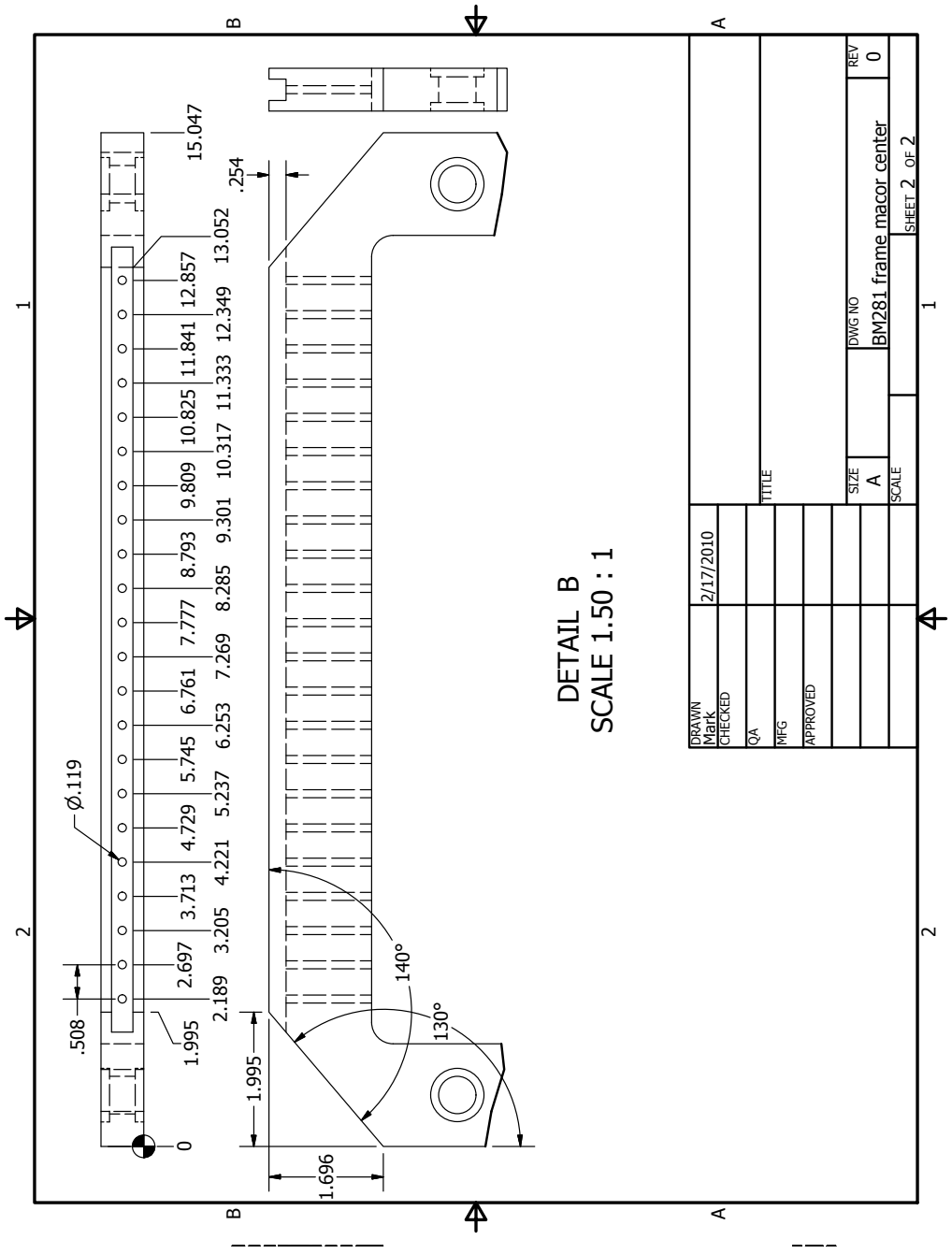

Figure B.6: Beam Monitor HV Frame. While macor is the specified material in the drawing PEEK was used.

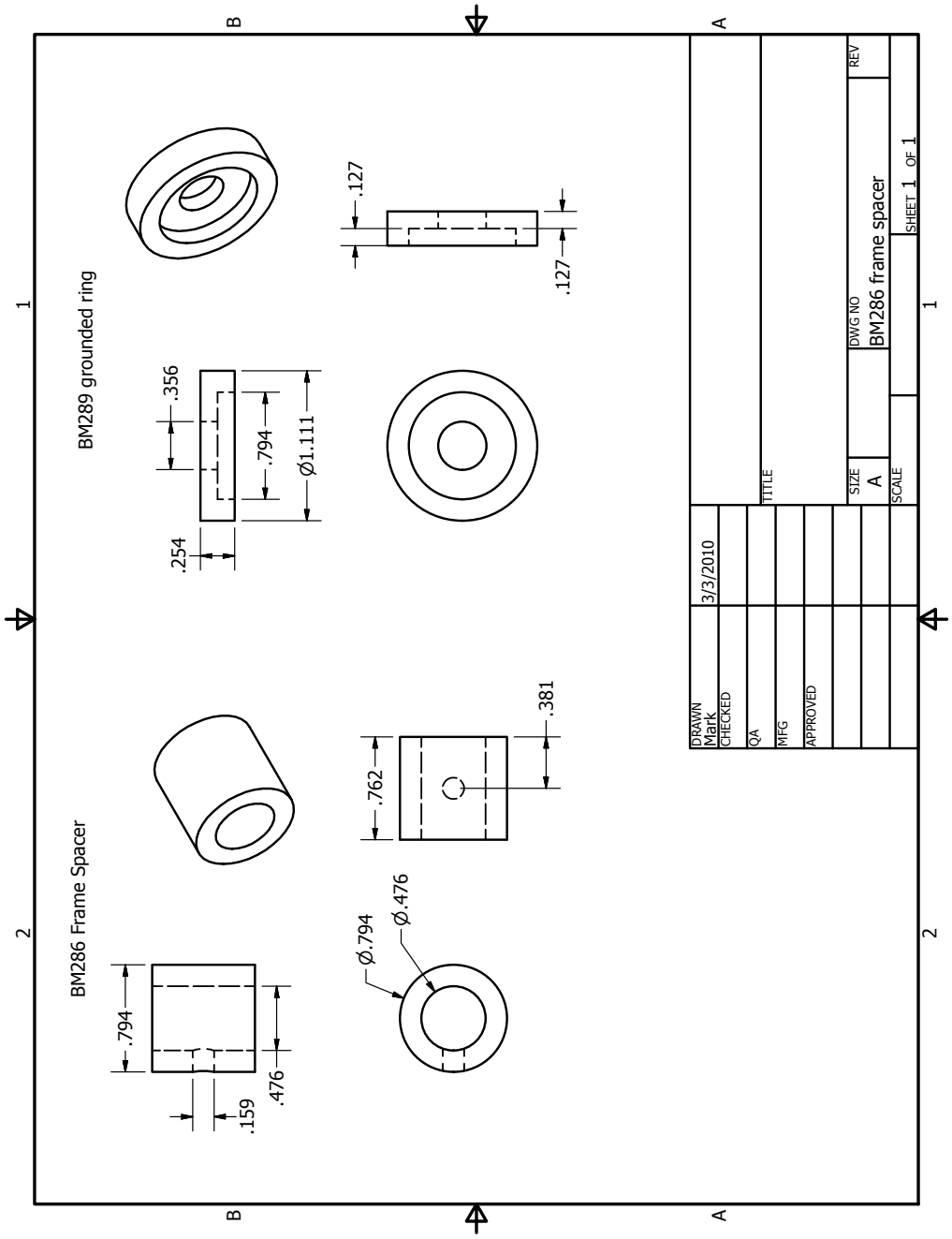

Figure B.7: Beam Monitor HV Frame

B.2 n3He Drawings

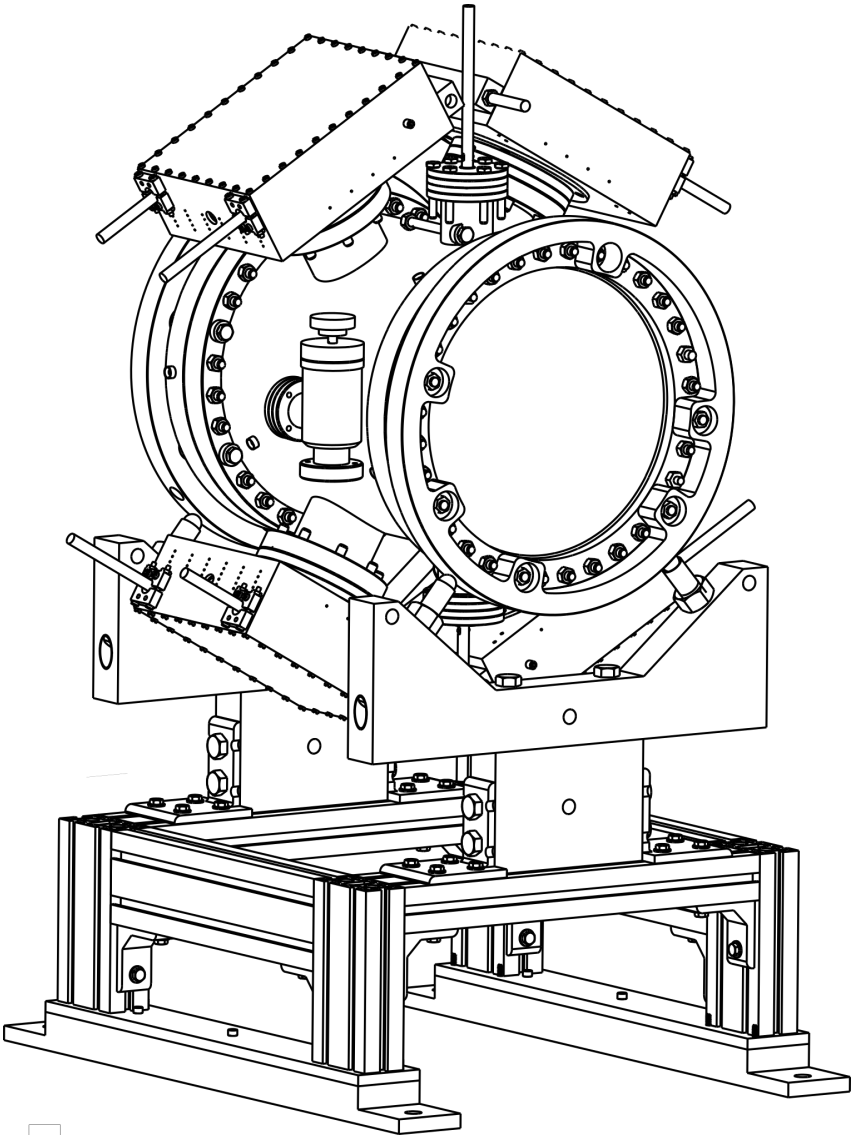

Figure B.8: Target Chamber on Stand.

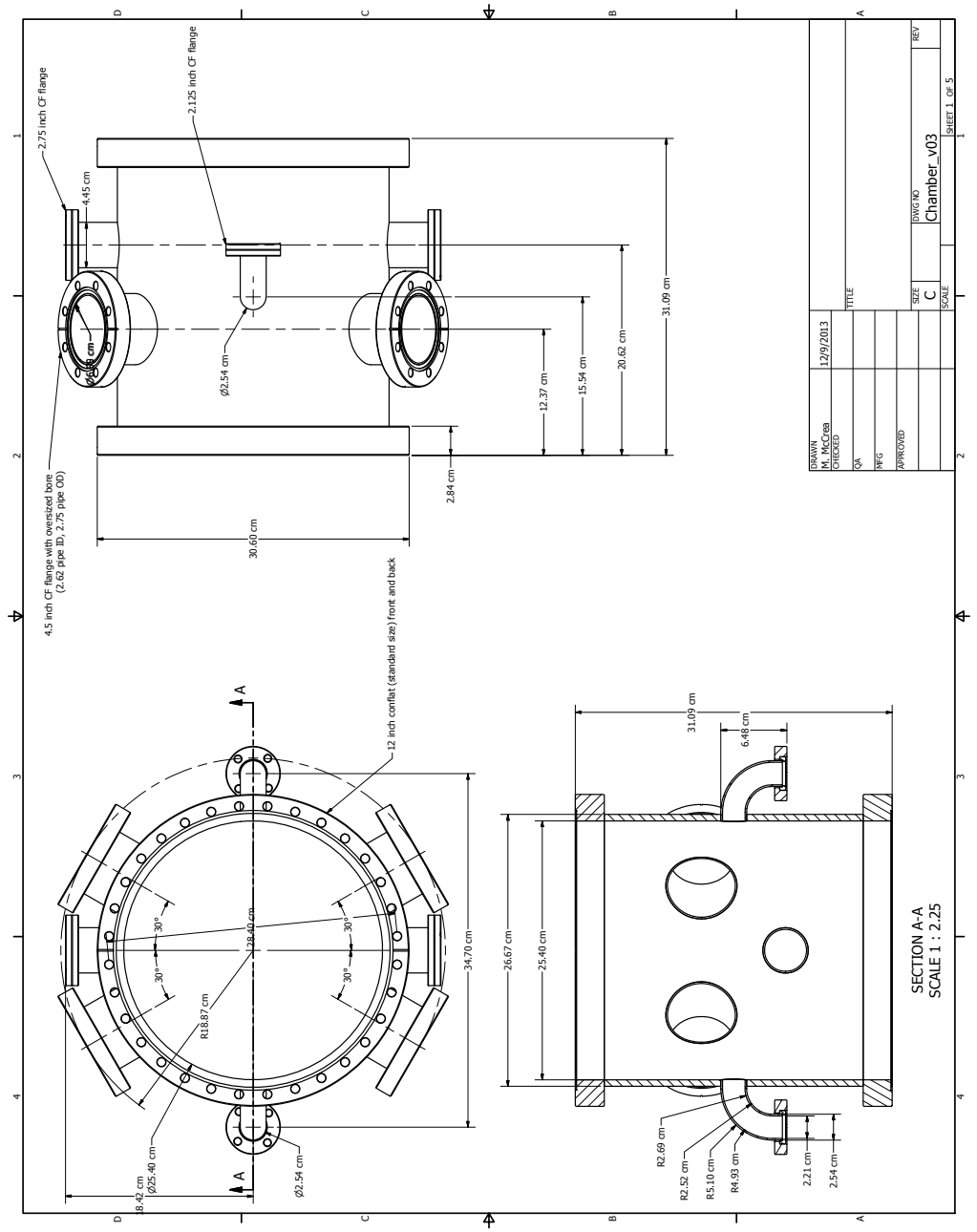

Figure B.9: n3He Target Housing Dimensions

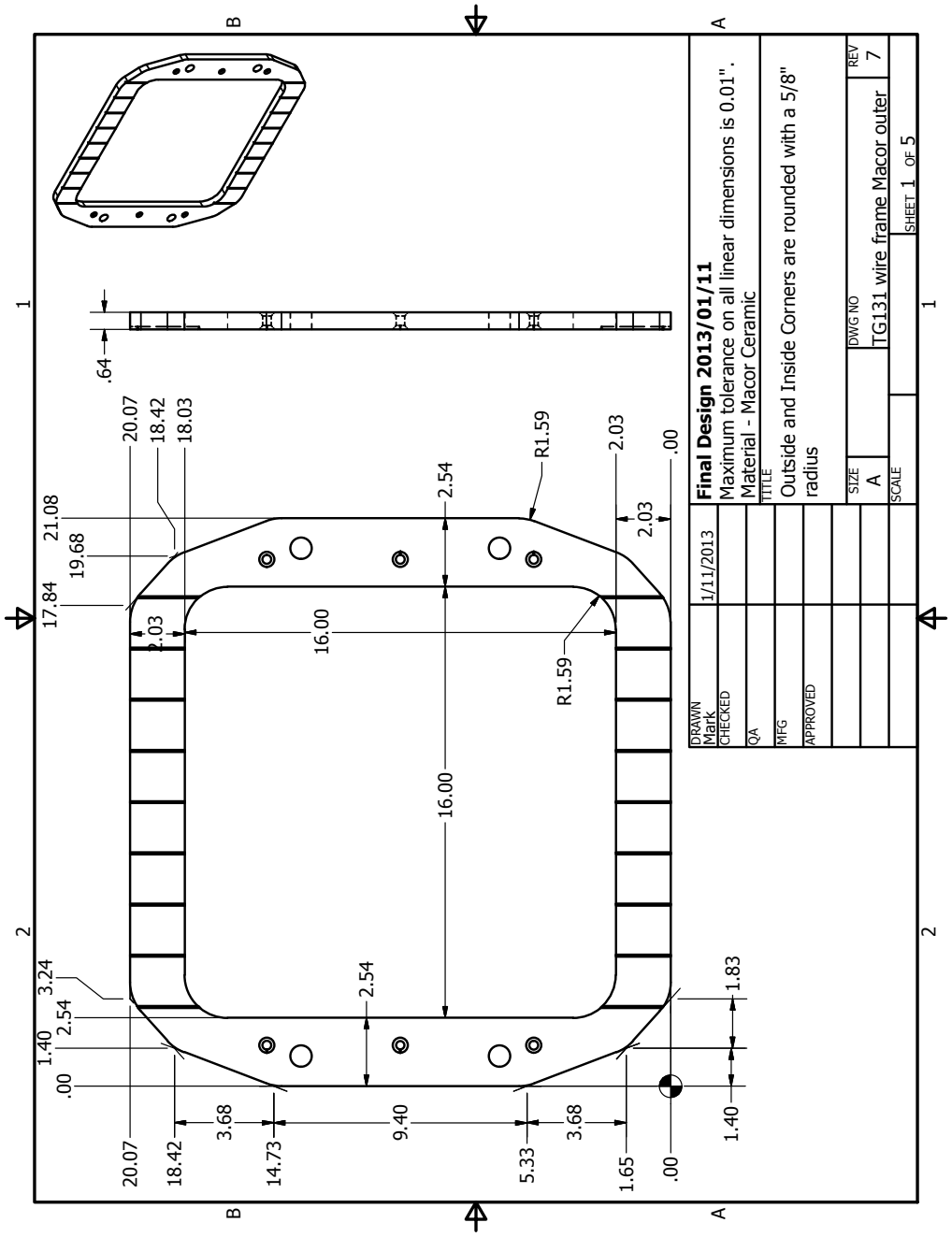

Figure B.10: n3He Signal Frame

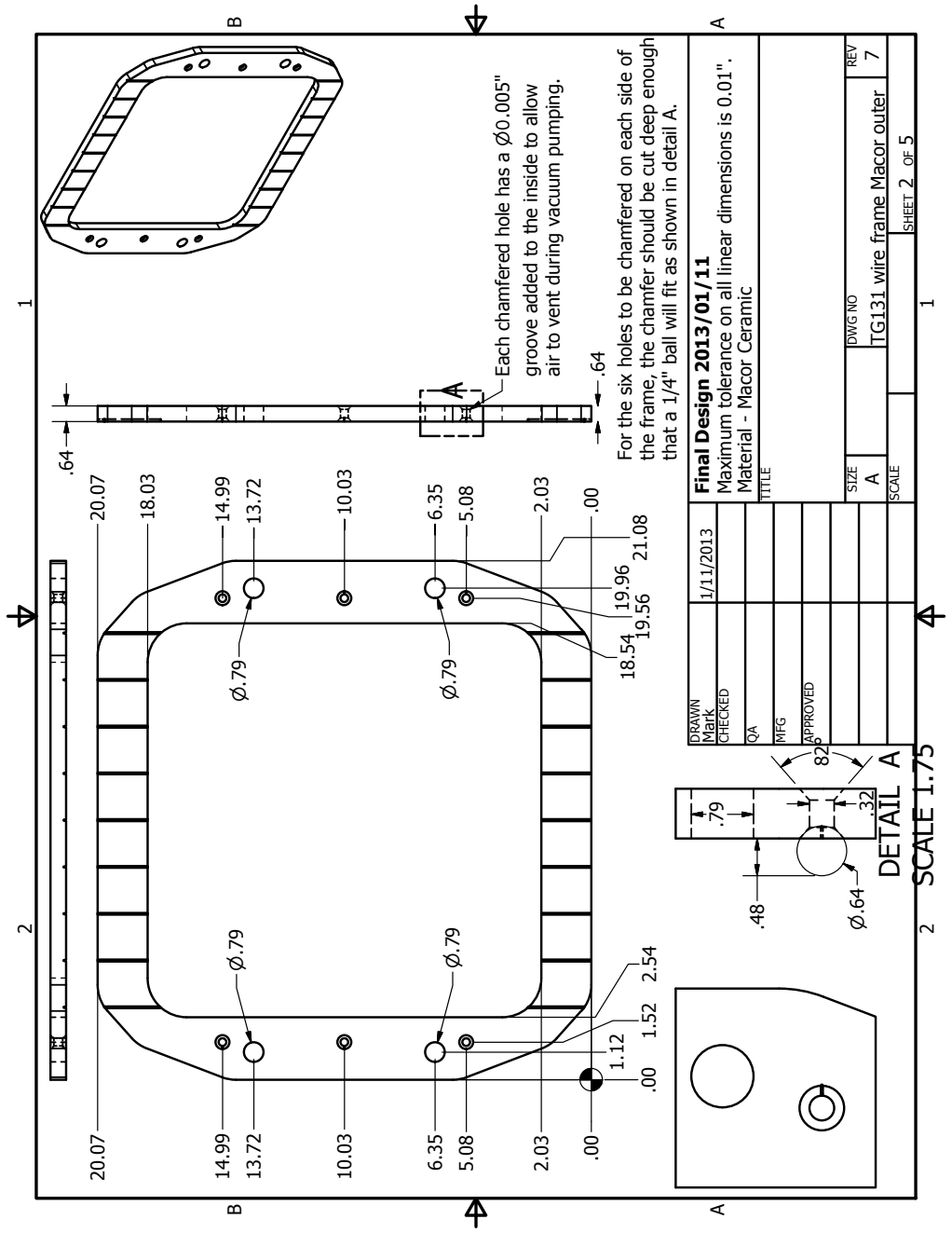

Figure B.11: n3He Signal Frame

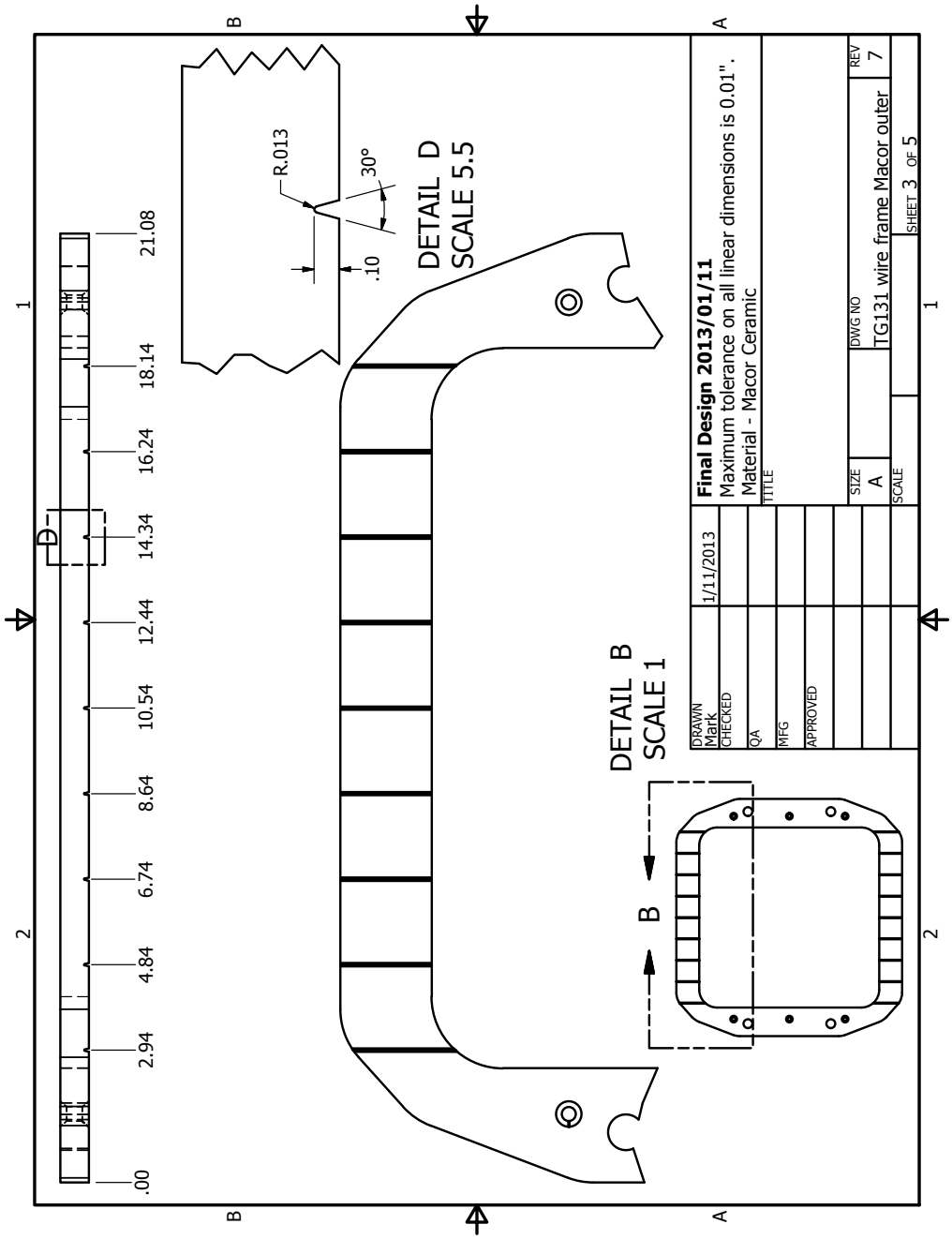

Figure B.12: n3He Signal Frame

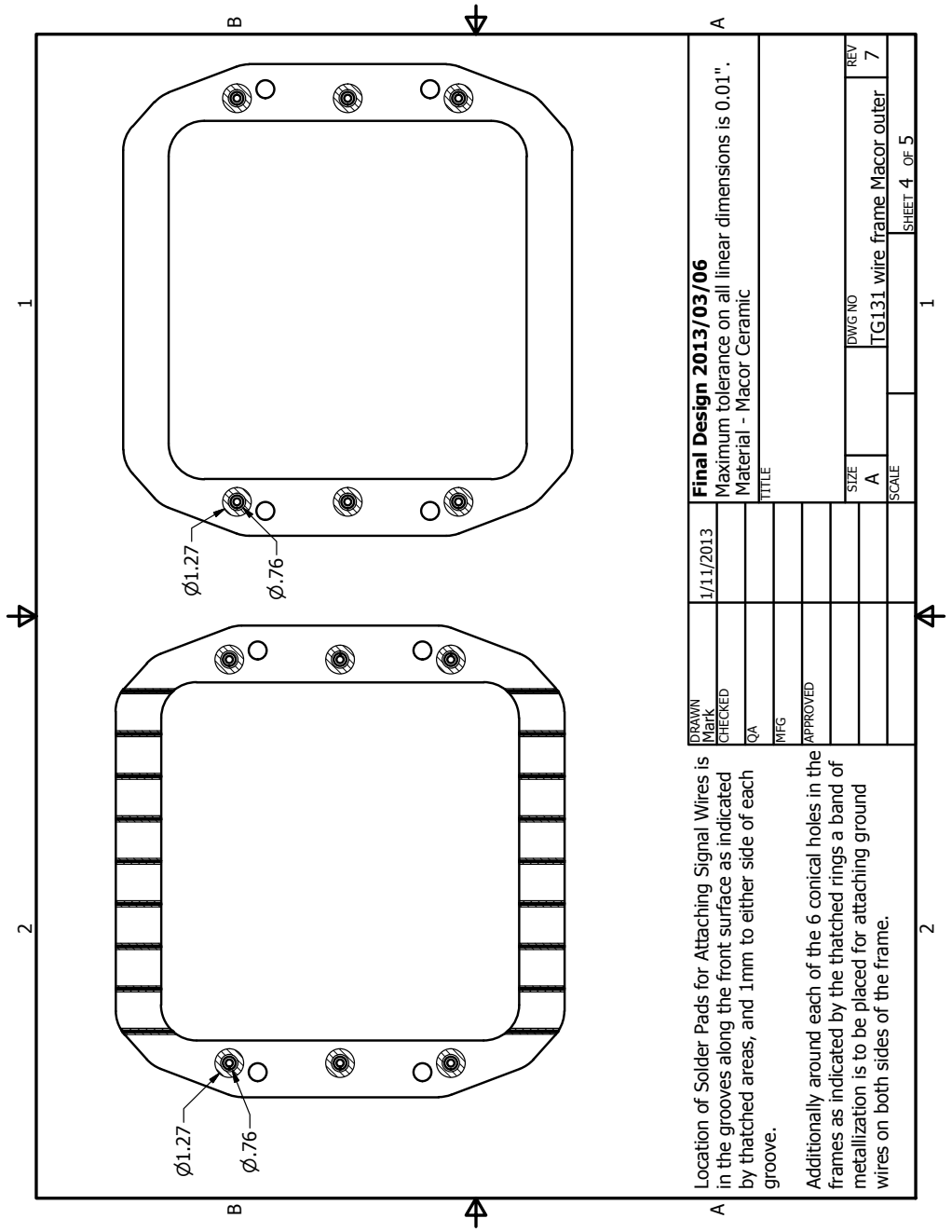

Figure B.13: n3He Signal Frame

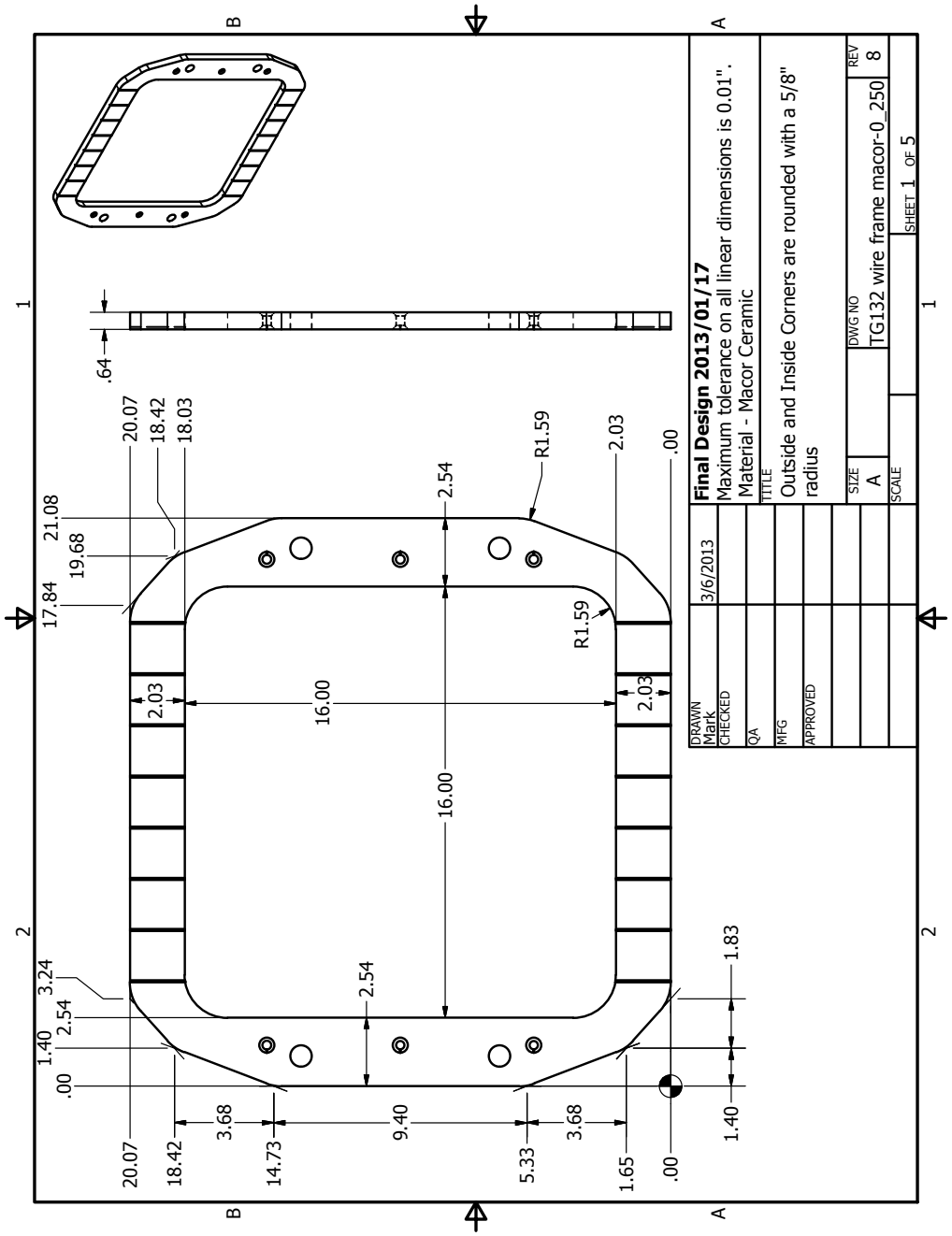

Figure B.14: n3He HV Frame

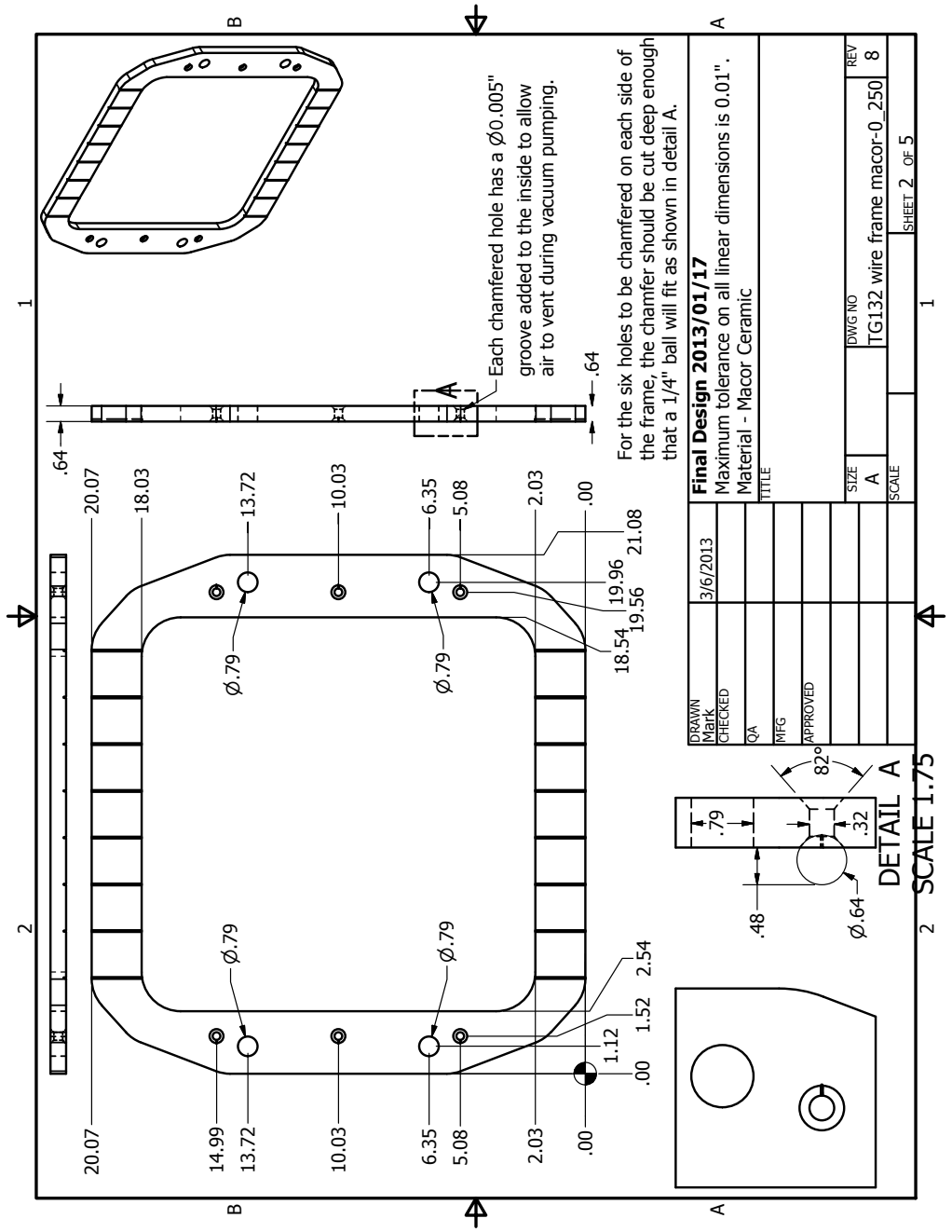

Figure B.15: n3He HV Frame

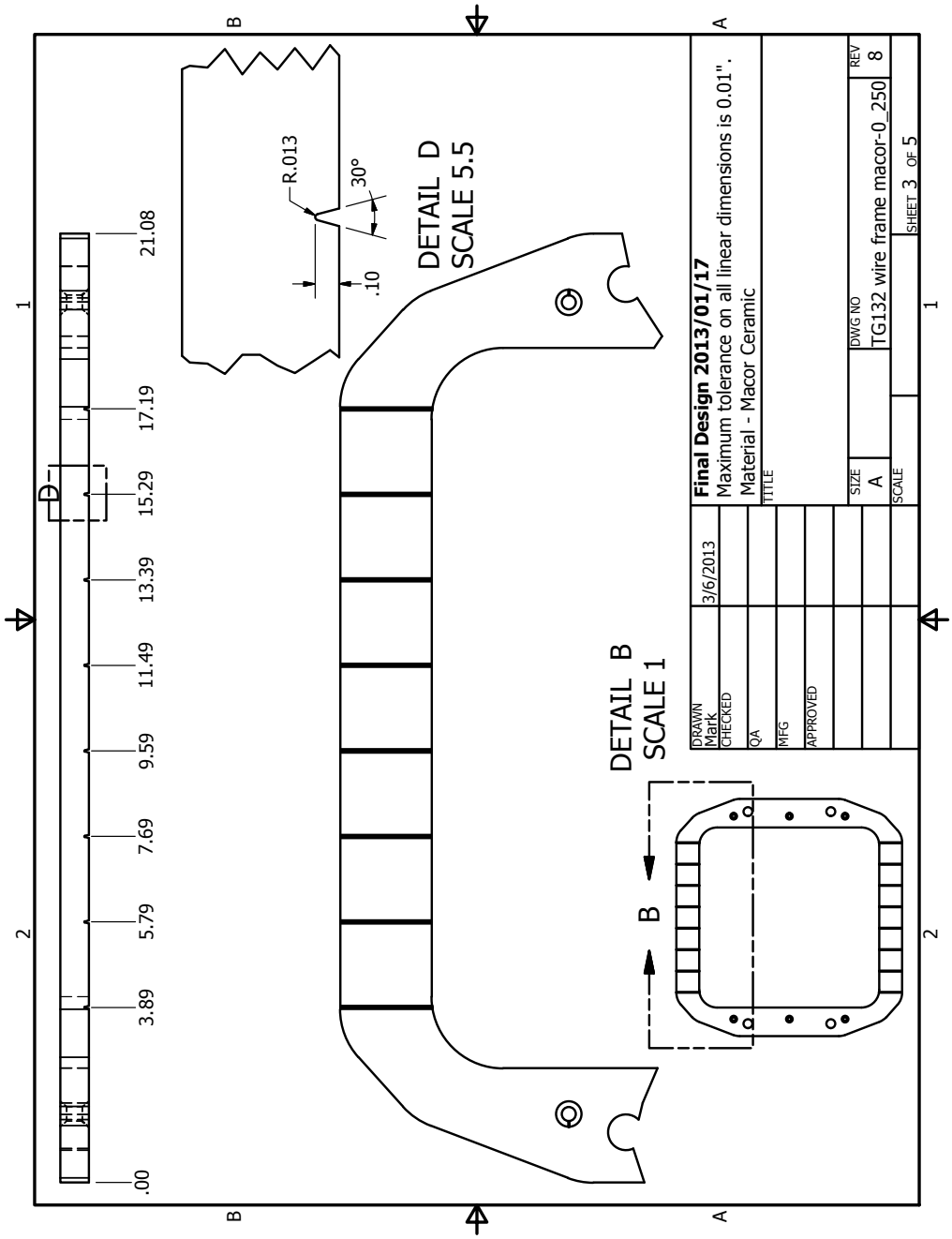

Figure B.16: n3He HV Frame

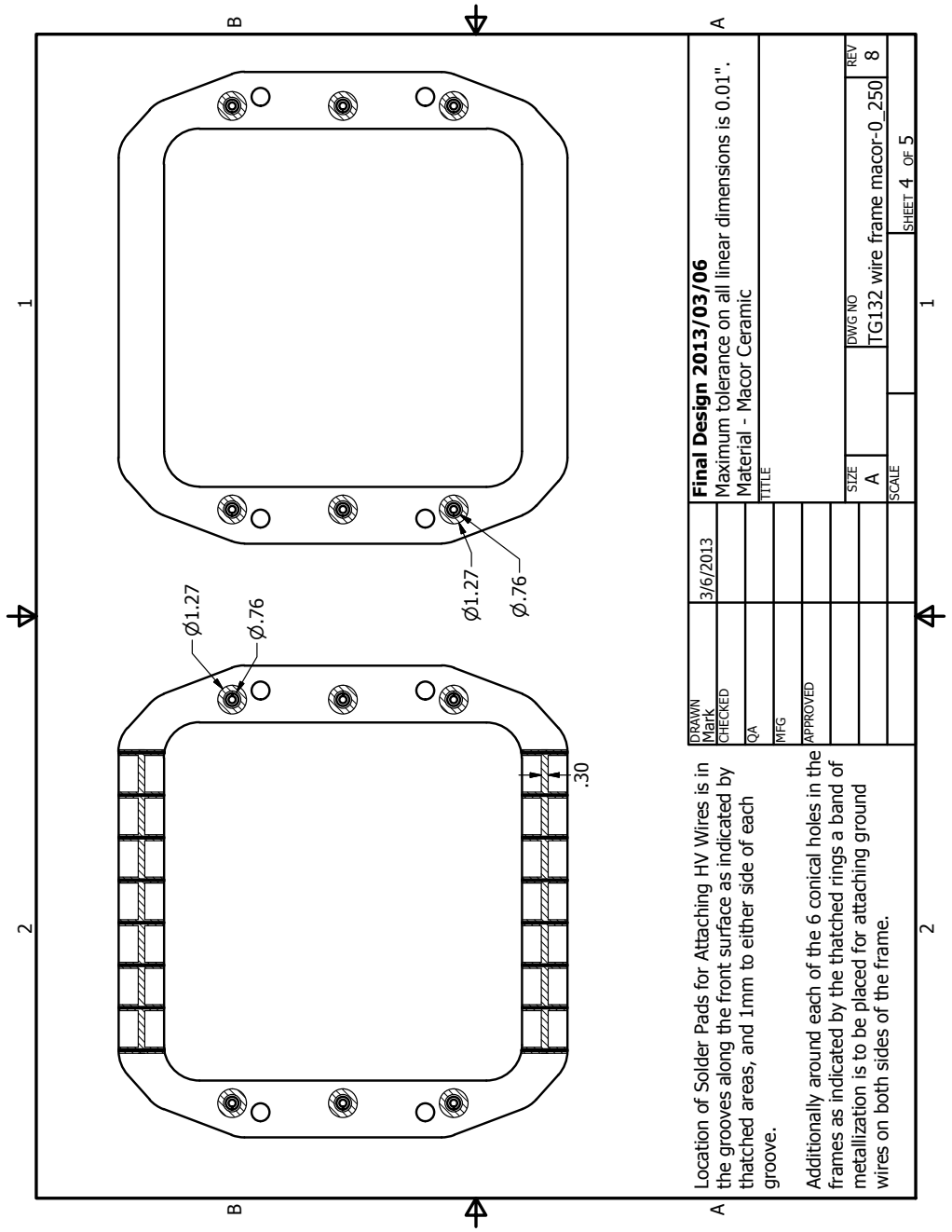

Figure B.17: n3He HV Frame

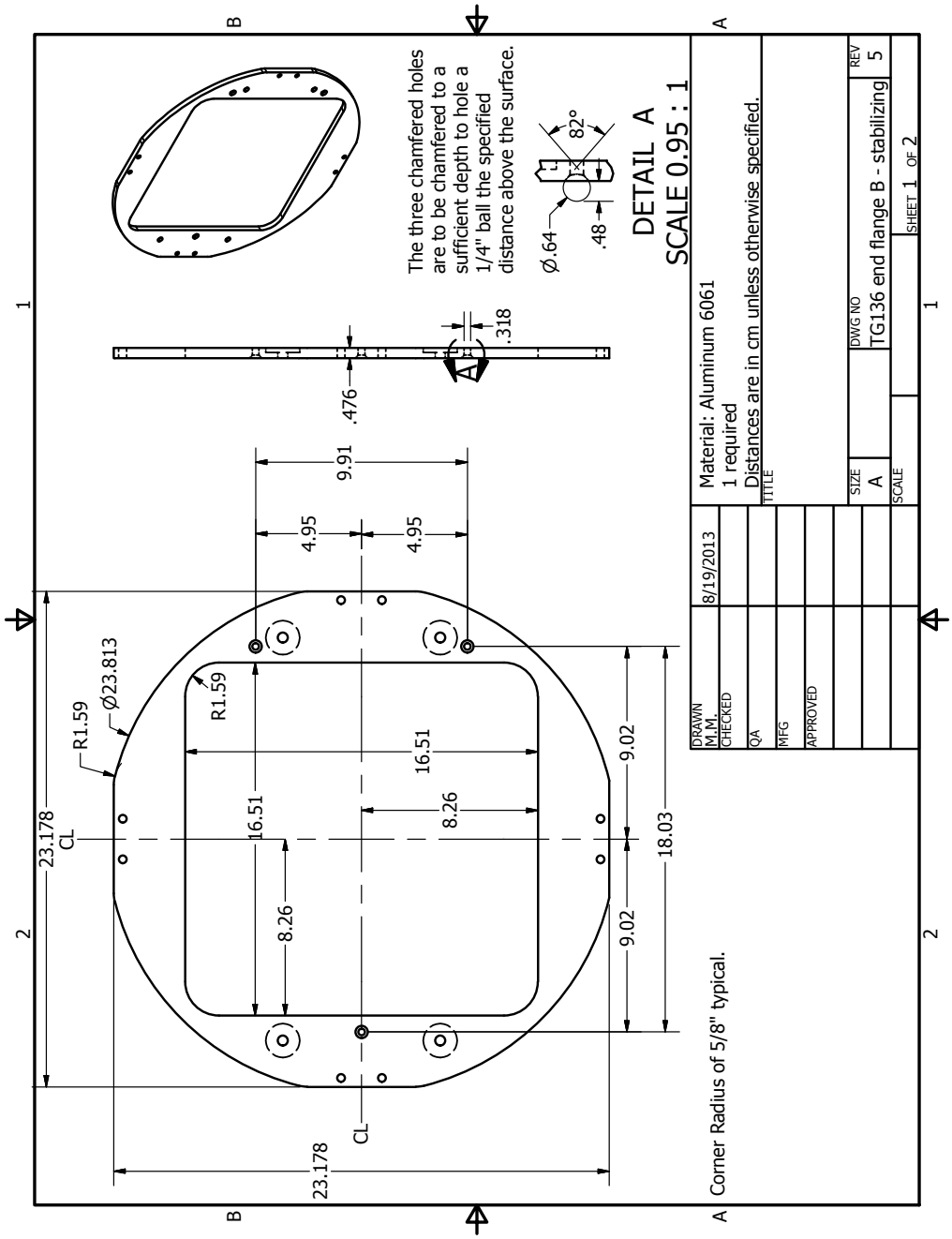

Figure B.18: Compression Plate.

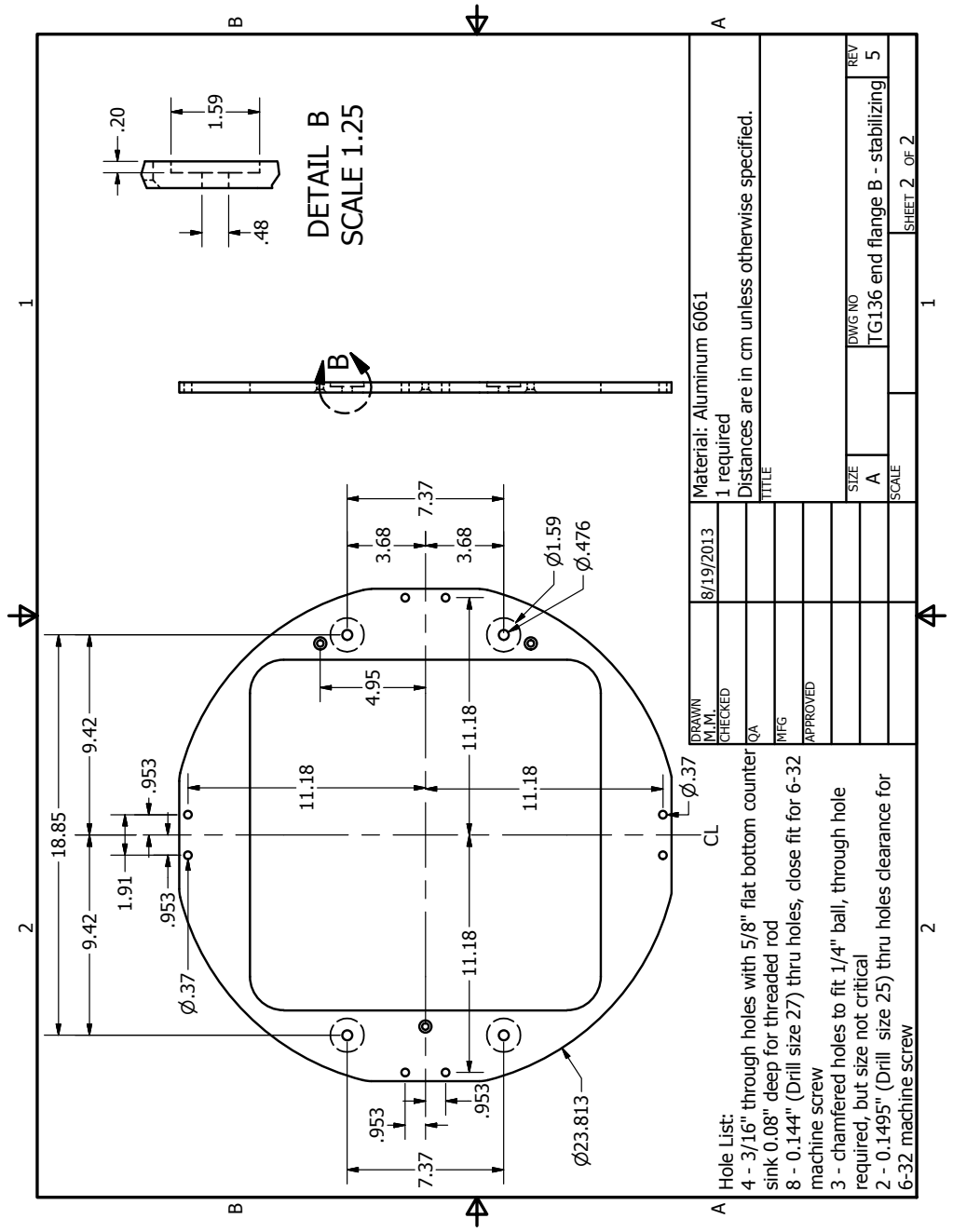

Figure B.19: Compression Plate.

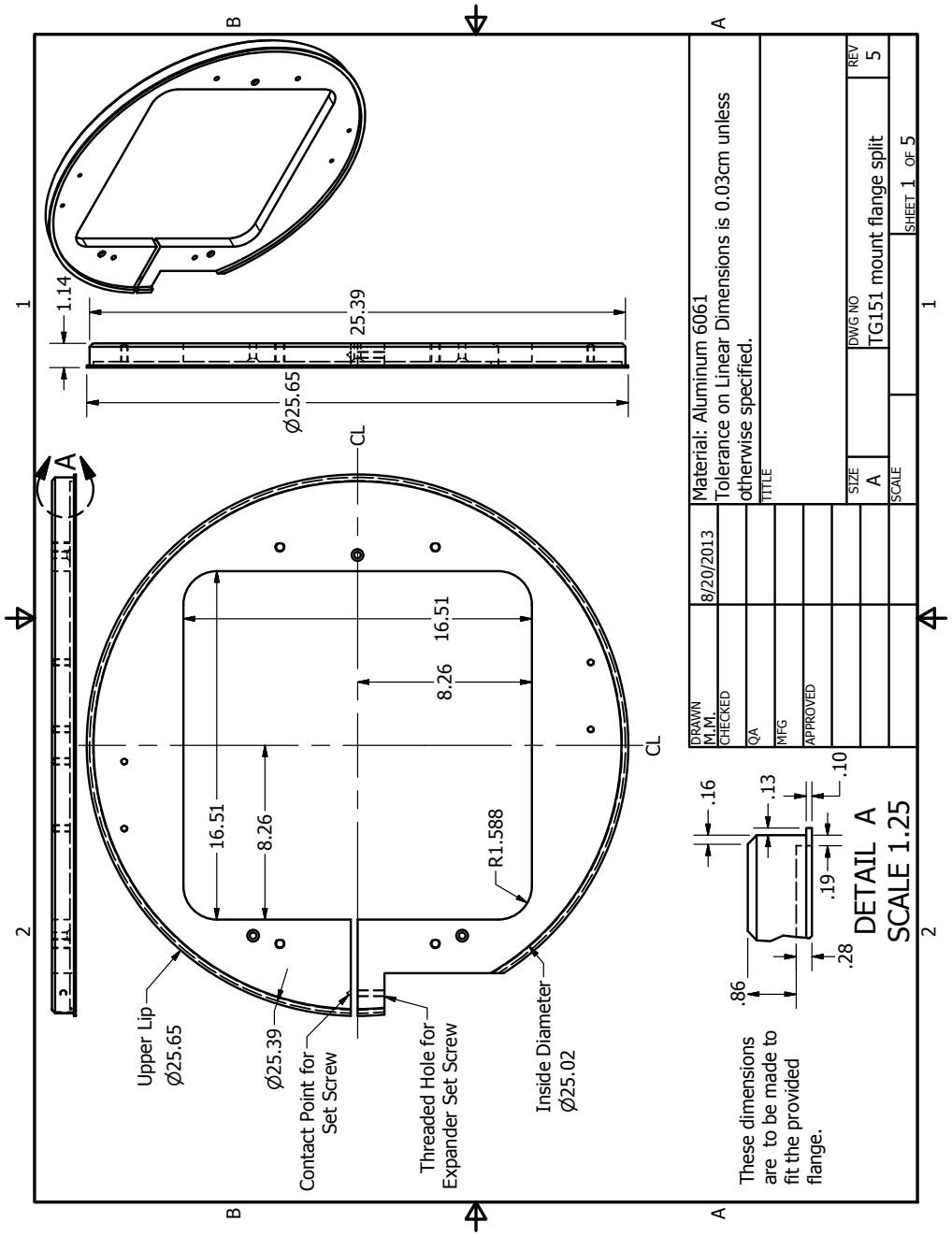

Figure B.20: Split Mount Plate

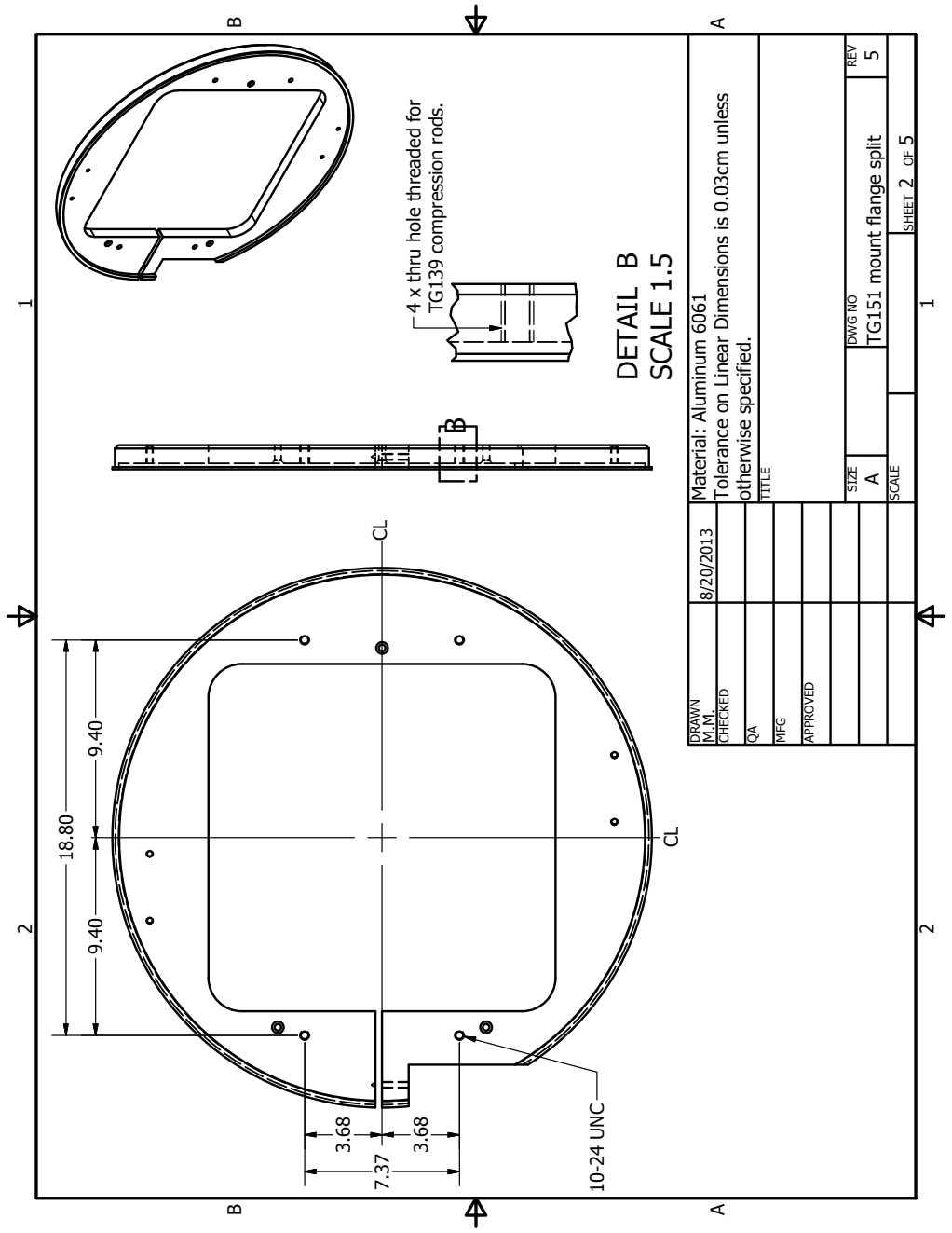

Figure B.21: Split Mount Plate

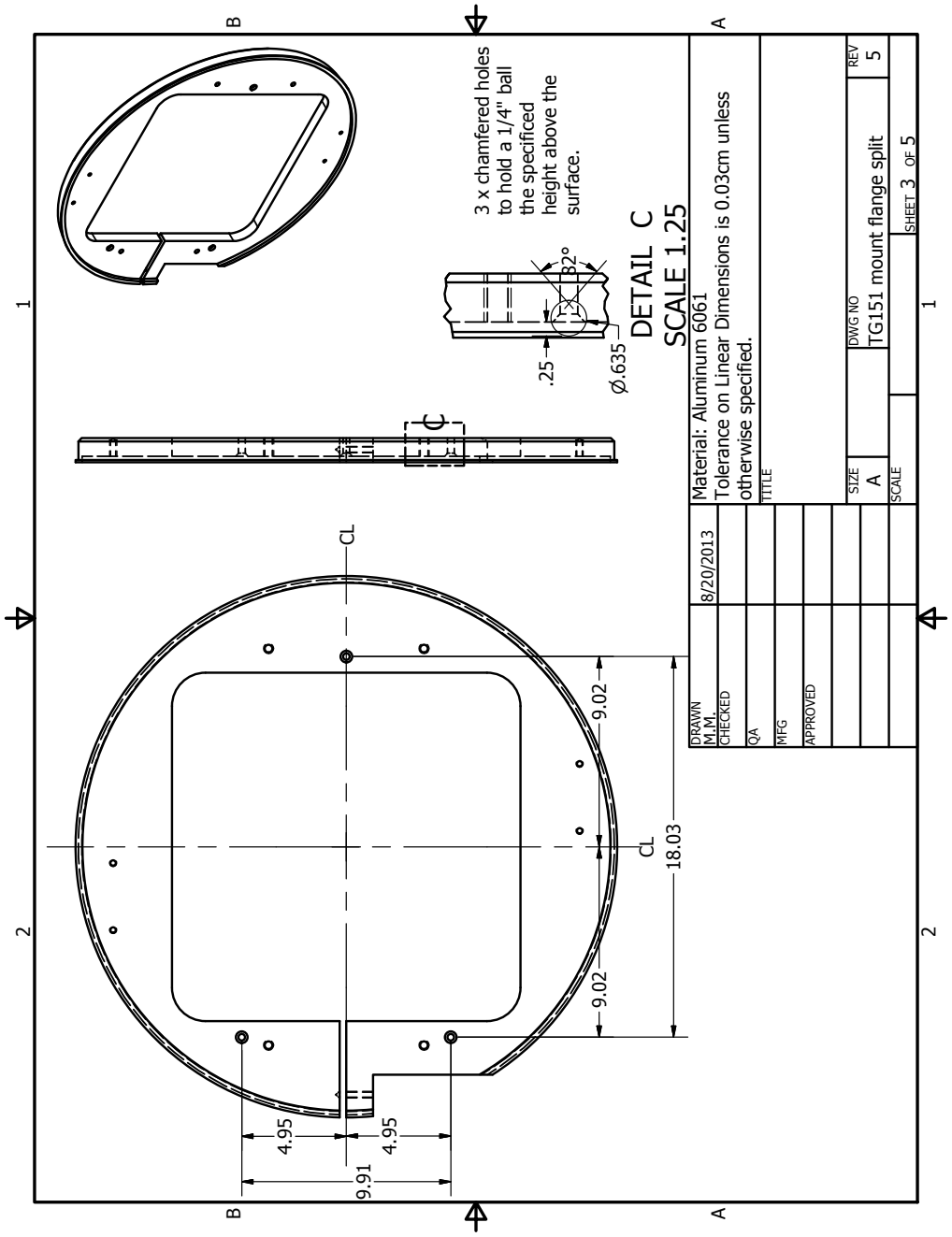

Figure B.22: Split Mount Plate

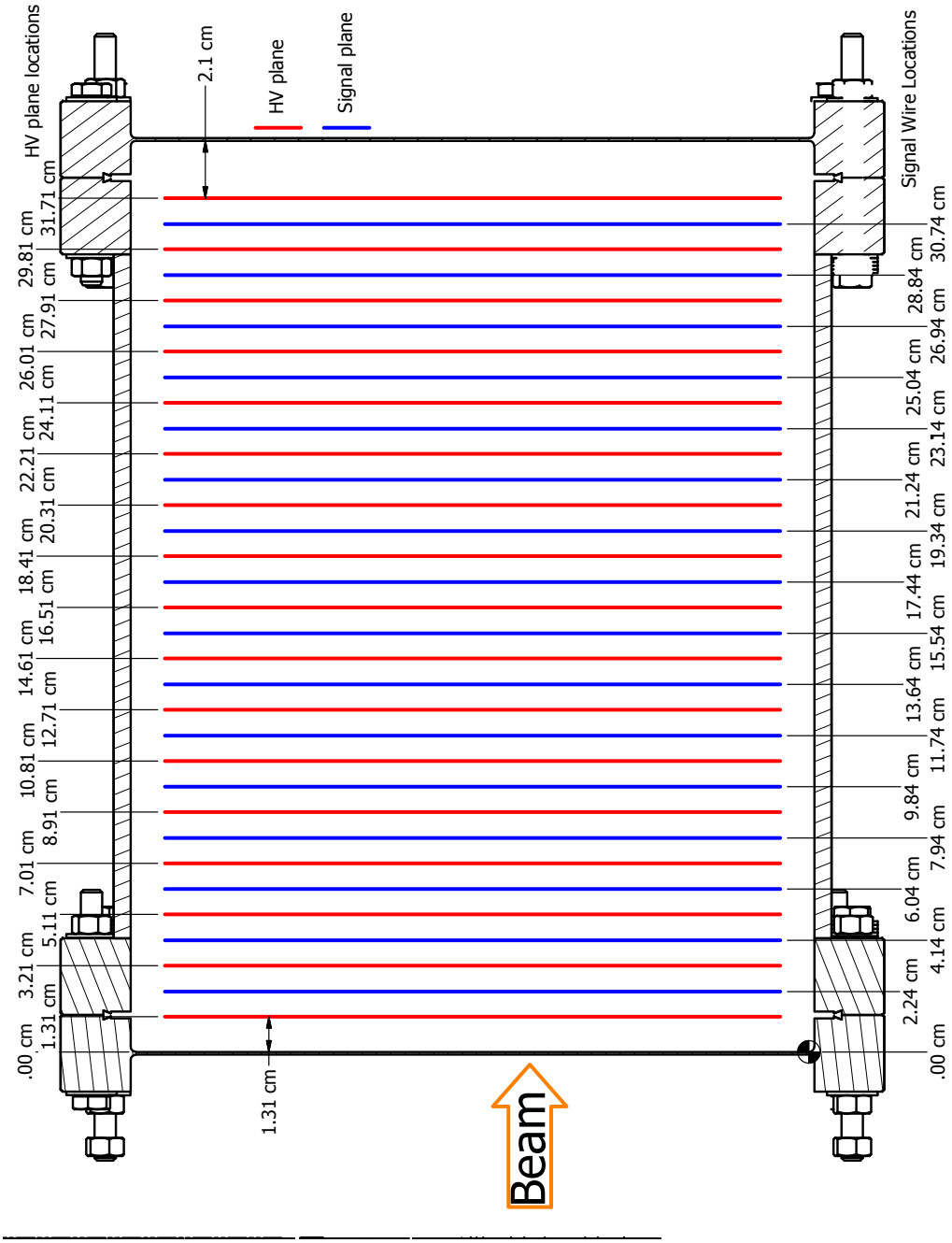

Figure B.23: n3He Frame Stack Wire Plane Locations

Appendix C

Wire Frame Stress Analysis

For the wire frames a stress analysis was performed using Autodesk Inventor 2014. The stress simulation uses finite element analysis methods to make stress and deformation calculations for parts with user determined shapes, constraints, and applied forces.

The first stage of the analysis is the setup of forces on the part. As signal frames would have the largest forces with 9 wires, and the maximum wire tension is 2 kg as calculated in section 4.1 from the wire cross section and yield strength. Two forces of 18 kg directed along the grooves in the wire frames towards the center of the frame were used. This created a set of balanced forces similar to what would be required to hold the wire in tension across the frame.

The second stage is to setup the constraints on the part motion. If the forces are not exactly balanced on the part sufficient constraints must be made to the part to reduce its degrees of freedom so that the simulation can be done. 2 fixed point constraints were used placed on the frame along the central line of the wire frame to

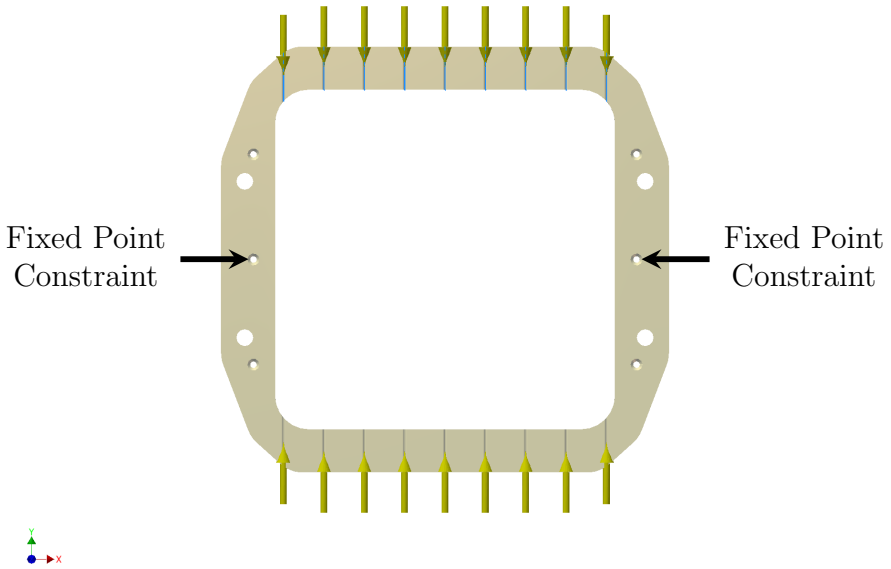

Figure C.1: Each group of 9 yellow arrows indicates where one of the 18 kg forces was distributed. The fixed point constraints were placed on the interior of the two three point mounts holes that are indicated by the arrow black arrows.

prevent rigid part motion such as sliding or rotation. These constraints were chosen so as to not interfere with the anticipated bowing of the frame.

From the standard macor ceramic thicknesses that are commercially available 0.125 inch, 0.1875 inch, and 0.25 inch thick frame designs were evaluated. The safety factor was used to evaluate if a frame thickness was usable. The safety factor is von Mises stress in the part divided by the yield strength of the material, and if it is lower than one in a frame section the part would undergo permanent deformation. Von Mises stress is an equivalent stress that relates the 3D dimensional stress and strain in the part in a single value. A minimum safety factor of $2 - 4$ is preferred in most

designs to allow for unexpected loads or shocks during and after assembly.

For the simulation an initial mesh is generated from the part model and then refined in areas where the forces were large or changed sharply. The refinement process increases the detail of the mesh in those areas to allow more accurate calculations. The refinement is repeated on each new mesh until the convergence criteria are reached, usually that the calculated von Mises stress changes by less than a certain percentage between refinements. If the model is working correctly the simulation results will converge over successive refinements, but it is possible for convergence to fail particularly in the presence of sharp edges. By examining the results over a range of refinement conditions the model can be verified.

To ensure the simulation is converging correctly the convergence was checked at 1% and 0.01% with a maximum of 10 refinement stages being allowed as shown in fig.C.2. While both converged according to the simulation criteria, it can be seen that the 0.01% requirement is converging towards a higher value, and is not converging smoothly.

As stress is concentrated in the wire grooves by increasing the mesh detail there before starting the refinement process convergence can be improved as shown in fig. C.3a. Since sharp corners in the model can cause problems in the FEA simulation a further improvement to convergence can be made by adding a radius to the the upper edges of the V groove, but this can reduce the maximum stress by removing the stress risers that occur at sharp edges the total stress can be somewhat underestimated. Since this seems to converge well and rapidly this setup was used for the frame stress calculations. As shown in fig. C.3b the use of the increased mesh detail and radiused

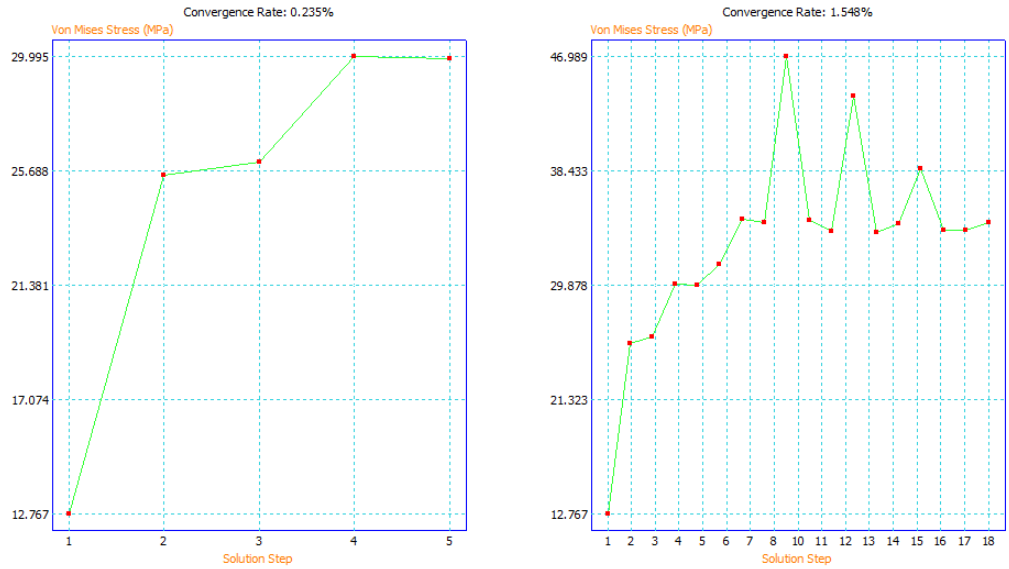

(a) 1% Convergence

(b) 0.1% Convergence

Figure C.2: Convergence plots of von Mises stress at different convergence requirements for the 1/4 inch thick frame. As can be seen in plot (b) the stress values are not converging smoothly and has increased significantly compared to plot (a).

corners converges smoothly, and is probably an accurate calculation.

The minimum safety factors of of the 0.1875 inch and 0.25 inch frames are both close to 2, and either would be usable. The 0.125 inch frame design is nearly 1, and would be excessively fragile even unstrung as the wire locator grooves have a depth of nearly half the thickness of this frame design.

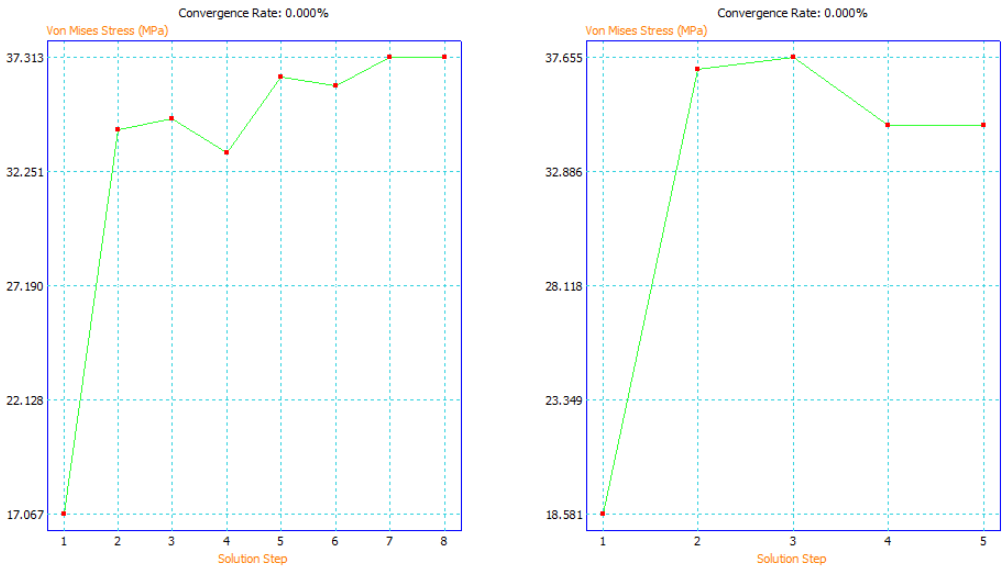

(a) Increased Mesh Detail (b) Increased Detail and Rounded Corners

Figure C.3: Stress convergence plots with modifications made to improve convergence.

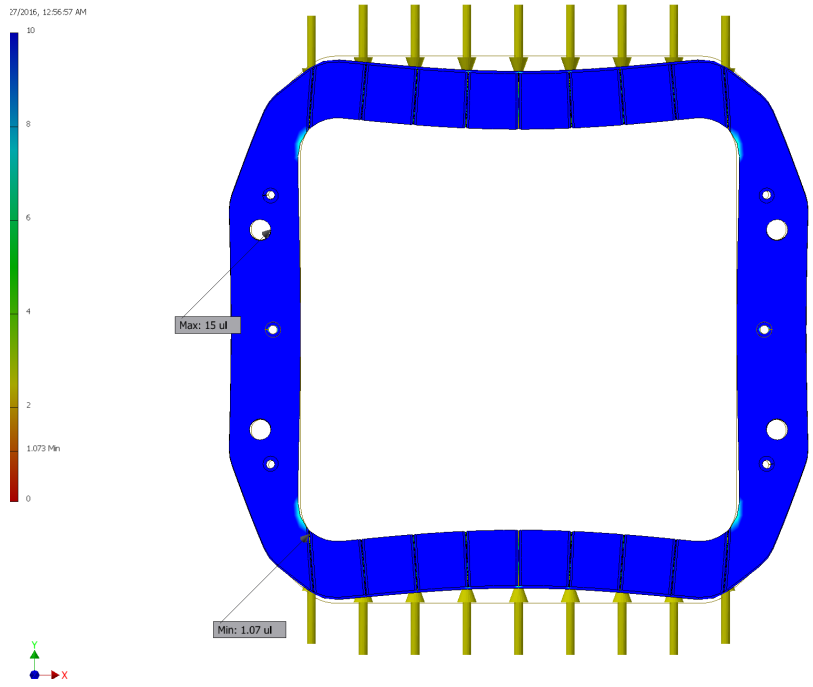

Figure C.4: Safety Factor of 1/8 inch frame design.

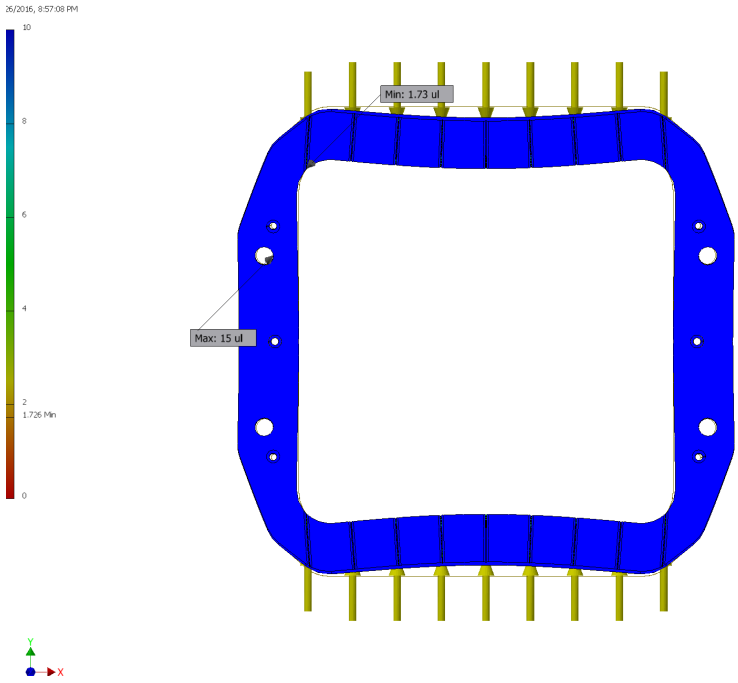

Figure C.5: Safety Factor of 3/16 inch frame design.

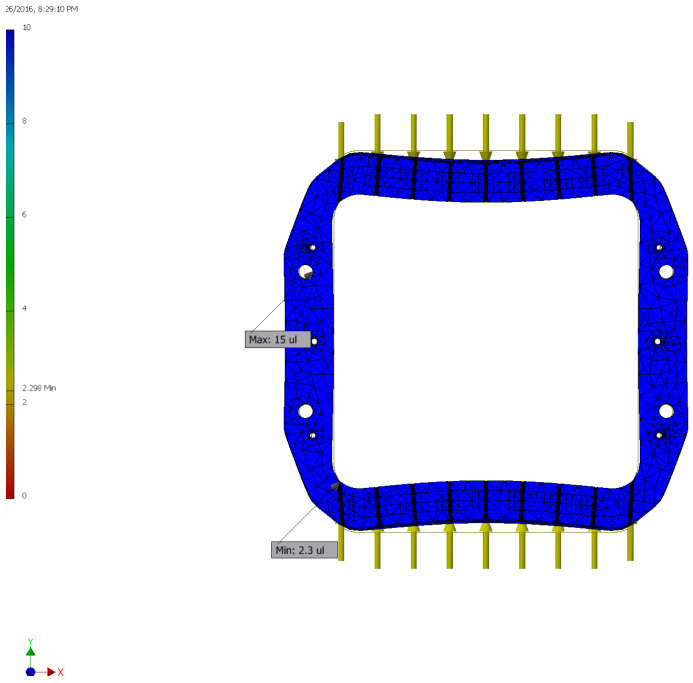

Figure C.6: Safety Factor of 1/4 inch frame design.

Appendix D

n3He Target Chamber

D.1 Parts and Assembly

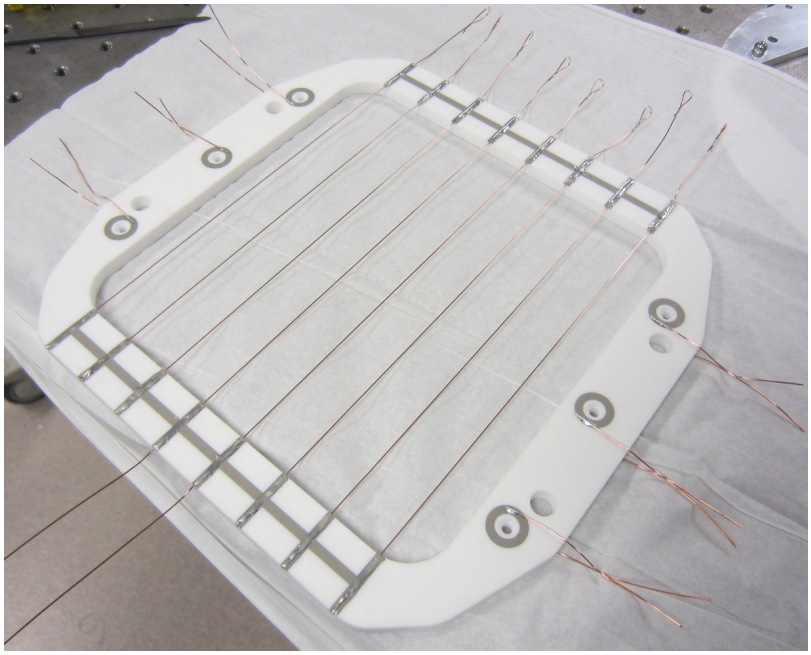

Figure D.1: Wire HV plane. Some wire ends have been clipped in preparation for assembly to the frame stack.

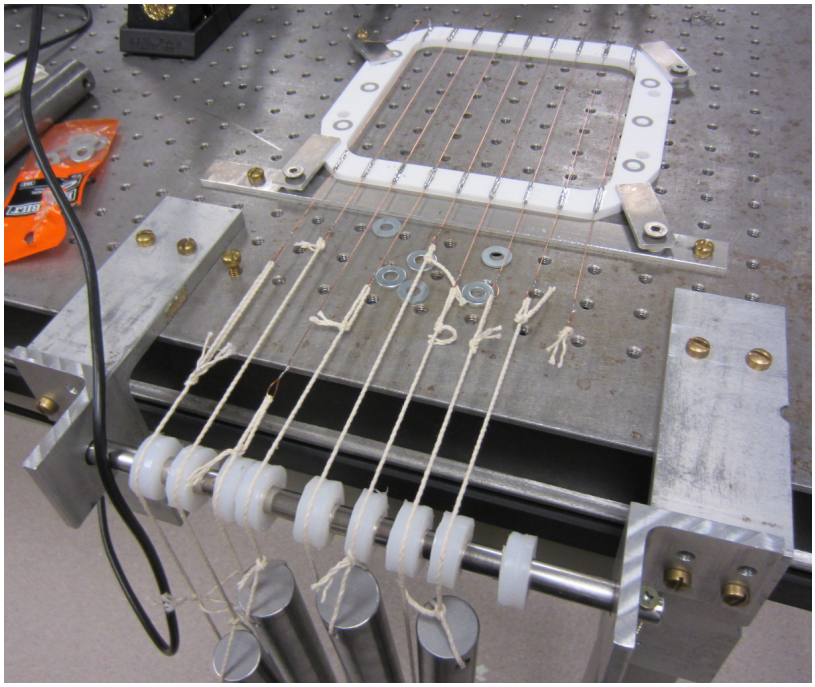

Figure D.2: Signal plane setup during soldering.

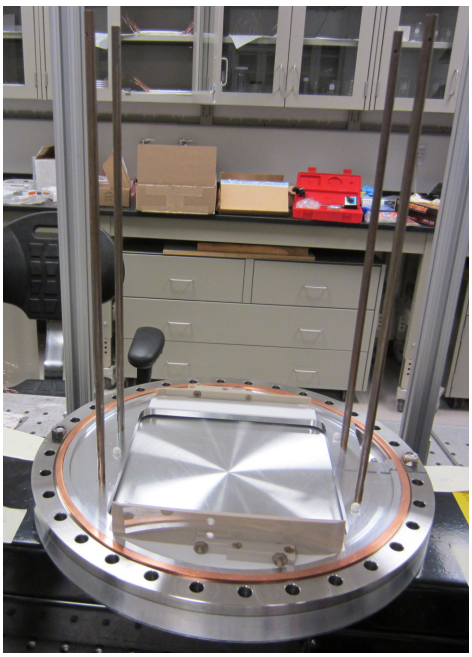

Figure D.3: Starting assembly with mount plate on window and compression rods.

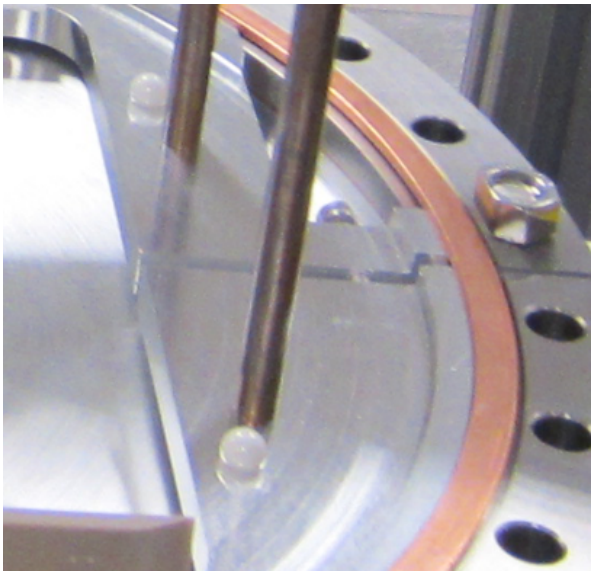

Figure D.4: Close up of ball and cone mounts from right side of mount plate.

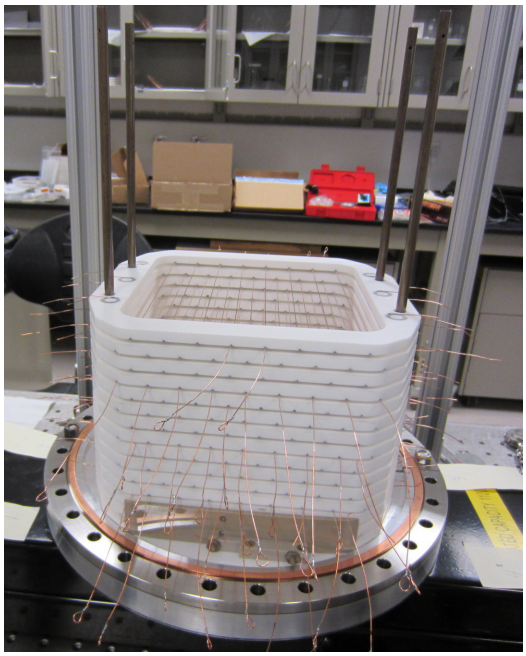

Figure D.5: Initial wire planes placed onto mount plate.

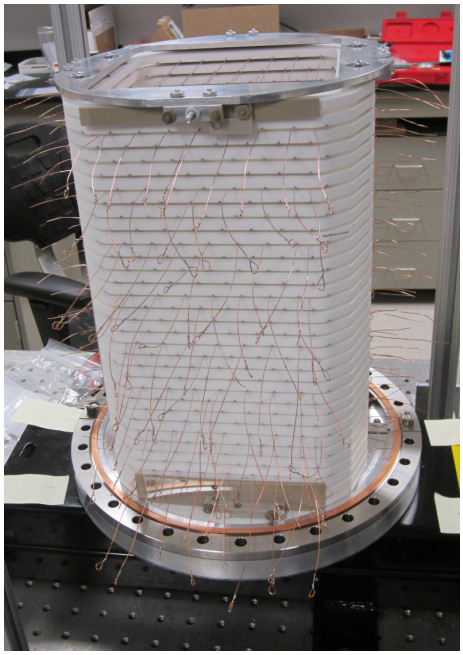

Figure D.6: Completed frame stack with compression plate on top.

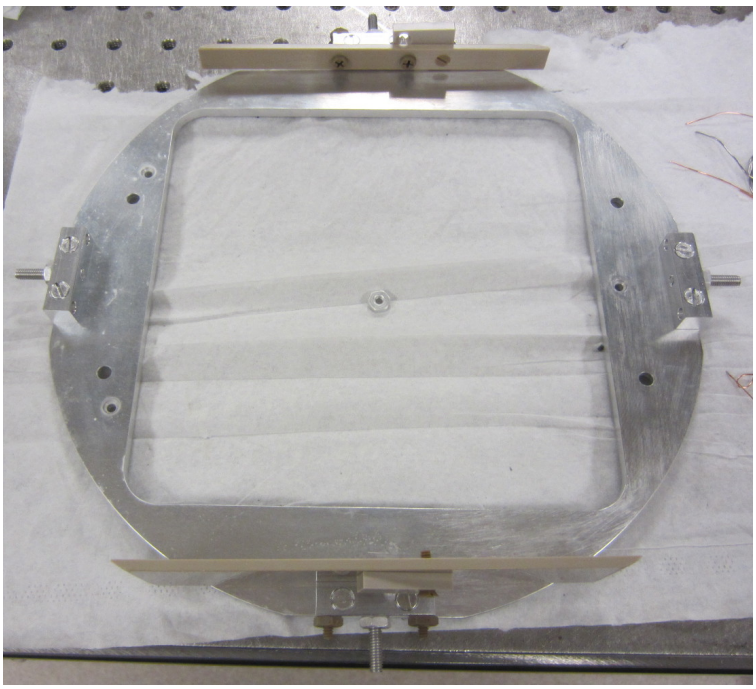

Figure D.7: Compression plate with attached HV shielding.

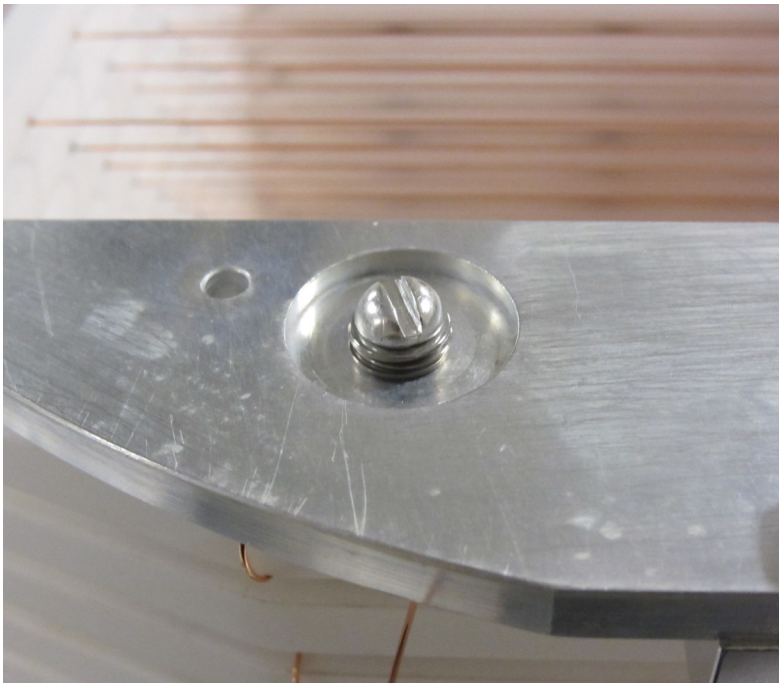

Figure D.8: Close up of bellville spring washers on compression plate.

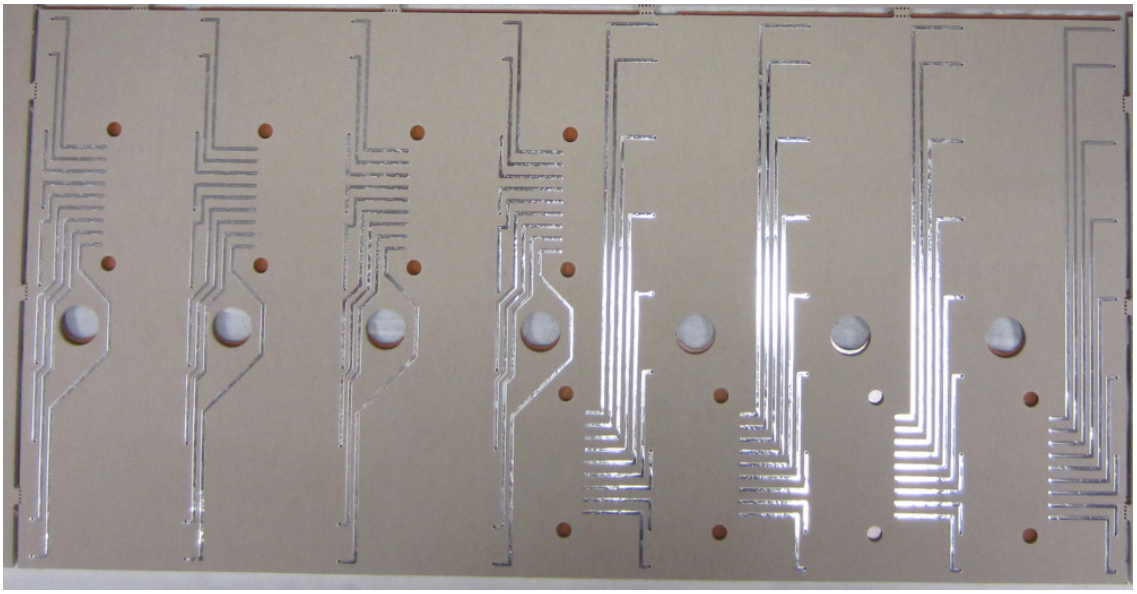

Figure D.9: One of the printed circuit boards used for the signal readout.

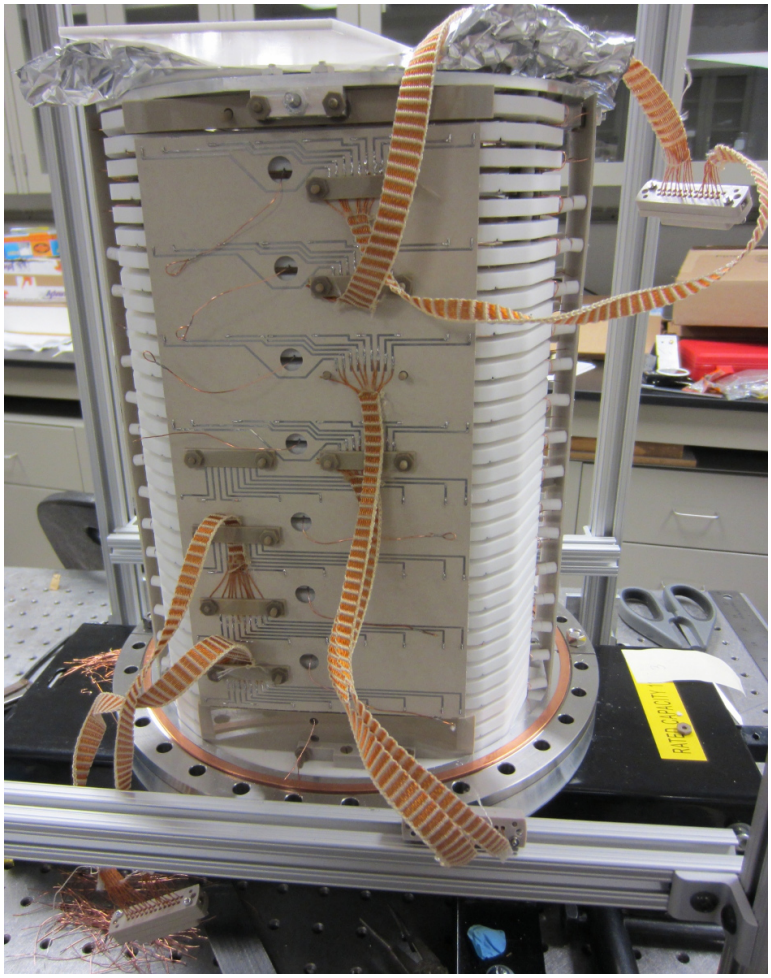

Figure D.10: One of the two signal read out boards soldered to signal planes. The brown peak stress relieving clamps are attached to the board. These were used to prevent damage to the solder joints while pulling the cables through the feed throughs on the housing.

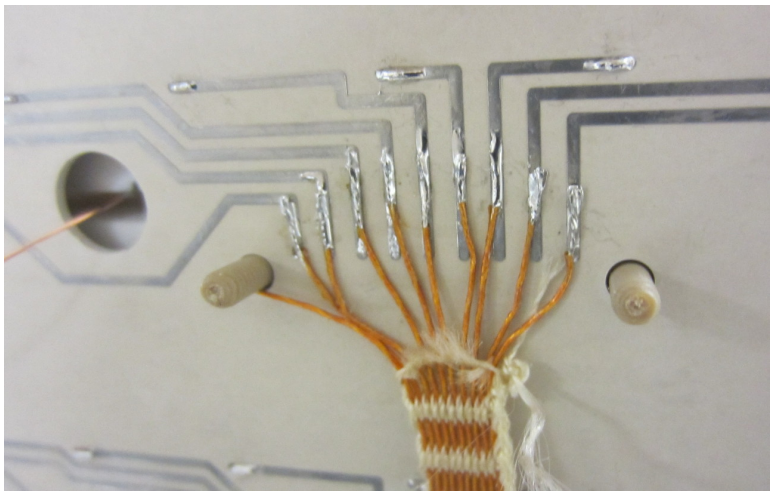

Figure D.11: Close up of kapton ribbon cable soldered to signal readout board.

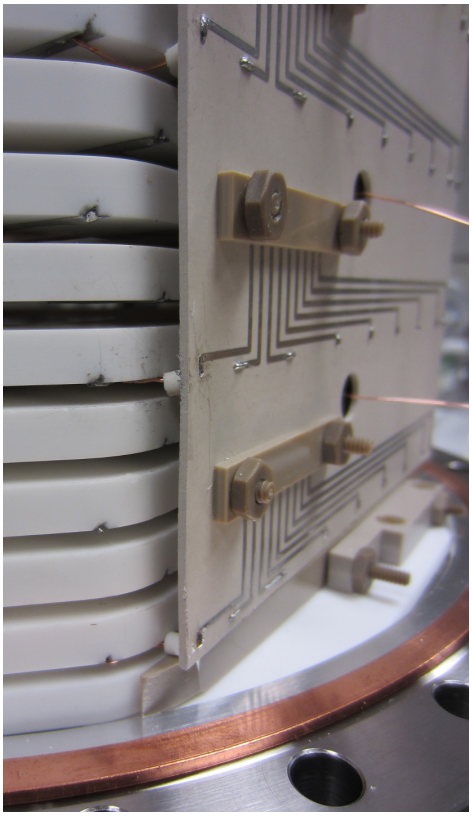

Figure D.12: Edge of signal read out PCB with one of the spacer beads visible.

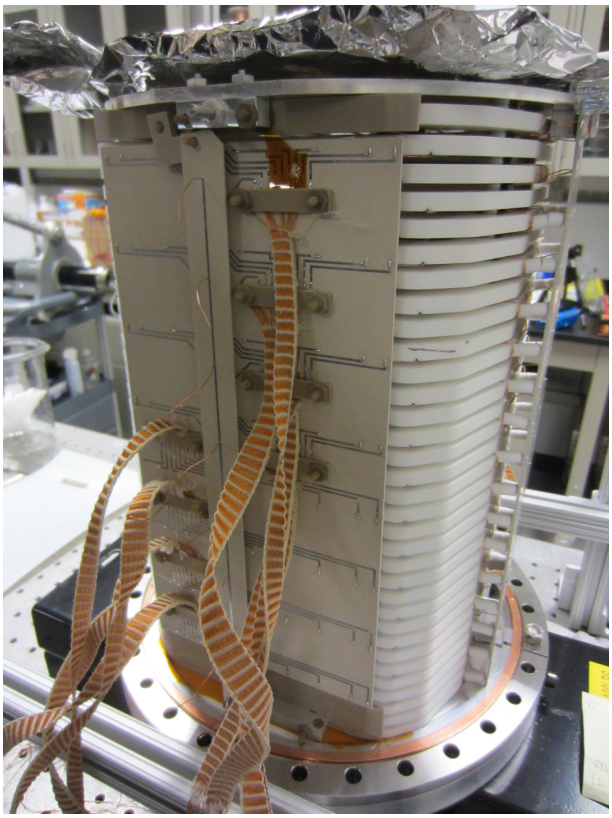

Figure D.13: HV distributor PCB being soldered into place.

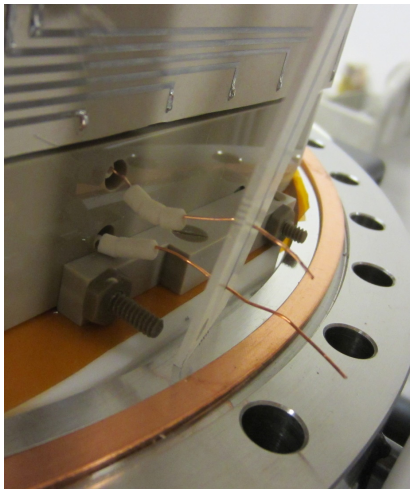

Figure D.14: Close up of ceramic insulating beads used to shield the HV wire and space it from the HV plane.

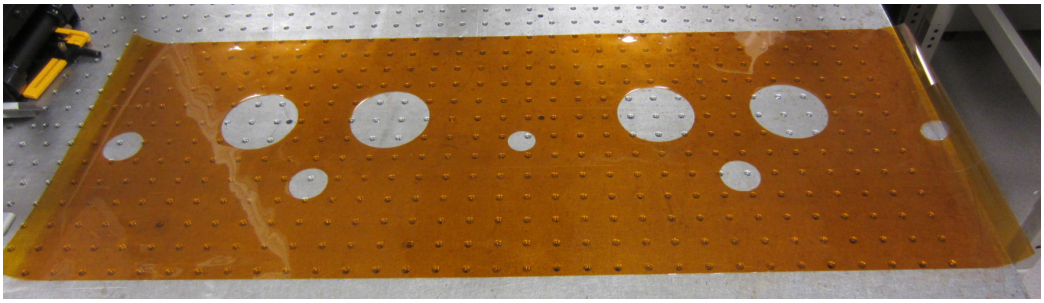

(a) Kapton shielding for the interior of housing with holes cutout for housing feed throughs.

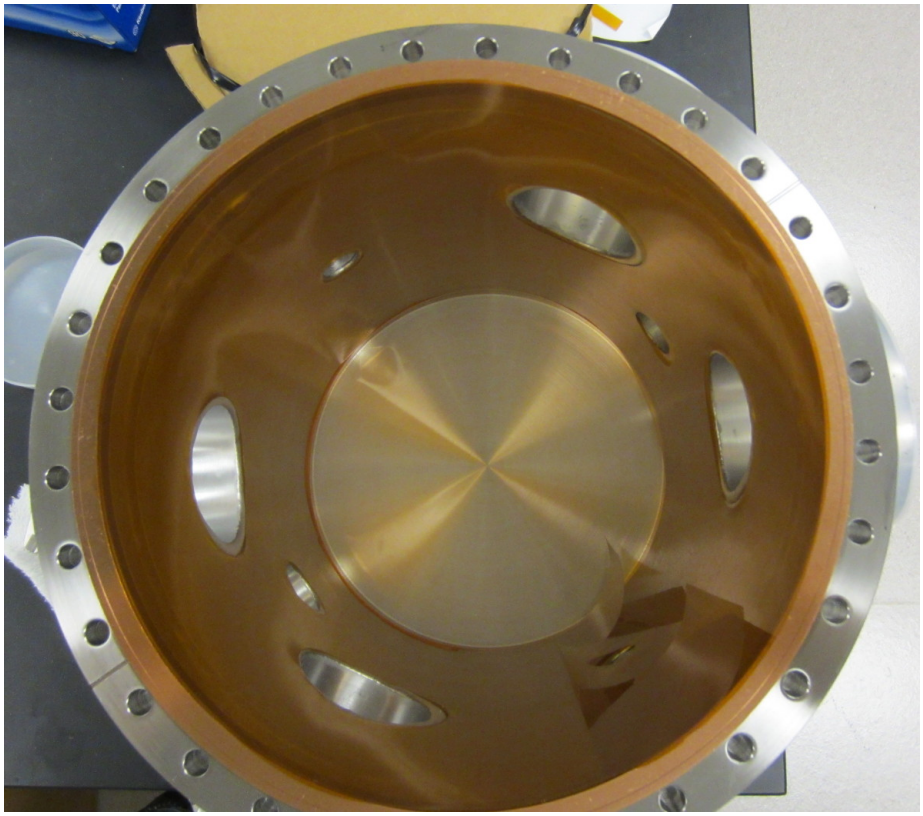

(b) Test fit in housing.

Figure D.15: A kapton shield was made to shield between the grounded housing and the HV by cutting holes in a kapton sheet to allow access to the feed throughs from from the frame stack.

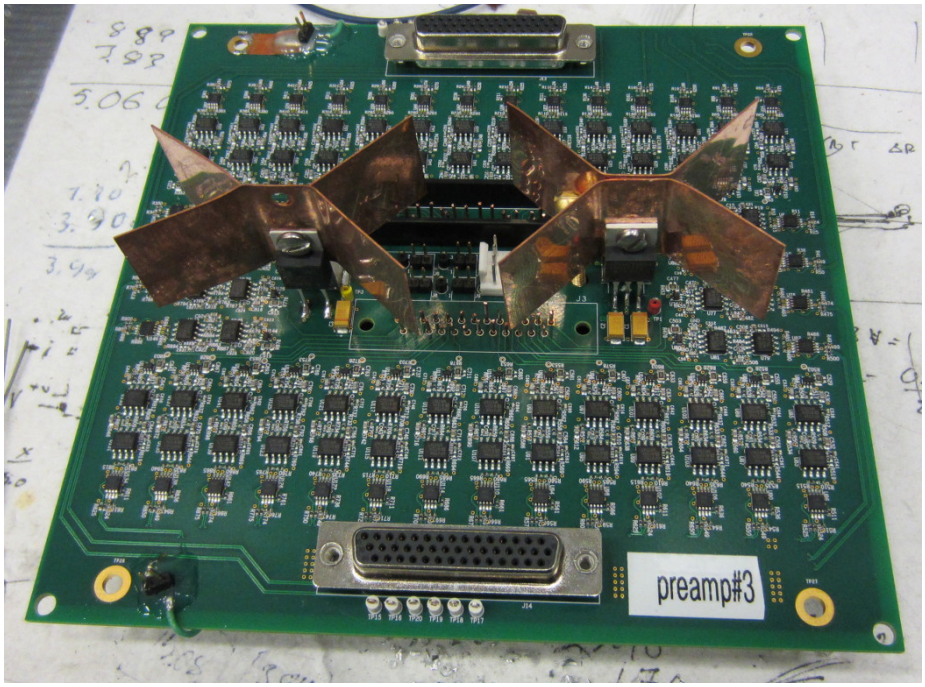

Figure D.16: Preamp Board Top side.

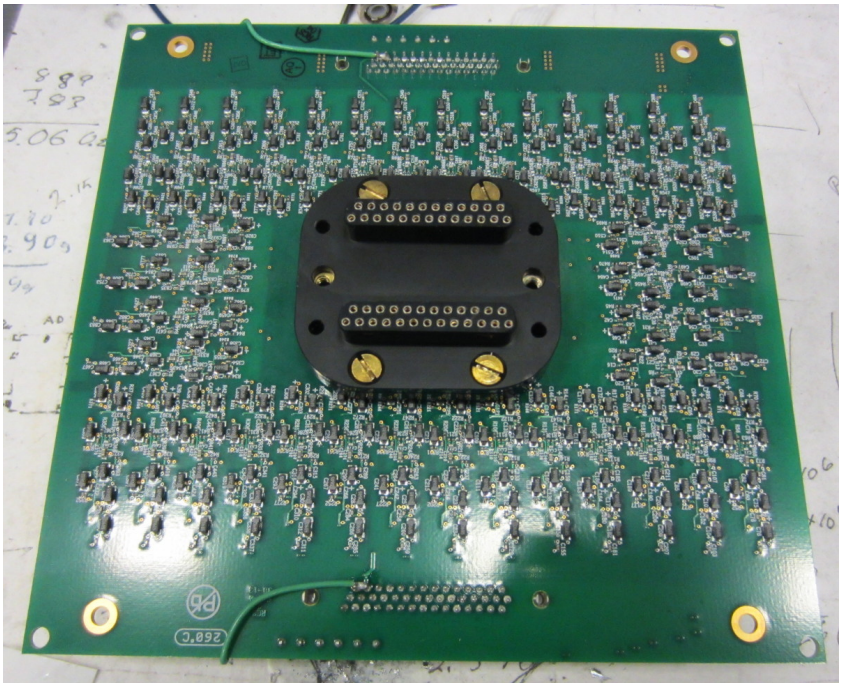

Figure D.17: Preamp board bottom with double 25 pin Dsub adapter plug.

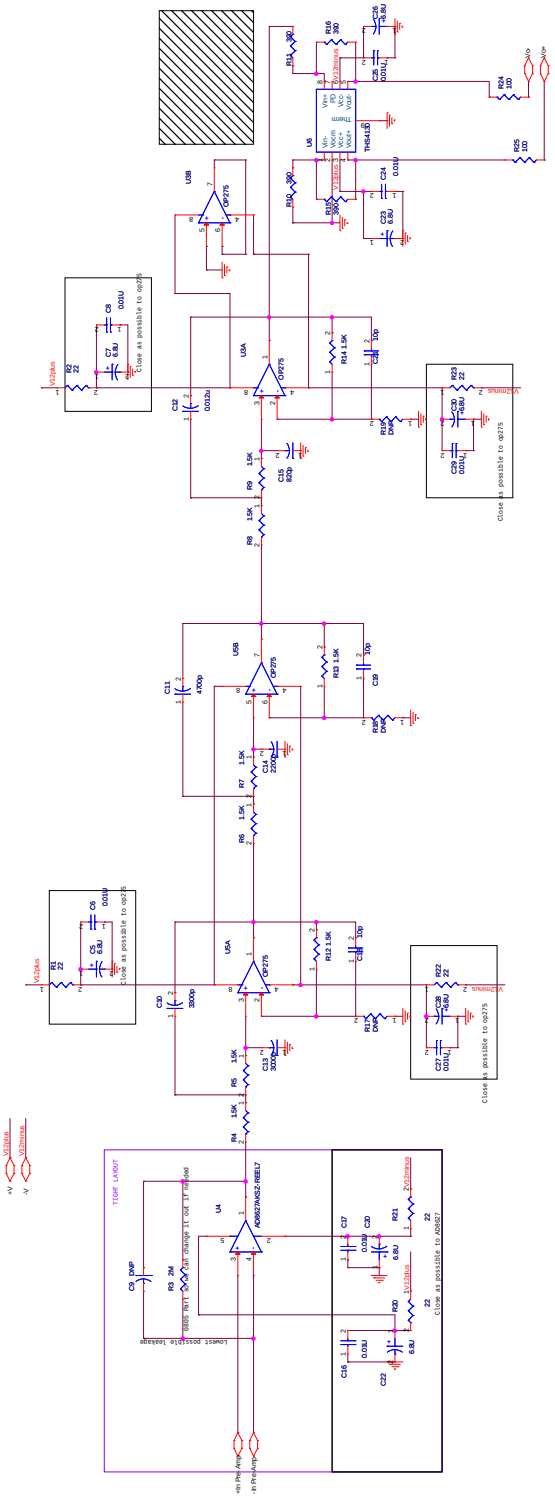

Figure D.18: Preamp Circuit Diagram. There are 36 preamps per board.

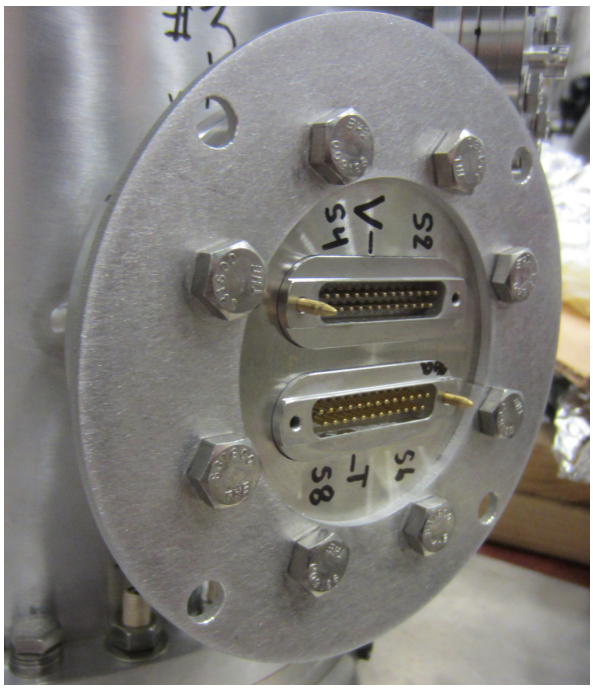

Figure D.19: Signal flange with guide pins and preamp housing mount plate.

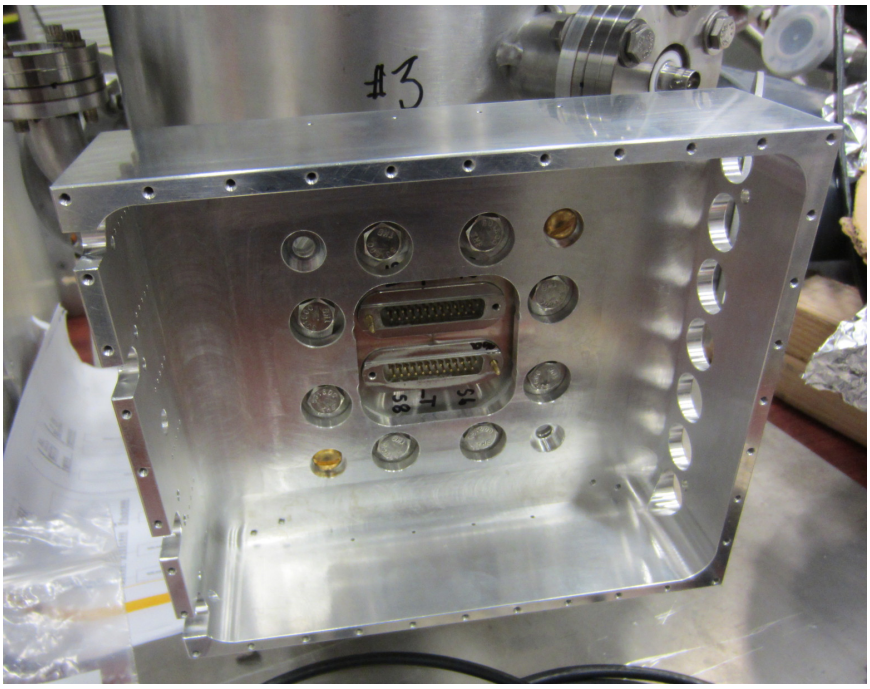

Figure D.20: Preamp housing mounted on signal flange.

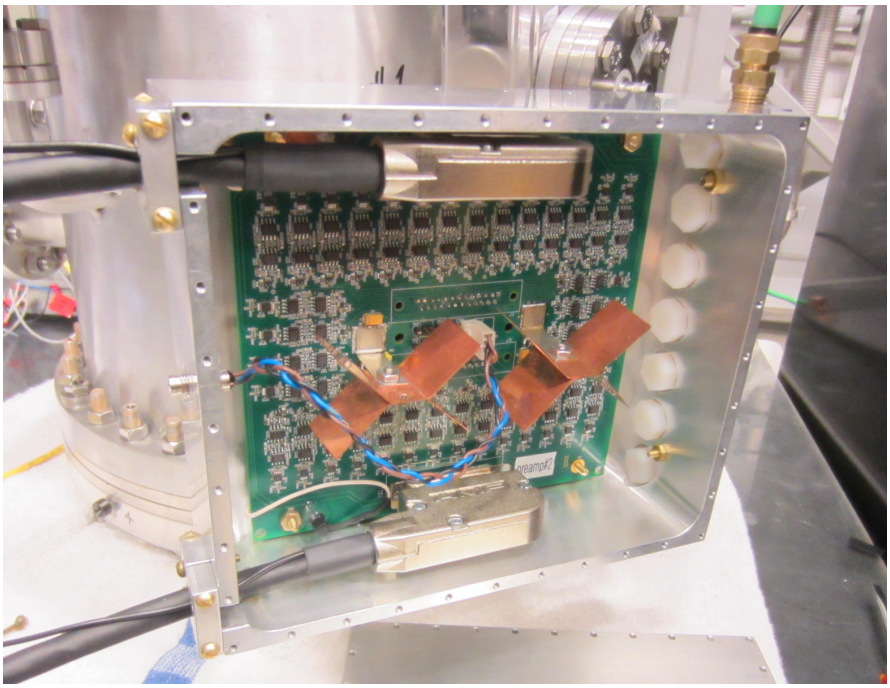

Figure D.21: Preamp board and cables connected to housing.

D.2 Wire Map

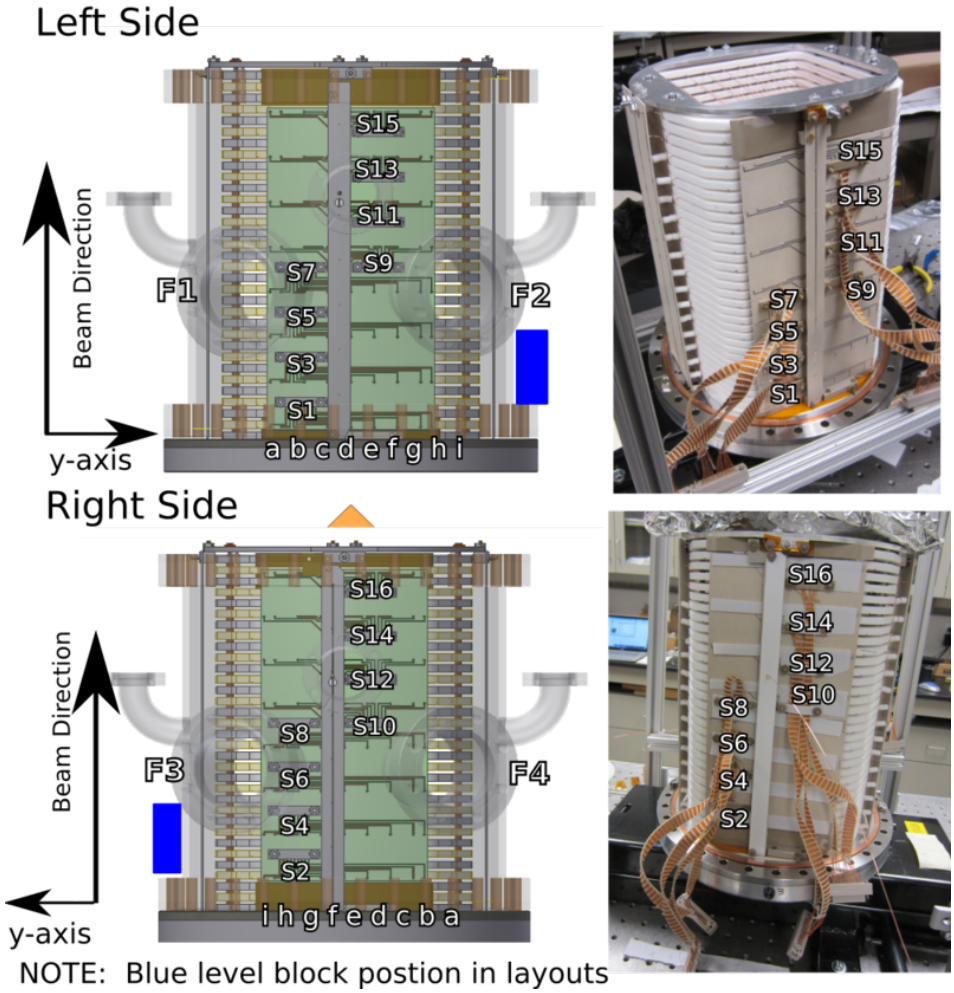

Figure D.22: Wire plane read out cabling. The blue rectange indicates the position of the leveling block on the target housing.

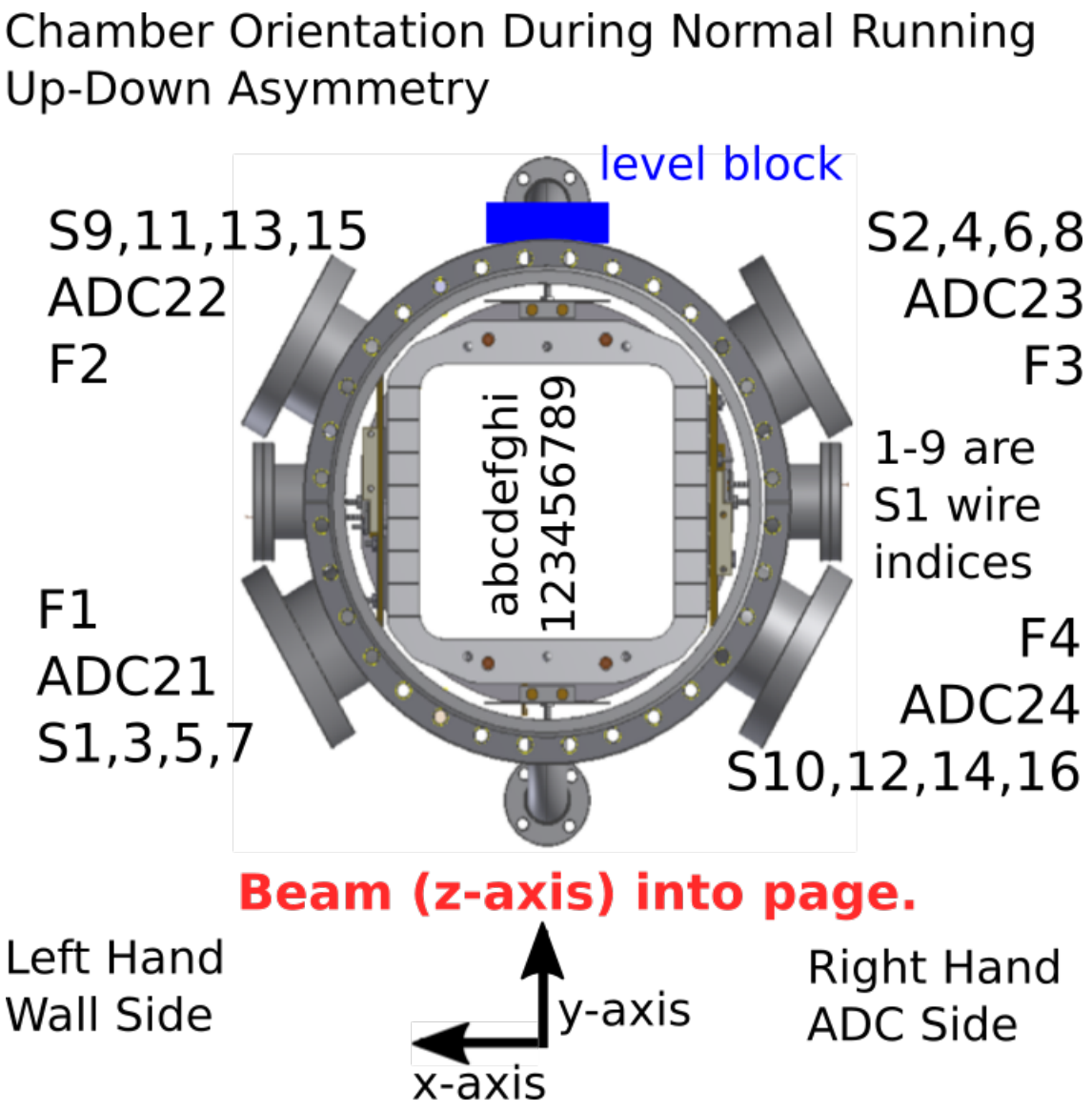

Figure D.23: CAD model of wire chamber orientation and cabling during PV asymmetry running.

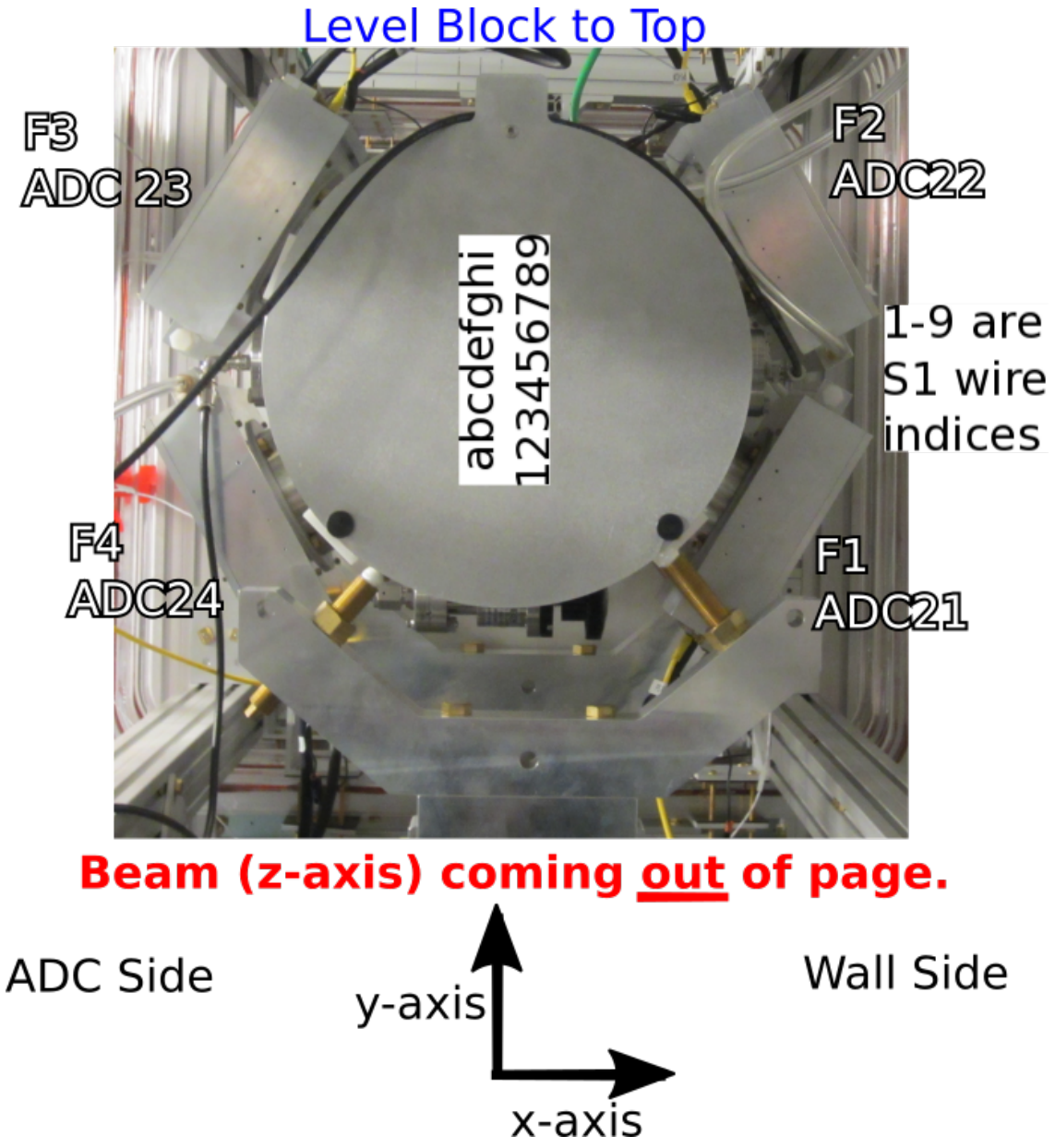

Figure D.24: Wire chamber orientation and cabling during PV asymmetry running.

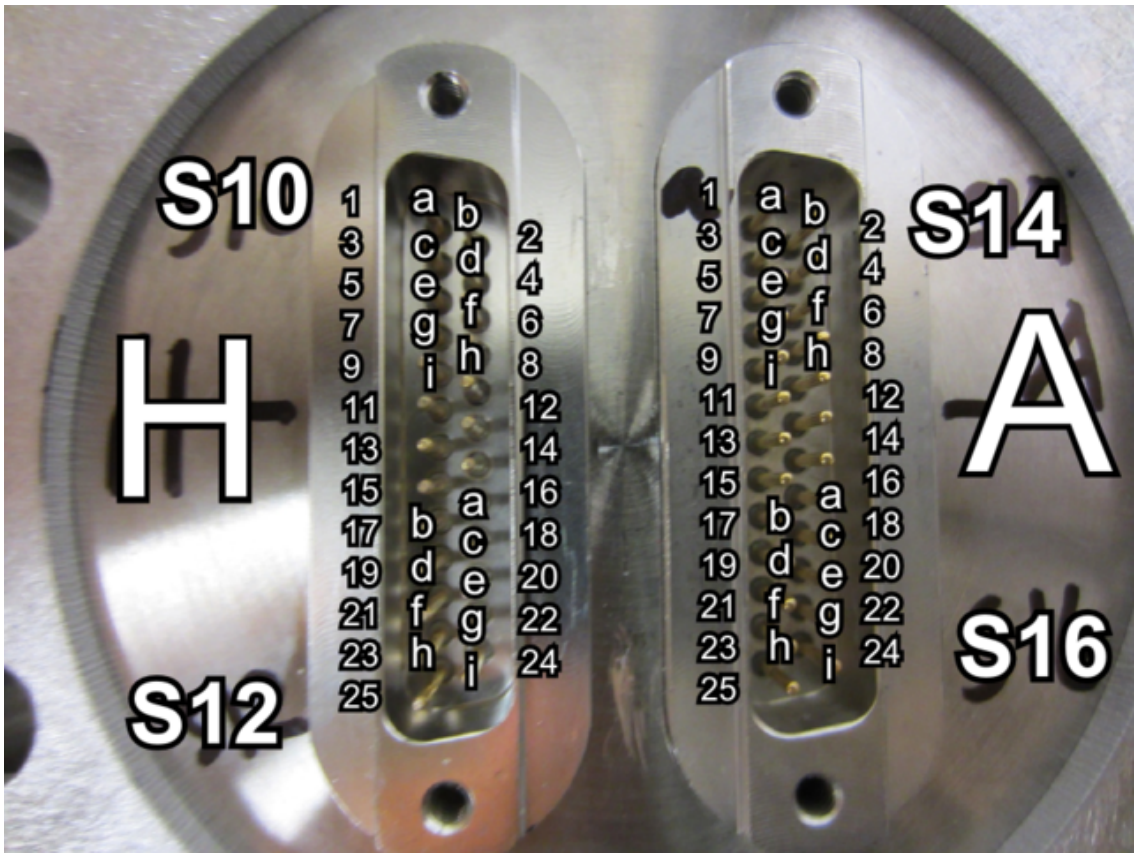

Figure D.25: Each flange had 4 connected signal cables that (labeled A and H on this feed through) that each had 2 signal planes connected. For the Dsub pins labeled 1-25 the pin connected to the wire planes are labeled a-h.

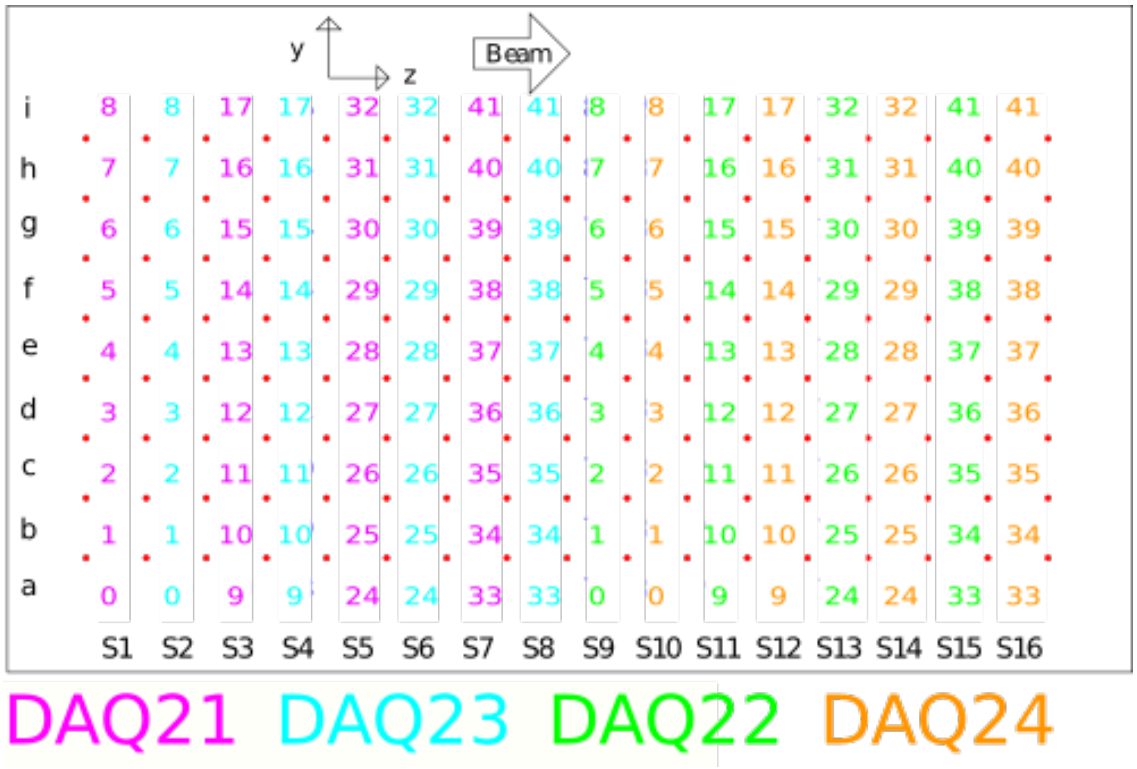

Figure D.26: Signal wire position to DAQ channel map.

Appendix E

n3He Target Voltage Scans

E.1 Fitting Parameters Plotted vs Wire Number

Fit parameters from n3He target chamber voltage scan in section 5.7. The plot are of the parameters for equations 5.8 and 5.9 being fit to the 144 signal wires.

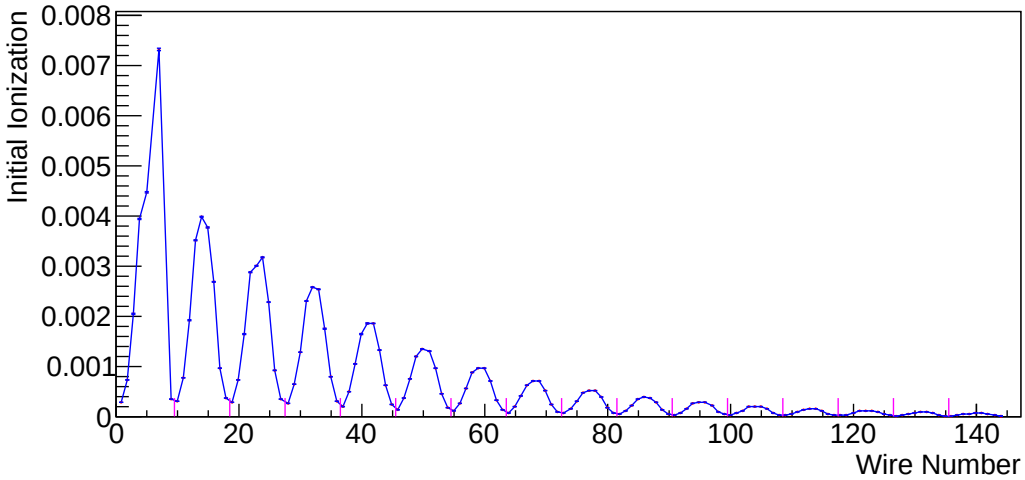

Figure E.1: I is related to the initial ionization in the cell.

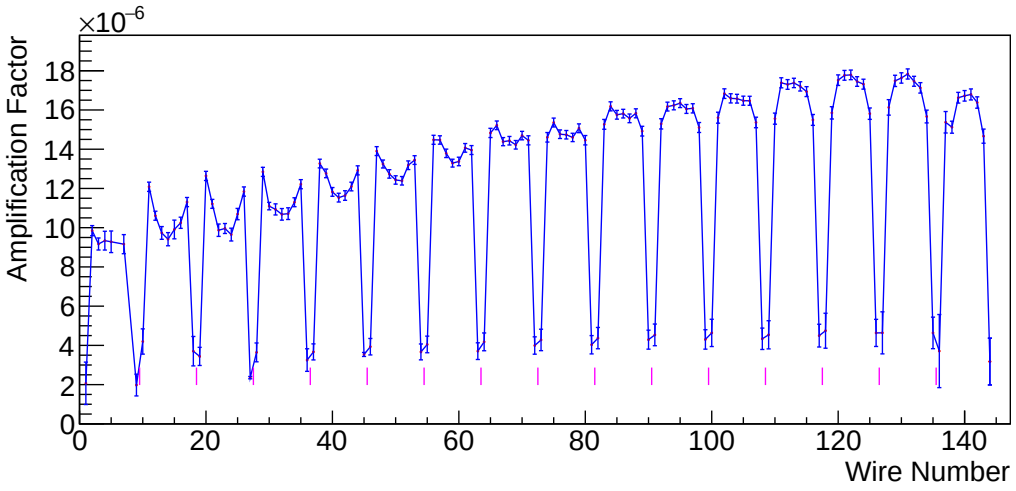

Figure E.2: The amplification factor from the fits for all wires.

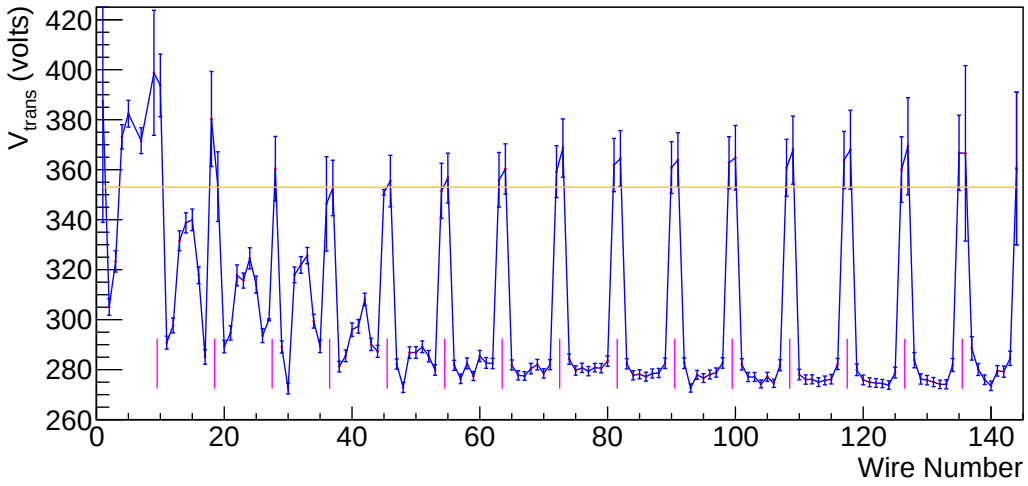

Figure E.3: The bias voltage for the transition to the amplification voltage region as determined from the fits.

E.2 Selection of Fits

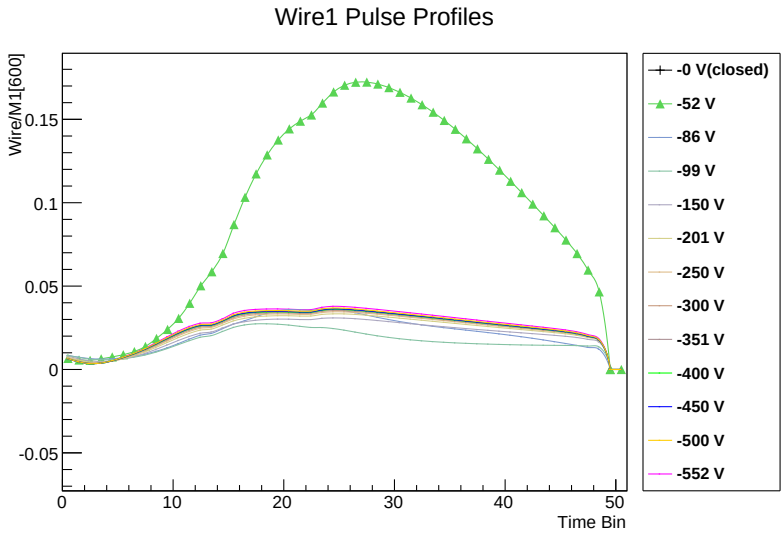

(a) Wire 1 pulse profiles for each run overlayed in one plot.

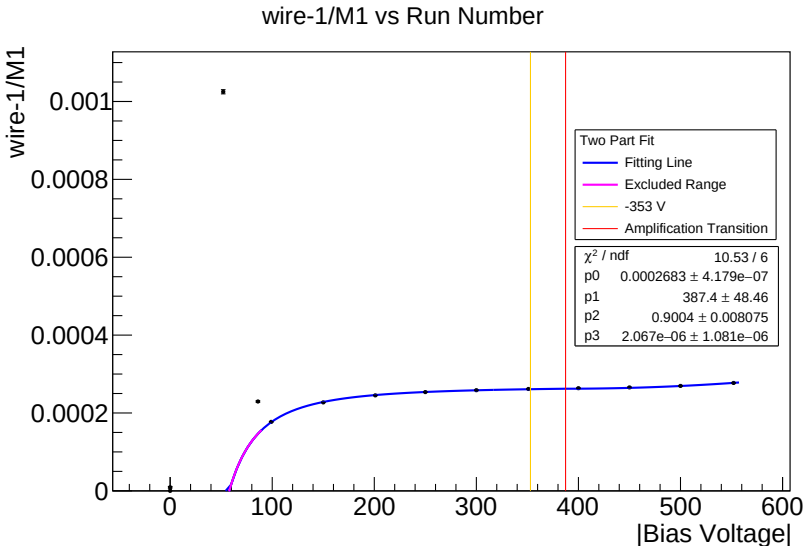

(b) Wire 1 integrated signal divided by M1 integrated signal plotted vs applied bias voltage.

Figure E.4: Wire 1 Voltage Scan

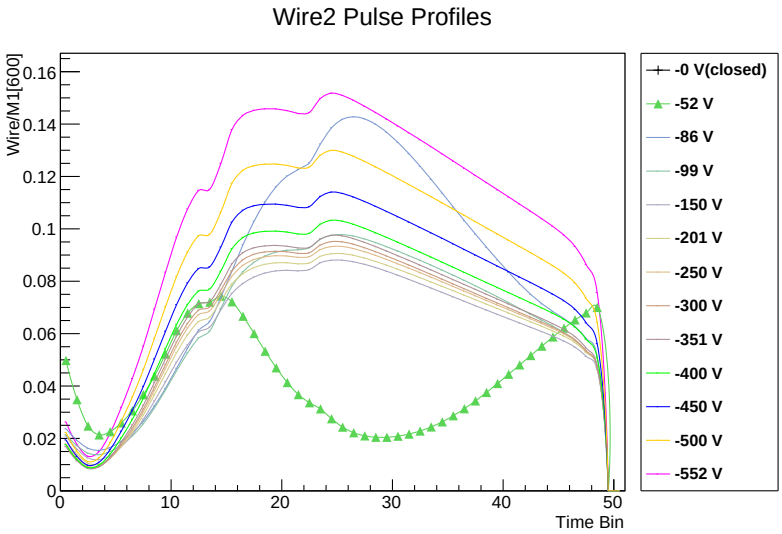

(a) Wire 2 pulse profiles for each run overlayed in one plot.

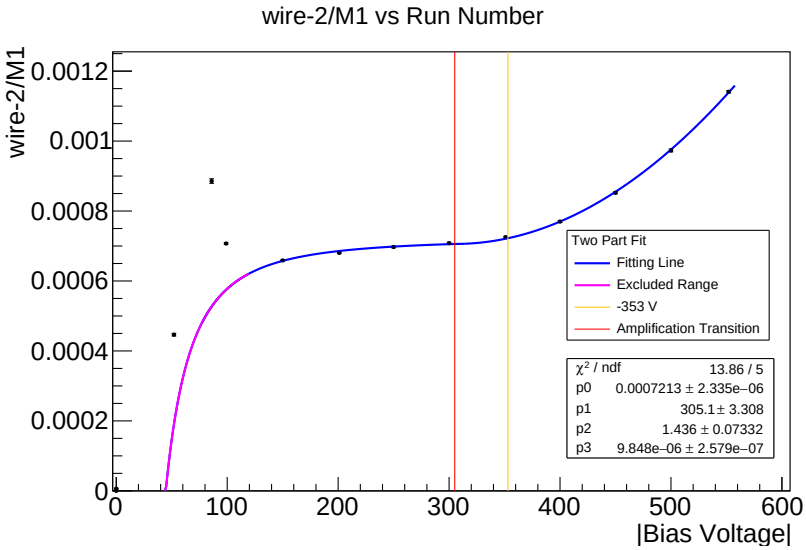

(b) Wire 2 integrated signal divided by M1 integrated signal plotted vs applied bias voltage.

Figure E.5: Wire 2 Voltage Scan

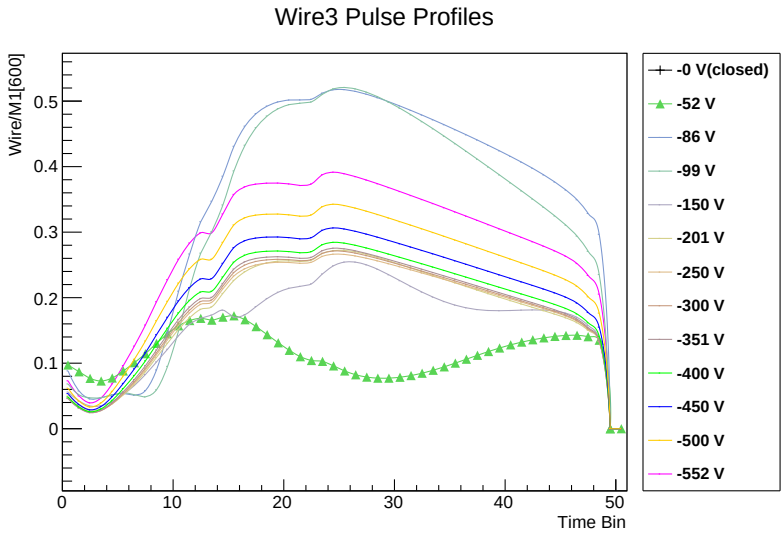

(a) Wire 3 pulse profiles for each run overlayed in one plot.

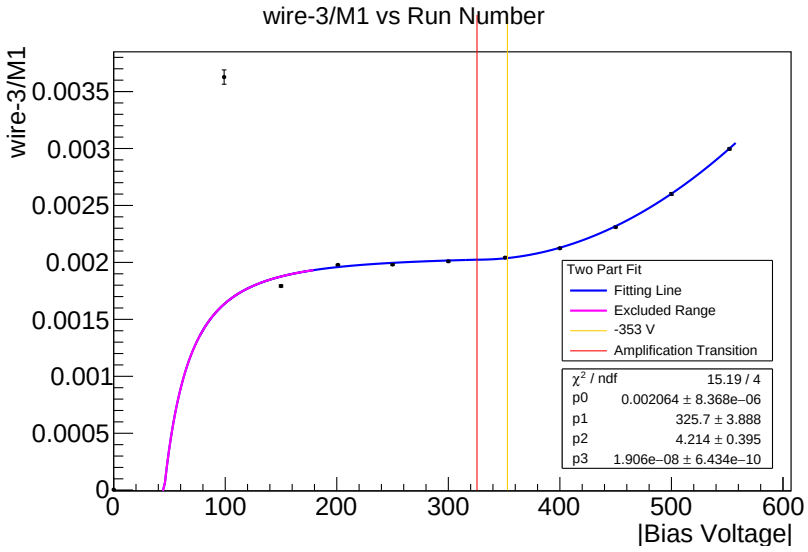

(b) Wire 3 integrated signal divided by M1 integrated signal plotted vs applied bias voltage.

Figure E.6: Wire 3 Voltage Scan

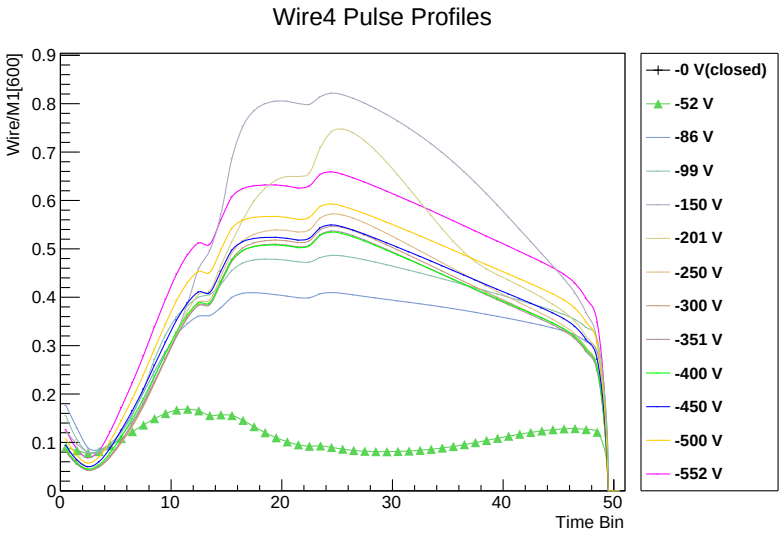

(a) Wire 4 pulse profiles for each run overlayed in one plot.

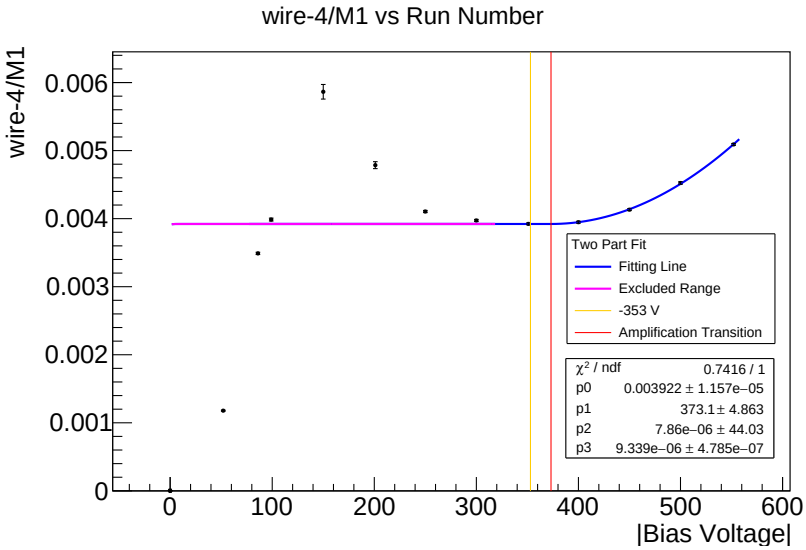

(b) Wire 4 integrated signal divided by M1 integrated signal plotted vs applied bias voltage.

Figure E.7: Wire 4 Voltage Scan

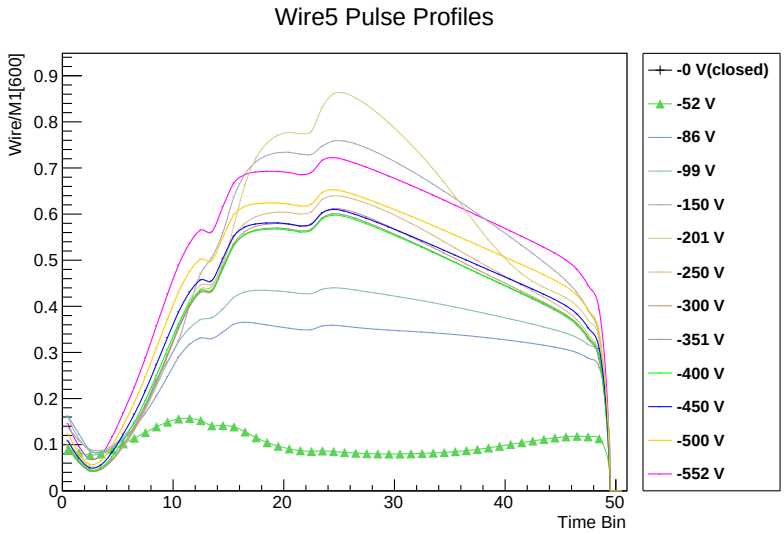

(a) Wire 5 pulse profiles for each run overlayed in one plot.

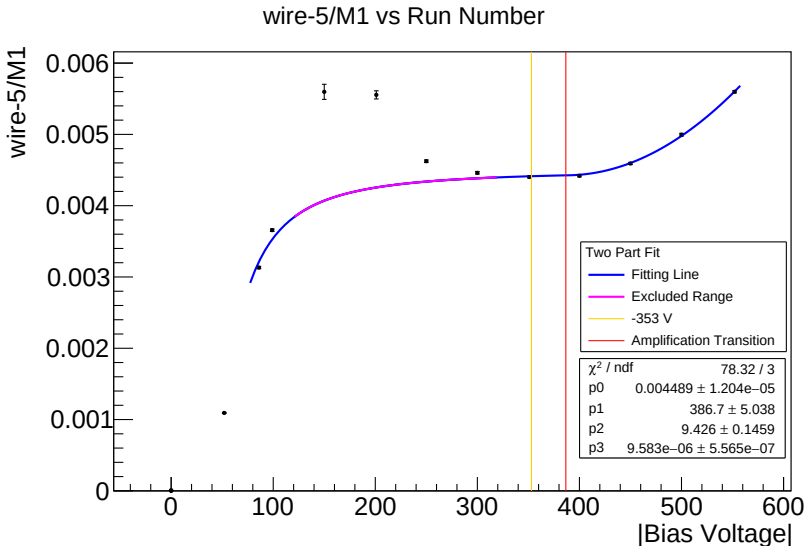

(b) Wire 5 integrated signal divided by M1 integrated signal plotted vs applied bias voltage.

Figure E.8: Wire 5 Voltage Scan

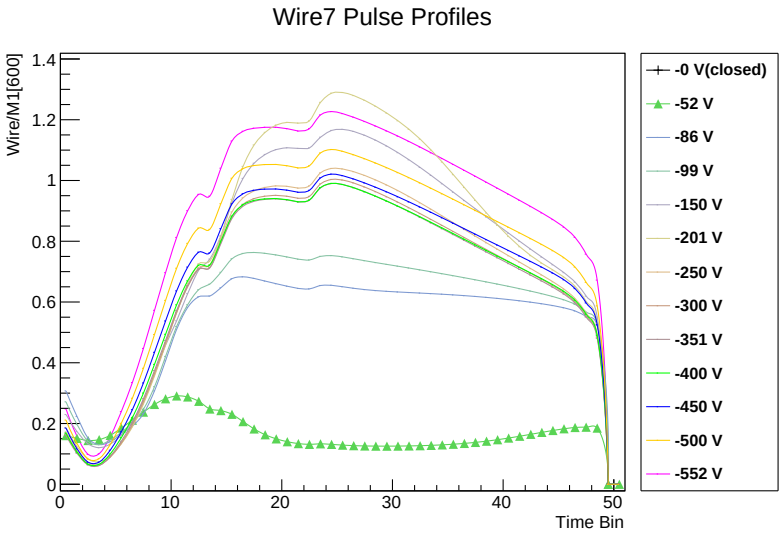

(a) Wire 7 pulse profiles for each run overlayed in one plot.

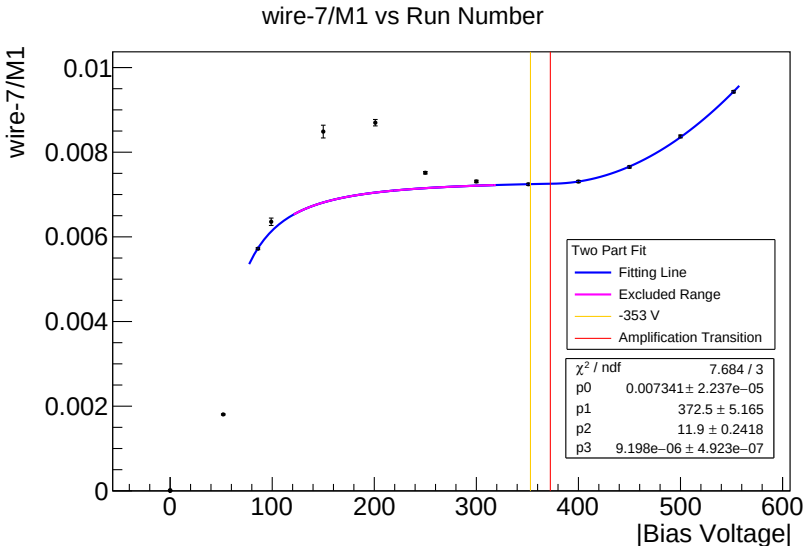

(b) Wire 7 integrated signal divided by M1 integrated signal plotted vs applied bias voltage.

Figure E.9: Wire 7 Voltage Scan

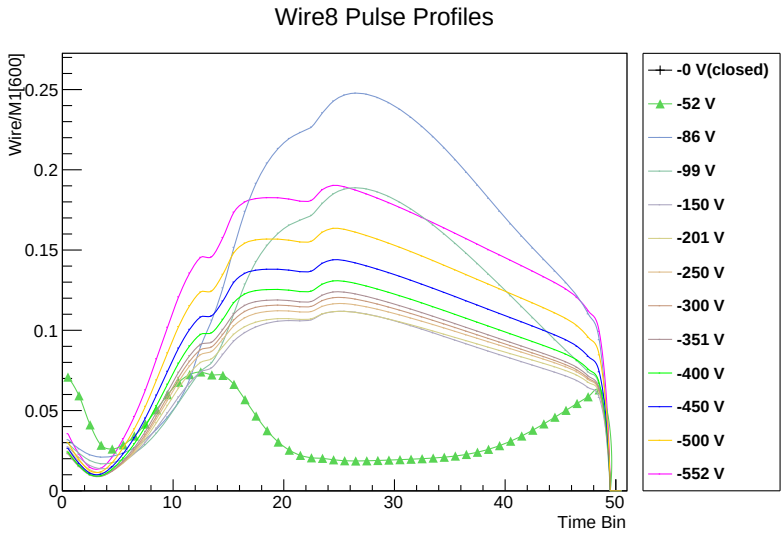

(a) Wire 8 pulse profiles for each run overlayed in one plot.

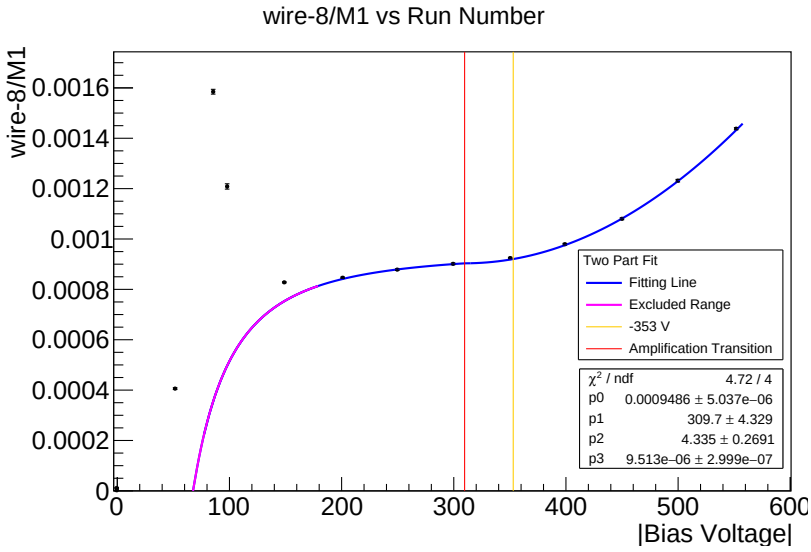

(b) Wire 8 integrated signal divided by M1 integrated signal plotted vs applied bias voltage.

Figure E.10: Wire 8 Voltage Scan

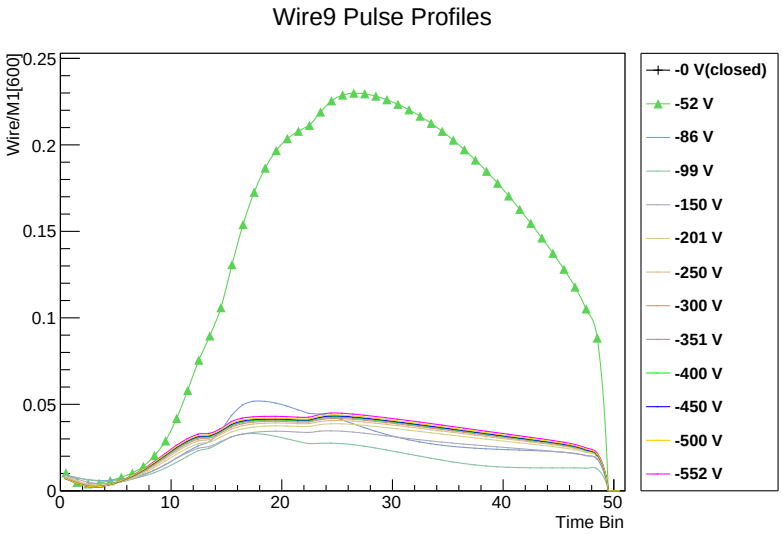

(a) Wire 9 pulse profiles for each run overlayed in one plot.

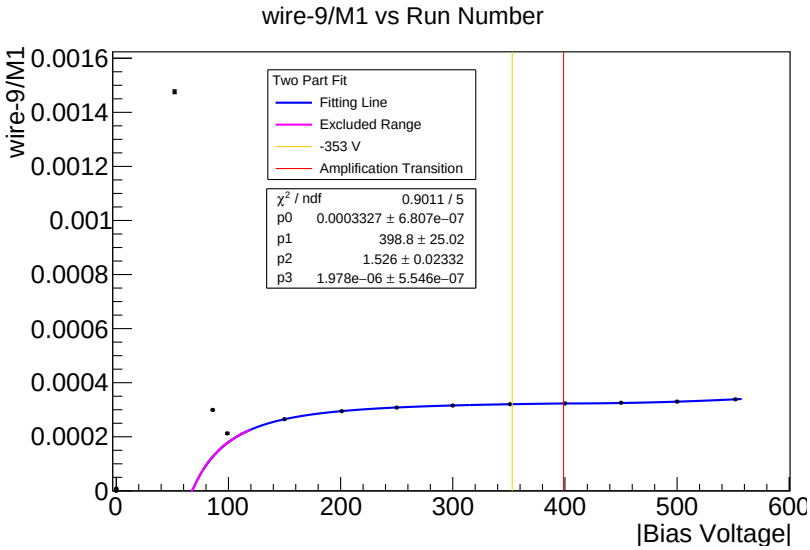

(b) Wire 9 integrated signal divided by M1 integrated signal plotted vs applied bias voltage.

Figure E.11: Wire 9 Voltage Scan

Appendix F

Intensity Scan Results

A selection of the beam intensity scan results.

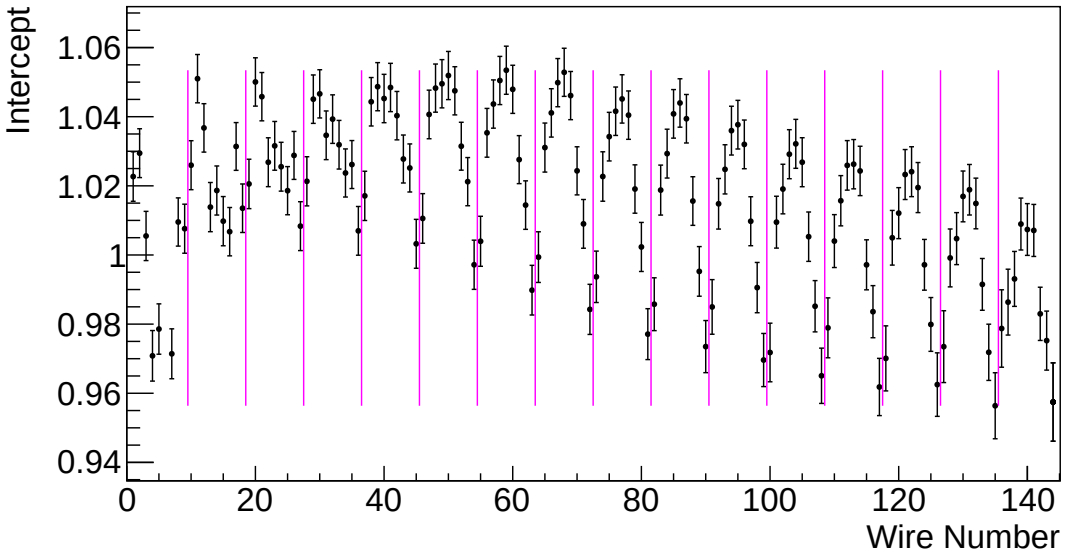

Figure F.1: Y-axis intercept from target chamber linearity curve fitting.

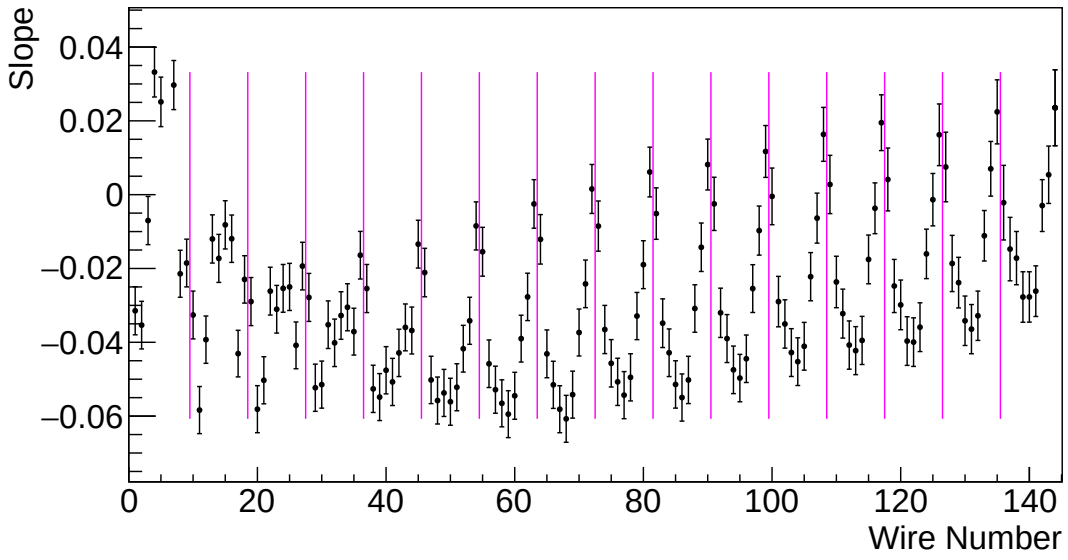

Figure F.2: Slope from target chamber linearity curve fitting.

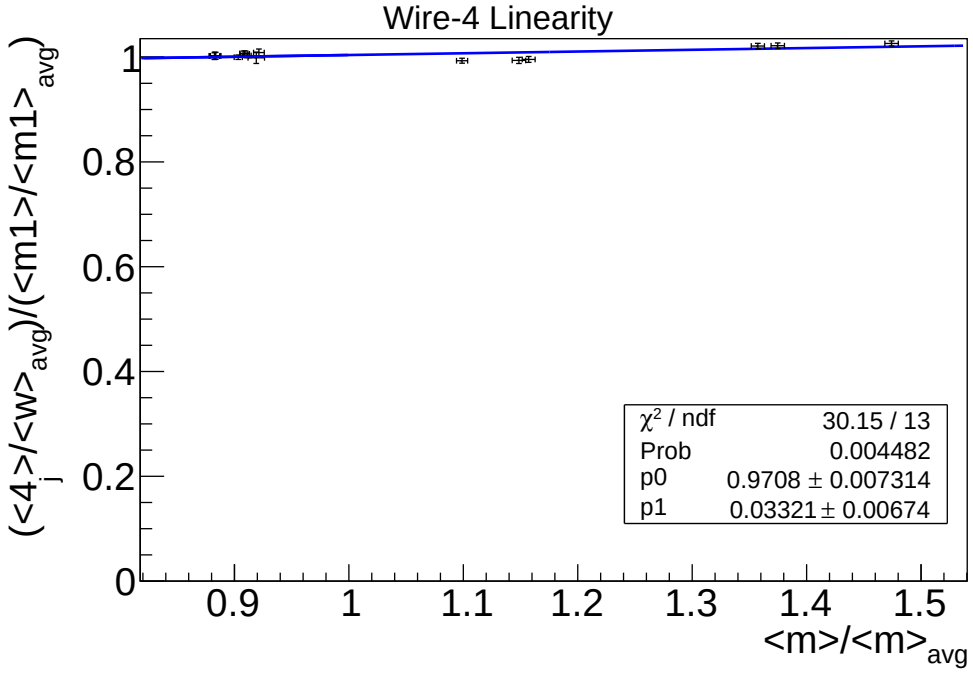

Figure F.3: Linearity plot for wire 4

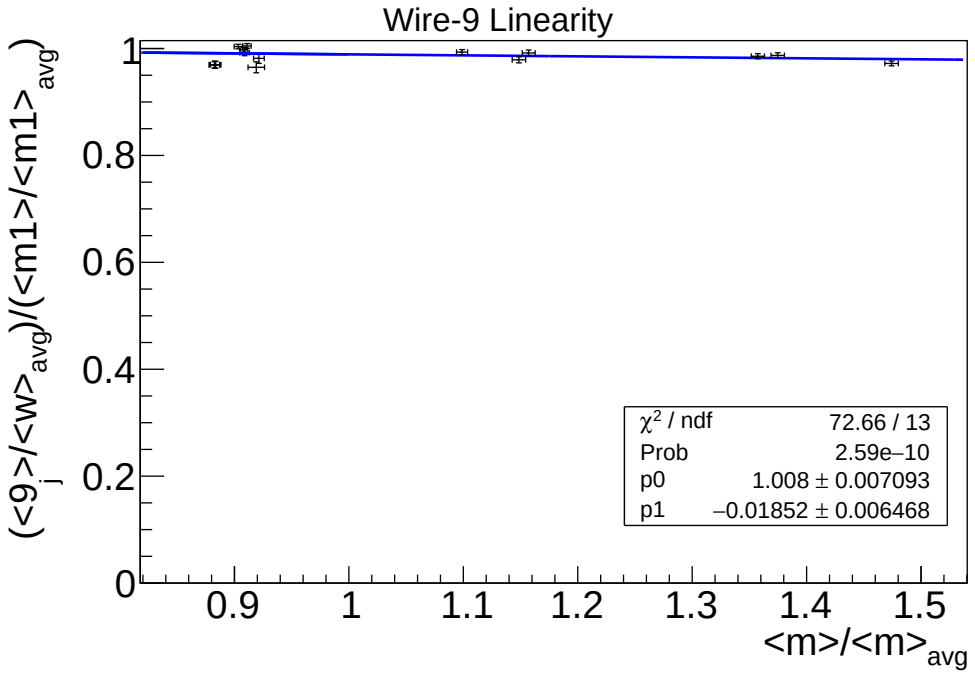

Figure F.4: Linearity plot for wire 9

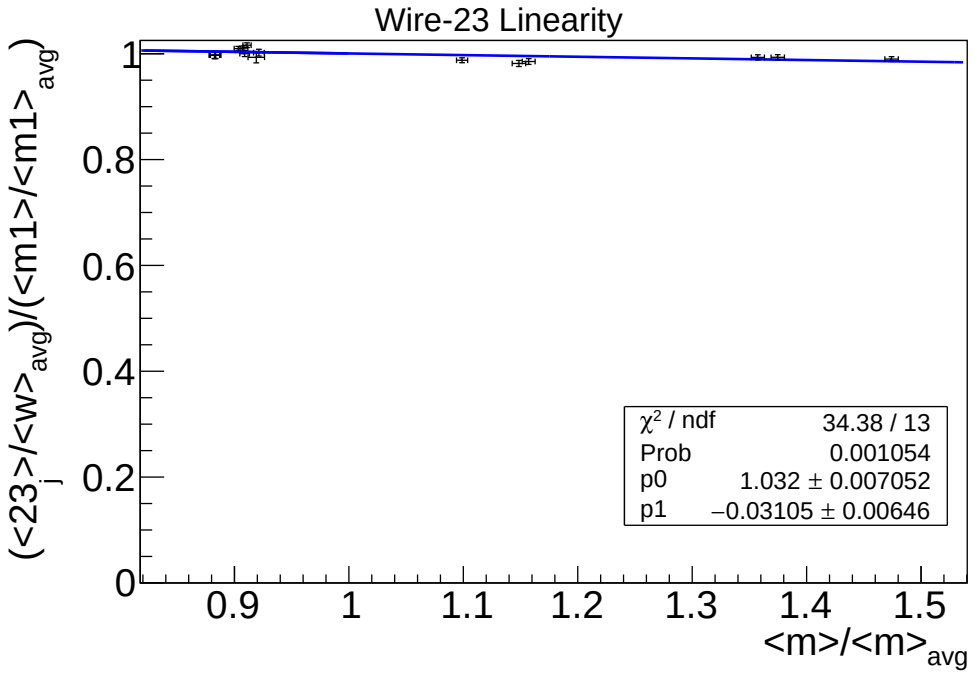

Figure F.5: Linearity plot for wire 23

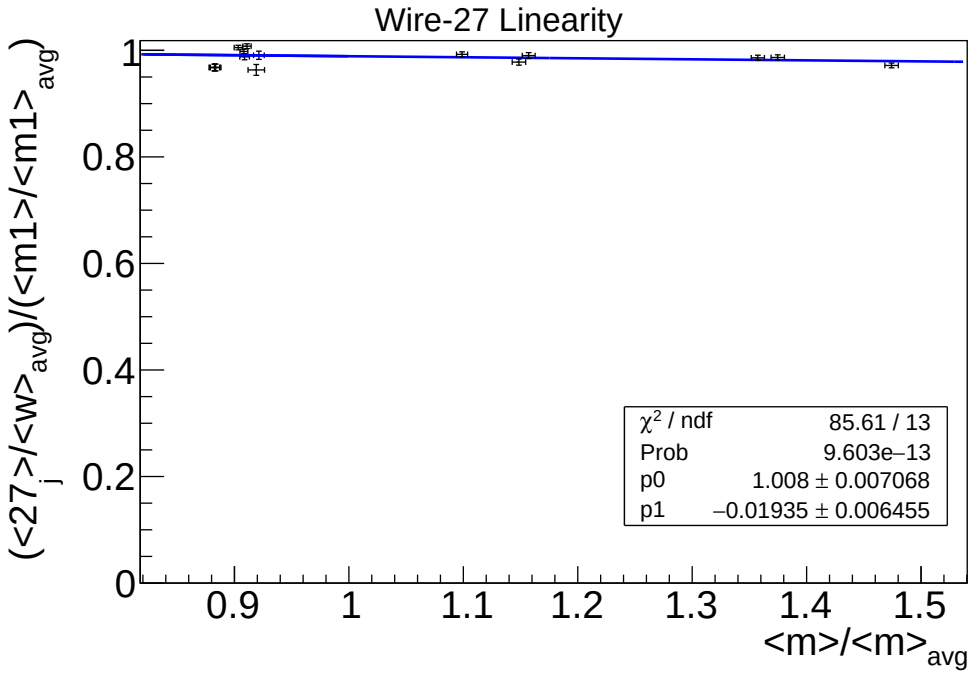

Figure F.6: Linearity plot for wire 27

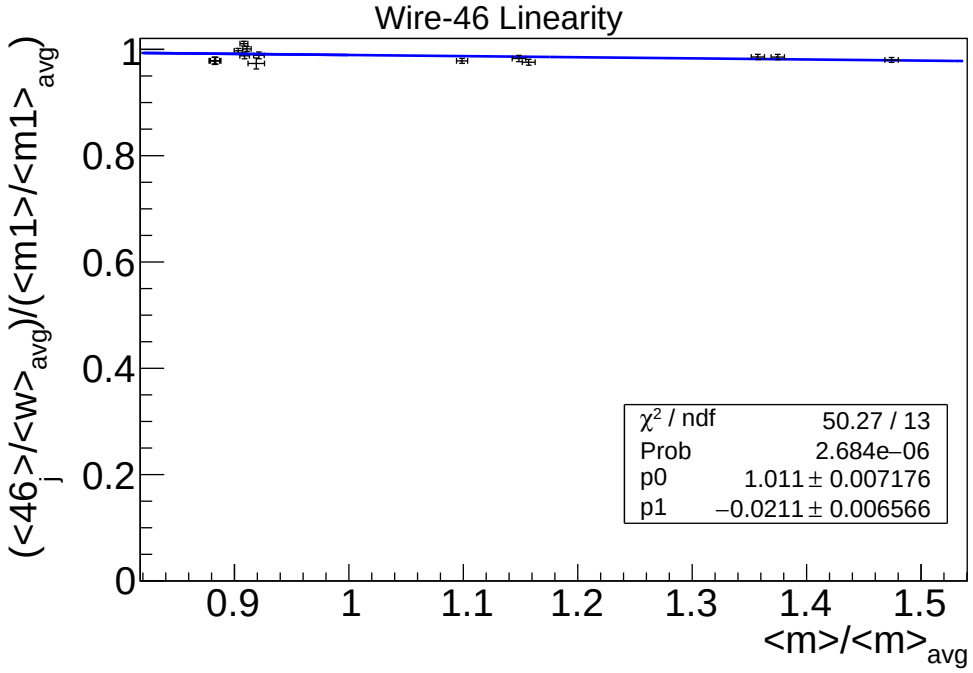

Figure F.7: Linearity plot for wire 46

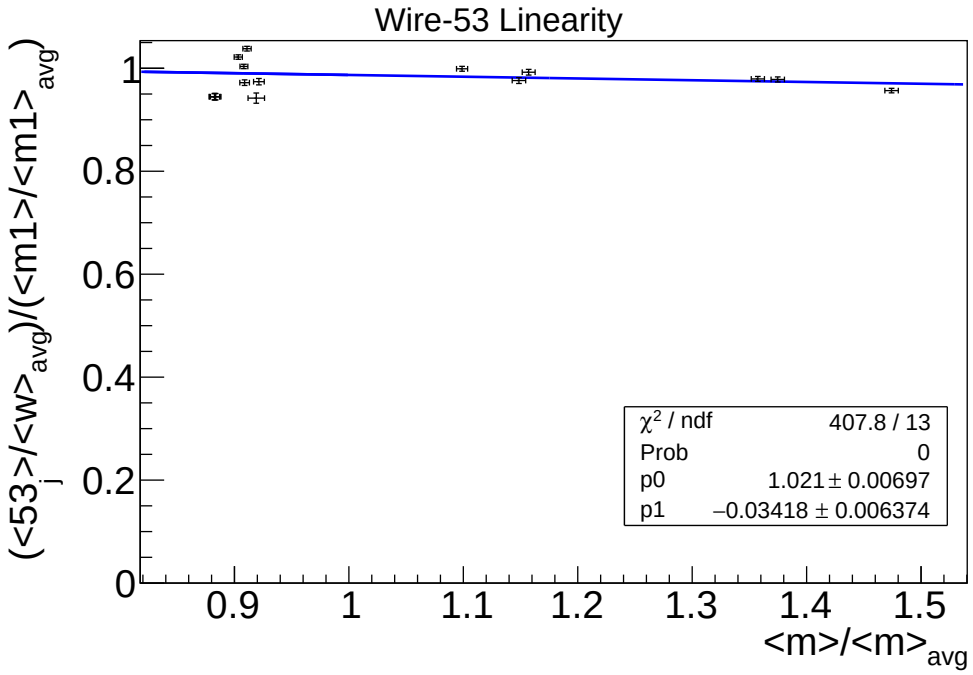

Figure F.8: Linearity plot for wire 53

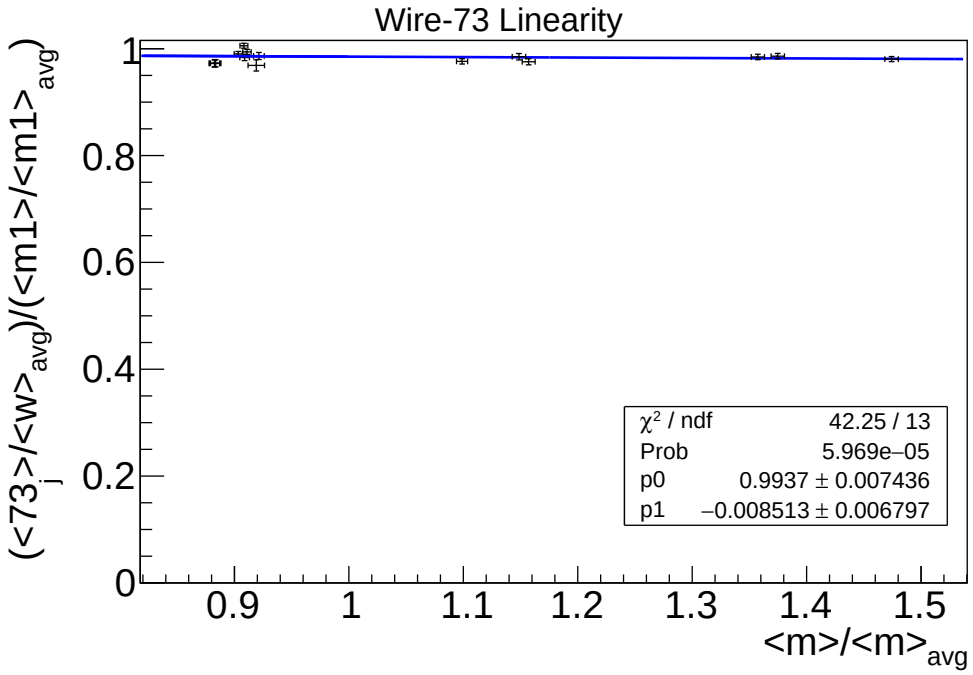

Figure F.9: Linearity plot for wire 73

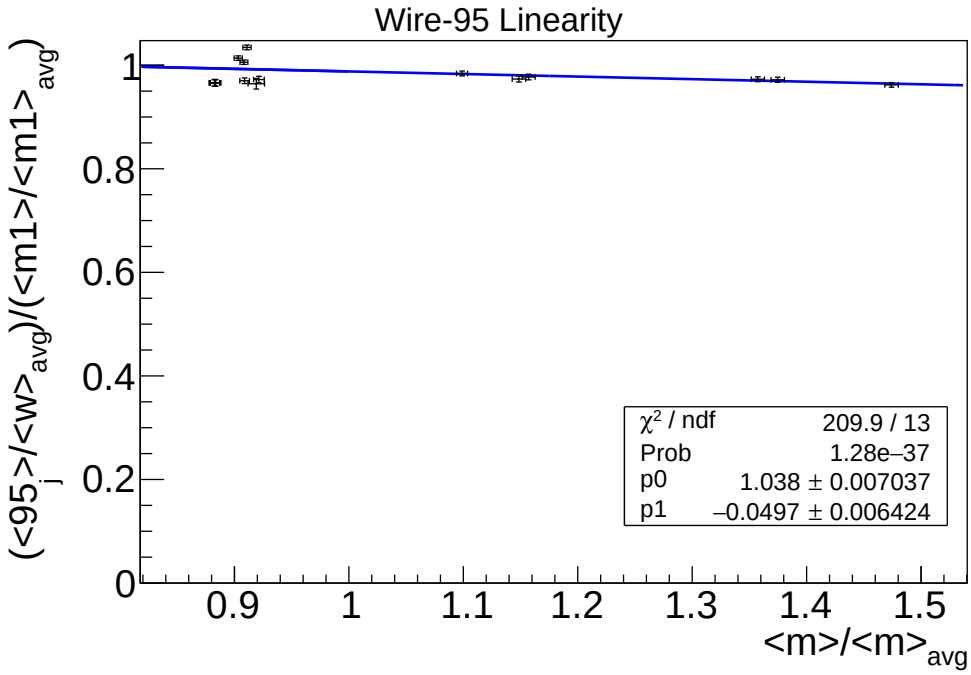

Figure F.10: Linearity plot for wire 95

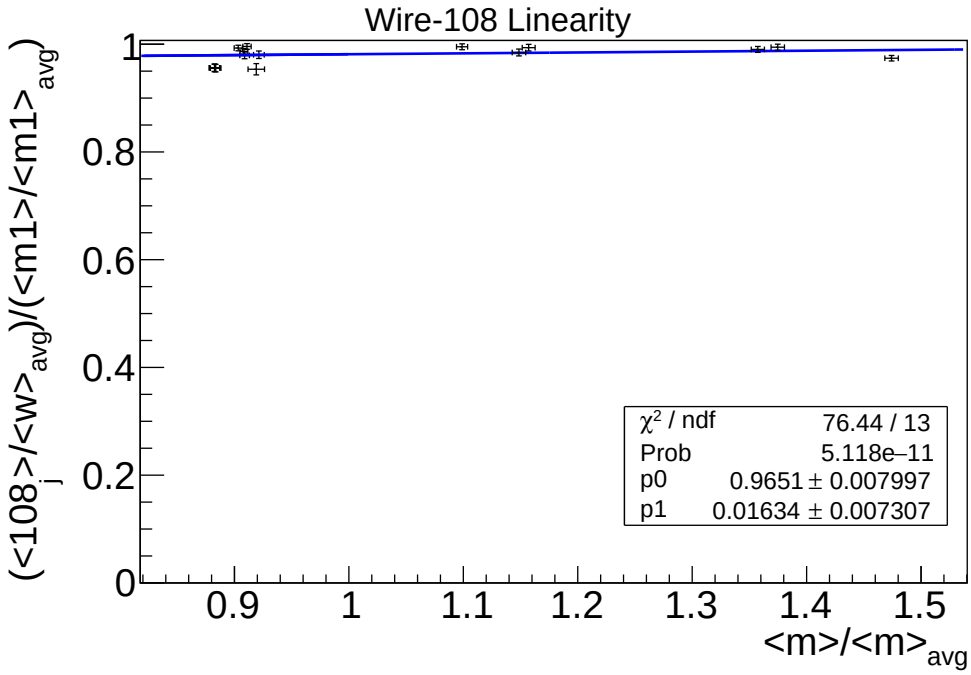

Figure F.11: Linearity plot for wire 108

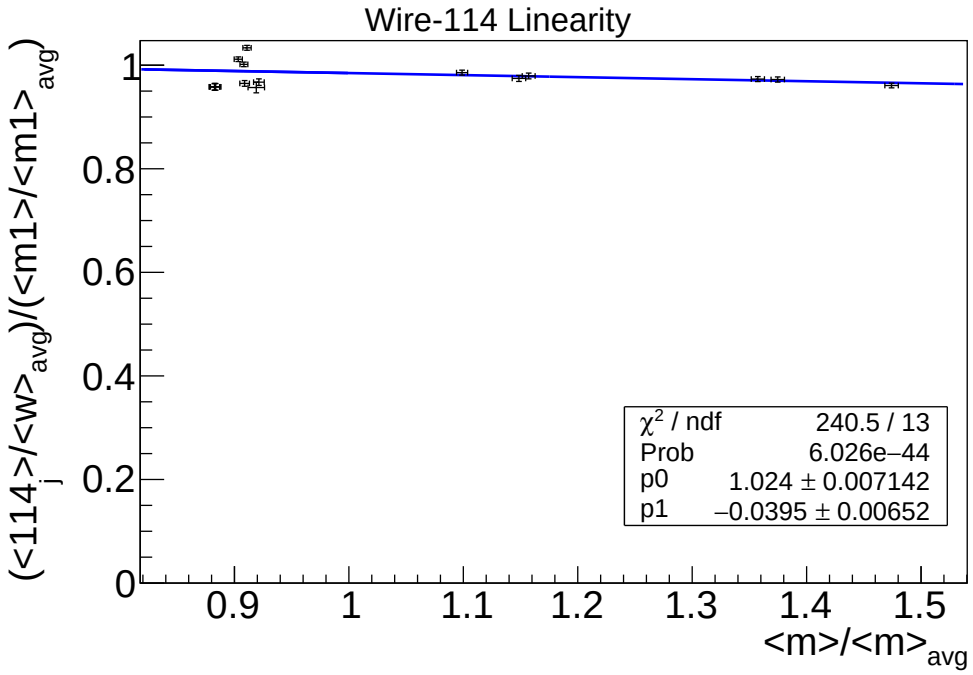

Figure F.12: Linearity plot for wire 114

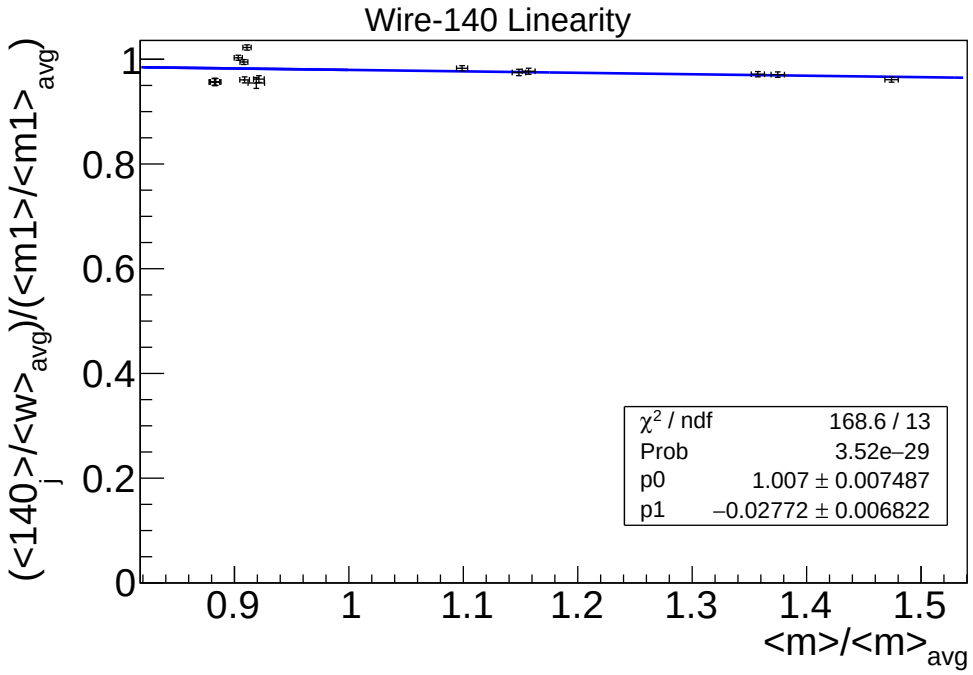

Figure F.13: Linearity plot for wire 140

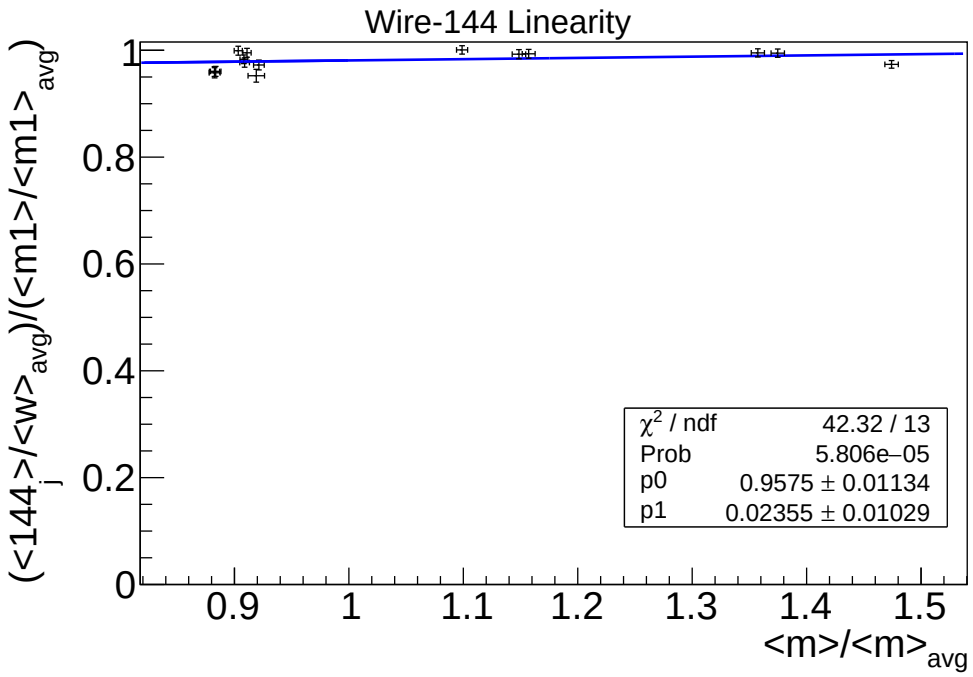

Figure F.14: Linearity plot for wire 144

Appendix G

Garfield++ Simulations Plots

G.1 Field Map Slices

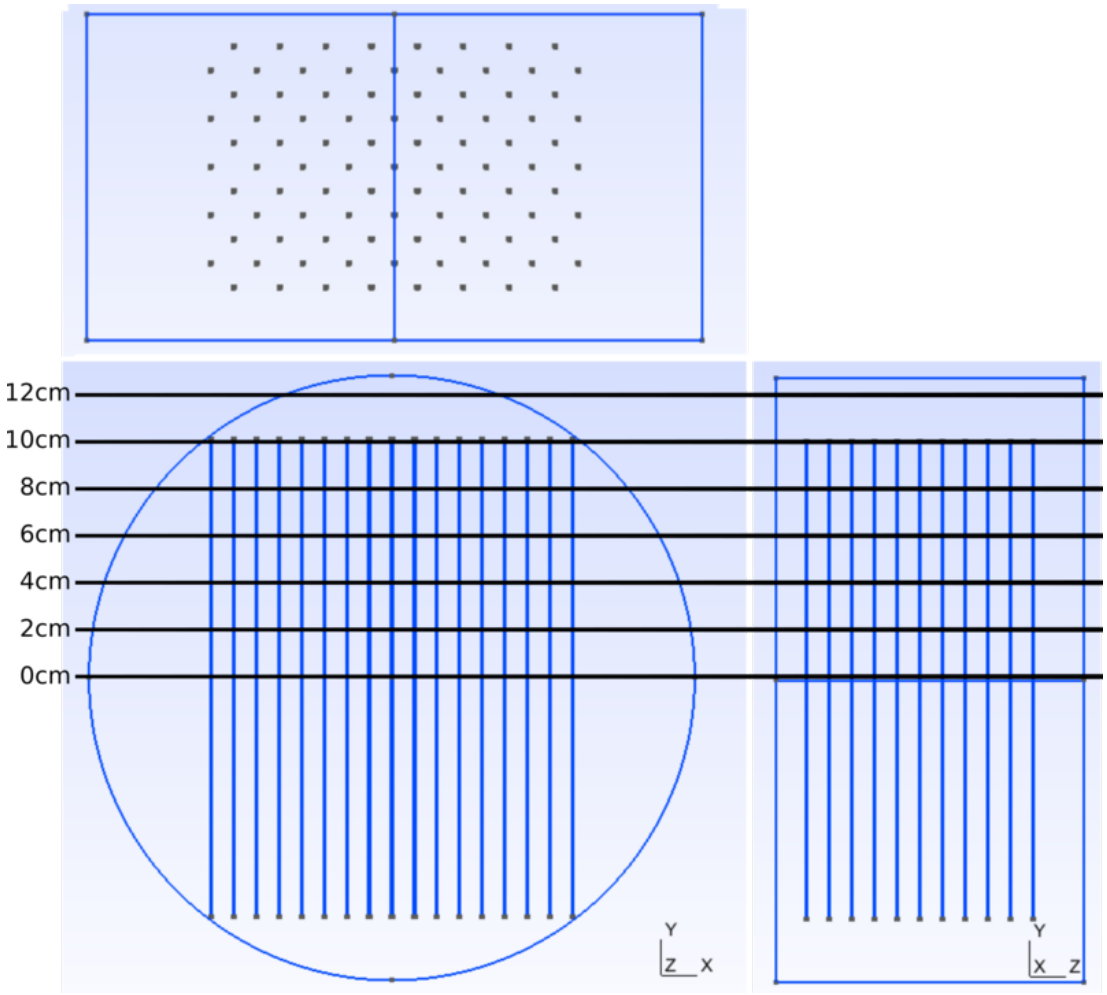

Figure G.1: Field map slice locations.

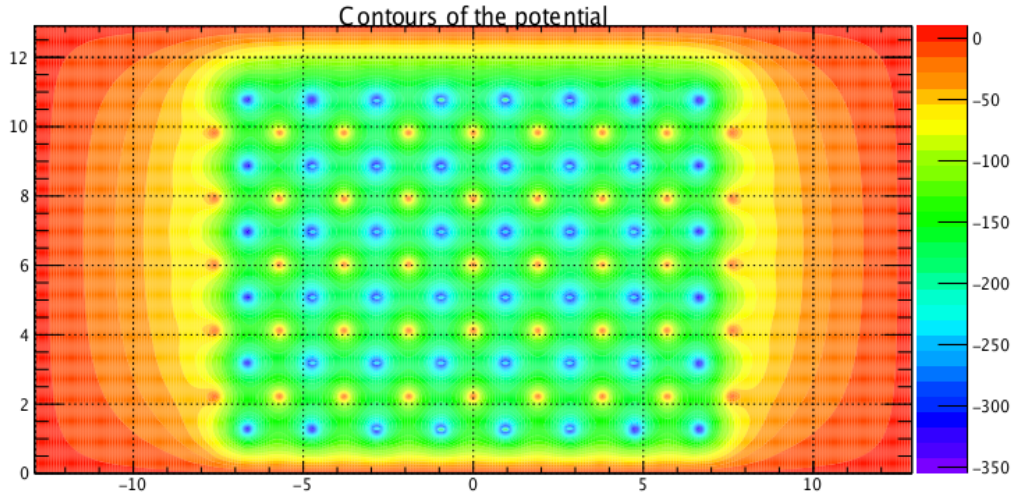

Figure G.2: Electric field cross section through central axis of the cylinder with the wires perpendicular to the page.

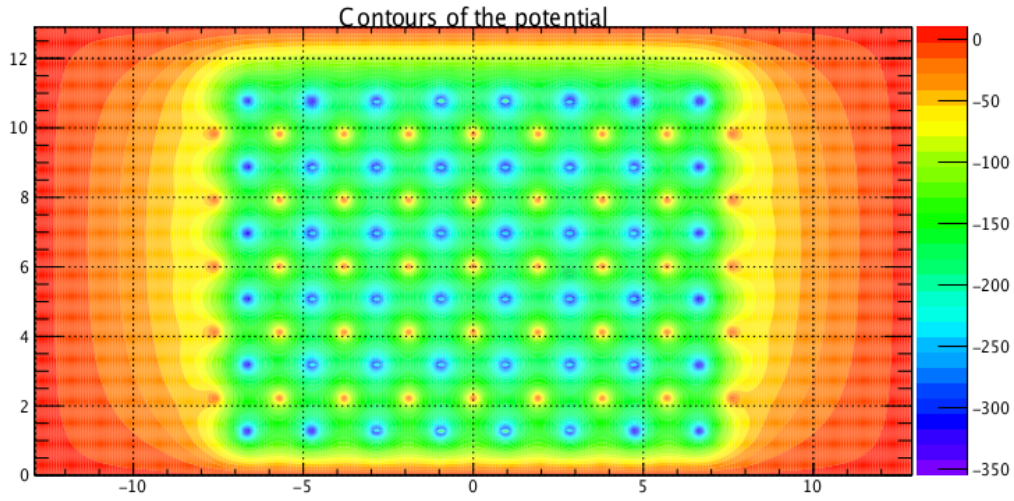

Figure G.3: Electric field cross section offset 2 cm from the axis of the cylinder with the wires perpendicular to the page.

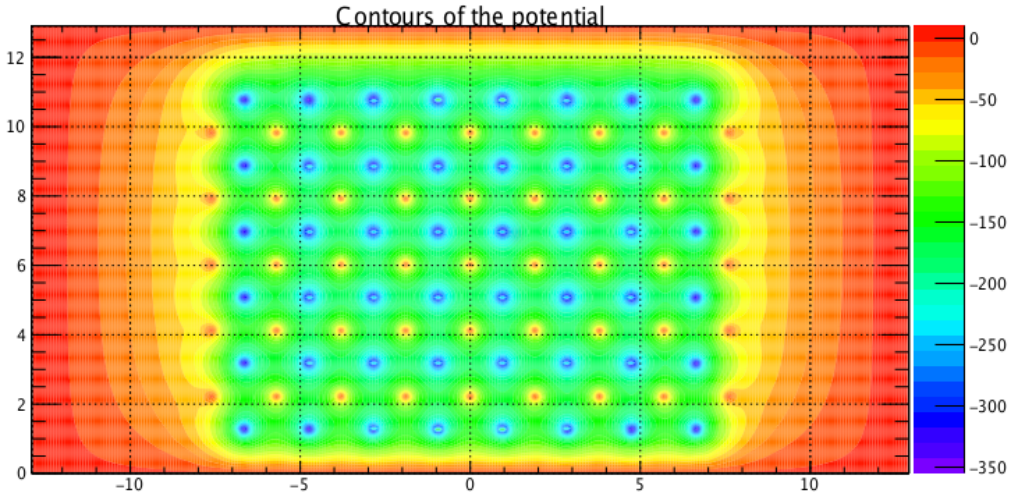

Figure G.4: Electric field cross section offset 4 cm from the axis of the cylinder with the wires perpendicular to the page.

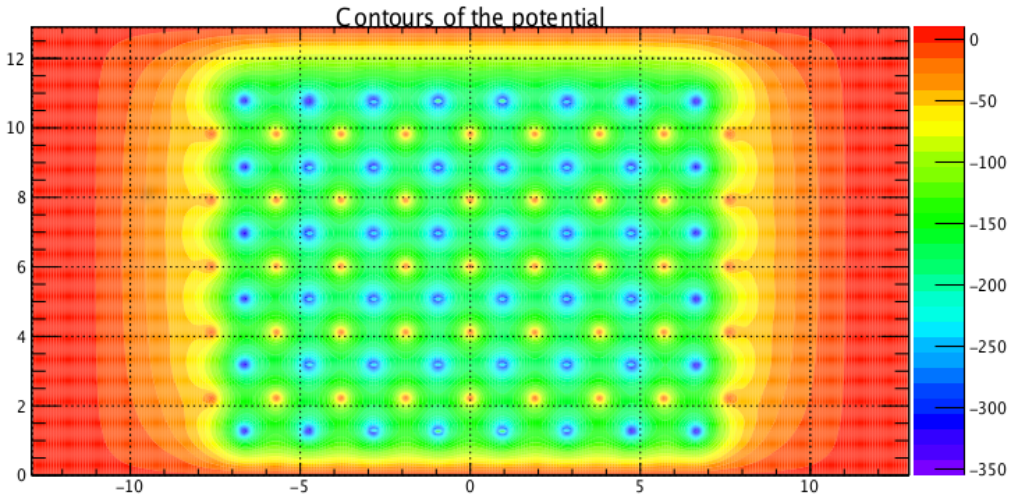

Figure G.5: Electric field for cross section offset 6 cm from the axis of the cylinder with the wires perpendicular to the page.

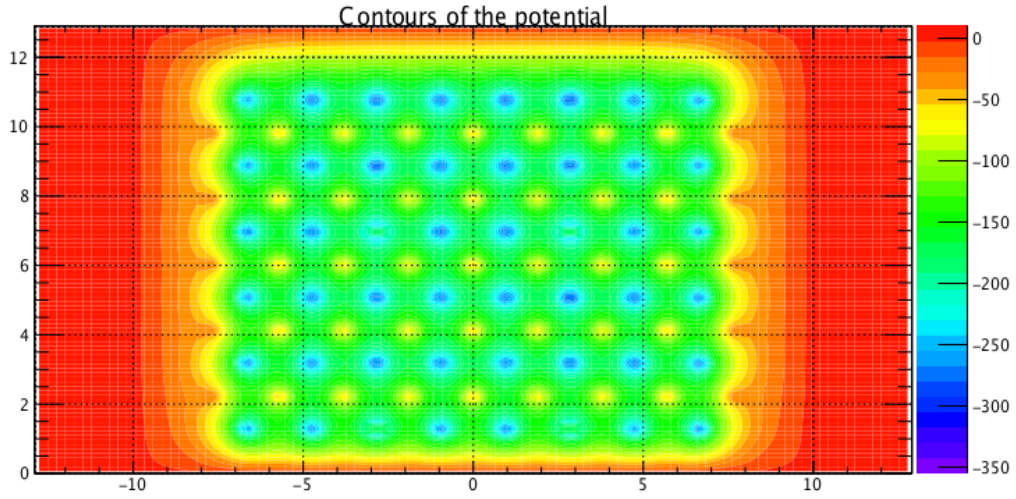

Figure G.6: Electric field for cross section offset 8 cm from the axis of the cylinder with the wires perpendicular to the page.

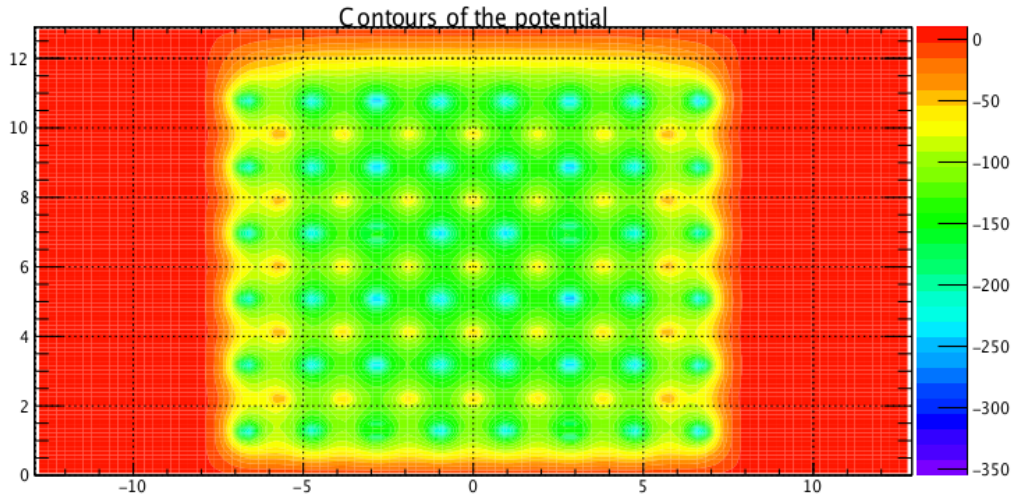

Figure G.7: Electric field for cross section offset 10 cm from the axis of the cylinder with the wires perpendicular to the page.

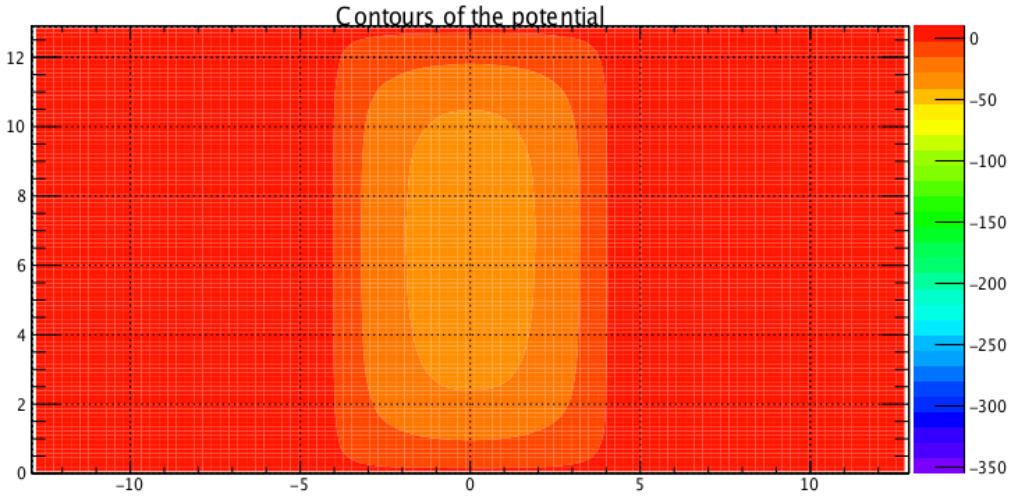

Figure G.8: Electric field for cross section offset 12 cm from the axis of the cylinder with the wires perpendicular to the page.

Bibliography

[1] P.F. Bedaque and U. van Kolck. "Effective field theory for few-nucleon systems". English. *Annual Review of Nuclear and Particle Science* 52 (2002), 339–396. ISSN: 0163-8998. DOI: 10.1146/annurev.nucl.52.050102.090637.

[2] CERN. *The Standard Model*. http://home.cern/about/physics/standard-model. Jan. 2016.

[3] *Standard Model of Elementary Particles*. https://commons.wikimedia.org/wiki/File:Standard_Model_of_Elementary_Particles.svg. accessed Jan. 20 2016. Orignal shared under Creative Commons Attribution-ShareAlike 3.0 Unported (http://creativecommons.org/licenses/by-sa/3.0/).

[4] K. A. Olive et al. "Review of Particle Physics". *Chin. Phys.* C38 (2014), p. 090001. DOI: 10.1088/1674-1137/38/9/090001.

[5] Gericke et al. "Measurement of parity-violating γ-ray asymmetry in the capture of polarized cold neutrons on protons". *Phys. Rev. C* 83 (1 Jan. 2011), p. 015505. DOI: 10.1103/PhysRevC.83.015505. URL: http://link.aps.org/doi/10.1103/PhysRevC.83.015505.

[6] B. Desplanques, J. F. Donoghue, and B. R. Holstein. "Unified Treatment of the Parity Violating Nuclear Force". *Annals of Physics* 124 (1980), pp. 449–495.

[7] W.M. Snow. "Neutron Measurements and the Weak Nucleon-Nucleon Interaction". *J. Res. Natl. Inst. Stand. Technol.* 110 (2005), pp. 189–194.

[8] J. D. Bowman, C. Crawford, and M. T. Gericke. "A Measurement of the Parity Violating Proton Asymmetry in the Capture of Polarized Cold Neutrons on ^{3}He, A proposal submitted to the SNS FNPB PRAC" (Nov. 2007).

[9] Michael J. Ramsey-Musolf and Shelley A. Page. "Hadronic Parity Violation: A New View Through the Looking Glass". *Annual Review of Nuclear and Particle Science* 56.1 (2006), pp. 1–52. DOI: 10.1146/annurev.nucl.54.070103.181255. eprint: http://www.annualreviews.org/doi/pdf/10.1146/annurev.nucl.54.070103.181255. URL: http://www.annualreviews.org/doi/abs/10.1146/annurev.nucl.54.070103.181255.

[10] Shi Lin Zhu et al. "Nuclear parity violation in effective field theory". *Nuclear Physics, Section A* 748.3-4 (Feb. 2005), pp. 435–498. ISSN: 0375-9474. DOI: 10.1016/j.nuclphysa.2004.10.032.

[11] C. S. Wu et al. "Experimental Test of Parity Conservation in Beta Decay". *Phys. Rev.* 105 (4 Feb. 1957), pp. 1413–1415. DOI: 10.1103/PhysRev.105.1413. URL: http://link.aps.org/doi/10.1103/PhysRev.105.1413.

[12] Matthias R. Schindler and Roxanne P. Springer. "Two parity-violating asymmetries from in pionless effective field theories". *Nuclear Physics A* 846.14 (2010), pp. 51 –62. ISSN: 0375-9474. DOI: 10.1016/j.nuclphysa.2010.

06.002. URL: http://www.sciencedirect.com/science/article/pii/S0375947410005300.

[13] M. Viviani et al. "Parity-violating asymmetry in the ^{3}He($\tilde{n}$, p)^{3}H reaction". *Phys. Rev. C* 82 (4 Oct. 2010), p. 044001. DOI: 10.1103/PhysRevC.82.044001.

[14] J. D. Bowman, C. Crawford, and M. T. Gericke. "A Proposal Update for A Measurement of the Parity Violating Proton Asymmetry in the Capture of Polarized Cold Neutrons on ^{3}He" (Nov. 2009).

[15] J. M. Carpenter. *Neutron Production, Moderation, and Characterization of Sources*. Tech. rep. Aug. 2004.

[16] *Artists Conception of SNS*. http://neutrons2.ornl.gov/facilities/SNS/works.shtml (accessed June 2016). Dec. 2015.

[17] *SNS aerial*. https://www.flickr.com/photos/departmentofenergy/8003094179/ (accessed June 2016). Sept. 2012.

[18] *How the Spallation Neutron Source Works*. http://neutrons-old.ornl.gov/facilities/SNS/works.shtml. Jan. 2016.

[19] *Behind the scenes of the Spallation Neutron Source - The linear accelerator*. https://www.youtube.com/watch?v=KWcyHXIRhwE. Mar. 2016.

[20] F. MEZEI. "Novel Polarized Neutron Devices - Supermirror and Spin Component Amplifier". *Communications on Physics* 773 (3 1976), pp. 81 –85.

[21] N. Fomin et al. "Fundamental neutron physics beamline at the spallation neutron source at ORNL". *Nuclear Instruments and Methods in Physics Research Section A: Accelerators, Spectrometers, Detectors and Associated Equipment* 1

(3 2015), pp. 45 –51. ISSN: 0168-9002. DOI: 10.1016/j.nima.2014.10.042. URL: http://www.sciencedirect.com/science/article/pii/S0168900214011991.

[22] P. Huffman et al. "Beamline Performance Simulations for the Fundamental Neutron Physics Beamline at the Spallation Neutron Source." *Journal of Research of the National Institute of Standards and Technology* 110(3) (2005), pp. 161–168.

[23] W. Kockelmann et al. "Energy-selective neutron transmission imaging at a pulsed source". *Nuclear Instruments and Methods in Physics Research A* (May 2007).

[24] G. L. Jones et al. "Precision Measurement of A_γ in $\vec{n} + p \to d + \gamma$, Letter of Intent/ Initial Proposal for FnPB at SNS" (Aug. 2005).

[25] J. F. Caviagnac et al. "Search for Parity Violation in Neutron Proton Capture". *Phys. Lett.* 67B.148 (1977).

[26] Michael Gericke. "The NPDGamma Experiment: The Weak Interaction Between Nucleons and Parity Violation in Cold Neutron Capture". PhD thesis. Indiana University, 2004.

[27] *Swiss Neutronics*. www.swissneutronics.ch (accessed July 2016). Bruehlstrasse 28, CH-5313, Klingnau, Switzerland.

[28] Chris Bradshaw Hayes. "Spin Flipper, Neutron Polarimetry and Simulation for the n3He Experiment". PhD thesis. University of Tennessee, Knoxville, 2016.

[29] Jiawei Mei. "Precision Measurement of Parity Violation in Polarized Cold Neutron Capture on the Proton: the NPDγ Experiment". PhD thesis. Indiana University, 2011.

[30] Seo P.-N. et al. "High-efficiency resonant rf spin rotator with broad phase space acceptance for pulsed polarized cold neutron beams". *Phys. Rev. ST Accel. Beams* 11 (8 Aug. 2008), p. 084701. DOI: 10.1103/PhysRevSTAB.11.084701. URL: http://link.aps.org/doi/10.1103/PhysRevSTAB.11.084701.

[31] Matthew Martin Musgrave. "Neutron Polarimetry with Polarized 3He for the NPDGamma Experiment". PhD thesis. University of Tennessee, Knoxville, 2014.

[32] M.B. Chadwick et al. "ENDF/B-VII.1 Nuclear Data for Science and Technology: Cross Sections, Covariances, Fission Product Yields and Decay Data". *Nuclear Data Sheets* 112.12 (2011). Special Issue on ENDF/B-VII.1 Library, pp. 2887 –2996. ISSN: 0090-3752. DOI: 10.1016/j.nds.2011.11.002.

[33] S. F. Mughabghab. *Atlas of Neutron Resonances*. 5th. 2006.

[34] K. B. Grammer et al. "Measurement of the scattering cross section of slow neutrons on liquid parahydrogen from neutron transmission". *Phys. Rev. B* 91 (18 May 2015), p. 180301. DOI: 10.1103/PhysRevB.91.180301. URL: http://link.aps.org/doi/10.1103/PhysRevB.91.180301.

[35] Zhaowen Tang. "Parity Violation in Polarized Neutron Capture on Parahydrogen and Aluminum". PhD thesis. Indiana University, 2014.

[36] M. T. Gericke et al. "A Current mode detector array for gamma-ray asymmetry measurements". *Nucl. Instrum. Meth.* A540 (2005), pp. 328–347. DOI: 10.1016/j.nima.2004.11.043. arXiv: nucl-ex/0411022 [nucl-ex].

[37] K. Grammer. *Calculation of Geometrical Factors for the Chlorine, Aluminum, and Hydrogen Targets and Measurement of the Detector Center of Response Shift Angles in the $n + p \to d + \gamma$ Experiment*. Tech. rep. 2013.

[38] N. Fomin and The NPDGamma Collaboration. "NPDGamma: Measurement of the Parity-Violating directional Gamma-ray Asymmetry in Polarized Neutron Capture on Protons". *Draft in Progress* (July 2015).

[39] M. Viviani et al. "Chiral effective field theory analysis of hadronic parity violation in few-nucleon systems". *Phys. Rev. C* 89 (6 June 2014), p. 064004. DOI: 10.1103/PhysRevC.89.064004. URL: http://link.aps.org/doi/10.1103/PhysRevC.89.064004.

[40] Eric Lee Plemmons. "Installation and Alignment of the N3He Experiment". MA thesis. University of Tennessee, 2015.

[41] Latiful Kabir. *Private Communications*. Mar. 2016.

[42] F. Sauli. *Principles of the Operation of Multiwire Proportional and Drift Chambers*. CERN European Organization for Nuclear Research, 1977.

[43] M.J. Berger et al. *ESTAR, PSTAR, and ASTAR: Computer Programs for Calculating Stopping-Power and Range Tables for Electrons, Protons, and Helium Ions (version 1.2.3)*. http://physics.nist.gov/Star (accessed Mar. 8 2016). 2005.

[44] W. Blum and L. Rolandi. *Particle Detection With Drift Chambers*. Springer-Verlag, 1994.

[45] Doug Sim. *Modified version of Detector Regions image*. `https://commons.wikimedia.org/wiki/File:Detector_regions.gif`. accessed April 22 2016. Orignal shared under Creative Commons Attribution-ShareAlike 3.0 Unported (`http://creativecommons.org/licenses/by-sa/3.0/`) and modified image is available under the same license.

[46] *Shockley-Ramo Theorem*. `https://en.wikipedia.org/wiki/Shockley-Ramo_theorem`. accessed: Jan. 27 2016.

[47] Helmuth Spieler. *Semiconductor Detector Systems*. Oxford University Press, 2005. ISBN: 978-0-19-852784-8.

[48] Michael A. Lieberman and Allan J. Lichtenberg. *Principles of plasma discharges and materials processing*. 2d. Wiley Interscience, 2005.

[49] William A. Campbell Jr. and John J. Scialdone. *Outgassing Data for Selecting Spacecraft Materials*. `https://outgassing.nasa.gov/`. Sept. 1993.

[50] M. Tavlet and van der Burgt H. "Radiation resistance and other safety aspects of high-performance plastics by ERTA". *Workshop on Advanced Materials for High Precision Detectors*. CERN. Sept. 1994.

[51] Precision Ceramics. *Macor Machinable Glass Ceramic*. `http://www.precision-ceramics.co.uk/macor-machinable-glass-ceramic-composition.htm` (accessed June 6 2016).

[52] W.A. Coghlan and F.W. Clinard. "Damage to Macor glass-ceramic from high-dose 14 MeV neutrons". *Journal of Nuclear Materials* 179 (1991), pp. 391 – 394. ISSN: 0022-3115. DOI: 10.1016/0022-3115(91)90107-I. URL: http://www.sciencedirect.com/science/article/pii/002231159190107I.

[53] *Autodesk Inc.* http://www.autodesk.com/products/inventor/overview (accessed April 2016).

[54] Atlas Technologies. *Aluminums Extreme Vacuum Performance.* http://www.atlasuhv.com/Technology/AluminumVacuum.aspx (access Feb. 4 2016).

[55] Atlas Technologies. *Atlas CF^{TM} Flange All-Metal Sealing for Aluminum Vacuum.* http://www.atlasuhv.com/bimetal/atlascfflange.aspx (accessed Feb. 4 2016).

[56] *Accu-Glass High Temperature UHV Compatible Epoxy.* http://accuglassproducts.com/product.php?productid=17221&cat=0&page=1 (accessed June 2016).

[57] Robert C. Weast. *CRC handbook of chemistry and physics: a ready-reference book of chemical and physical data, 91st edition.* English. 2010. URL: http://www.hbcpnetbase.com/.

[58] ProkopHapala. *Standard Model of Elementary Particles.* https://commons.wikimedia.org/wiki/File:Common_light_element_moderators,_reflectors_and_absorbers.svg. accessed Aug. 2 2016. Orignal shared under Creative Commons Attribution-ShareAlike 3.0 Unported (http://creativecommons.org/licenses/by-sa/3.0/).

[59] NIST. *Neutron scattering lengths and cross sections*. http://www.ncnr.nist.gov/resources/n-lengths/. Oct. 2011.

[60] Donald E. Groom, Nikolai V. Mokhov, and Sergei I. Striganov. "Muon stopping power and range tables 10-MeV to 100-TeV". *Atom. Data Nucl. Data Tabl.* 78 (2001), pp. 183–356. DOI: 10.1006/adnd.2001.0861.

[61] Richard J. Mathar. "Solid angle of a recatangular plane" (2015).

[62] Elise Marin. *Elog 167 - Calibration of M2 and Triple Monitor*. Tech. rep. NPDGamma Collaboration, 2011.

[63] Libertad Barron. *Efficiency of the Triple Monitor*. Tech. rep. NPDGamma Collaboration, 2011.

[64] S. Balascuta, Tang Zhaowen, and David Bowman. *The measurement of the neutron flux at the center of the NPDGamma detector array*. Tech. rep. NPDGamma Collaboration, July 2011.

[65] Atlas Technologies. http://www.atlasuhv.com/ (accessed June 2016).

[66] Latiful Kabir. *Private Communications*. June 2016.

[67] Rogers Corporation. https://www.rogerscorp.com/acs/producttypes/6/RT-duroid-Laminates.aspx. July 2016.

[68] Rogers Corporation. *The Effect of Nuclear Radiation Exposure to RT/duroid® PTFE-Based Composites*. https://www.rogerscorp.com/documents/753/acs/The-Effect-of-Exposure-of-RT-duroid-PTFE-Based-Composites-to-Nuclear-Radiation.pdf (accessed July 2016). 2015.

[69] Michael Gericke. *GEANT4 Dilution Factor Simulation Results*. https://n3he.wikispaces.com/Simulations (accessed July 27 2016). Jan. 2015.

[70] Chris Coppola. *MCSTAS Simulation*. https://n3he.wikispaces.com/Simulations (accessed July 27 2016). July 2014.

[71] H. Schindler. *Garfield++ User Guide 2015.1*. http://garfieldpp.web.cern.ch/garfieldpp/documentation/ (accessed Sept. 2015).

[72] C. Geuzaine and J. Remacle. "Gmsh: A 3D finite element mesh generator with builtin pre and postprocessing facilities". *International Journal for Numerical Methods in Engineering* 79.11 (2009), pp. 1309–1331.

[73] Christophe Geuzaine and Jean-Fran¸cois Remacle. *Gmsh: a three dimensional finite element mesh generator*. URL: geuz.org/gmsh.

[74] *Elmer: Open Source Finite Element Software for Multiphysical Problems*. http://www.csc.fi/english/pages/elmer.

[75] Josh Renner. *Detector Simulation in Garfield++ with Open-Source Finite Element Electrostatics*. http://garfieldpp.web.cern.ch/garfieldpp/examples/elmer/garfield_elmer_doc.pdf (accessed Sept. 2015).

[76] H.W. Ellis et al. "Transport properties of gaseous ions over a wide energy range". *Atomic Data and Nuclear Data Tables* 17.3 (1976), pp. 177 –210. ISSN: 0092-640X. DOI: 10.1016/0092-640X(76)90001-2. URL: http://www.sciencedirect.com/science/article/pii/0092640X76900012.